

**DEVELOPMENT OF MEMBRANE-ACTIVE SMALL MOLECULES WITH
ANTIBACTERIAL ACTIVITY**

AN ABSTRACT

SUBMITTED ON THE TWENTY-NINTH DAY OF AUGUST, 2022

TO THE DEPARTMENT OF CHEMISTRY

IN PARTIAL FULFILLMENT OF THE REQUIREMENTS

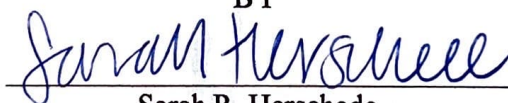
OF THE SCHOOL OF SCIENCE AND ENGINEERING

OF TULANE UNIVERSITY

FOR THE DEGREE OF

DOCTOR OF PHILOSOPHY

BY



Sarah R. Herschede

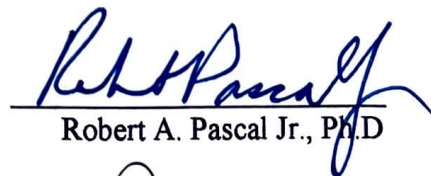
APPROVED:



Nathalie Busschaert, Ph.D.
Advisor



Bruce C. Gibb, Ph.D.



Robert A. Pascal Jr., Ph.D.



Igor V. Rubtsov, Ph.D.

ABSTRACT

Developing receptors for membrane lipids is a growing area of research because of its potential in antibiotic and cancer therapy. Previous work in lipid recognition has largely focused on electrostatic attraction, which may be unselective or limit usefulness in drug design from poor bioavailability. Additionally, membrane-active antibiotics can overcome many resistance mechanisms, but their mode of action is not well defined. This work aims to contribute to the understanding of phospholipid recognition in bacteria and the mechanistic pathways of membrane-active antibiotics. In **Chapter 2**, three bis-ureas were designed to target the two phosphate groups of cardiolipin. The bis-ureas showed minimal activity in lipid binding and antibiotic assays. Cardiolipin's large size and anionic nature made this lipid challenging to work with in binding studies, so subsequent work focused on zwitterionic lipids. In **Chapter 3**, a urea functionalized crown ether exhibited selective lipid binding of phosphatidylethanolamine and antibiotic activity toward certain Gram-positive bacteria. This suggests that small molecules can be designed for lipid recognition and antibiotic therapy, despite the unsuccessful results from **Chapter 2**. Interestingly, a simple urea designed as a control analog for phosphatidylethanolamine exhibited higher antibiotic activity than others and no measurable lipid binding. **Chapter 4** determined that the urea was acting as a membrane-targeting antibiotic using an image-based profiling assay. Since ureas are well known for their chloride transport ability, this was also examined, which determined that its activity likely comes from chloride transport.

**DEVELOPMENT OF MEMBRANE-ACTIVE SMALL MOLECULES WITH
ANTIBACTERIAL ACTIVITY**

A DISSERTATION

SUBMITTED ON THE TWENTY-NINTH DAY OF AUGUST, 2022

TO THE DEPARTMENT OF CHEMISTRY

IN PARTIAL FULFILLMENT OF THE REQUIREMENTS

OF THE SCHOOL OF SCIENCE AND ENGINEERING

OF TULANE UNIVERSITY


FOR THE DEGREE OF

DOCTOR OF PHILOSOPHY

BY


Sarah R. Herschede

APPROVED:


Nathalie Busschaert, Ph.D.
Advisor


Bruce C. Gibb, Ph.D.


Robert A. Pascal Jr., Ph.D.


Igor V. Rubtsov, Ph.D.

ACKNOWLEDGEMENTS

The research described in this dissertation would not have been possible without the support and inspiration from my peers and advisors at Tulane University. First, I would like to thank my supervisor, Dr. Nathalie Busschaert, for selecting me as her first graduate student and exposing me to the study of supramolecular chemistry. I would also like to thank the members of the Busschaert Group, Sarah Marshall, Elliot Williams, Rayhanus Salam, Surid Chowdhury, Mario Gonzáles, and Hassan Gneid, for their insight.

Additionally, I would like to thank Dr. Louis Lawson and Dr. Scott Grayson for sharing their labs with me at the beginning of my Ph.D. I am also grateful for the different technical expertise that was available to me from Tulane University. Assistance from Dr. Debby Grimm in Tulane University's Coordinated Instrument Facility allowed me to develop the assays used in **Chapter 4**. Funding for my work was also partially fulfilled by Tulane University, which I am thankful for.

Of course, I must also thank my friends, family, boyfriend, and dog. Their emotional support and inspiration helped me to complete my Ph.D.

TABLE OF CONTENT

Acknowledgements.....	i
Table of content.....	ii
Chapter 1 Introduction.....	1
1.1 The antibiotic resistance crisis.....	1
1.2 How supramolecular chemistry can combat antibiotic resistance.....	8
1.2.1 Foundation of supramolecular chemistry.....	9
1.2.2 Anion binding.....	10
1.2.3 Lipid binding.....	26
1.3 Membrane-targeting antibiotics.....	39
1.3.1 Structure of antimicrobial peptides.....	39
1.3.2 Mechanisms of antimicrobial peptides.....	40
1.4 Aim of this dissertation.....	44
Chapter 2 Developing neutral receptors for cardiolipin.....	45
2.1. Introduction.....	45
2.2. Results and Discussion.....	51
2.2.1. Design and synthesis of receptors for cardiolipin.....	51
2.2.2. ¹ H NMR binding studies.....	52
2.2.3. Liposome-based binding studies.....	56
2.2.4. Bacterial testing.....	59
2.3. Conclusion.....	61
Chapter 3 Urea functionalized crown ethers target phosphatidylethanolamine in bacterial membranes.....	63
3.1 Introduction.....	63
3.2 Results and discussion.....	71
3.2.1. Design and synthesis of novel phosphatidylethanolamine receptors.....	71
3.2.2. ¹ H NMR binding studies.....	72
3.2.3. Fluorescence titrations with POPE and POPC in liposomes.....	76
3.2.4. Calcein leakage assay.....	78
3.2.5. Lipid flip-flop.....	80
3.2.6. Antibacterial activity.....	81

3.3	Conclusions	87
Chapter 4	Identification of the Mechanism of Action for Urea-Based Antibiotics using Bacterial Cytological Profiling.....	88
4.1	Introduction	88
4.1.1	Development of BCP.....	89
4.1.2	BCP workflow	91
4.2	Results and Discussion	99
4.2.1	MIC determination of potential novel antibiotics	99
4.2.2	Selection of antibiotics with known MOA	103
4.2.3	Cell fixation and staining	105
4.2.4	Cell imaging	106
4.2.5	Statistical image analysis	112
4.2.6	Anion transport studies	122
4.3	Conclusion.....	124
Chapter 5	Materials and Methods.....	126
5.1	General	126
5.2	Synthesis and characterization	128
5.2.1	Synthesis and characterization of novel compounds in Chapter 2	128
5.2.2	Synthesis and characterization of novel compounds in Chapter 3	130
5.3	¹H NMR titrations	133
5.3.1	Cardiolipin binding.....	134
5.3.2	Zwitterionic lipid binding.....	135
5.4	Computational modeling.....	136
5.5	Liposome-based assays	136
5.5.1	Cardiolipin binding in Triton X-100 micelles.....	136
5.5.2	NAO displacement assay	137
5.5.3	Fluorescence titrations with POPC and POPE.....	138
5.5.4	Lipid flip-flop assay	140
5.5.5	Calcein leakage assay	142
5.5.6	Anion transport assay.....	143
5.6	Hemolysis.....	145
5.7	Bacterial Assays.....	146
5.7.1	Minimum Inhibitory Concentration (MIC) studies	146
5.7.2	Bactericidal activity assay	148
5.7.3	Imaging studies in Chapter 2	148
5.7.4	Membrane depolarization assay	149
5.7.5	BCP image collection	152
5.7.6	BCP CellProfiler analysis	153
5.7.7	BCP statistical analysis.....	155
Appendix A	Supplementary Information for Chapter 2	156
A.1	¹H NMR and ¹³CNMR spectra of novel compounds.....	156
A.2	¹H NMR titrations	159

Appendix B	Supplementary Information for Chapter 3	161
B.1	¹ H NMR and ¹³ CNMR spectra of novel compounds	161
B.2	Binding studies with POPE and POPC	166
B.3	Fluorescence titrations with POPC and POPE	175
B.4	Lipid flip-flop	179
B.5	Bacterial selectivity assay	180
B.6	Growth curves from MIC studies	182
B.7	Bactericidal activity	185
B.8	Bacterial imaging with <i>B. cereus</i>	186
B.9	Membrane depolarization assay	194
Appendix C	Supplementary information for Chapter 4	202
C.1	Hemolysis data	202
C.2	Software metadata from cell imaging	202
C.3	Object selection in CellProfiler™	205
C.4	Example images of object selection in CellProfiler™	206
C.5	Variable plots and Euclidean distance tables from XLSTAT	209
C.6	Boxplots for cell object measurements	211
Glossary		223
References		228
Biography		241

CHAPTER 1

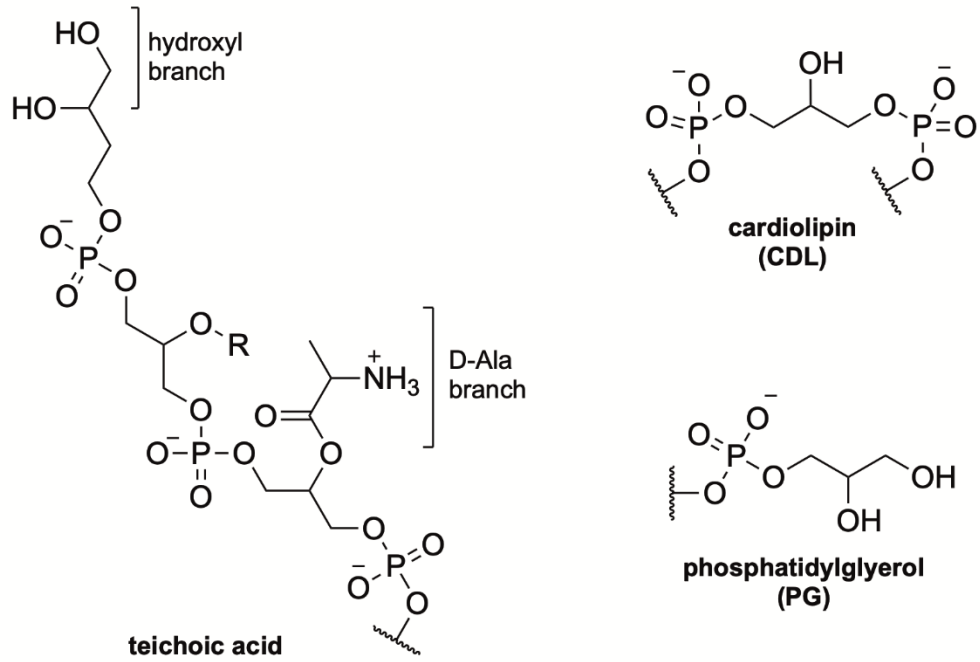
INTRODUCTION

1.1 The antibiotic resistance crisis

The primary goal of this thesis is to develop novel antibiotics to combat multidrug resistant bacteria and deepen our understanding of membrane-based antibiotic mechanisms. Bacteria are microorganisms that can contribute to health or cause serious infections. These infections may lead to hospitalization or death because of untreatable *multidrug resistant* bacteria. Bacteria become resistant to drugs, or *antibiotics*, through innate or learned defense mechanisms. This is due to the cellular structure of the bacteria (discussed below) or genetic mutations that bacteria incur in response to antibiotic treatment. In 2019, (the most recent study available because of the COVID pandemic) bacterial infections caused 1.2 million deaths worldwide despite available treatment options. This was more than either HIV/AIDS or malaria.¹ To combat the growing number of antibiotic resistant bacteria, there is a need for the development of new antibiotics to overcome the more facile defense mechanisms of bacteria.

Bacteria are broadly grouped into two categories by their extracellular architecture. *Gram-positive* bacteria are surrounded by an external peptidoglycan wall rich in anionic

teichoic acids (**Scheme 1.1**) and *Gram-negative* bacteria have an outer membrane surrounding their cell wall rich in anionic phospholipids (cardiolipin, phosphatidylglycerol – **Scheme 1.1**) and lipopolysaccharides (LPS). The anionic nature of bacteria allowed for the first classification of Gram-positive and Gram-negative by Hans Gram in 1882. Gram used a cationic trimethylamine dye, crystal violet, to identify bacteria in tissue cells. Gram noticed that some bacteria retained a purple stain after washing samples with ethanol while others were discolored.² Gram-positive organisms appear dark purple because of the high concentration of dye accumulated in their outer peptidoglycan wall. Gram-negative organisms appear lighter in color because less of the stain was able to reach the inner peptidoglycan wall and ethanol is used to remove the outer membrane bilayer before visualization (**Figure 1.1**). The association of crystal violet to the anionic bacteria is one approach that uses non-covalent interactions to form supramolecular associations with bacterial cells.



Scheme 1.1: The major anionic components of the external bacterial cell

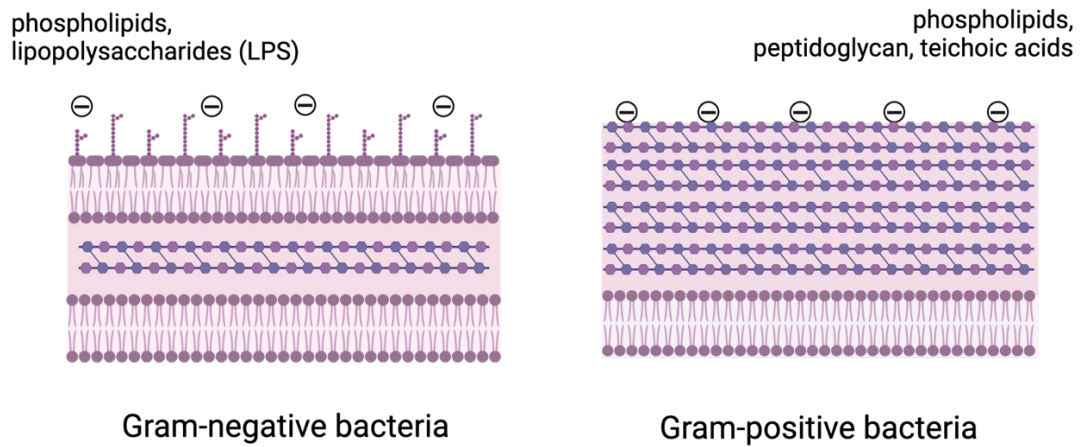


Figure 1.1: Simplified outer wall structures of Gram-negative and Gram-positive bacteria.

Most bacterial infections can be treated with antibiotics. However, there are a growing number of bacteria resistant to commonly used antibiotics (this is called the 'antibiotic resistance crisis'). To understand the reason behind the emergence of antibiotic resistance, it is important to review how antibiotics function. One of the first widely used antibiotics was penicillin, which was discovered by Alexander Fleming in the 1940's.³ Fleming noticed a fungus, *Penicillium notatum* was inhibiting the growth of bacteria in his laboratory which contained the β -lactam we know as penicillin (**Scheme 1.2**). Antibiotics disrupt bacterial growth through various pathways by targeting cellular building blocks or by physically disrupting the cell. Some of the primary antibiotic pathways are included in **Figure 1.2**. Folate synthesis, protein synthesis and RNA synthesis are all necessary for bacterial reproduction. Cell wall targeting antibiotics and membrane targeting antibiotics both disrupt the physical integrity of the cell, which can cause cell death.^{4,5} Most antibiotics act on internal targets, while very few directly target the extracellular membrane or cell wall. Unfortunately, there are numerous pathways for bacteria to develop resistance to internally targeted antibiotics.⁶ Developing new antibiotics targeting the cell membrane or cell wall could combat antibiotic resistance.

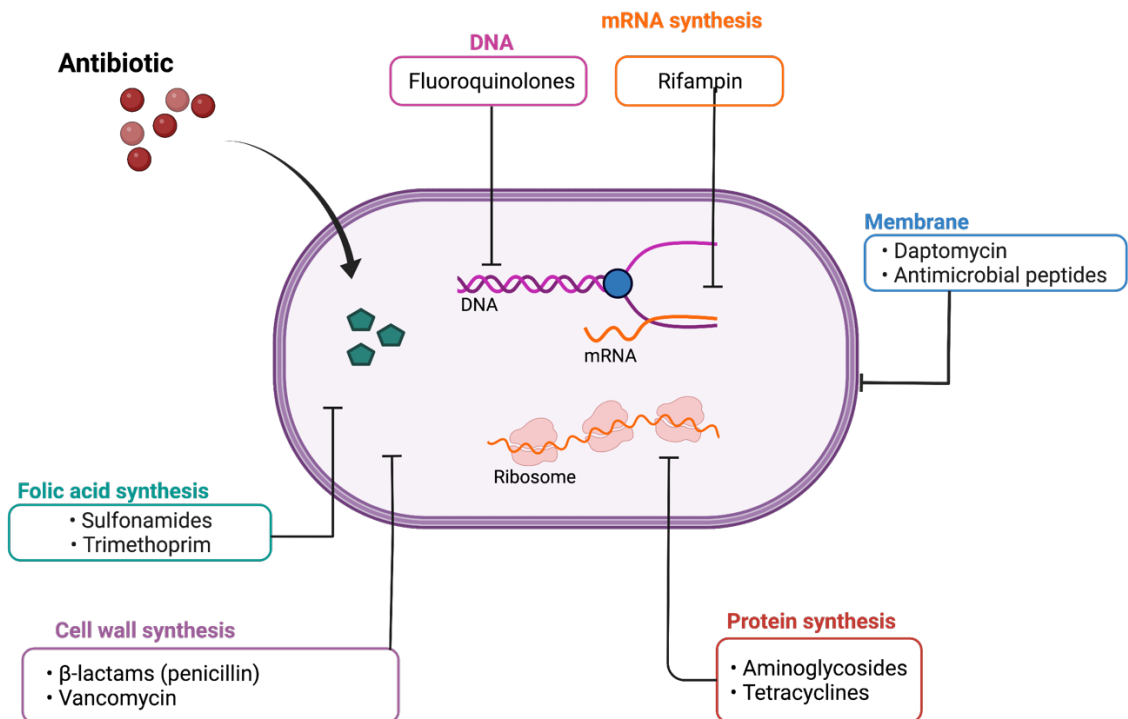


Figure 1.2: Common antibiotic targets in bacteria. Figure made using BioRender.⁸

Resistance to antibiotics is either innate or acquired through genetic mutations over time. Organisms with innate immunity to an antibiotic have properties that are normally expressed without exposure to the drug.⁷ Acquired immunity develops in response to antibiotic exposure. Common resistance pathways include efflux pumps, target modifications and enzyme degradation (**Figure 1.3**). Multidrug resistant (MDR) efflux pumps are the most common method of antibiotic resistance because they can actively transport out a variety of structurally unrelated substrates.⁷ Target modifications include a variety of binding sites within or outside of the membrane (lipid, DNA, enzyme binding site) that are usually covalently modified to block antibiotic binding. Enzyme degradation is caused by enzymes that inactivate or modify the drug before it reaches its

target. Antibiotics that bind to internal targets must cross the membrane bilayer in addition to evading any internal resistance mechanisms. This means that membrane and extracellular cell wall targeting antibiotics have less resistance mechanisms to overcome.

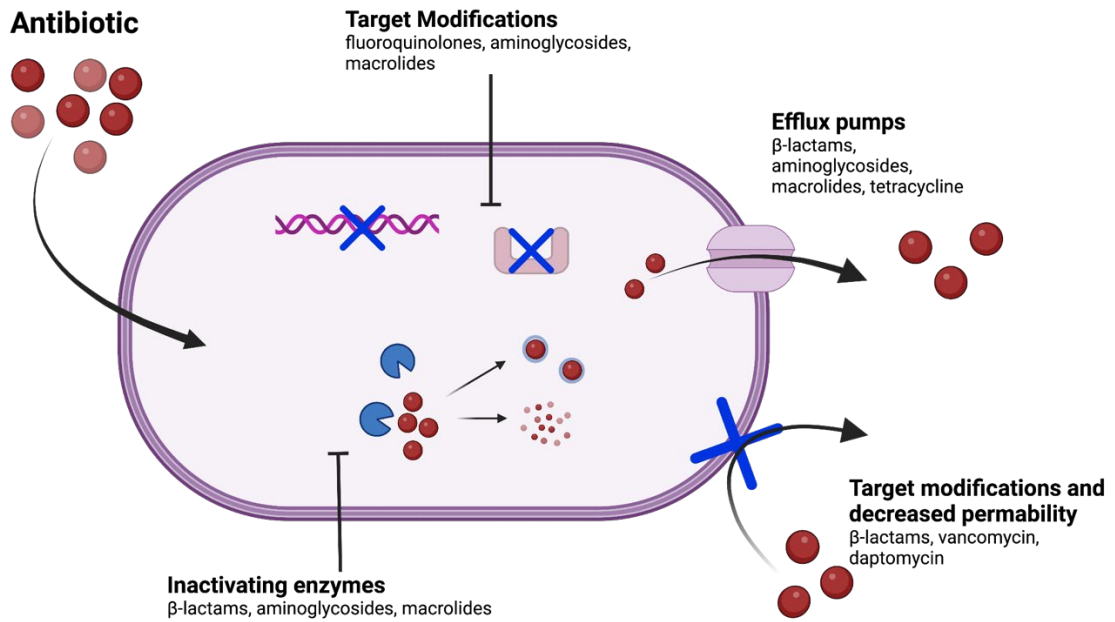
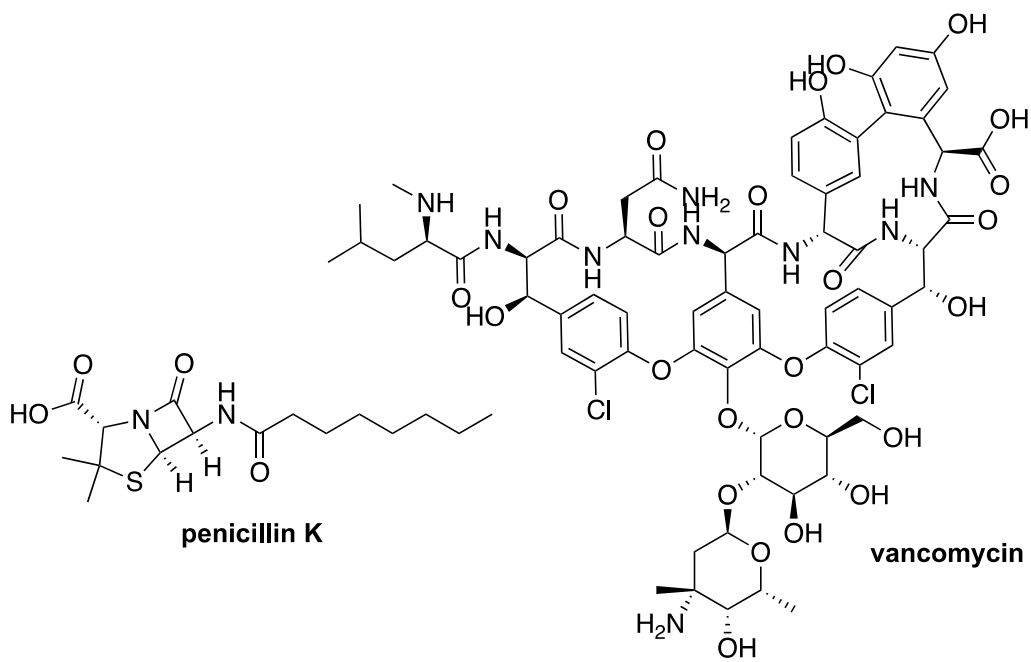


Figure 1.3: Common mechanisms of antibiotic resistance. Figure made using BioRender.⁸

The benefits of extracellular targeting antibiotics can be seen by comparing the timeline of bacterial resistance to penicillin and vancomycin. Penicillin and vancomycin (**Scheme 1.2**) are two antibiotics isolated from natural sources that target different sites in cell wall (CW) synthesis. Gram-negative bacteria have an innate resistance to both because the outer membrane blocks uptake (penicillin) or the binding site (vancomycin).⁷ Gram-positive bacteria have developed resistance over time to both cell wall-targeting

antibiotics, but vancomycin resistant bacteria are much less prevalent because it targets the exposed cell wall.^{9 10}



Scheme 1.2: Clinically relevant cell wall targeting antibiotics

Conversely, penicillin targets intracellular penicillin binding proteins.¹¹ Penicillin analogs are highly susceptible to enzymes, target modifications and efflux pumps in different strains of bacteria.¹² Vancomycin was used in clinical settings for 44 years before the first resistant strain of *S. aureus* was detected.¹⁰ Vancomycin physically blocks cell wall construction by binding to the D-Ala-D-Ala of the growing peptide chain (see **Section 1.2.2**).¹⁰ In response, *S. aureus* developed a mutation to increase the thickness of the cell wall to block vancomycin's binding site.² The acquired immunity of *S. aureus* is concerning since vancomycin has been one of the only effective treatments for methicillin resistant *Staphylococcus aureus* (MRSA) infections.¹⁰ Fortunately, vancomycin resistant *S. aureus*

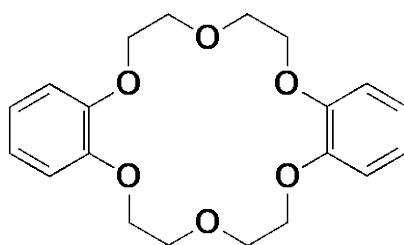
is still rare in hospital settings through restricted use and complicated cell wall modifications required by bacteria.¹⁰ Acquired resistance toward externally-targeted antibiotics occurs through target modifications (peptidoglycan wall, membrane lipids, curvature) and extracellular secretion of proteases.¹³ Targeting the membrane or cell wall overcomes efflux pumps, the most common method of antibiotic resistance. Membrane-active antibiotics also limit resistance by causing rapid cell death so that the pathogens have less time to develop mutations.¹⁴ To understand the chemistry behind membrane-active antibiotics and the physical noncovalent forces that drive bilayer formation/stability, we will discuss the foundational supramolecular interactions that occur. As bacterial membranes are negatively charged, the next section will focus on the supramolecular chemistry of anionic species.

1.2 How supramolecular chemistry can combat antibiotic resistance

The bacterial membrane is a supreme target for developing new antibiotics that are less prone to resistance. A biological membrane is a supramolecular assembly of amphiphilic lipids, driven by the hydrophobicity of the hydrocarbon tails. Membranes are held together by these *hydrophobic effects* as well as other noncovalent interactions, which could be disrupted by molecules that bind to the lipids in the membrane. As this is essentially a supramolecular chemistry challenge, this section will provide a brief introduction on supramolecular chemistry, followed by discussion different ways to bind anions and lipids.

1.2.1 Foundation of supramolecular chemistry

Charles Pedersen was one of the founders of supramolecular chemistry through his discovery of crown ether complexes. During his research on inactivating metals at DuPont, he found dibenzo-18-crown-6 (**1.1**) forming a complex with alkali metal ions.¹⁸ The electron-poor cavity within the crown ether could be optimized by the size (number of oxygens) and flexibility to allow discriminant binding of different cations.¹⁹



1.1

The host (receptor) is the crown-ether, where the guest (ligand) is the metal cation. Any chemical reaction is driven by the formation of the most kinetically or thermodynamically stable product. Thermodynamic favorability can be summarized by changes in the free energy (ΔG), which is defined by the Gibbs-Helmholtz equation²⁰:

$$\Delta G = \Delta H - T\Delta S$$

The free energy (ΔG) describes the favorability of a reaction, while the entropy (ΔS) and enthalpy (ΔH) define the changes in the overall structure or organization. For a spontaneous reaction ($\Delta G < 0$), the energy needed to overcome conformational changes must be low ($\Delta H < 0$) or complexation must lead to a more disordered system ($\Delta S > 0$). The strength of an interaction is defined by its association constant (K_a), or the reciprocal

dissociation constant ($K_d = 1/K_a$).²¹ Within a 1:1 complex, the association constant, K_a can be defined as:²²

$$K_a = [HG]/[H][G]$$

A higher K_a refers to stronger binding of the host-guest. The binding constant (K_a) is heavily dependent on the solvent used and temperature of the system.²³ It is related to the free energy by the following equation (where R = the gas law):

$$\Delta G = RT\ln(K_a)$$

The most thermodynamically stable complexes are formed by more organized hosts with low solvation, defined as the principal of *preorganization*.²⁴ However, this may not be the most kinetically favored. The kinetically favored products are those that react the fastest. $K_a = k_1/k_{-1}$ where k_1 is the rate constant of the forward reaction (formation of complex) and k_{-1} is the rate of the reverse.²⁵

1.2.2 Anion binding

This section will serve as a general outline for different types of attractive forces that can be used to develop selective anion receptors. Examples are given throughout the next few sections that demonstrate the application of supramolecular chemistry in the development of hosts for various anionic species. Anions are diverse molecules that can exhibit different geometry, charge, polarity, and specific hydrogen bonding ability.²⁶ An example of the different geometries seen within anions is displayed in **Figure 1.4**.

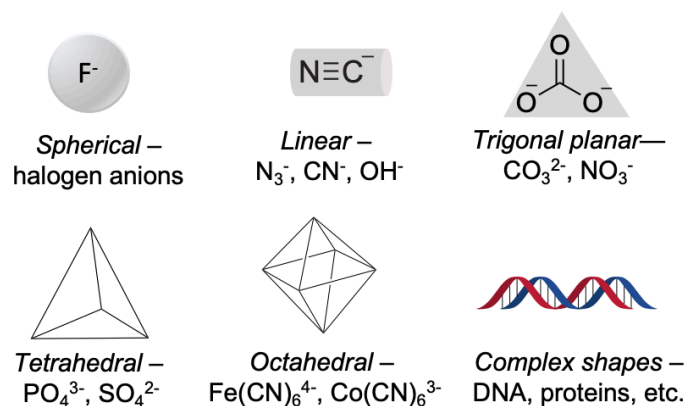


Figure 1.4: Geometries of anions

Hydrogen bonding is one of the dominant forces in anion receptor chemistry. The hydrogen bond is an attractive force between an H-bond donor (HBD) and an electronegatively rich H-bond acceptor (HBA). When the two species get close enough, the resulting interaction is formed: X-H \cdots A. Hydrogen bonds are a mixture of electrostatic, charge transfer, and Van der Waals forces.²⁶ The strength of the bond is dependent on several factors, some of which include electrostatics, electronegativity, delocalization, polarity, and distance in space.²⁶ A few examples of relative trends in HBD or HBA affinity examined by Chris Hunter's group are listed in **Table 1.1**.^{27,28}

Table 1.1: Trends in neutrally charged hydrogen bond donor ability and strength of anionic hydrogen bond acceptors.^{27,28}

A general trend in neutral hydrogen bond donors:²⁸

PO₄H₄ >> urea > imidazole > amide > water > alcohol > amine > R-X > alkane

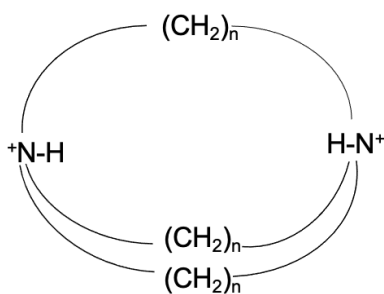
The relative strength of anionic HBA:²⁷

BzO⁻ > AcO⁻ > ⁻OP(OR)₂ > Cl⁻ > MeSO₃⁻ > NO₃⁻ ~ Br⁻ > HSO₄⁻ > CF₃SO₄⁻ >>> PF₆⁻ >>> neutral

Phosphoric acid and the phosphate dianion both contribute to hydrogen bonding due to the polarizability of the P-O bonds. Conversely, PF_6^- shows poor HBA ability because of the anion's lack of polarizability or ability to form coordination.²⁷ The electron-withdrawing fluorine atoms do not participate in any resonance stabilization and the molecular geometry cancels out any overall dipole effect. The directionality of the hydrogen bond is important for thermodynamic stability and selectivity. Anions with Y-shapes can participate in multiple hydrogen bonding interactions, which contributes to the high HBD affinity of carboxylate and phosphate anions (**Table 1.1**).²⁷

The ability of the solvent to participate in the reaction or shield reactants is based on the solvent polarity and ligand structure. Solvation is dictated by weak van der Waals and dispersion forces.²⁷ The affinity for non-polar ligands to form aggregates in solvents, known as the *hydrophobic effect*, is one way to rationalize how solvation effects the thermodynamic stability of the product in aqueous environments. The "classical" definition of the hydrophobic effect is when a reaction is driven by desolvation or increase in entropy upon binding. The non-classical definition is when enthalpy is the primary driving force in complexation.²⁹ It has been suggested that these terms do not accurately describe the complex thermodynamic process.³⁰ Instead, competitive solvents, like polar protic solvents (H_2O , MeOH), form complex hydrogen bonding networks leading to higher hydration in smaller molecules (radius < 10 Å).³⁰ The influence of solvation can be used in receptor design to optimize the thermodynamic stability of the complex.

Ion-ion interactions occur between two formally charged species. Electrostatic interactions are the strongest intermolecular associations, but they are limited in selectivity.³¹ Caged molecules may use size exclusion in addition to ion-ion interactions to increase the selectivity of a receptor. The use of size exclusion as well as incorporating multiple binding sites is known as the *macrocyclic effect*. Early work in anion binding by Park and Simmons showed a series of diazabicyclo[n,n,n]alkane-ammonium ions (**1.2**) that could coordinate to halogen anions when protonated at a low pH.³² The size of the cavity dictated the preference of the anion. Anions Cl⁻ and Br⁻ bound to the cavity of **1.2** where n = 3 or 4, and I⁻ could only bind to the pocket of the larger n = 4. Small cavities (n = 1 or 2) were unable to accommodate any of the halides.³³ This concept of designing the optimal fit for anions would be pivotal in the progression of anion-binding chemistry.



1.2

Many early receptors for phosphate binding were inspired by naturally occurring polyamines that aid in crucial cellular processes.³⁴⁻³⁶ One example is spermidine, **1.3** (**Figure 1.5**), a polyamine which facilitates DNA packing by stabilizing the charge of the phosphate backbone of deoxyribonucleic acid (DNA).^{34, 37} Polyamines are unique because

they bare a cationic charge at pH 7.4 (shown in **1.3** as its neutral form) and the flexible binding pocket can adapt to a wide variety of guests.^{35, 38-39} Many variations of cyclic polyamines have been developed over the years for anion recognition for this reason.^{35,}

37

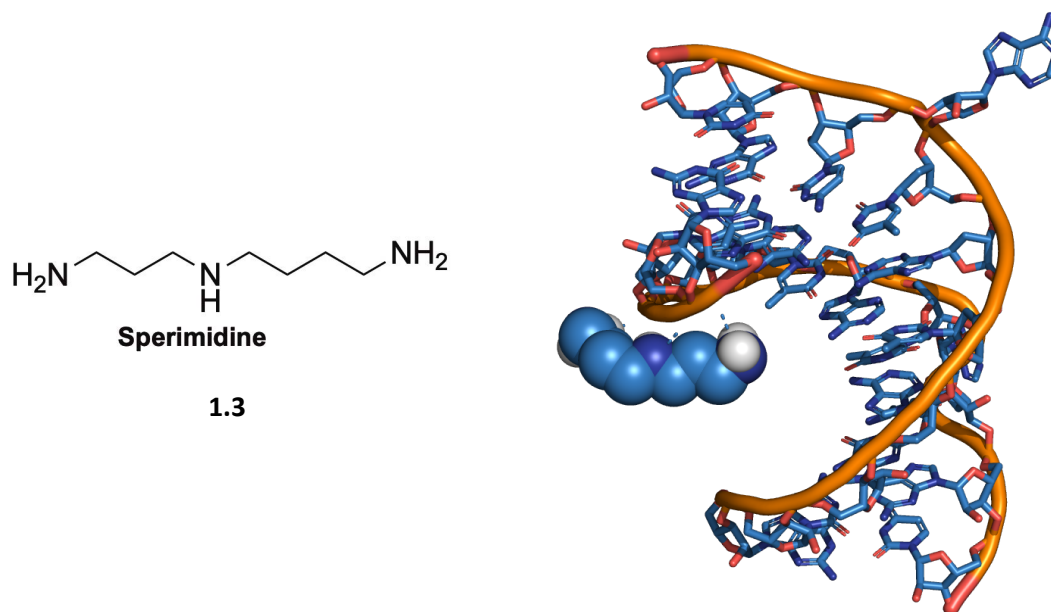
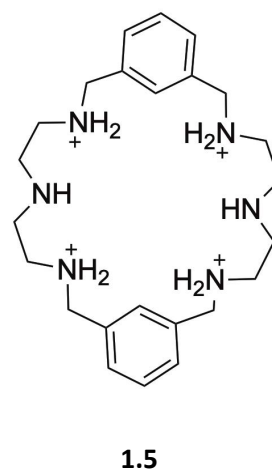
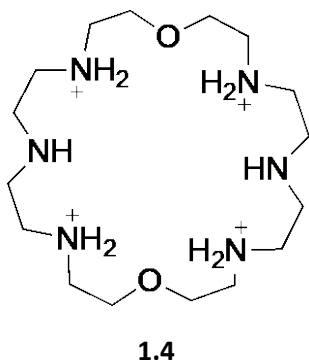


Figure 1.5: The structure of a polyamine, spermidine (left) and spermidine interacting with the phosphate backbone of an RNA/DNA duplex. Hydrogen atoms are omitted for clarity but polar hydrogens of spermidine are shown in white. Carbon atoms are shown in light blue, nitrogen in dark blue, phosphate in orange and oxygen in red.

PDB ID: 1I2X

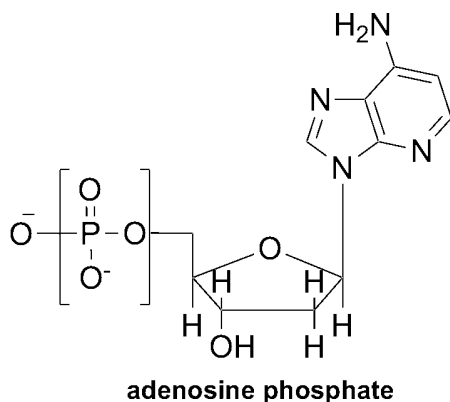
Two early examples of cationic polyamines in phosphate recognition include azacrown receptors **1.4** and **1.5**.³⁷ At pH ~ 7.4 (physiological pH), the receptors have four cationic binding sites located within the macrocycle. This allows for stable, highly charged cavities that can participate in anion binding. The azacrowns bound to dianions (HPO_4^{2-} ,

SO_4^{2-} , $\text{CH}_2(\text{COO}^-)_2$) with higher affinity than monoanions (NO_3^- , Cl^-) in potentiometric titrations because of the size of the binding pocket and complimentary electrostatic charges.⁴⁰ The more highly negative dianion is attracted to the additional cationic charge and stabilized with minimal electrostatic repulsion in the large, flexible pocket.⁴¹



Comparable trends were seen in binding studies of **1.5** with adenosine monophosphate (AMP), diphosphate (ADP) and triphosphate (ATP).³⁷ Binding was enhanced with an increase in charge of the phosphate. At high pH, the monophosphate could be selectively targeted over the diphosphate. At lower pH the diphosphate was favored because of the increase in electrostatic charge.⁴¹ Additionally, binding of **1.5** to any of the adenosine phosphates (AMP, ADP, ATP – **1.6**) was 3-6x higher compared to mono-, di-, or triphosphate anions (HPO_4^{2-} , PO_7^{4-} , PO_{10}^{5-} , respectively).⁴¹ This is due to the additional π - π coordination of the phenyl rings on the macrocycle and the nucleotide aromatic ring.^{40,42} Aromatic interactions are another important supramolecular technique that can be used to enhance binding affinity between the host and guest.⁴³ In π - π stacking,

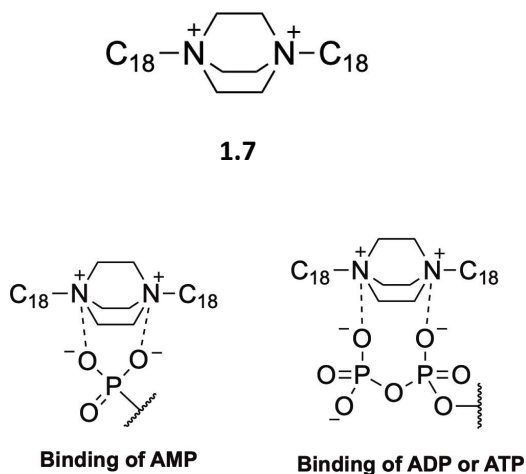
the electron rich sp^2 orbitals of one aromatic ring overlap with the electron deficient hydrogens of the other. Creating more specific binding pockets, like the addition of aromatic rings for hosts with complimentary structure, lead to higher binding affinity.



1.6

Despite the benefits of these amine-based receptors, they are limited to aqueous environments at the appropriate pH to ensure protonation of the amine. This ultimately limits their use in anion recognition. Quaternary ammonium groups are stable, covalently tethered cationic nitrogen groups that can be used in anion recognition in a wider range of solvents. Receptor **1.7** was also designed for recognition of AMP, ADP, and ATP phosphates. The stearyl trimethylammonium chloride salt (**1.7**) was designed with spacing between the cationic charges complimentary to the distance between phosphate dianions (2.4 Å).⁴³ Receptor **1.7** bound selectively to ATP, AMP, or ADP depending on the pH (**Scheme 1.3**).⁴⁴ At pH 3, **1.7** facilitated nucleotide anion transport from chloroform to water with the highest selectivity for ATP > ADP > AMP. At pH 8, transport of AMP increased, consistent with the relationship of electrostatic interactions. Transport of the

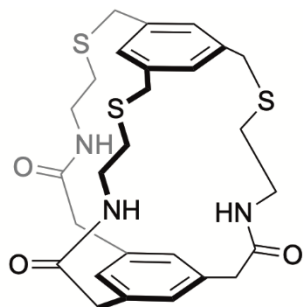
anions from the aqueous solution is one example of how the hydrophobic effect is used in anion recognition. Phase catalysts like crown ethers or **1.7** move ions from one solvent to another, frequently via ionic bonding.



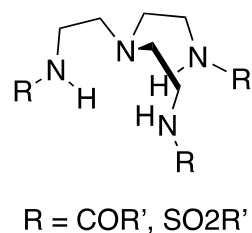
Scheme 1.3: Receptor **1.7** and the proposed binding interactions with ADP, ATP or AMP⁴⁴

Foundational work in neutral anion-receptor chemistry includes the amide-based cyclophane **1.9** and tris(2-aminoethyl) amine (TREN)-based amides **1.10**.^{45,46} Like previous macrocycles, these hosts rely on chelating and complimentary shape for anion selectivity. The amide hydrogen bonds of **1.8** provide directionality within the binding pocket,⁴⁵ whereas the tripodal amide and sulfonamide receptors (**1.10**) demonstrated selectivity toward tetrahedral anions such as H_2PO_4^- over HSO_4^- and Cl^- by utilizing complimentary C_3 symmetry.⁴⁶⁻⁴⁸ Receptor **1.9** bound to the tetrahedral anions in a 2:1 host:guest complex with a $K_a = 142,000 \text{ M}^{-1}$ for H_2PO_4^- compared to HSO_4^- ($K_a = 38 \text{ M}^{-1}$) and Cl^- ($K_a = 1600 \text{ M}^{-1}$). The preorganization of the receptor and strength of the sulfonate hydrogen bond

donation contribute to the stability, but the heightened affinity for phosphate is likely due to the C_3 symmetry of the receptor.

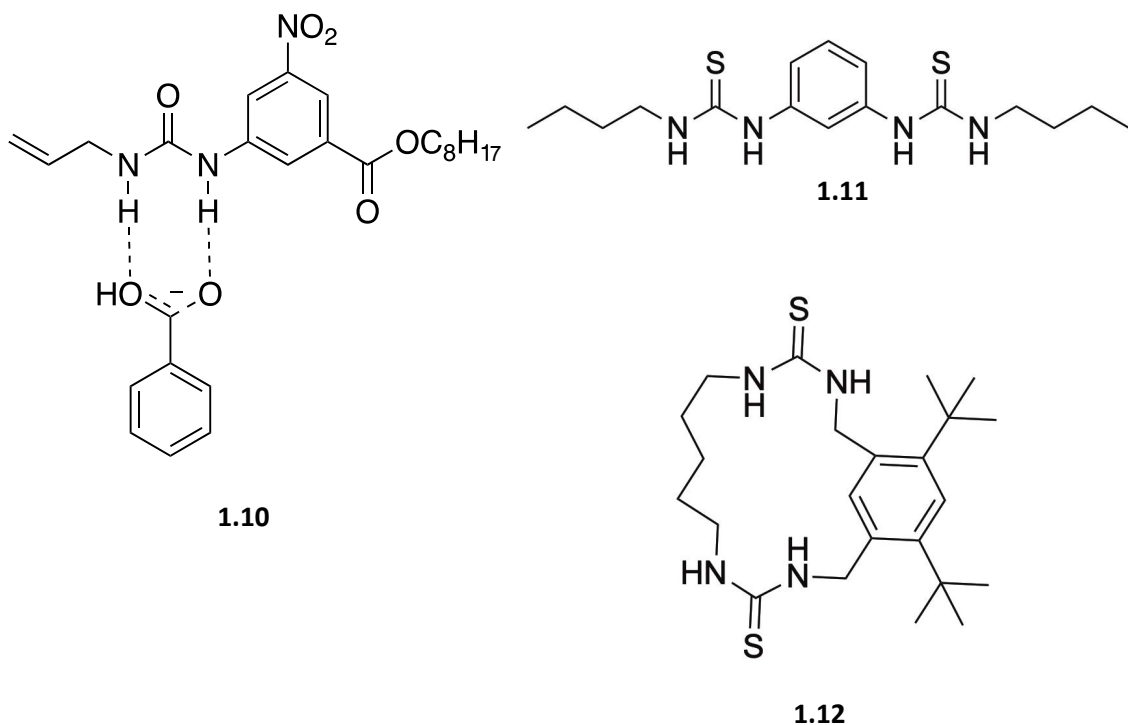


1.8

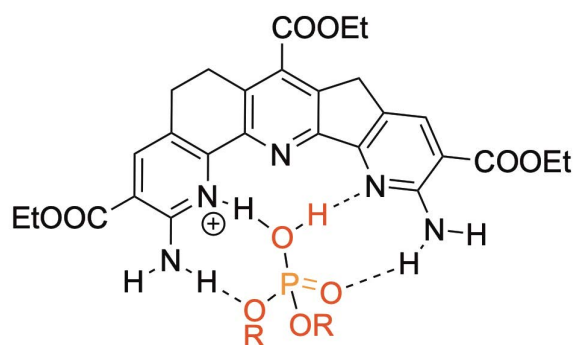


1.9

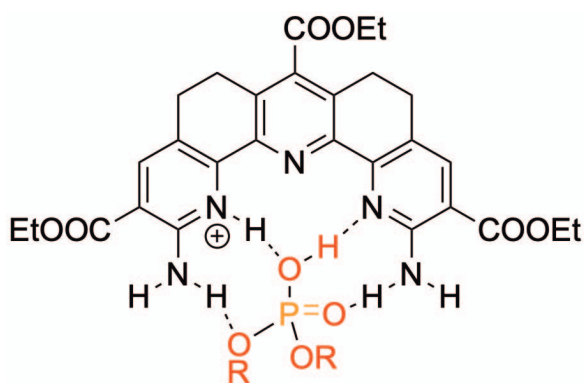
Urea and thiourea groups are widely used as anion receptors due to their preference for Y-shaped anions.⁴⁹⁻⁵⁰ The two hydrogen bonding sites are well positioned for the coordination of anions like COO⁻, SO₄²⁻, and PO₄²⁻. An early example of urea binding from Wilcox and co-workers found that ureas (**1.10**) bound to oxoanions (sulfonates, phosphates and carboxylates) with high affinity ($K_a \geq 6,000 \text{ M}^{-1}$) in CDCl₃ during ¹H NMR studies.⁵¹ Additionally, bis-thiourea **1.11** exhibited remarkable selectivity for dihydrogen phosphate ($K_a = 195,000 \text{ M}^{-1}$) over other oxoanions, with essentially no binding of Cl⁻ in DMSO.⁵² Reexamination of the binding of these two anions in a less polar environment using 1,2-dichloromethane found H₂PO₄²⁻ and Cl⁻ had almost identical binding constants, $K_a = 19,000 \text{ M}^{-1}$ (H₂PO₄²⁻), $K_a = 13,000 \text{ M}^{-1}$ (Cl⁻). Cyclic thiourea **1.12** also showed high specificity for H₂PO₄²⁻ in DMSO ($K_a > 10^4 \text{ M}^{-1}$).⁵³ The cyclization limits solvent interference and increases size selectivity along with the directional HBD hydrogen bonds from the thioureas.



Solvent interactions can also be limited by the rigidity of the receptor. Polyaza-clefts **1.13** and **1.14** with hydrophobic anion-binding pockets were designed by Anslyn and co-workers as potential phosphate transporters (**Scheme 1.4**).⁵² Coordination of **1.13** with dibenzyl hydrogen phosphate in chloroform using ¹H NMR titrations resulted in a high binding constant ($K_a = 8.9 \times 10^4 \text{ M}^{-1}$) and low overall free energy ($\Delta G = -6.75 \text{ kcal/mol}$).⁵² The rigidity of the binding pocket and addition of benzyl groups for secondary charge stabilization is likely what led to the strong association. Additionally, other polyaza-clefts, like **1.14**, showed a lower affinity for dibenzyl phosphate. This dissimilarity emphasizes the importance of size complementarity between the anion and receptor.



1.13

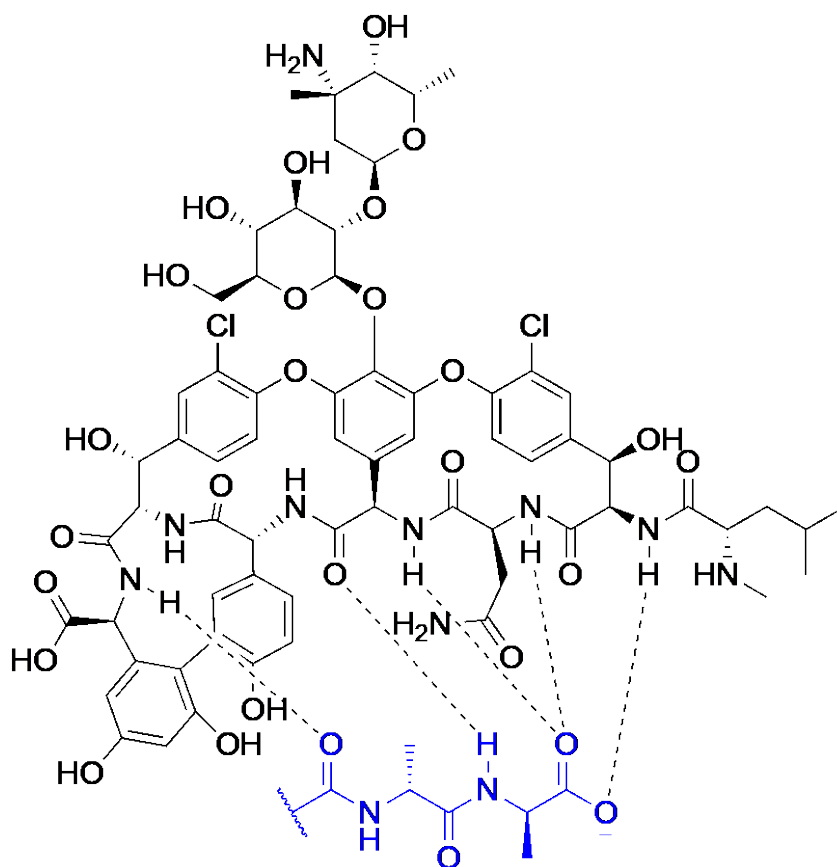


1.14

Scheme 1.4: Poly-aza clefts developed by Eric Anslyn's lab, R = benzyl.

Natural products typically have complex binding sites and hydrophobic areas to bind to the target of interest and pass through the lipophilic membrane. As mentioned in **Section 1.1**, the antibiotic vancomycin binds to the D-Ala-D-Ala in the growing peptidoglycan chain of bacterial cell walls. This occurs through multiple hydrogen bonding interactions and hydrophobic insertion of the cyclic peptide antibiotic (**Scheme 1.5**).⁵⁴ Peptide backbones are rich with hydrogen bond donors (amide NH) and acceptors (carbonyls, carboxylic acid) that many natural products and synthetic drugs use as targets.

The proposed binding mechanism (**Scheme 1.5**) was determined by analyzing key interactions of vancomycin with various D-Ala-D-Ala analogues in ^1H NMR (1:9 $\text{D}_2\text{O}:\text{H}_2\text{O}$, 4.5 pH, 298 K) and UV (NaPO_4 buffer, 4.5 pH, 298 K) titrations.⁵⁴ The experiments by Dudley William's lab found that initial binding of vancomycin was highly dependent on the electrostatic attraction of the anionic carboxylate.^{54,55} Methylation of the terminal carboxylate had the highest impact on binding affinity between analogues. However, substitution of more hydrophobic residues for one alanine (Ala) increased binding of vancomycin to the peptide.⁵⁴ After initial binding through electrostatic interactions, weaker van der Waals forces facilitate insertion into the bacterial membrane, known as the hydrophobic effect.



Scheme 1.5: The association between vancomycin and the D-Ala-D-Ala (blue) in the growing peptidoglycan cell wall.

The hydrophobic effect is an essential driving force for self-assembly or anion binding in aqueous environments. Lipophilic resorcin[4]arene container molecules developed by Bruce Gibb's lab can form diptotic ion complexes to control self-assembly in aqueous environments (**Figure 1.6**).⁵⁶ The pyridinium anion receptors form a four arm "crown" for anion recognition while the upper hydroxyls can participate in cation binding. A library of pyridinium salts were added to the cavity with the highest binding affinity seen by the most lipophilic butyl pyridinium iodide salt via ¹H NMR titrations in D₂O ($K_a = 560 \text{ M}^{-1}$).⁵⁶ The moderate binding affinity compared to other anion-binding studies

mentioned is possibly due to the electrostatic repulsion of the anion-cation pair within the resorcin[4]arene or the flexible pyridinium receptors of the anion binding “crown”.⁵⁶

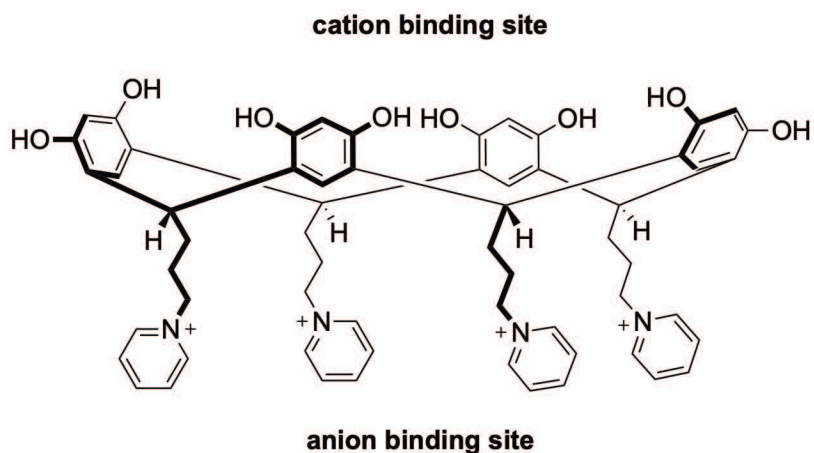
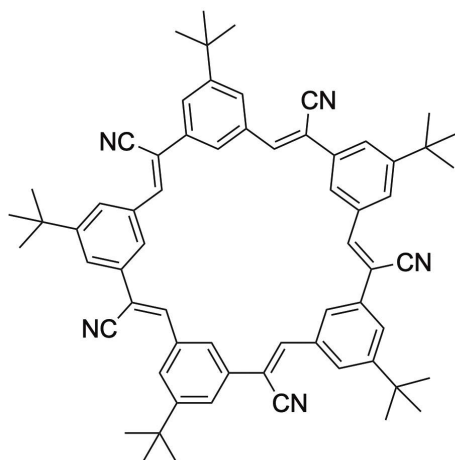
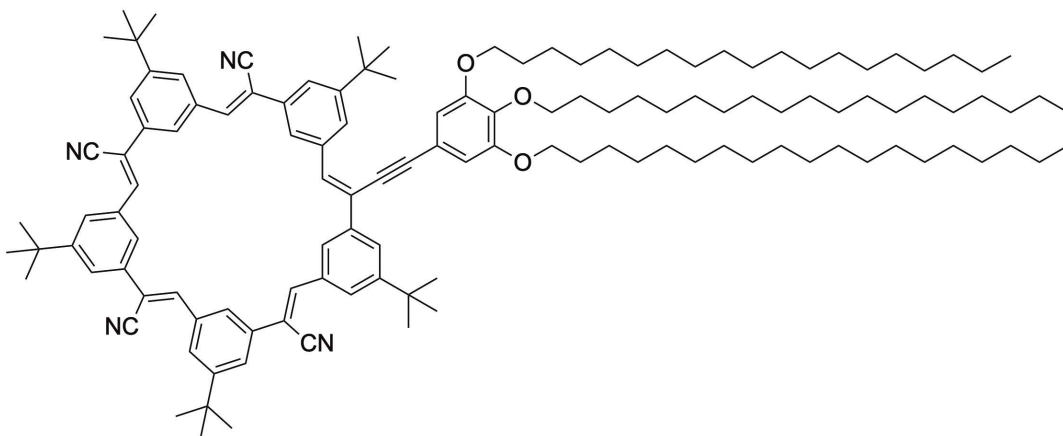


Figure 1.6: Resorcin[4]arene container with ditopic binding sites.⁵⁶

As mentioned previously, the rigidity of the binding pocket increases the complimentary shape of the anion while also decreasing the solvation of the receptor. More rigid structures, like the cyanostar (**1.15**) designed by Amar Flood’s group, are less susceptible to solvation. Cyanostar macrocycles show high 2:1 binding affinity ($K_a \sim 10^{12} \text{ M}^{-2}$) for many large, weakly coordinating anions (PF_6^- or BF_4^-) that complement the size or C_5 symmetry of the binding cavity.⁵⁷ The rigidity gained from the aromatic rings also hinders the cyanostar’s solubility. The addition of hydrophobic tails to **1.15** resulted in an amphiphilic macrocycle capable of forming bilayers at the air-water interface.⁵⁷ Cyanosurf (**1.16**) forms organized monolayers in the presence of PF_6^- or ClO_4^- in pure water as a 2:1 complex (**Figure 1.7**).⁵⁸



1.15



1.16

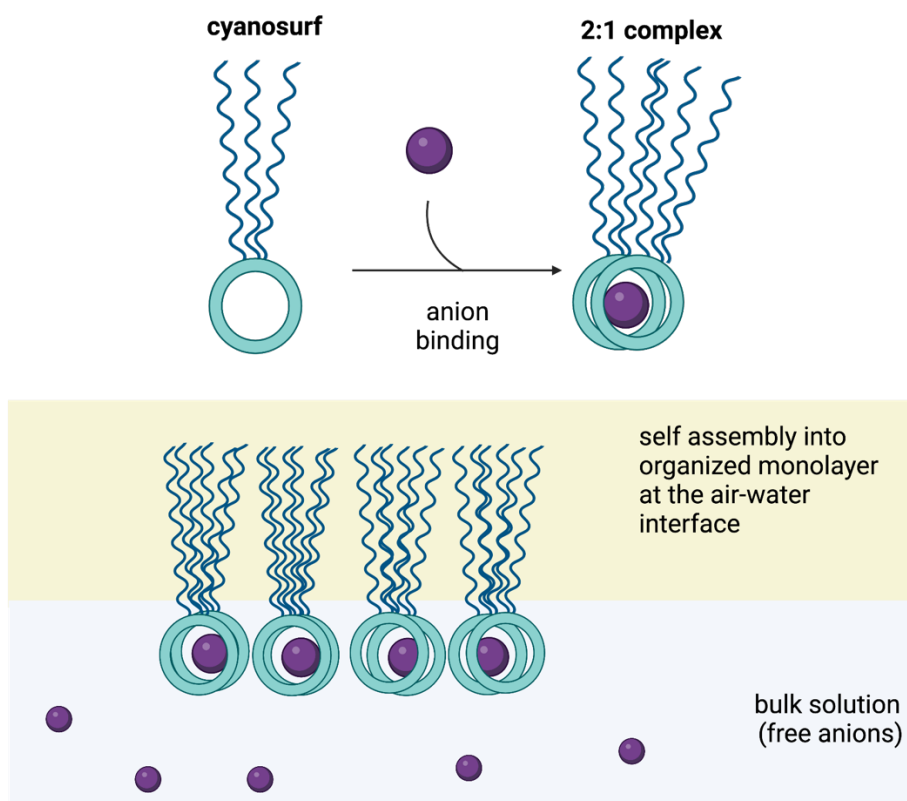


Figure 1.7: Cyanosurf (**1.16**) forms bilayers at the air-water interface upon complexation of PF_6^- and ClO_4^- anions.⁵⁸

More hydrophilic anions, Cl^- and H_2PO_4^- , did not form the same interfacial bilayer despite previous studies showing high affinity for phosphate binding of **1.15** in organic solvents.^{57,58} This discrepancy may be due to the higher solvation of phosphate compared to more hydrophobic anions. Desolvation of the anion may not have been energetically favorable since there were no electrostatic interactions.

Anion receptor chemistry is a highly adaptable, growing field within supramolecular recognition. Inorganic or biological phosphate anions are interesting targets because of their importance in biological systems (energy transfer (ATP), protein kinases) and inorganic nutrient cycles (eutrophication) as well as their tuneability as

anions.^{49, 59-60} While this section is meant to serve as a brief overview of noncovalent interactions that can be used in membrane recognition, it does not represent the true diversity of receptor design. More examples will be given below to outline the breadth of supramolecular recognition.

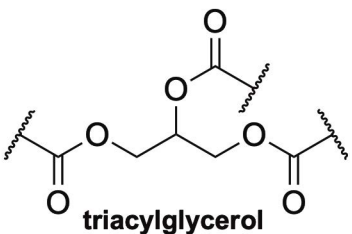
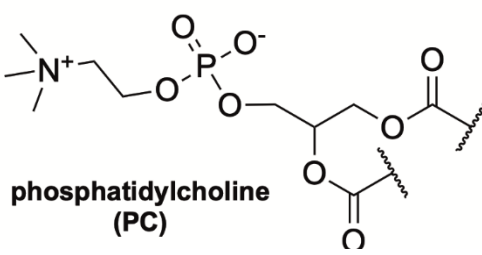
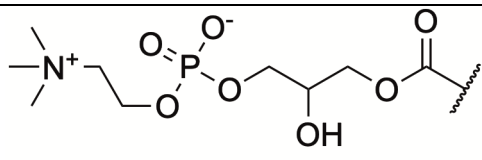
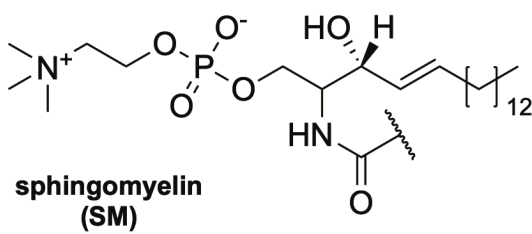
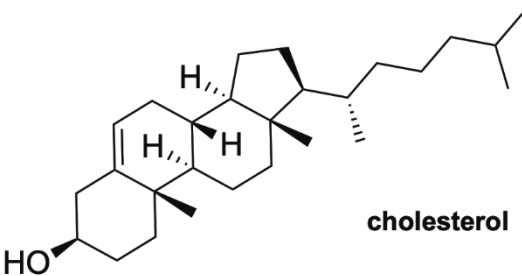
1.2.3 Lipid binding

Recognition of phosphate anions has been central to the growth of supramolecular chemistry, yet the development of synthetic receptors for phospholipids remains understudied. This is partially due to the difficulty of working with lipids. Their amphiphilic nature means that lipids are likely to form aggregates in aqueous solutions and have low solubility. Nonetheless, this section should convince the reader that development of supramolecular receptors for phospholipid recognition is important for biological applications.

1.2.3.1 The importance of lipids in biology

There are more than 1000 lipid species in a cell that contribute to different biological processes (for some important examples, see **Table 1.2**), yet there has been very little progress in developing lipid receptors.⁶¹ Lipid recognition could assist in understanding cellular processes or detect tumors and infections. Lipids are essential for three primary biological functions. First, hydrogenated lipids like fatty acids and triacylglycerols are used for energy storage.^{64,65} Their reduced state allows for an anhydrous form of energy storage that can be used in membrane biogenesis.

Table 1.2: Some lipids important for biological activity. Adapted from Clear et al. ⁶²

Lipid Class	General Structure	Function
Acylglycerols	 <p style="text-align: center;">triacylglycerol</p>	Energy storage, signaling ⁶⁵
Phosphoglycerolipids (phospholipids)	 <p style="text-align: center;">phosphatidylcholine (PC)</p>	Membrane lipid, signaling ⁶⁶
Lysophospholipids	 <p style="text-align: center;">lysophosphatidylcholine (Lyso-PC)</p>	Signaling ⁶⁷
Sphingolipids	 <p style="text-align: center;">sphingomyelin (SM)</p>	Membrane lipid, signaling ⁶⁸
Steroids	 <p style="text-align: center;">cholesterol</p>	Maintain membrane integrity, signaling ⁶⁹

Second, polar lipids have unique contributions to membrane packing and formation, which drives the diversity of membranes in different species, cells, and organelles.⁶²⁻⁶³ Phospholipids and sphingolipids are primarily responsible for membrane structure. Third, lipids control cellular processes essential for cell division, signaling, and molecular recognition.⁶¹ Due to this diversity, lipid-targeting receptors should be used in future drug design.

1.2.3.2. Structural diversity of phospholipids

Phospholipids are of particular interest because they contain supramolecular targets that can be used for drug design or recognition. Phospholipids are composed of a phosphate head group and a hydrophobic carbon tail (**Figure 1.8**). These lipids can differ by the head group or acyl group (length, structure, or placement of the double bond). The length and saturation of the acyl chain contributes to the membrane fluidity and the size of the head group (compared to the lipid tail) determines the 3D self-assembly.⁶² The primary phospholipid in human membranes, 1-palmitoyl-2-oleoyl-*sn*-glycerol-3-phosphocholine (POPC, 16:0-18:1 PC, **Figure 1.8**), gets its name from the hexadecanoyl (palmitoyl, 16:0) and *cis*-9-octadecadienoyl (oleoyl, 18:1) acyl groups attached to a phosphatidylcholine (PC) head group. The long lipid tails allow anchoring in the membrane and the single *cis* bond allow efficient packing of hydrocarbon tails to increase stability.

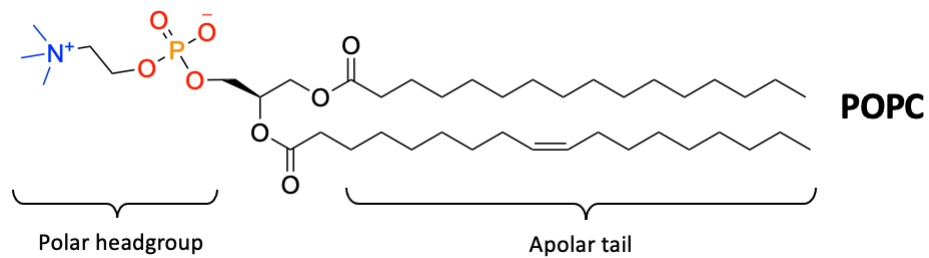


Figure 1.8: Membrane bilayers are primarily composed of POPC lipids.

The most common assemblies formed by lipids are micelles, bilayers and reverse micelles (**Figure 1.9**). Larger headgroups create an inverted cone architecture, forming micelles. This is mainly seen in synthetic detergents, but phospholipids with only one acyl chain (lysophospholipids) also form micelles.⁷⁰ Bilayers are formed by cylindrical phospholipids (similar cross section for the headgroup and tails) like sphingomyelin, phosphatidylethanolamine (PE), phosphatidylserine (PS), and phosphatidylinositol (PI). On the other hand, cardiolipin (CDL), phosphatidylethanolamine (PE), and cholesterol have smaller headgroups that form cone shaped lipid structures which create negative curvature (“reverse micelle”).⁶² The structures of the headgroups for these lipids are shown in **Figure 1.9**.

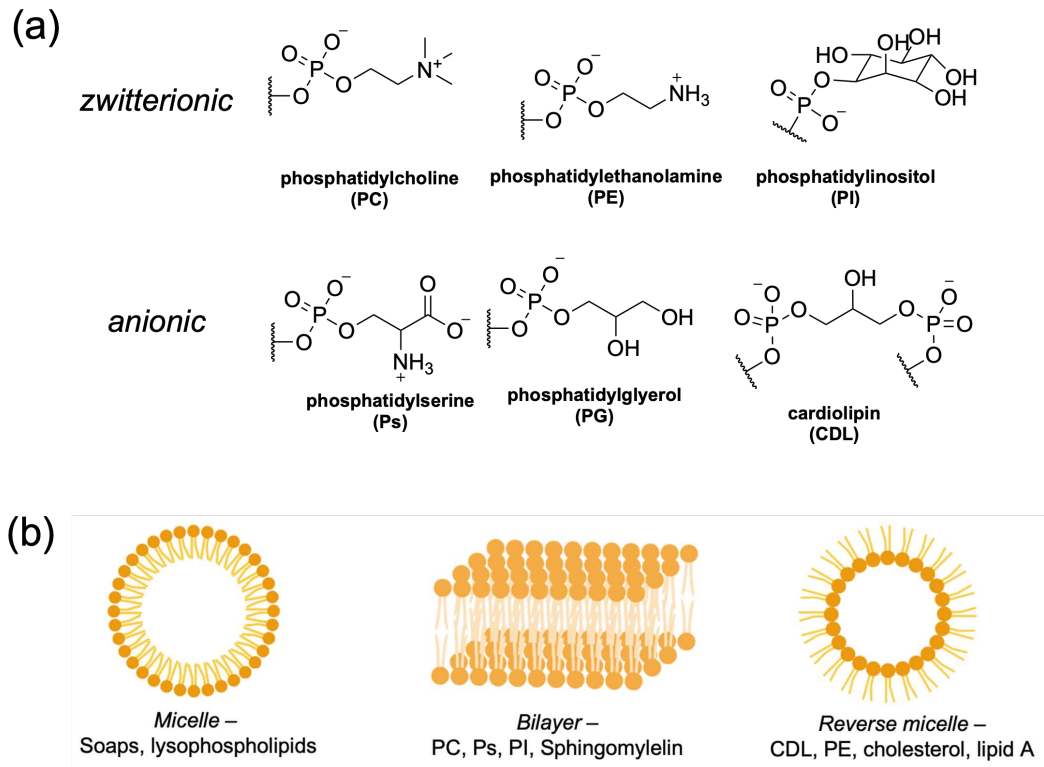


Figure 1.9: Geometries of lipid packing. a) Structurally significant phospholipid headgroups. b) 3D geometries formed by lipids. Figure made with BioRender.⁸

Human membranes are composed primarily of POPC and sphingomyelin (SM). The ~20% of PE found within mammalian cells is primarily found in the inner bilayer, or cytoplasmic membrane (CM). The inverted cone geometry of PE is important for budding, fission, or fusion. **Table 1.3** lists the relative abundance of different phospholipids in human erythrocytes, mitochondria, and some bacteria.^{17 62} Regulation of lipid expression in the inner or outer leaflet of eukaryotic cells is controlled by peripheral membrane proteins and translocase enzymes (flippases, floppases and scramblases).⁷¹ These large molecules have specific lipid binding sites that can recognize the phospholipid headgroup of a particular lipid and initiate signaling events.

Table 1.3: The distribution of phospholipids in different organisms, shown as a percentage of total lipid content.

	Typical mammalian cell ⁷²	Mammalian PM ⁷²	Mitochondria ⁷²		<i>S. aureus</i> ⁷³	<i>E. coli</i> ⁷⁴	
			CM	PM		CM	PM
PC	45-55	43	41	49	0	0	0
PE	15-25	21	38	34	0	82	90
PI	10-15	7	2	9	0	0	0
PS	5-10	4	1	1	0	0	0
SM	5-10	23	2	2	0	0	0
CDL	2-5	0	16	5	42	12	6
PG	<1	0	0	0	58	6	3

Data represents phospholipid composition (% weight) averaged from multiple sources, as shown in the review articles cited above. CM = cytoplasmic (inner) membrane, PM = plasma (outer) membrane

Phospholipid binding in nature can be highly specific (based on stereospecific recognition of components) or non-specific, targeting a physical property of the membrane (charge, amphiphilicity, curvature). Receptors may interact with the membrane through lipid tail binding, headgroup binding, or ditopic binding (tail and headgroup).⁶² Phosphate headgroups contain a variety of functional groups (e.g., carboxylate, ammonium, hydroxyl) that can be used for selective targeting of certain lipids. Natural products, proteins and small molecules are known to target the phosphate headgroups of different lipids through hydrogen bonding and electrostatic interactions. For this reason, we will focus on phospholipid headgroup recognition in the next sections.

1.2.3.3. Lipid binding via electrostatic interactions

Peripheral membrane proteins utilize stereospecific, electrostatic, and hydrophobic interactions to recognize phospholipid headgroups in the membrane. Annexin V is a Ca^{2+} -dependent phosphatidylserine (PS) receptor found in humans. Phosphatidylserine is an anionic phospholipid that resides on the inner leaflet of healthy cells, but during apoptosis it is translocated to the outer membrane where it accumulates Ca^{2+} ions for stabilization.⁷⁵ Annexins bind to PS in response to a change in extracellular Ca^{2+} , using the ions to coordinate to the phosphate and carboxylate groups of the lipid in the outer leaflet (**Figure 1.10**).^{62, 76} Fluorescently tagged annexin V is used for the detection of cell death and to identify tumors.⁷⁷ Bradley Smith's group developed synthetic receptors for PS based on zinc-coordinated molecular tweezers (**1.17**).⁷⁸ These interact with the carboxylate or phosphate functionalities of PS and generate a fluorescent response that can also be used to identify tumors in mice studies.⁷⁹

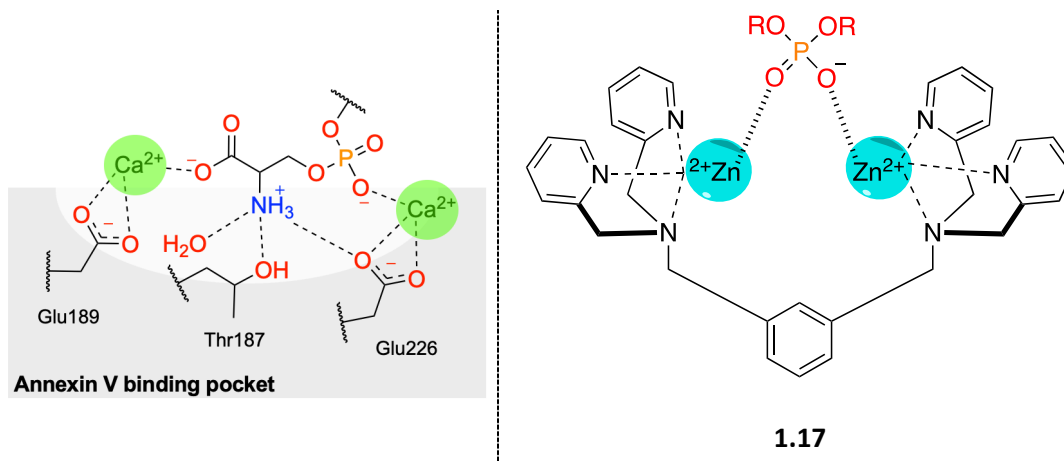
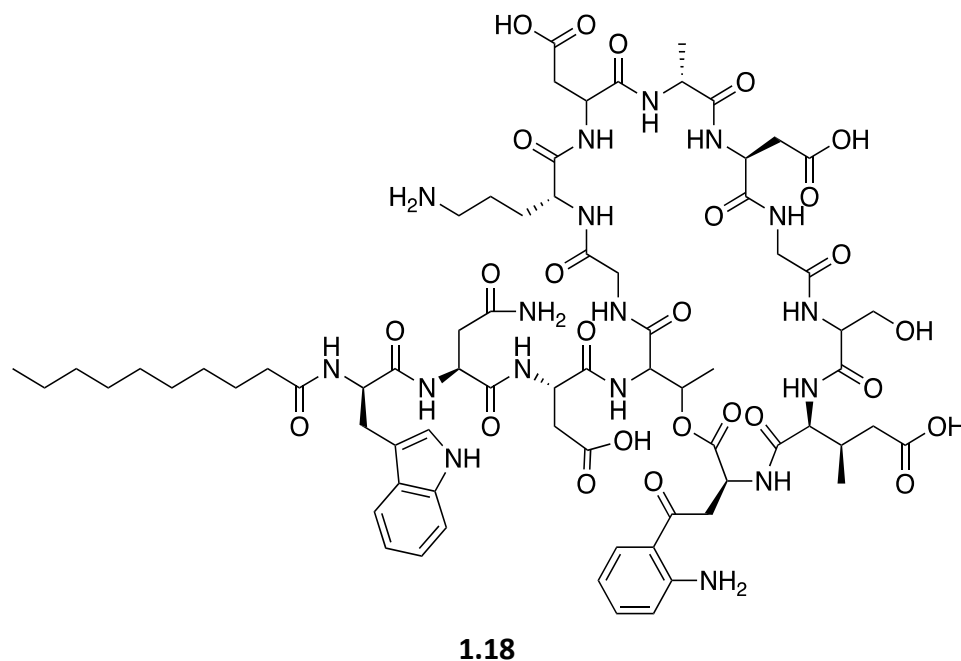


Figure 1.10: Metal coordinated binding to phospholipid headgroups

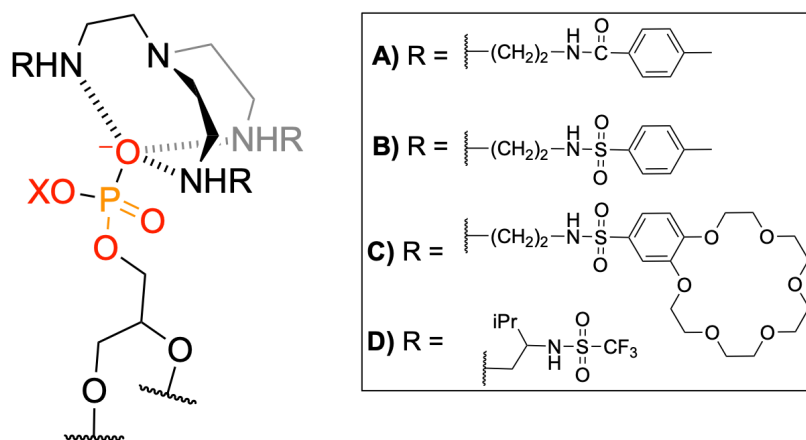
Cation-assisted recognition of anionic phospholipids is seen in recognition of bacterial membranes as well. Although its exact mechanism of action is unknown, daptomycin (**1.18**) requires Ca^{2+} ions to coordinate to the cell wall of Gram-positive bacteria. Anionic lipids (PG, CDL) in the outer membrane and teichoic acids both contain negatively charged areas that daptomycin can use for membrane destabilization, leading to cell death.^{80 81}



Electrostatic interactions are important in receptor design, but they are limited in their selectivity. Unfortunately, most membrane-targeting antibiotics rely on Coulombic and hydrophobic forces which can cause off-target membrane lysis or result in poor bioavailability (discussed further in **Section 1.3**). Developing synthetic, neutral receptors can overcome these issues with lipid binding.

1.2.3.4. Lipid binding via hydrogen bonding

Few synthetic receptors have been designed to target membrane phospholipids through hydrogen bonding. Bradley Smith's group developed tris(2-aminoethyl)amine (TREN) receptors (**Scheme 1.6**) that facilitate lipid flip-flop through hydrogen bonding to the phosphate headgroup.^{62,82} Binding to the phosphate headgroup reduces polarity and allows for translocation through the hydrophobic bilayer.



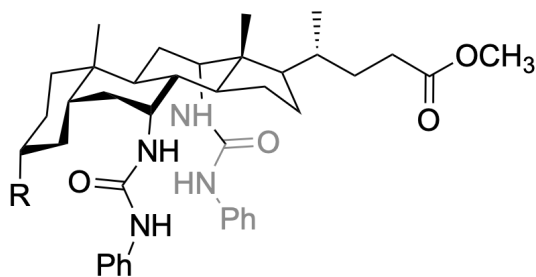
1.19

Scheme 1.6: Receptors developed by Smith and coworkers for synthetic lipid flip-flop.

Sulfonamide receptors (**1.19 B-D**) with more acidic N-H groups displayed greater complexation to the lipid headgroup compared to **1.19 A**. Receptor **1.19-B** (38 μ M) was able to enhance the inward translocation of fluorescently labeled 7-nitrobenz-2-oxa-1,3-diazol-4-yl (NBD)-PC within 4 min.⁸² Substitution of benzo 18-crown-6 (**1.19-C**) or trifluorocyanate (**1.19-D**) for the tosyl group allowed for selective translocation of NBD-PE over NBD-PC. Translocation of NBD-PE was induced by **1.19-D** (8 μ M) whereas **1.19-C**

(100 μM) displayed slower translocation (100 min) despite its ammonium-binding crown ether.⁸³ The bulkiness of the tri-substituted crown ether likely delayed the movement of the lipid. The addition of the isopropyl group in **1.19-D** may have been bulky enough to displace the alkylated ammonium of the PC to target PE-headgroups.

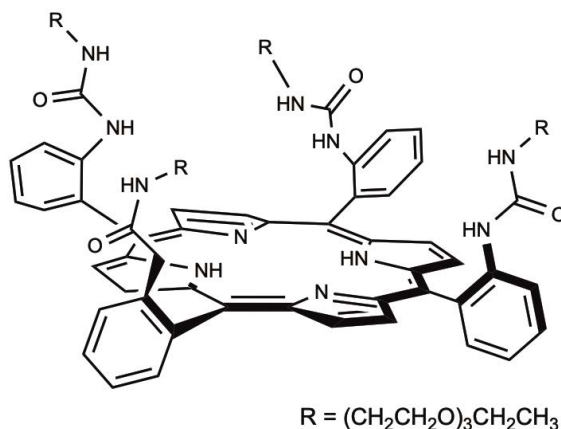
Davis and Smith also developed steroid-based receptors (**1.20**) that bound to NBD-PC more effectively than TREN-based receptors (**1.19**). Lipophilic cholate bis-ureas (**1.20 A-B**) were able to coordinate to two of the phosphate oxygens due to the spacing of the ureas and geometry of the phosphate. Addition of a cationic trimethyl ammonium group (**1.20-B**) to the receptor allowed for translocation of anionic NBD-PS and NBD-PG lipids 4x faster than the zwitterionic NBD-PC.⁷¹ However, the binding constants from UV-titrations in 99:1 $\text{CHCl}_3:\text{MeOH}$ at 295 K were not as selective between lipids ($K_{\text{PS}} = (3.4 \pm 0.9) \times 10^5 \text{ M}^{-1}$ and $K_{\text{PC}} = (2.2 \pm 0.5) \times 10^5 \text{ M}^{-1}$).⁷¹ Future work in receptor design should target more sites of the phospholipid headgroup and avoid cationic charges to increase selectivity.



A) R = OAc
B) R = OC(O)CH₂N⁺((CH₃)₃)

1.20

Other urea-based receptors include the picket porphyrin (**1.21**) developed to target PG-headgroups in polar organic solvents.⁸⁴ PG is the primary anionic phospholipid in bacterial membranes, so it is of interest for future antibiotic design. Urea groups were added so that they align with the phosphate and the glycerol hydroxyl group of PG.⁸⁴ ITC binding studies in DMF found an enthalpically favored 1:1 association of the porphyrin and PG lipid ($K_a = 3700 \pm 450 \text{ M}^{-1}$, $\Delta H = -1210 \text{ cal/mol}$), likely due to the formation of neutral hydrogen bonds.⁸⁴

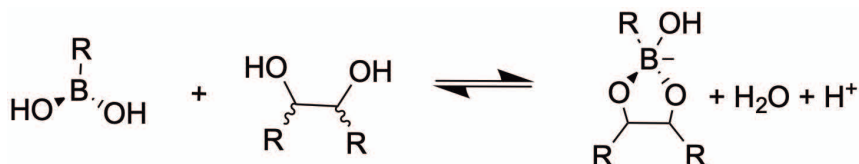


1.21

1.2.3.5. Lipid binding via reversible covalent bonding

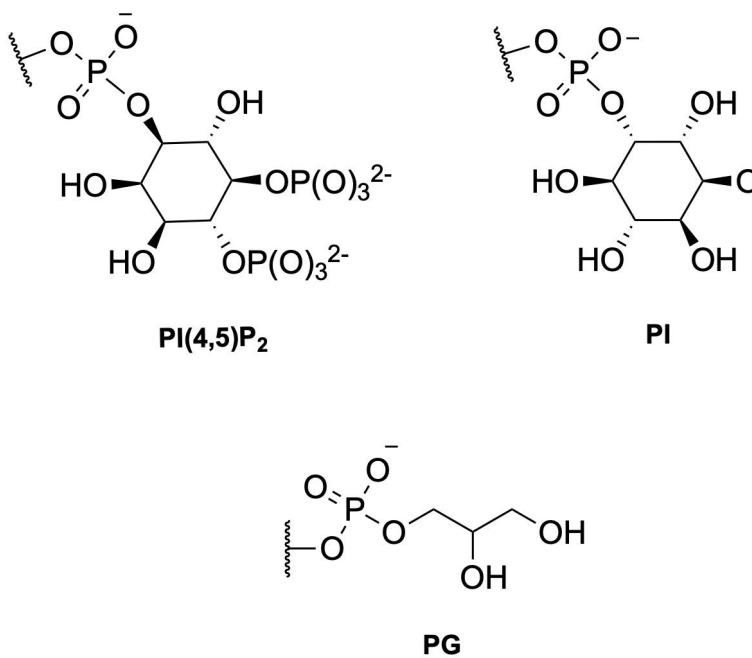
Other non-covalent interactions include reversible covalent binding, via the formation of a boronic ester (**Scheme 1.7**). Trisubstituted boron species have weak Lewis acidity and act as a receptor for hard anions (CN^- , HO^- , F^-). In addition, boronic acids have been shown to react rapidly and reversibly with dicarboxylic acids, α -hydroxy carboxylic

acids, 1,2- and 1,3-diols in non-aqueous or basic aqueous conditions to form boronate esters (**Scheme 1.7**).⁸⁵⁻⁸⁶ Boronic acids have been used for recognition of PG and PI lipids due to their 1,2-diol moieties.



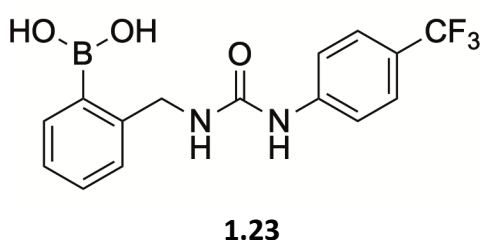
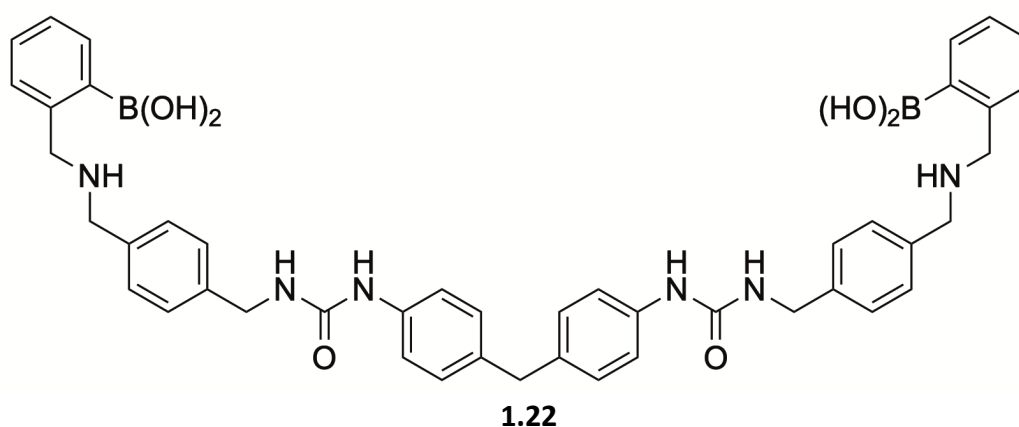
Scheme 1.7: formation of a boronic ester with a 1,2-diol

Receptors **1.22** and **1.23** bind to lipid headgroups through hydrogen bonding between the urea phosphate and boronate ester formation with the 1,2 diol of the PI or PG headgroup (**Scheme 1.8**).



Scheme 1.8: Phospholipid head groups of phosphatidylinositol (PI), phosphatidylinositol (4,5)-bisphosphate (PI(4,5)P₂) and phosphatidylglycerol (PG)

Phosphatidylinositol (4,5)-bisphosphate (PI(4,5)P2) is a minor lipid component (0-30 %wt) in eukaryotic membranes responsible for ion channel regulation, endocytosis, and actin polymerization in the cytoskeleton.^{62, 87 88} Receptor **1.22** was able to selectively bind to PI(4,5)P2 compared to other PI analogs with low micromolar affinity (**Scheme 1.8**).⁸⁸ The 2:1 lipid:receptor complex is largely driven by the formation of the boronic ester.



Recent work by the Busschaert group has also exploited this boronate chemistry for antibiotic PG-binding receptors. Receptor **1.23** showed selective binding of PG over PC, in 99.5% DMSO-*d*₆:0.5% MilliQ at 37 °C in ¹H NMR titrations ($K_{PG} = (7.6 \pm 1.1) \times 10^2 \text{ M}^{-1}$ compared to $36 \pm 26 \text{ M}^{-1}$ for K_{PC}).¹⁹⁶ Boronic acids have unique chemistry that can be exploited for future membrane sensors. However, formation of the covalent ester is also

highly dependent on the pH of the solution and pK_a of the boronic acid or diol. Detailed discussion on boron receptors is beyond the scope of this thesis but there are many review articles available.^{85, 89}

1.3 Membrane-targeting antibiotics

Membrane-targeting antibiotics are thought to have a lower chance of developing resistance due to the rapid bactericidal effect of membrane disruption, and the fact that lipid mutations are less trivial than protein mutations. Cationic antimicrobial peptides (AMP) are amphiphilic, cationic peptides produced by organisms to defend against infection. AMPs target pathogens through electrostatic attraction of the bacteria's negatively charged lipids. Once AMPs are coordinated, hydrophobic regions of the peptide insert into the membrane to trigger rapid cell death.⁹⁰⁻⁹¹ AMPs can be used as antibiotics because the human membrane contains much fewer anionic lipids and is largely neutral in charge (**Table 1.3**). However, clinical use of AMPs is limited due to off-target effects of their cationic charges and poor bioavailability.^{73, 92}

1.3.1 Structure of antimicrobial peptides

AMPs fold or assemble into 3D structures to create hydrophobic and cationic pockets for membrane recognition and insertion (**Figure 1.11**). There are many different types of AMPs but generally, the most active antibacterial AMPs are composed of 12-55 amino acids (AA) with 30-70% hydrophobic residues and a net positive charge of +1 to +10.⁹³ Many AMPs display broad spectrum activity since all bacteria have anionic charges,

but certain AMPs are not capable of penetrating the membrane of Gram-negative bacteria.⁹³ This can be due to charge density or stability of the peptide's secondary structure. Higher cationic charges increase the electrostatic attraction toward bacterial membranes and more complex secondary structures (cross-linking) decrease protease degradation.⁹⁴

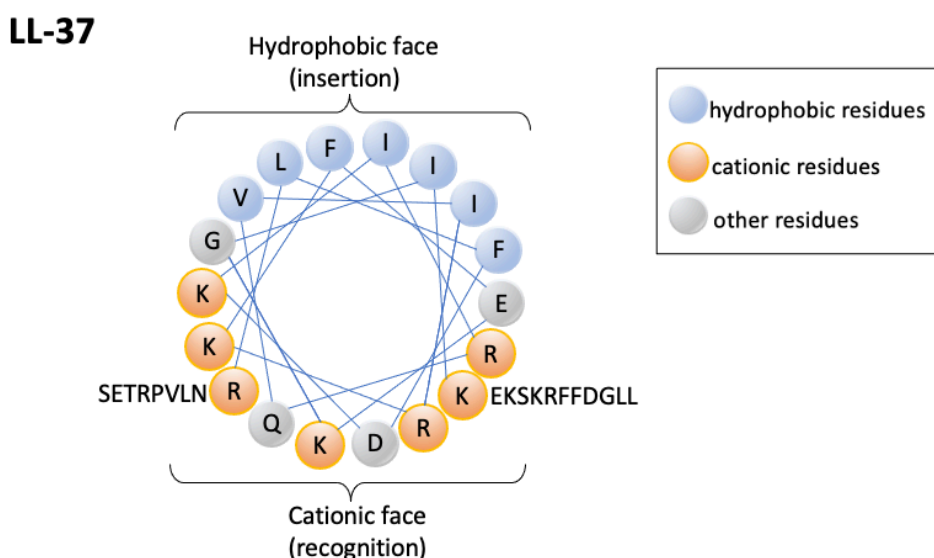


Figure 1.11: Helical wheel structure of LL-37 outlining the cationic and hydrophobic residues necessary for the peptide's membrane-lytic activity.⁹⁵

1.3.2 Mechanisms of antimicrobial peptides

Bacterial species may differ in their lipid composition, but they all possess anionic membranes from the expression of PG, CDL, lipopolysaccharides and teichoic acids in the outer leaflet. Teichoic acids and lipopolysaccharides are important for cellular function and FDA-approved antibiotics exist that target these extracellular features, while lipid-binding remains mostly under explored.^{96,98} Lipids in the membrane are an ideal

candidate for antibiotic development because changes in the membrane fluidity or polarity causes rapid cell death or interference of vital protein functions.^{96 73}

LL-37 (Figure 1.11) is an α -helical AMP with a net +6 charge produced by human leukocytes in response to infections.⁹⁷ Hydrophobic and cationic faces allow the attraction of **LL-37** to anionic species to cause membrane thinning and destabilization. **LL-37** displays potent activity towards *P. aeruginosa* in biofilms (0.001-1 μ M), but it does not appear to have any selectivity for a particular target.⁹⁸ Modifications of lipopolysaccharide (LPS) and PG membrane components both decrease its efficacy.^{81, 98} Proposed mechanisms of **LL-37** include aggregation in the inner membrane to cause pore formation, micellization, or interference of cell wall biogenesis (**Figure 1.12**). **LL-37** also displays cytotoxic effects on most eukaryotic cells, which supports the membrane destabilization pathways.

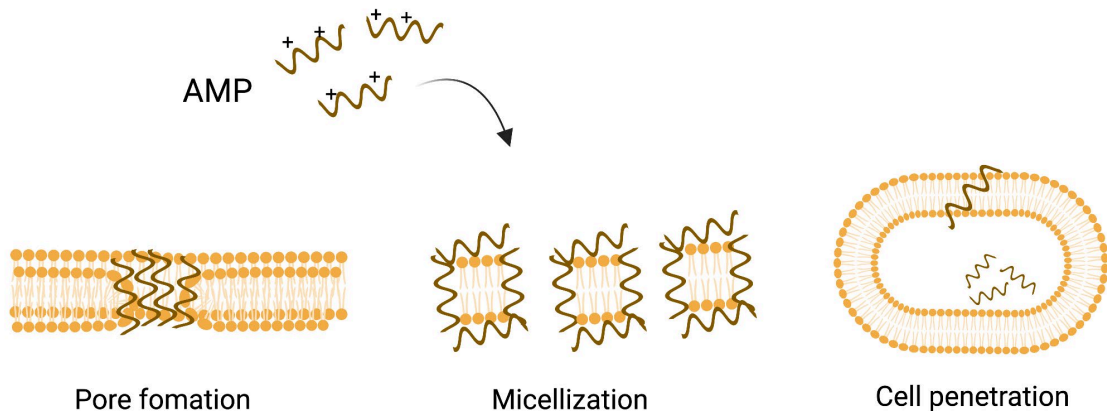


Figure 1.12: Potential mechanisms of antimicrobial peptide antibiotics

Other AMPs have shown higher selectivity for membrane recognition. Cinnamycin and duramycin are two lantibiotics that specifically target PE in bacterial membranes. Duramycin and cinnamycin are almost identical (**Figure 1.13**), differing only at one amino acid residue (lysine (K) or arginine (R) at the second position). The lantibiotic family is defined by the presence of thioether amino acids, formed from cross linking of a cystine residue. The complexity of cross linking lowers the risk of protease degradation (better bioavailability), and well-defined three-dimensional structure allows for more selective targeting.⁹⁹

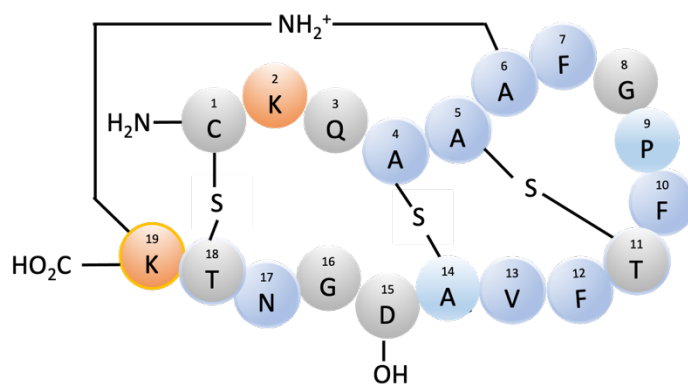


Figure 1.13: The structure of duramycin using the one-letter amino acid codes. Residues are color coded for hydrophobic (blue), cationic (orange), and other (grey).

Duramycin has been approved for veterinary use but remains too toxic in humans. This is surprising, since recent work found that cinnamycin bound to PE with much higher affinity than PC in molecular modeling experiments. The alkylation of the amine group seems to be too large to fit in the lantibiotics binding site. Isothermal titration calorimetry (ITC) binding studies also found duramycin bound preferentially to PE in liposomes of 9:1 PC:PE with an association of $(2.1 \pm 0.4 \times 10^8 \text{ M}^{-1})$.¹⁰⁰ Binding affinity increased in more highly curved liposomes. Accumulation of the antibiotic in the outer membrane led to

translocation of PE to promote more binding sites and negative curvature. Expectedly, duramycin-resistant *B. subtilis* has shown a decrease expression of PE and CDL lipids to reduce curvature.¹⁰¹ Sequestering of PE in the membrane also leads to inhibition of phospholipase A2, an enzyme responsible for the hydrolysis of membrane phospholipids.¹⁰² It is unknown which mechanism is directly related to duramycin's activity, but likely a synchronous combination of the three. A deeper understanding of how these different mechanisms contribute to cell death could help with decreasing toxicity in humans. However, PE-binding is an interesting area of research since unhealthy mammalian cells also express PE in their outer leaflet. Progress in the development of PE-sensors will be discussed in more detail in **Chapter 3**.

These are only two specific examples of antimicrobial peptides, which do not illustrate their biodiversity. Some AMPs have been approved as topical antibiotics which overcome cytotoxicity or enzyme degradation. Very few synthetic antibiotics have been designed to target membrane phospholipids (which will be discussed through this thesis). Overall, there is an urgent need for the development of antibiotics that are less susceptible to bacterial resistance pathways. There is also a need for better understanding of AMP mechanisms, which could be done through the development of receptors for bacterial lipids. Better understanding of membrane-based mechanisms and development of membrane-targeting antibiotics will decrease hospitalizations for patients world-wide.

1.4 Aim of this dissertation

The primary goal of this thesis is to develop novel receptors for membrane lipids using neutral hydrogen bonding interactions. Membrane recognition is useful in many biological processes. The diversity of phospholipids allows for selectivity of a certain organism or health concern. Receptors for lipid binding can assist in deeper understanding of anionic membrane interactions, which historically rely on electrostatic interactions rather than more selective hydrogen bonding. Receptors may also act as antibiotics through membrane-active pathways. Membrane targeting antibiotics are the most resilient class of antibiotics since external membrane-binding overcomes internal pathways. Since phospholipids contain polar headgroups with unique chemistry, supramolecular receptors should be utilized to further the work in this field.

CHAPTER 2

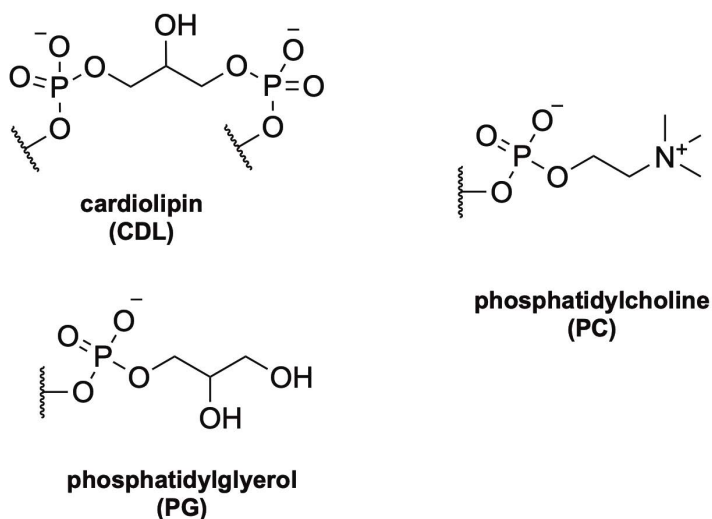
DEVELOPING NEUTRAL RECEPTORS FOR CARDIOLIPIN

In this chapter, we develop neutral receptors for cardiolipin, an anionic phospholipid crucial for many cellular processes in Gram-positive and Gram-negative bacteria. Moreover, it is only present in the human mitochondria rather than the outer leaflet of the cell membrane, which allows for selective targeting of bacterial cells. Currently, there are no neutral receptors designed to target cardiolipin. Those available are cationic and show little selectivity over other anionic bacterial phospholipids. Supramolecular receptors containing bis-urea analogs were designed to target the phosphate groups of cardiolipin. Binding studies and antimicrobial susceptibility assays were performed to determine the efficacy of the bis-ureas with cardiolipin.

2.1. Introduction

Cardiolipin (CDL) and phosphatidylglycerol (PG) are the primary anionic phospholipids in bacteria (**Scheme 2.1**). Cardiolipin is the minor component in anionic lipids, making up 0-25% of the total membrane lipids in Gram-positive and Gram-negative bacteria. CDL's negative curvature is essential for cellular processes. During cell growth,

CDL may enrich the dividing plane of bacteria at the expense of PG lipids.¹⁰³ This creates a curved, highly anionic region used for recognition of integral membrane proteins.¹⁰⁴ During sporulation, CDL concentration is increased from 2 to 20% of the total lipid composition in *B. subtilis*.¹⁰⁵ Despite the biological importance of CDL in bacterial membranes, no neutral hosts have been designed to target the headgroup of cardiolipin.



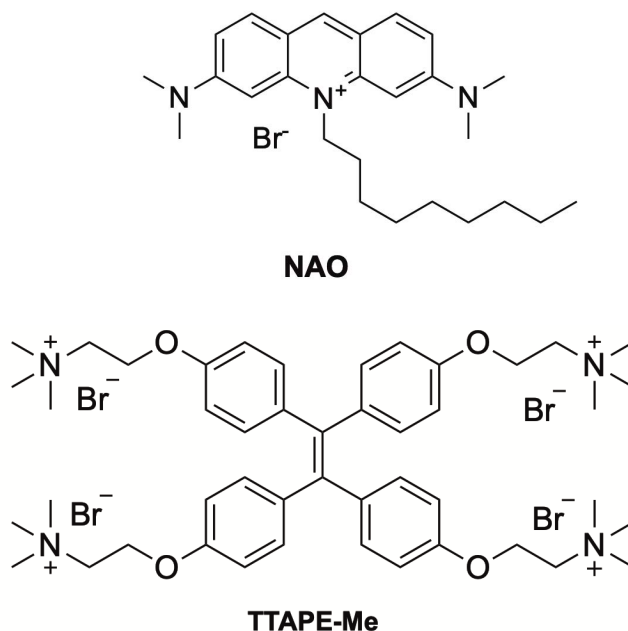
Scheme 2.1: Anionic bacterial lipids present in bacteria (PG, CDL) and the primary phospholipid in human membranes (PC).

Cardiolipin has a dimeric structure with two phosphates surrounding a central glycerol unit (**Scheme 2.1**). Both phosphates can be deprotonated to give a di-anionic lipid headgroup. Protonation of the first acidic phosphate occurs rapidly ($pK_{a,1} \approx 2.18$) in biologically relevant conditions, comparable to other phospholipids.^{106 107 108} However, there is still debate about the ionization range of the second phosphate. Scientists originally suggested the lipid headgroup has a much higher ionization constant for the

second phosphate ($pK_{a,2} > 8$) due to stabilization by a glycerol bridge.¹⁰⁹ More recent studies have also shown both phosphates of the CDL headgroup assert similar ionization constants ($pK_{a,1,2} = 2-3$) in aqueous dispersion and liposome-based assays (50% CDL/50% PC, 25 mM HEPES-KOH).^{110,106} Availability of both phosphates would allow effective supramolecular targeting of the bacterial membrane. If only one phosphate was available, it would be more difficult to design receptors that target CDL over PG lipids.

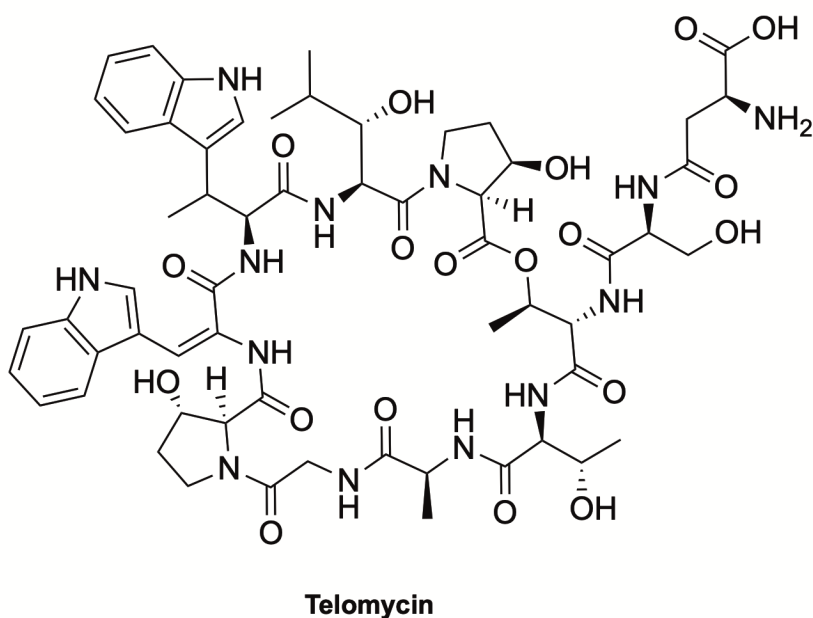
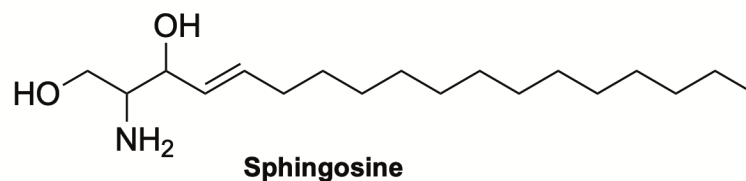
Historically, CDL-binding has been limited to cationic recognition. Very few receptors have been designed specifically for cardiolipin and many of these still exhibit some affinity for PG because of their similar anionic phosphatidylglycerol units. When CDL is removed from membranes, many “CDL-specific” antibiotics can still kill bacteria because of the anionic charge and similar structure in PG headgroup.¹¹¹ This section will discuss the previous work in CDL recognition in bacteria.

Visualization of lipids in membranes is useful in many applications. Nonyl acridine orange (**NAO**) is a molecular probe designed to visualize CDL in mitochondria membranes and was later adapted in *E. coli* to discover CDL-enriched domains at the cell poles (**Scheme 2.2**).¹¹²⁻¹¹⁴ **NAO** contains a quaternary ammonium that forms an electrostatic interaction with any negatively charged lipid. Fluorescence increases when **NAO** binds to CDL (2 **NAO**:1 CDL) or PG (1 **NAO**:1 PG) in membranes. Recent work by Lueng *et al.* developed a new probe with four quaternary amines lipophilic tails to increase CDL-selectivity (**TTAPE-Me, Scheme 2.2**).¹¹⁵ It is likely that this molecule will still coordinate to other anionic lipids. Neutral receptors for CDL could aid in selectivity of molecular probes as well as antibiotics.



Scheme 2.2: Fluorescent probes for the detection of cardiolipin.

Antibiotics that target CDL are typically dependent on the highly anionic charge that accumulates in CDL-rich domains. **Sphingosine** (Scheme 2.3) is an amino alcohol found in nasal, bronchial, and tracheal epithelial cells used as the body's natural defense against pathogens.⁶⁸ **Sphingosine** has been shown to exhibit bacteriostatic activity against *E. coli* and *P. aeruginosa* through interaction of the protonated amino alcohol and CDL-rich clusters. A recent study by Verhaegh *et al.* found that mutants of *E. coli* deficient in cardiolipin were resistant to sphingosine unless incubated with 4x the MIC value (5 μ M).¹¹⁶ This allows for insertion of the membrane through coordination of PG-lipids, which are more dispersed.¹⁰⁴ Developing receptors that target specific lipids could overcome this and create more durable antibiotics in the future.



Scheme 2.3: Some naturally occurring antibiotics that bind to cardiolipin. Shown in their neutral form for clarity.

Telomycin (Scheme 2.3) is a cationic AMP isolated from *Streptomyces canus* with bactericidal activity against MRSA (MIC ~2 μM) and other Gram-positive organisms.¹¹⁷ Recent work by Fu *et al.* found that **telomycin** may have a CDL-dependent mechanism, since resistant strains of *S. aureus* and *B. subtilis* displayed a mutation in the cardiolipin synthase gene.¹¹⁷ Other binding studies have not been done to confirm any selective recognition of CDL over PG in bacterial membranes.

Another use for lipid-specific receptors is drug delivery. Drug delivery may increase selectivity of new antibiotics (decrease side effects or require lower dosages) as well as provide new pathways for antibiotic action. Transcription factors are proteins involved in transcribing DNA to RNA. Blocking this pathway with decoy oligonucleotides would provide a new pathway for the antibiotic target. Unfortunately, oligonucleotides are typically large (~4-14 kDa) hydrophilic polyanions that face issues with bioavailability and crossing the bacterial membrane.¹¹⁸ Bolaamphiphiles are large amphiphilic molecules with two hydrophilic headgroups linked by a hydrophobic chain that are increasingly being used as drug-delivery vehicles.¹¹⁹ Recently, novel bolaamphiphile (**12-bis-THA nanoplex**) was designed to target cardiolipin domains for enhanced delivery of transcription-inhibiting oligonucleotide antibiotics (**Figure 2.1**).¹²⁰

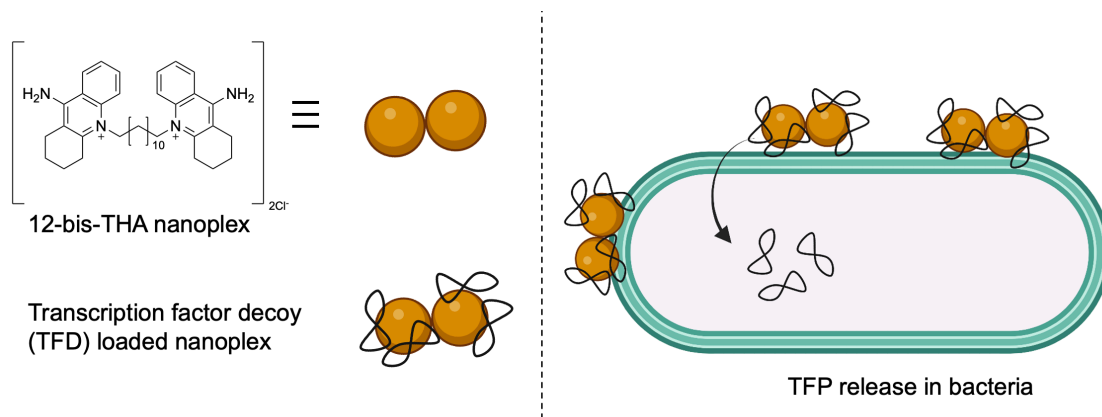


Figure 2.1: Cationic 12-bis-THA nanoplex delivers transcription factor decoy (TFD) to cytoplasm of Gram-negative bacteria.

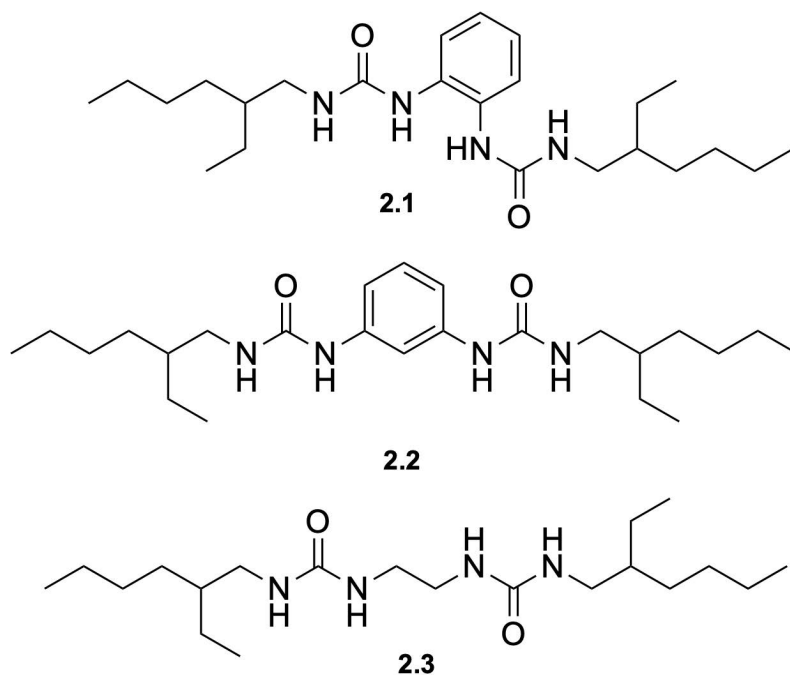
The nanoplex was reported to target cardiolipin domains for the delivery of transcription-inhibiting antibiotics in *C. difficile* and *E. coli* model liposomes.¹²⁰ However, addition of an Alexa 488 dye to the oligonucleotide revealed only moderate increase in uptake in CDL-

rich compared to PG-rich liposomes. Development of neutral, more selective receptors could aid in drug delivery mechanisms that target CDL rather than anionic lipids in membranes.

2.2. Results and Discussion

2.2.1. Design and synthesis of receptors for cardiolipin

To design receptors for cardiolipin, we utilized the two phosphate groups as targets. Urea functionalities served as phosphate receptors and long, branched alkyl chains were incorporated as lipophilic anchors for increased membrane permeability. We tried three different rigid and flexible spacers between the urea groups to get a range of hosts that may interact with the CDL headgroup (**Scheme 2.4**).



Scheme 2.4: Novel compounds designed to bind to cardiolipin

Synthesis of the bis-ureas was completed by reacting 2 equivalents of 2-ethylhexyl isocyanate with *o*-phenylenediamine (**2.1**), *m*-phenylenediamine (**2.2**), or ethylenediamine (**2.3**) overnight in DCM (**2.1- 2.2**) or pyridine (**2.3**). Purification of the aromatic bis-ureas required column chromatography while **2.3** was able to be recrystallized in DCM. Detailed synthesis and characterization can be found in **Chapter 5** (Materials and Methods), and ¹H and ¹³C NMR spectra are given in **Appendix A**.

2.2.2. ¹H NMR binding studies

First, we wanted to identify the interaction of **2.1-2.3** with cardiolipin using ¹H NMR titrations. ¹H NMR provides information on the binding affinity and stoichiometry of the complex via monitoring the change in chemical shifts ($\Delta\delta$) in relation to the concentration of guest added.¹²¹ Obtaining useable binding data for cardiolipin was challenging due to solubility issues with the receptor and lipid. In all studies, we used the shortest alkyl chains available from Avanti Lipids (CDL 14:0), but the lipid still contained 4 carbon chains that limited solubility. Mixtures of different deuterated solvents (CD₃OD, CD₃CN, CDCl₃, DMSO-*d*₆) were tested with low concentrations of the bis-urea and lipid (1 mM compound, 15 mM CDL) but it was difficult to obtain a homologous solution.

Compound **2.1** showed the best solubility with CDL, but the mixture crashed out of solution in DMSO-*d*₆ at only 1 eq. CDL. Cardiolipin is shipped with a sodium counter ion (CDL-Na₂), so we attempted to increase solubility of the CDL by complexation of the Na⁺ with 15-crown-5.¹²² This did not yield any change in solubility between bis-ureas and cardiolipin. Next, we developed a method to exchange the Na⁺ with a bulkier organic counter ion, tetra-butyl ammonium (TBA⁺) that may reduce competition of CDL-binding

to bis-ureas. Ion exchange with TBA⁺ was performed in two steps: protonation of CDL and titration of CDL-H₂ with 2 equivalents TBA-OH to yield a disubstituted CDL-TBA₂. The successful formation of CDL-TBA₂ could be seen in ¹H NMR by comparison of the integrations of TBA and CDL in listed in **Figure 2.2**.

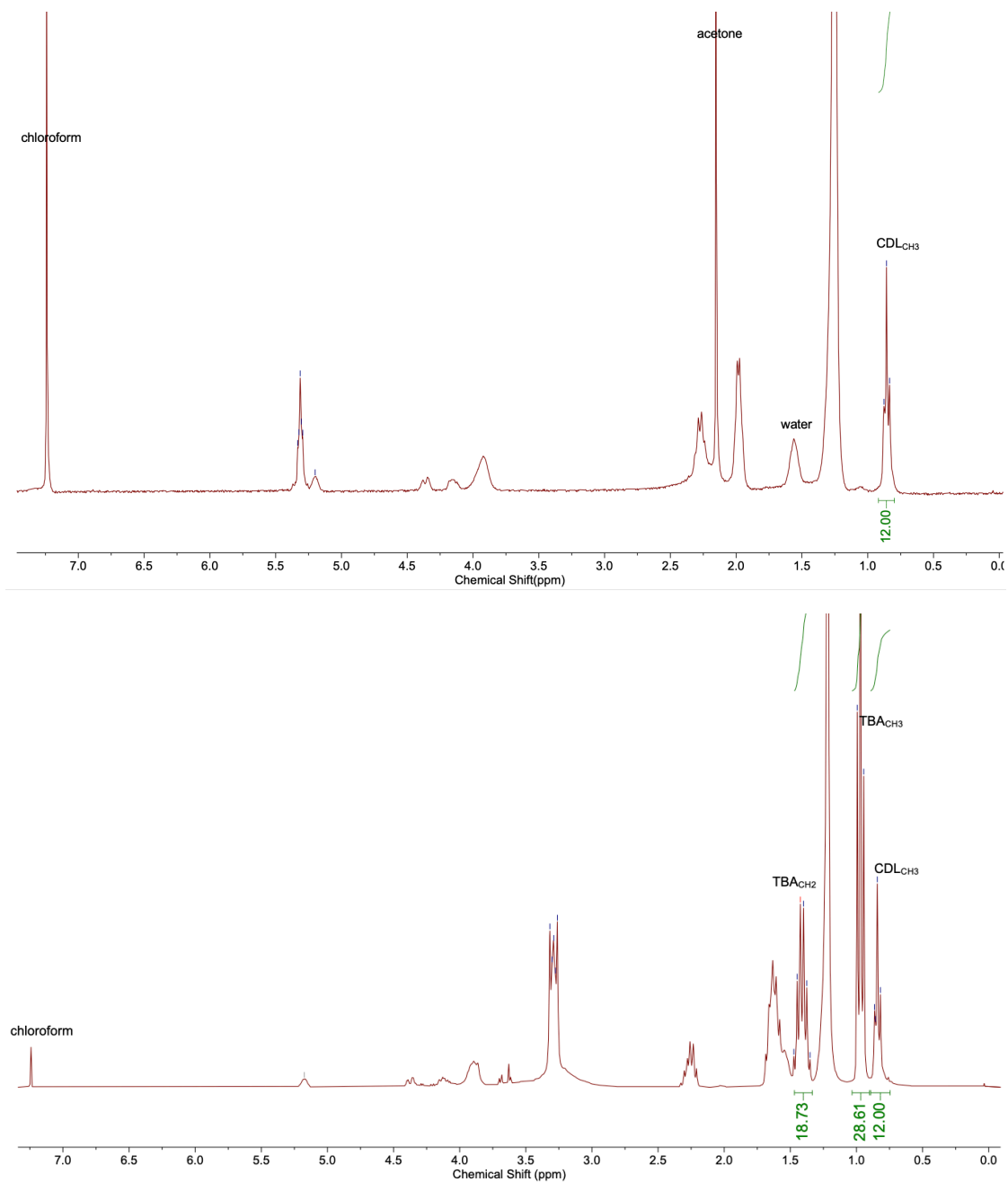


Figure 2.2: (top) ¹H NMR of cardiolipin 14:0 (Avanti #750332) in CDCl₃ before ion exchange with 2 eq. TBA-OH. CDL_{CH3} refers to the terminal CH₃ of the alkyl chains of CDL. **(bottom)** ¹H NMR of cardiolipin 14:0 (Avanti #750332) in CDCl₃, after TBA⁺ cation exchange. integrations are referenced by the terminal CH₃ in CDL (CDL_{CH3}). Both ions contain 4 terminal CH₃ groups that are symmetrical. Integration of cardiolipin CDL_{CH3} and counter cation TBA_{CH3} show the formation of 2TBA:1CDL.

Solubility was enhanced after obtaining the CDL-TBA₂ salt, but binding to cardiolipin with any of the bis-ureas during ¹H NMR studies in DMSO-*d*₆ was still undetectable. **Figure 2.3** shows the result for the titration of **2.2**, while the titrations of **2.1** and **2.3** are given in **Appendix A**. Compounds **2.1** and **2.2** showed better solubility than **2.3**, which crashed out of solution at 1.5 eq. CDL-TBA₂. Some shift in urea NHs occurred in **2.2** with the addition of CDL but the shift in N-H was < 0.1 ppm after 2.5 eq. CDL-TBA₂ added (**Figure 2.3**). We also saw a change in the intensity of the urea N-H of **2.1** with the addition of 2.5 eq CDL but we were unable to increase the concentrations to obtain binding data from ¹H NMR titrations. To try to overcome the solubility issues, we moved on to liposome-based binding studies.

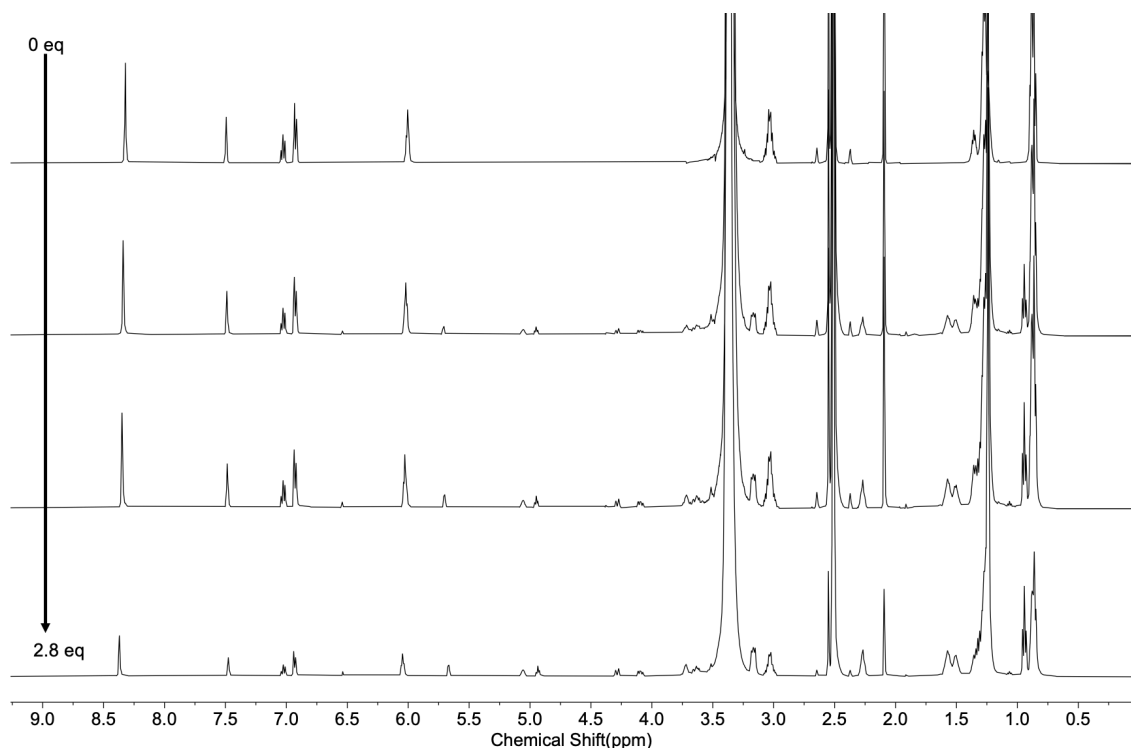


Figure 2.3: ^1H NMR titration of **2.2** with CDL-TBA₂ in 0.5% Milli-Q H₂O:99.5% DMSO-*d*₆ at 298 K. No measurable binding was observed from urea NHs at $\delta_A = 6.02$ ppm and $\delta_B = 8.32$ ppm.

2.2.3. Liposome-based binding studies

Liposomes are spherical bilayers commonly used for model membranes in binding or ion transport studies. Cardiolipin's cone shaped geometry prevents the lipid from forming bilayers in 100% CDL liposomes, so bilayer lipids (PC, PG) are needed for stability. This increases competition for binding to CDL since other lipids are present, but binding events should still be detectable if the receptors bind selectively to CDL over the other lipids in the bilayer. Different approaches included Triton-X 100 micelles and NAO-probe displacement. Each of these is outlined in detail in **Chapter 5** (Materials and Methods). Unfortunately, liposome studies were not able to reveal any binding data either.

Triton X-100 has been previously used to study binding of PS, PC, and PI phospholipids in mixed micelles.¹²³ The non-ionic surfactant is useful because there is a low chance of competition with CDL's anionic headgroup. Micelles had been previously formed containing $\leq 0.9\%$ lipid, so we used 0.4% molar eq. 1,1',2,2'tetraoleoyl cardiolipin[4-(dipyrromethene boron difluoride)butanoyl] (TopFluor® BODIPY-CDL) in Triton X-100.¹²³ Unfortunately, the micelles were unable to form. We added excess of Triton-X 100 to the cuvette while stirring without any change in solubility, then allowed for the solution to sit overnight but it was too cloudy to be used in any experiments (Figure 2.4).

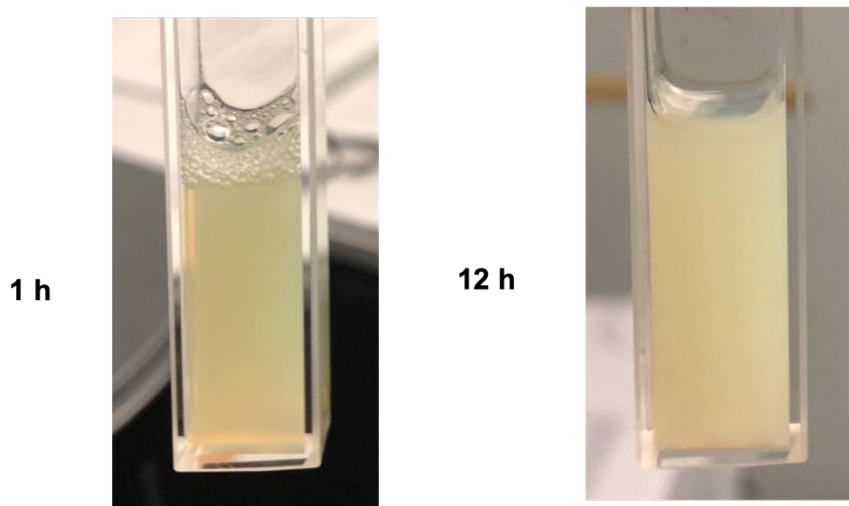


Figure 2.4: Triton X-100 with 0.4% BODIPY-CDL did not form micelles to study CDL-binding. Pictures were taken after stirring in a cuvette for 1 hour and overnight (12 h).

At the time we were unaware that CDL's reverse micelle geometry inhibited micelle formation with Triton-X 100. As mentioned in **Chapter 1**, the geometry of the lipid can dictate packing arrangement in micelle or lamellar bilayer formation.¹²⁴ Detergents

(Triton X-100) have a “inverted cone” geometry and preferentially form micelles, while CDL has a small headgroup compared to its bulky tetra alkyl chains and creates a “cone” shaped geometry.⁶² This leads to a reverse micelle structure which likely inhibited formation of the micelles, even at the very low concentration of CDL used ($\leq 0.4\%$ molar eq. CDL to Triton X-100). Previous work had used cylindrical lipids that form bilayers rather than using lipids with negative curvature.

Next, we tried a dye displacement study using **NAO**. If compounds bind to cardiolipin, **NAO** is displaced from the membrane which should cause a change in fluorescence intensity. Mixed liposomes (7:3 POPE:CDL) were formed in a buffer solution of Tris-HCl (10 mM, pH 7.4) and **NAO** fluorescence intensity was measured after 5 minutes of stirring upon each addition using excitation/emission wavelengths of 488/520 nm.¹²⁵ Our study found a marginal decrease (12%) in **NAO** fluorescence when treated with 20 μM **2.2** (10x the **NAO** concentration, 5x the CDL concentration) but addition of other compounds or EtOH (negative control) led to an increase in fluorescence (**Figure 2.5**). It is possible that **2.2** causes some interaction with CDL but does not associate well enough to substantially displace **NAO**. Additionally, the increase in fluorescence seen by the ethanol control and other compounds may be caused by crashing out of the compounds or liposome stability. To verify if compounds **2.1-2.3** could bind to cardiolipin, we began antimicrobial testing.

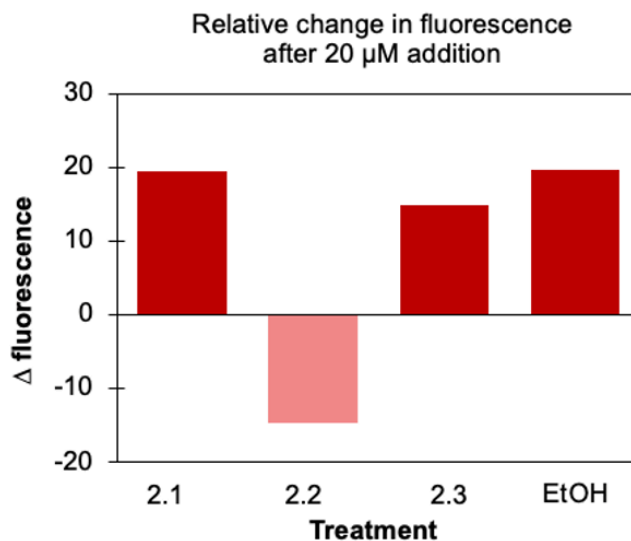


Figure 2.5: Binding of cardiolipin headgroups lead to a change in **NAO** fluorescence. Our studies showed unreliable data that did not indicate any CDL-binding (changes in fluorescence intensity where comparable to negative control).

2.2.4. Bacterial testing

Because we were unable to obtain any binding data due to solubility problems and other experimental factors, we wanted to test the activity of **2.1-2.3** in bacterial studies. Bacterial studies are easy to perform, and the overall aim of this chapter was to develop compounds that target CDL and subsequently kill bacteria. Therefore, if compounds **2.1-2.3** do not display any bacterial activity, there would be little reason to continue to optimize binding studies with CDL. Efficacy of antibiotics is determined by the minimum inhibitory concentration (MIC), which is the minimal concentration needed to impede bacterial growth for 24 hours. Compounds **2.1-2.3** were dissolved in DMSO and incubated with *S. aureus*, *E. coli* and *P. aeruginosa* in 96-well plates using the broth microdilution method for antibiotic susceptibility testing. Broth microdilution methods are useful for testing a wide range of concentrations of an antibiotic through serial dilutions of the

antibiotic in broth. The antibiotic is dissolved in a suitable water miscible solvent (water, DMSO, or methanol) and added to bacteria inoculum in broth for a final concentration of 5×10^5 colony forming units (CFU)/mL in 200 μ L. The concentration of bacteria is standardized to 5×10^5 CFU/mL to ensure reproducibility between biological repeats.

In this study the bis-ureas were dissolved in DMSO due to solubility reasons. The maximum amount of DMSO that did not appear to influence bacteria growth was 4% the total well volume (8 μ L in 200 μ L) and a DMSO control was included in each MIC study. Bacterial growth was measured by an increase in absorbance at 600 nm (OD_{600}) over 24 h. The 96-well plate was continuously shaken between spectrometer readings to limit any precipitation of the bis-ureas and allow aeration for bacterial growth. Concentrations of 1-100 μ M were tested for **2.1-2.3** with Gram-positive (*S. aureus*) and Gram-negative (*E. coli*, *P. aeruginosa*) organisms that contained various amounts of CDL in the membrane. It was most likely for the ureas to work against *S. aureus* because of its high CDL-content and the fact that Gram-positive organisms only contain one protecting bilayer. Compounds **2.1-2.3** showed similar absorbance values at 600 nm as the DMSO control, indicating that they were not able to kill bacteria at any of the concentrations tested (**Figure 2.6**). This is consistent with the lack of membrane interaction seen in the previous liposome and ^1H NMR studies.

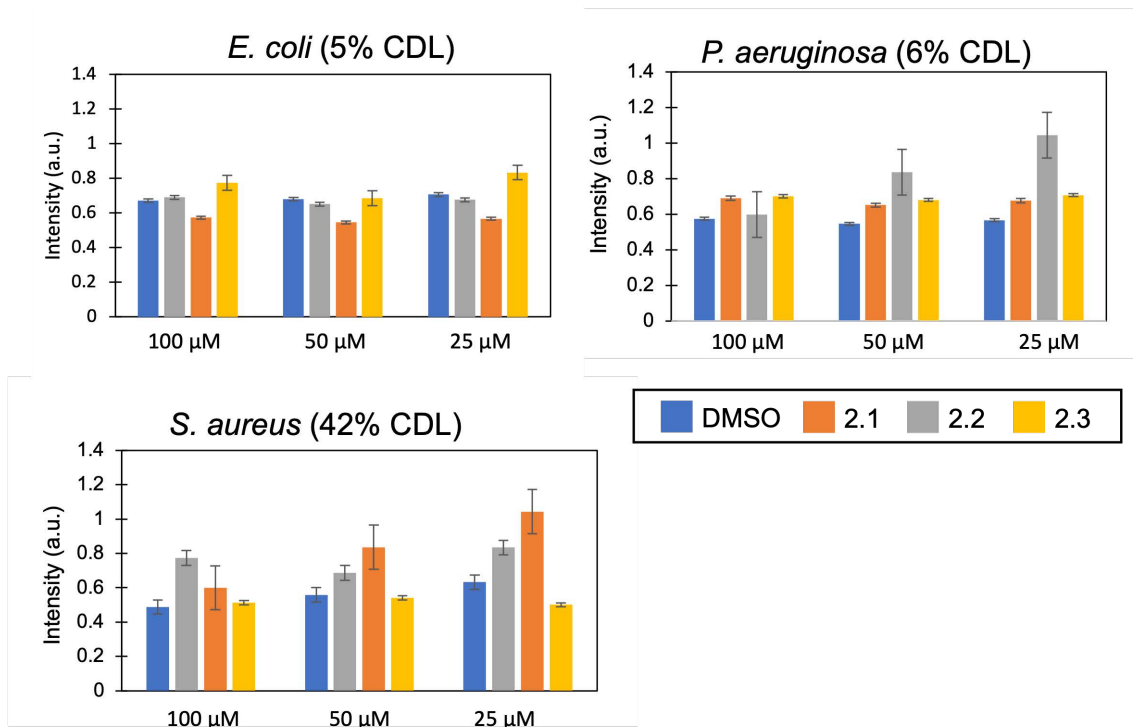


Figure 2.6: Change in growth of bacteria after 24 h, as measured by the absorbance (Abs) intensity at 600 nm after 24 h incubation at 35 °C. Data displayed is the average of three biological repeats with error bars showing the standard deviation. The bis-urea compounds did not significantly decrease growth of any bacteria compared to the DMSO control.

2.3. Conclusion

In this chapter, we were unsuccessful at creating a neutral host for cardiolipin. There was no measurable binding between **2.1-2.3** and cardiolipin in ¹HNMR titrations or liposome-based assays. The large size of cardiolipin compared with the poor solubility of the bis-ureas made binding data less reliable. Once we tested the compounds with common strains of Gram-positive and Gram-negative bacteria, no antibiotic activity was

detected even though *S. aureus* has a cardiolipin-rich membranes. Cardiolipin is still a valuable target for future antibiotic development because of its importance in bacterial division and biofilm integrity.¹²⁴ Future work should continue to test phosphate receptors for antibiotic activity and to learn about the binding mechanisms of natural products that target CDL.

CHAPTER 3

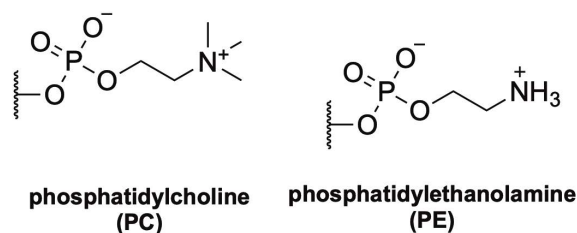
UREA FUNCTIONALIZED CROWN ETHERS TARGET

PHOSPHATIDYLETHANOLAMINE IN BACTERIAL MEMBRANES

The results in this chapter have been previously published as "Bactericidal urea crown ethers target phosphatidylethanolamine membrane lipids", S. Herschede., H. Gneid, T. Dent, E. Jaeger, L. Lawson, N. Busschaert. Organic & Biomolecular Chemistry 19.17 (2021): 3838-3843. Reproduced with permission of The Royal Society of Chemistry.

3.1 Introduction

Due to the struggles of working with anionic lipids discussed in **Chapter 2**, we focused on neutral phospholipids that were present in bacterial membranes. Phosphatidylethanolamine (PE) is a zwitterionic phospholipid found in most Gram-negative bacteria and in certain Gram-positive bacteria.^{96, 126-127} In healthy mammalian cells, PE is limited to the inner leaflet of the plasma membrane or mitochondrial membrane. The most common zwitterionic lipid found in the outer leaflet is phosphatidylcholine (PC).¹²⁸ PE and PC have a similar headgroup but differ in methylation of the ammonium group (**Scheme 3.1**). Selective recognition of bacterial zwitterionic lipids could therefore be achieved by designing receptors that target the ammonium and phosphate of PE.



Scheme 3.1: Phospholipid headgroups of human (PC) and bacterial (PE) zwitterionic phospholipids.

PE is a non-bilayer forming phospholipid like cardiolipin. Hence, PE shares a similar structural role in membrane fusion and distribution at cell division sites.⁶¹ PE also plays a similar role in apoptosis as phosphatidylserine (PS), although it is much less studied.¹²⁹⁻¹³⁰ During apoptosis, PE is translocated from the inner membrane to the outer membrane by flippases, floppases or scramblases for recognition by proteins. In healthy cells, PE is found in low quantities (~5%) on the outer membrane, so PE-targeting antibiotics should have low cytotoxicity.¹³¹ Additionally, PE could act as a narrow-spectrum antibiotic. Although PE is one of the most abundant lipids that make up bacterial membranes, it is primarily found on the inner leaflet of the outer membrane in Gram-negative bacteria and only present in certain Gram-positive bacteria: *Bacillus* spp. and *Clostridium* spp.

Cinnamycin and duramycin are two lantibiotics that specifically target PE in bacterial membranes. Duramycin and cinnamycin are almost identical, differing only at one amino acid residue (**Figure 3.1**).¹³² The lantibiotic family is defined by the presence of thioether amino acids, formed from cross-linking of a cystine residue. The complexity of the crosslinks both lowers the risk of protease degradation and adds complexity to the binding site. The binding affinity of duramycin and cinnamycin has been experimentally

studied through ITC liposome studies (100 nm, 90% POPC: 10% POPE) which prove the 1:1 association of PE with cinnamycin ($K_a = 10^8 \text{ M}^{-1}$) and duramycin ($K_a = (2.1 \pm 0.4) \times 10^8 \text{ M}^{-1}$).¹³³⁻¹³⁴ ¹⁰⁰ Antibacterial activity of the peptides can be caused by multiple mechanisms, as discussed in **Chapter 1**.^{90, 101} These include membrane permeability, reorganization of PE in the membrane (flip/flop), and inactivation of phospholipase A2.

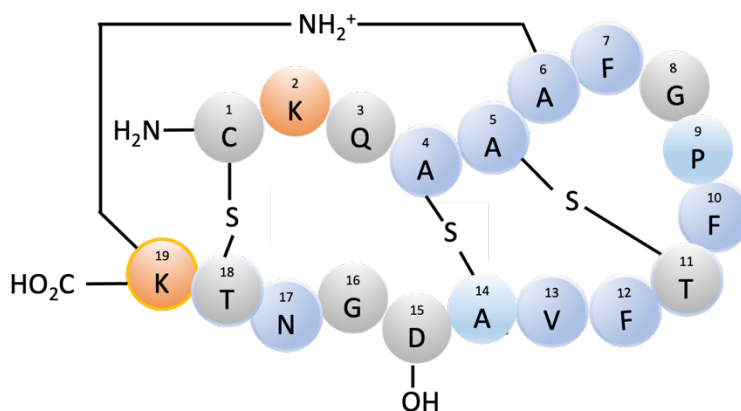


Figure 3.1: The structure of duramycin (cinnamycin differs at the second position with an arginine (R) group instead of lysine (K)). Hydrophobic residues are shown in blue, cationic in orange and other residues in grey.

The proposed binding mechanism of PE in the hydrophobic pocket of cinnamycin has been examined by ^1H NMR studies for cinnamycin and lyso-phosphatidylethanolamine (Lyso-PE). ^1H NMR of the cinnamycin-lipid complex in $\text{DMSO-}d_6$ found the ammonium to bind in a tight hydrophobic pocket that “was unlikely to accommodate other glycerophospholipids.”¹³⁵ Lyso-PE lacks one of the acyl chains and was presumably used to minimize interference of the acyl tails, which can cause aggregation due to the hydrophobic effect and block binding sites. Binding of the ammonium head group was

thought to occur with hydroxy aspartic acid (D15), with a hydrophobic pocket created by Glycine (G8), Proline (P9), and Valine (V13), and no interaction of the tail (**Figure 3.2**).¹³⁵

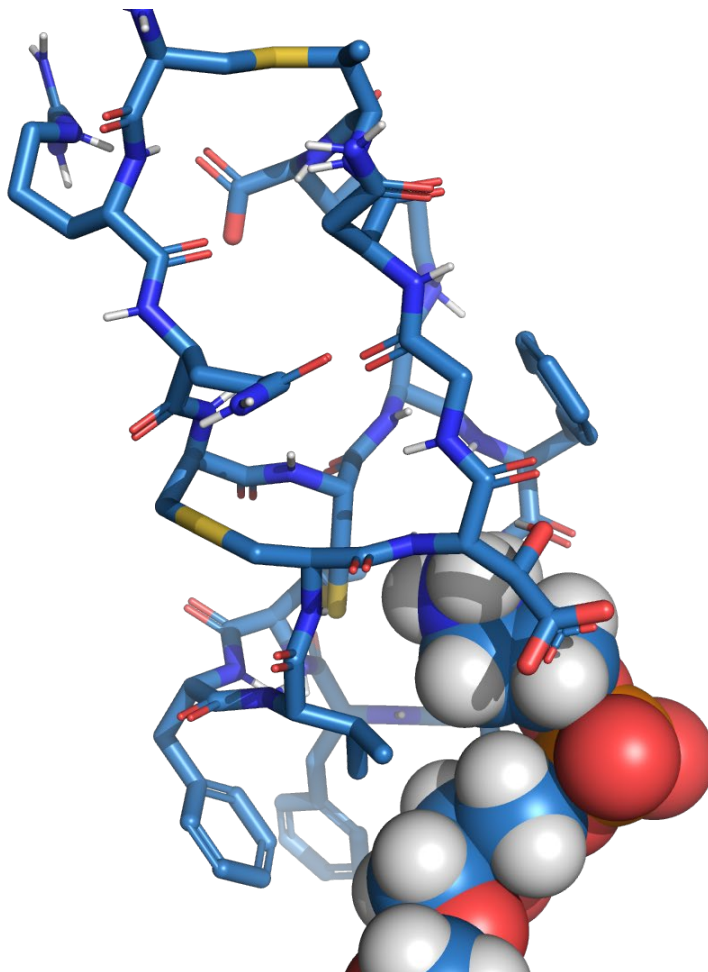


Figure 3.2: Binding pocket of cinnamycin with Lyso-PE from ¹HNMR, PDB: 2dde_1. ¹³⁵
The image was generated using Pymol. Atom colors: carbon (light blue), phosphate (orange), oxygen (red), nitrogen (dark blue), and hydrogen (grey)

Further work used molecular dynamics to create a model of the lowest energy conformation of 12:0 PE and cinnamycin using water, dimethyl sulfoxide, and ethanol. This predicted additional interactions between the peptide and lipid, as shown in **Figure 3.3**.¹³⁴ The ammonium of PE appears to interact with the hydroxyl groups of the backbone

phenylalanine (F7) and valine (V13) and carboxylate of hydroxy aspartic acid (D15) in cinnamycin. This also predicted a slightly different arrangement of the hydrophobic pocket, which involved additional hydrogen bonding of threonine (T11), V13, F12, and F10 with the phosphate headgroup.¹³⁴ Molecular dynamics found a much lower binding affinity between cinnamycin-PC under the same conditions. This is likely due to the size of the pocket (which cannot accommodate PC), the lack of hydrogen bonding ability of the methyl ammonium, and the lower hydrophobicity of the PC headgroup.¹³⁴ Despite the selectivity of cinnamycin for PE over PC lipids, the lantibiotics have limited clinical applications because of their cytotoxicity and poor pharmacokinetics (as seen with most AMPs).

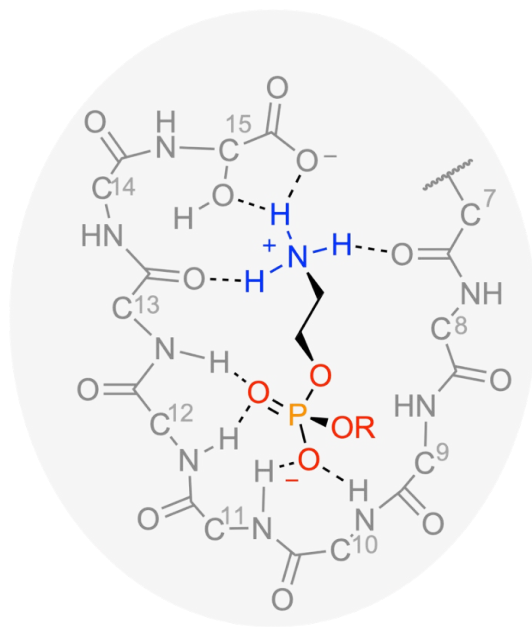
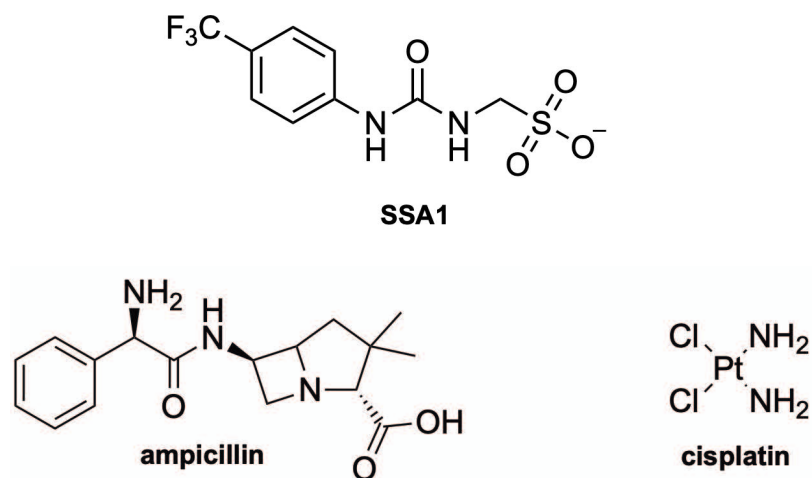


Figure 3.3: Cinnamycin-PE binding complex generated from molecular dynamics studies by Vestergaard et al.¹³⁴

Imaging probes have been developed using cinnamycin or duramycin for selective PE sensing in different biological and laboratory assays.^{136 137 131 138} Conjugates are

covalently modified at the *N*-terminal of the peptide with the desired probe and used in low concentrations to avoid toxicity. The specificity for PE-binding makes the lantibiotics attractive in cancer or cell-death imaging.¹³⁶⁻¹³⁸ Synthetic receptors for PE have been a recent area of interest in supramolecular chemistry because of their wide applicability.

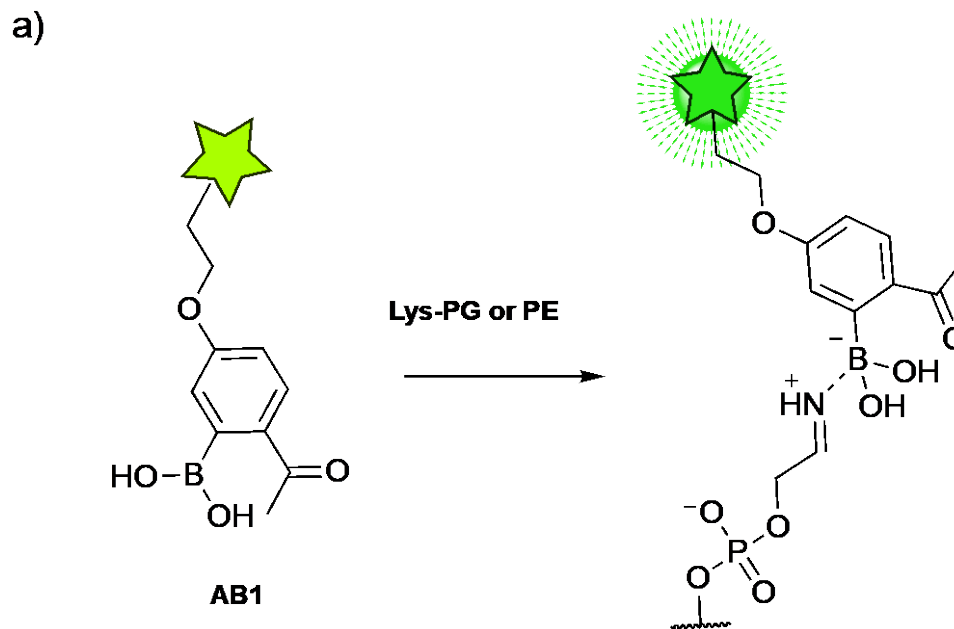
Other recent work in PE-binding receptors includes a library self-associating amphiphiles (**SSA**) recently developed by Jenifer Hiscock's group.¹³⁹⁻¹⁴² The small molecules contain hydrogen bond donor (urea) and acceptor (sulfonamide) moieties that can adopt multiple hydrogen bonding modes simultaneously (**Scheme 3.2**).^{139 140} Binding studies found a strong preference in **SSA1** binding in *E. coli* model membrane (67% PE, 23% PG, 10% CDL) over PC in lipid nanodiscs.¹⁴³ Selectivity of PE or PG can be achieved through hydrogen bonding interactions of the sulfonate with the glycerol hydroxide (PG) or ammonium (PE). In PC, methylation of the ammonium only allows for sterically hindered weak electrostatic interactions.¹⁴¹ Additionally, **SSA1** has been used to enhance the uptake of **ampicillin** and **cisplatin** (**Scheme 3.2**) in *E. coli* and cancer cell lines, respectively.¹⁴² **Ampicillin** is a cell wall targeting antibiotic that is unable to cross the lipid bilayer of Gram-negative bacteria. **Cisplatin** is an anticancer drug that exhibits high cytotoxicity which could be decreased by targeted drug delivery.¹⁴³⁻¹⁴⁴ The biological activity of **ampicillin** and **cisplatin** was increased when **SSA1** and drug were added as a combination therapy (one after another). This suggests the **SSA1** is interacting with the membrane via drug transport or increased permeation. The unique properties of the anionic molecules show promise for future PE-binding receptors. However, these are likely facilitating drug transport rather than acting as membrane-binding antibiotics.



Scheme 3.2: Amphiphilic self-associating amphiphile (**SSA1**) developed by Hiscock et al. with potential PE-binding selectivity.^{140, 142}

Another synthetic receptor, **AB1**, contains a boronic acid for reversible covalent binding to amine-containing lipids (**Scheme 3.3**).¹⁴⁵ **AB1** showed selectivity for PE and lysyl-phosphatidylglycerol (Lys-PG) over phosphatidylglycerol (PG), phosphatidylserine (PS), and PC. *Ortho*-substituted boronic acids have been known to form inter- and intramolecular iminoboronate bonds with tertiary amines.^{146 147} Additionally, the iminoboronate bond is highly susceptible to pH and small molecules, thus it is easily reversed. AlexaFluor 488 tagged **AB1** was added to liposomes with 100% PC or 60% PC: 40% PE, PG, PS, or Lys-PG to monitor the selectivity of lipid binding in model membranes. The fluorescence only increased in Lys-PG and PE-rich liposomes, indicating the formation of the iminoboronate (**Scheme 3.3**). This was also confirmed in ¹¹B NMR and mass spectrometry by lyophilizing the **AB1** complex with Lys-PG vesicles and then dissolving the complex in 2:1 CDCl₃:CH₃CD.¹⁴⁶ **AB1** was also able to fluorescently label PE- and Lys-

PG-rich membranes of *B. subtilis* and *S. aureus*, respectively. The quaternary amine of PC is unable to participate in the iminoboronate bond and the additional carboxylic acid of the PS head group may sterically block the interaction.



Scheme 3.3: Boronic acid receptor **AB1** binds selectively to amine-containing lipids. **AB1** is fluorescently tagged with AlexaFluor 488, and binding of PE or Lys-PG in membranes causes an increase in fluorescence.

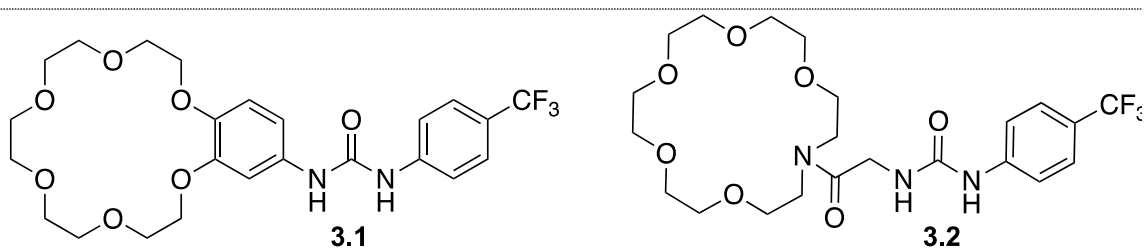
In this chapter we will discuss a novel small molecule capable of targeting PE over PC in different membrane compositions. The ditopic receptor is designed to target both the phosphate and ammonium of PE through hydrogen bonding. This should lead to a better understanding of PE-binding mechanisms for future drug development.

3.2 Results and discussion

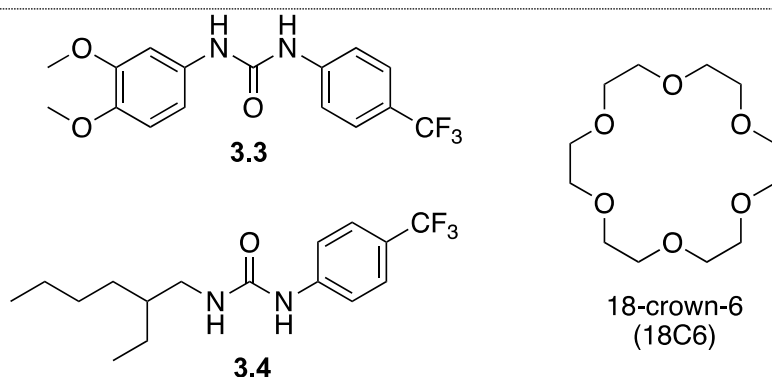
3.2.1. Design and synthesis of novel phosphatidylethanolamine receptors

Our approach utilizes a urea functionality to bind to the phosphate moiety, 18-crown-6 to bind to the ammonium group, and a trifluoromethyl-substituted phenyl substituent as a lipophilic membrane anchor for PE recognition.¹⁴⁸⁻¹⁵⁰ The urea and crown ether functionality are linked together through a rigid linker (**3.1**) or a flexible linker (**3.2**) to determine the optimal geometry that allows the best binding to the headgroup. Control compounds **3.3** and **3.4** were also synthesized to investigate the importance of the urea moieties in the molecular recognition of PE lipids (**Scheme 3.4**). Commercially available 18-crown-6 was also included in our studies to assess the importance of having both the urea and crown ether moiety present in the PE-binding compounds. Synthetic details are given in **Chapter 5** and characterization details are provided in **Appendix B**. Crown ether derivatives have been reported as antimicrobial agents due to their ability to function as ionophores for K^+ ions.¹⁵¹ However, the low membrane selectivity of ionophores has impaired their clinical usefulness. In contrast, our design takes advantage of 18C6's ability to selectively bind to primary ammonium cations over more substituted ammonium cations.¹⁴⁹ Combined with the phosphate-binding unit and membrane anchor, the crown ether derivatives become PE-selective membrane-active agents with improved antibacterial potency.

PE-binding compounds



Control compounds



Scheme 3.4: Compounds designed for PE-binding.

3.2.2. ^1H NMR binding studies

To assess the selectivity of **3.1** and **3.2** for PE over PC lipids, we initially performed a set of ^1H NMR titrations in organic solvents. Under these conditions the lipids do not form membranes but are free in solution. While this is not a perfect mimic of biological conditions, it allows an accurate determination of association constants and a good indication of the inherent headgroup selectivity of each compound. The titrations were performed with compounds **3.1-3.4** and **18C6** as the host and POPE (1-palmitoyl-2-oleoyl-*sn*-glycero-3-phosphoethanolamine) or POPC (1-palmitoyl-2-oleoyl-glycero-3-phosphocholine) as guest. Binding was measured by the shift in the urea N-H peaks for compounds

3.1-3.4 or the shift in the ammonium POPE for **18C6**. The titrations were carried out in a solvent mixture (0.5% Milli-Q H₂O, 24.5% DMSO-*d*₆ and 75% CDCl₃) for solubility reasons. Dimethyl sulfoxide is a more competitive solvent since it can act as a hydrogen bond acceptor, so we determined the minimal amount needed to solubilize the mixture.²⁶ The data was fitted using Bindfit¹⁵² and the obtained association constants (K_a) are given in **Table 3.2**. Representative titrations and fitting curves are provided in **Appendix B**.

Table 3.1: Overview of the PE-binding ability of hosts **3.1-3.4** and **18-crown-6**. All data is the average of at least 3 independent repeats and errors represent standard deviations

Host	K_a (M ⁻¹), NMR ^[a]	
	POPE	POPC
3.1	531±56	72±6
3.2	weak ^[b]	weak ^[b]
3.3	263±18	129±9
3.4	weak ^[b]	22±3
18C6	180±45	n.d. ^[c]

[a] Association constant (K_a , M⁻¹) obtained through ¹H NMR titrations in 0.5% H₂O:24.5% DMSO-*d*₆:75% CDCl₃ at 298 K. [b] No significant change in chemical shift was observed. [c] Not determined (n.d.) due to lack of protons capable of H-bonding.

It was found that compound **3.1** preferentially binds to POPE ($K_a = 530$ M⁻¹) over POPC ($K_a = 26$ M⁻¹). The ¹H NMR spectra and Bindfit graphs for **3.1** with POPE are included in **Figure 3.4**. Upon binding to POPE, the urea NHs of **3.1** shift downfield in response to a change in the environment. The data was fitted to a 1:1 binding curve and a fitplot (**Figure 3.4, b**) shows the shift in urea NHs in relationship to the amount of POPE added. The residual plot (**Figure 3.4, c**) visualizes how well the data fits the binding curve. It is

expected for the data to be scattered randomly, which correlates to random error rather than fitting the data to the wrong stoichiometry.

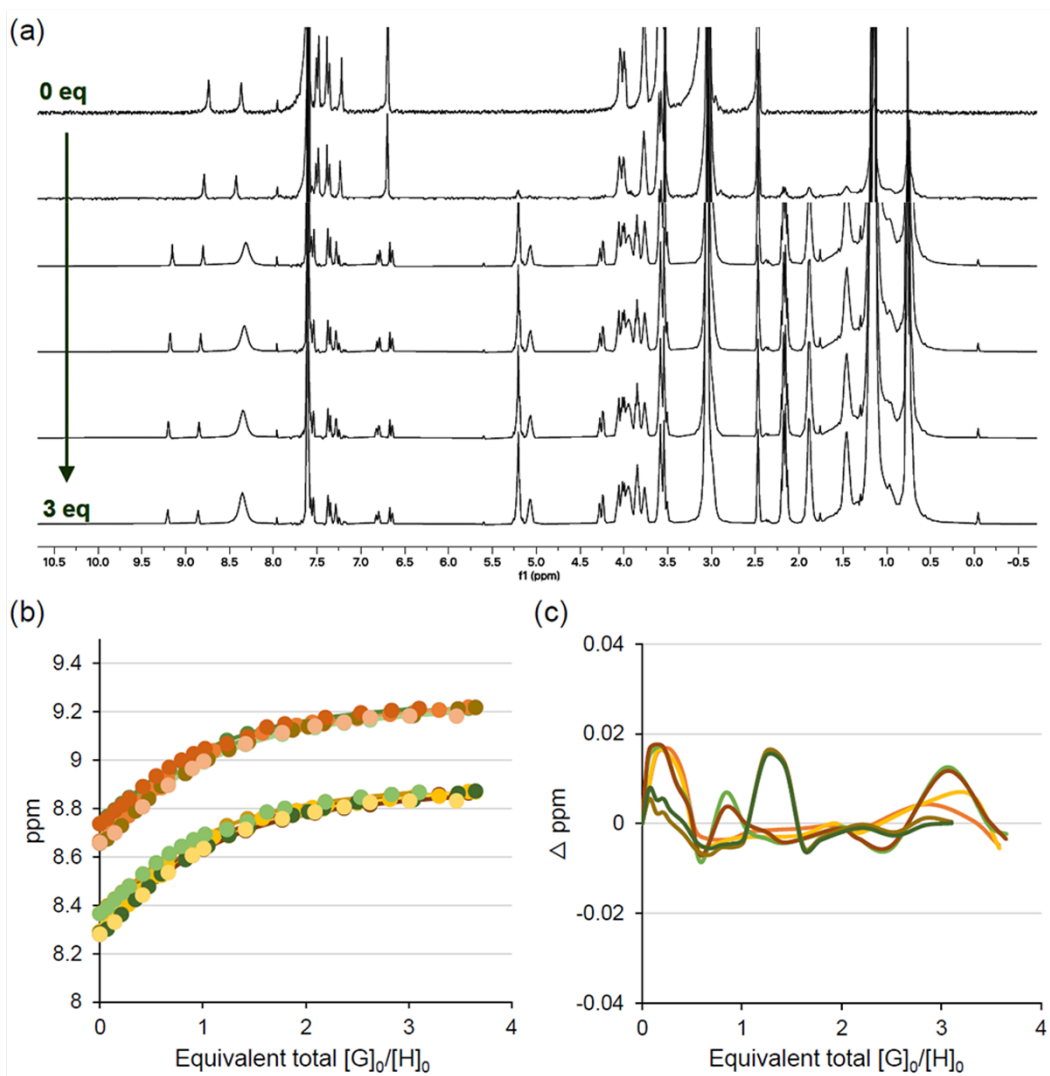


Figure 3.4: ^1H NMR titration of **3.1** with POPE in 0.5% Milli-Q H_2O :24.5% DMSO-d_6 :75% CDCl_3 at 298 K. (a) Stack plot of selected spectra of a representative titration. (b) Fitplot for the urea NHs at $\delta_A = 8.37$ ppm and $\delta_B = 8.74$ ppm using global analysis and 1:1 binding stoichiometry. Data from 3 independent repeats are overlaid. (c) Plot of the residuals for urea NHs at $\delta_A = 8.37$ ppm and $\delta_B = 8.74$ ppm using global analysis and 1:1 binding stoichiometry. Data from 3 independent repeats are overlaid.

Surprisingly, the flexible crown ether analog **3.2** showed no measurable interactions with either lipid. Computational modelling using Molecular Operating Environment (MOE) suggests that the flexible linker allows an intramolecular H-bond between the urea NHs and crown ether oxygens, thereby blocking the binding site (**Figure 3.5**).

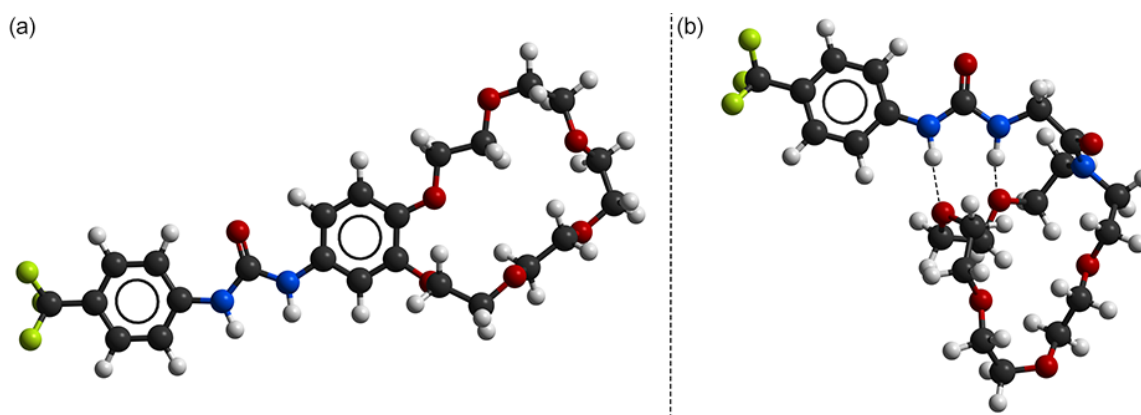


Figure 3.5: Lowest energy conformation of (a) compound **3.1**, and (b) compound **3.2** obtained using the Molecular Operating Environment software (MMFF94x force field with an implicit 75:25 chloroform:DMSO solvent to mimic conditions used in ^1H NMR titrations using a generalized Born solvation model).

The control compounds **3.3**, **3.4** and **18C6** did not bind as effectively either. The “rigid control” **3.3** showed non-selective binding to both lipids, while the “flexible control” **3.4** only showed minimal binding to POPC (**Table 3.2**). The stronger interaction of POPE with **3.3** versus **3.4** is likely due to hydrogen bonding between the methoxy substituents of **3.3** and the ammonium group of POPE. Association constants with 18-crown-6 could only be determined for POPE due to the lack of protons capable of H-bonding in both POPC and **18C6**. However, binding studies clearly showed that the crown ether was able

to complex POPE ($K_a = 263 \text{ M}^{-1}$), but to a smaller extent than **3.1**, which can coordinate both the ammonium and phosphate groups of POPE.

3.2.3. Fluorescence titrations with POPE and POPC in liposomes

After observing selective binding in organic solvents, we investigated the interaction of the compounds with lipids in phospholipid membranes using fluorescence titrations. To detect binding, we used 7-nitrobenz-2-oxa-1,3-diazol-4-yl (NBD) attached to one of the acyl chains of PC or PE (NBD-PE, NBD-PC). This ensures that the fluorophore would not block binding to the PE or PC headgroup. Binding to the headgroup can still be seen by changes in NBD-fluorescence because the polar fluorophore localizes in the lipid/water interface (membrane surface) via “backfolding” of the lipid chain.¹⁵³ The fluorophore is therefore closer to the binding site in the membrane surface so environmental changes (binding) cause fluorescence quenching.

Due to the inability of pure POPE to form stable liposomes,¹⁵⁴ the titrations were performed with either POPC liposomes containing 1 mol% 18:1-06:0 NBD-PC, or 1:1 POPE:POPC liposomes containing 1 mol% 18:1-06:0 NBD-PE (**Appendix B**). The addition of **3.1** to PE-containing liposomes caused complete quenching of the NBD fluorophore (**Figure 3.6**). Fluorescence quenching was less pronounced when **3.1** was added to PC liposomes, suggesting selective binding of PE over PC.

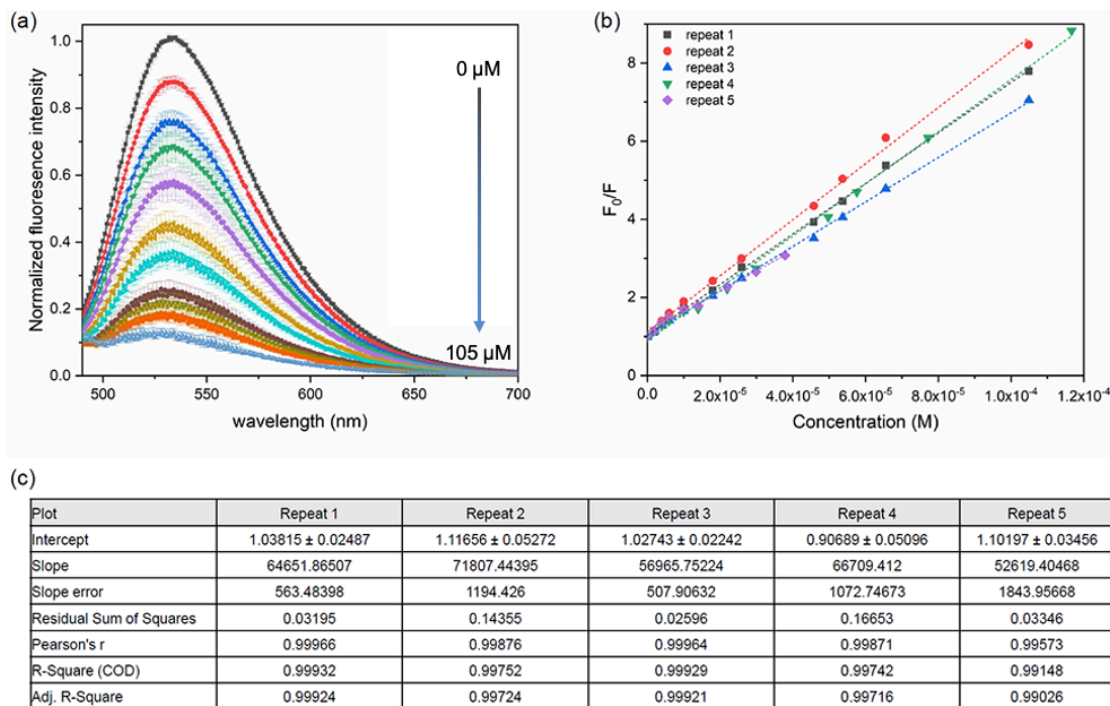


Figure 3.6: Fluorescence titration of **3.1** (10 mM stock in DMSO) into a solution of 100 nm large unilamellar vesicles (1:1 POPC:POPE liposomes containing 1 mol% NBD-PE). Excitation wavelength = 470 nm. (a) Normalized fluorescence spectra, average of at least 2 repeats. (b) Stern-Volmer plots for all individual repeats. (c) Results of the linear fit of the Stern-Volmer plots. The slope corresponds to the Stern-Volmer constant K_{SV} .

Quenching of the NBD-labelled lipids by compound **3.1** showed a Stern-Volmer relationship and the obtained Stern-Volmer constants (K_{SV}) were used to estimate the binding selectivity with PE and PC in liposomes (**Table 3.2**). The K_{SV} values confirmed the selectivity of **3.1** for PE over PC (PE $K_{SV} = (6.3 \pm 0.8) \times 10^4 \text{ M}^{-1}$ and PC $K_{SV} = (1.3 \pm 0.1) \times 10^4 \text{ M}^{-1}$). However, it must be noted that the titrations had to be performed using 1:1 POPC:POPE liposomes and the K_{SV} value for **3.1** with PE is therefore likely an underestimate. It is also noteworthy that the Stern-Volmer constants are nearly two orders of magnitude larger than the association constants obtained using the ^1H NMR titrations in organic solutions. We presume that the stronger binding in liposomes is the

result of additional hydrophobic effects in aqueous solution that help partition the compounds into the membrane. Overall, this data supports our findings from the ^1H NMR titrations that **3.1** can bind strongly and selectively to PE lipids. The data for **3.2** and **18C6** is provided in **Appendix B** (compounds **3.3** and **3.4** were not soluble enough in aqueous solution to perform titrations with liposomes). Similar to the ^1H NMR titrations, **3.2** and **18C6** did not cause any quenching of the NBD fluorophore in liposomes, thus highlighting the importance of the rigid urea functionality and membrane anchor.

Table 3.2: Overview of the PE-binding in liposomes of hosts **3.1-3.4** and **18-crown-6**. All data is the average of at least 3 independent repeats and errors represent standard deviations.

Host	K_{SV} (M^{-1}), fluorescence ^[a]	
	NBD-PE	NBD-PC
3.1	$(6.3 \pm 0.8) \times 10^4$	$(1.3 \pm 0.1) \times 10^4$
3.2	n.d. ^[b]	n.d. ^[b]
3.3	weak ^[c]	weak ^[c]
3.4	n.d. ^[b]	n.d. ^[b]
18C6	weak ^[c]	weak ^[c]

[a] Stern-Volmer constant (K_{SV} , M^{-1}) obtained through titrations of the hosts into POPC or 1:1 POPE:POPC liposomes containing NBD-labelled lipids. [b] Not determined (n.d.) due to insolubility. [c] No significant change in fluorescence intensity was observed.

3.2.4. Calcein leakage assay

To investigate whether the hosts can cause major disruptions in PE-containing membranes, a standard calcein leakage assay was performed (with the help of Dr. Nathalie Busschaert).¹⁵⁵ For this assay, liposomes are prepared encapsulating the fluorophore calcein at high concentrations where it self-quenches. If membrane binding

causes leakage, calcein is released from the liposomes and diluted into the bulk solution, which causes the fluorescence intensity increases (excitation wavelength = 490 nm, emission wavelength = 520 nm). Compounds **3.1-3.4** and **18C6** were therefore added to 1:1 POPC:POPE liposomes to test membrane lysis ability. Pure POPE liposomes were unable to be used in the leakage assay because the inverted cone geometry of PE inhibits liposomes formation.⁶² No significant calcein leakage was observed in any of the hosts (**Figure 3.7**). This does not indicate that **3.1** is not binding to PE, but that it does not induce membrane leakage. To further understand what happens to the membrane when **3.1** interacts with POPE, we used a lipid flip-flop assay to quantify translocation of lipids across the membrane.

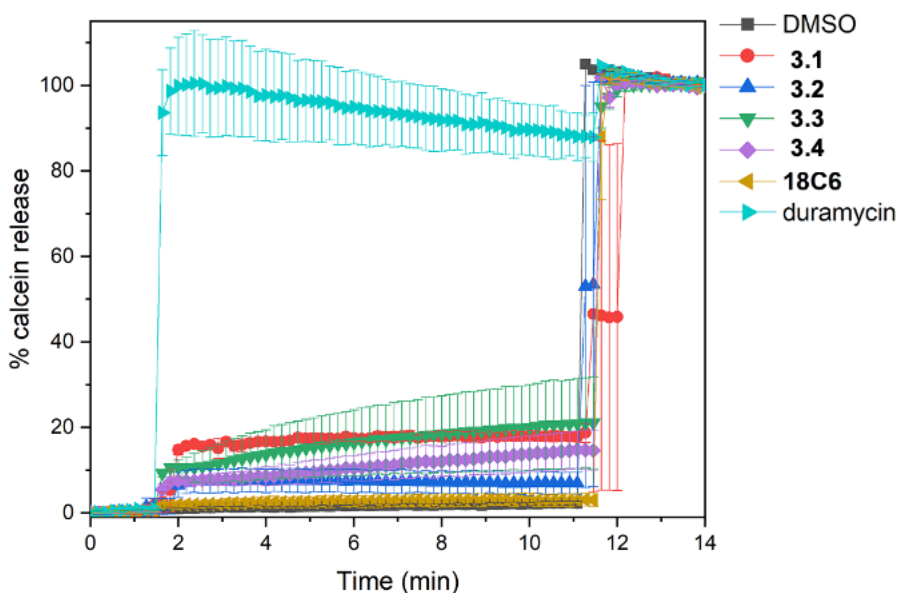


Figure 3.7: Calcein leakage mediated by 100 μM hosts **3.1**, **3.2**, **3.3**, **3.4** and **18C6** from 100 nm 1:1 POPE:POPC large unilamellar vesicles (10 μM) loaded with 70 mM calcein, 150 mM NaCl, 10 mM Tris buffer at pH 7.4. DMSO was used as a negative control and duramycin was used as a positive control. The results are the average of 2 biological x 2 technical repeats and the error bars represent standard deviations.

3.2.5. Lipid flip-flop

The rate of lipid flip-flop, or translocation across the membrane, can be used to quantify lipid headgroup selectivity in liposome model membranes.⁶² Translocation or 'flip-flop' of phospholipids across a lipid bilayer is normally a very slow process with a half-life of a few hours.¹⁵⁶ In the presence of molecules that can bind to the lipid headgroup, the polarity of the headgroup can be reduced and lipid translocation can be facilitated.⁸²⁻⁸³ To detect flip-flop, the NBD group of lipids in the outer leaflet can be selectively quenched via reduction with membrane-impermeable dithionite.¹⁵⁷ Residual fluorescence will be the result of flip-flop of the NBD-labelled lipid from the outer leaflet of the membrane to the inner leaflet.

In this assay, 100 nm unilamellar DOPC (1,2-dioleoyl-*sn*-glycero-3-phosphocholine) liposomes were prepared containing 1 mol% NBD-PE or NBD-PC in the outer leaflet of the membrane (assay was performed with the help of REU-student Taylor Dent). The results for the PE flip-flop assay are given in **Figure 3.8** and **Appendix B**. Only **3.1** can facilitate PE translocation, in agreement with the stronger PE binding observed in the ¹H NMR and fluorescence titrations. In fact, facilitated PE flip-flop could be observed for **3.1** at concentrations as low as 3.125 μ M (**Appendix B**), which is a significant improvement on a previously reported synthetic crown ether sulfonamide that could only mediate modest PE flip-flop at high concentrations (100 μ M).⁸³ Flip-flop of PC lipids was not observed for any of the compounds, further confirming the high selectivity of for PE over PC (**Figure 3.8**).

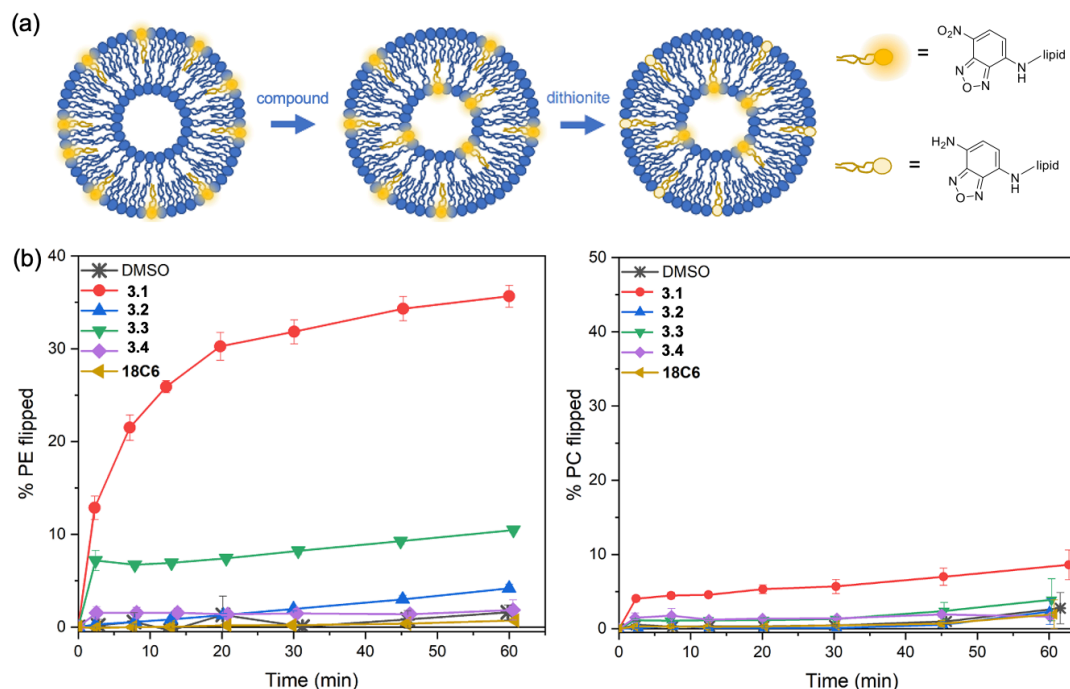


Figure 3.8: Lipid flip-flop induced by **3.1-3.4**. (a) Experimental set-up: 100 nm POPC liposomes containing fluorescent NBD-PE or NBD-PC (top right) in the outer leaflet of the membrane are incubated with 25 μM **3.1-3.4**, 18-crown-6 or DMSO to induce lipid flip-flop. At certain time intervals, the fluorescence of the NBD-lipid in the outer leaflet is quenched by the addition of dithionite to calculate the % of NBD-lipid flipped by the compounds. (b) Percent of NBD-PE (left) or NBD-PC (right) flipped by 25 μM **3.1-3.4**, 18-crown-6 or DMSO over a time scale of 60 minutes. Plots are the average of at least 4 independent repeats, and error bars represent standard deviations.

3.2.6. Antibacterial activity

Lastly, we wanted to determine if the PE-targeting compounds possess antibacterial activity (all experiments were performed with the help of Dr. Hassan Gneid). PE is found in the inner membrane and the inner leaflet of the outer membrane of Gram-negative bacteria, rendering access to PE in Gram-negative bacteria challenging.¹⁵⁸⁻¹⁵⁹ On the other hand, most Gram-positive bacteria lack PE, except for species of *Bacillus* and *Clostridium*. Any compound targeting PE is expected to function as a narrow-spectrum antibacterial agent against these bacterial species.¹⁶⁰ With this in mind, a screening assay incorporated

the compounds into a Müller-Hinton agar medium, and the agar was subsequently inoculated with the bacterial species *S. simulans* (0% PE), *B. subtilis* (20-30% PE), and *B. cereus* (40-50% PE) (**Figure 3.9** and **Appendix B**).¹⁶¹⁻¹⁶³ Compounds **3.2**, **3.3** and 18-crown-6 did not inhibit the growth of any of the bacteria, consistent with their lack of activity in the assays described above. In contrast, **3.4** showed antibacterial activity against all bacteria tested, regardless of their PE content. This indicates that **3.4** exerts its antibacterial activity through a mechanism that does not involve PE binding, consistent with its lack of PE binding observed in the ¹H NMR titrations and flip-flop assays. More interestingly, **3.1** had no effect on the growth of *S. simulans*, caused a significant delay in the growth of *B. subtilis* and complete inhibition of bacterial growth of *B. cereus*. The correlation with the PE-content of these bacterial species suggests that the mechanism involves binding to PE lipids.

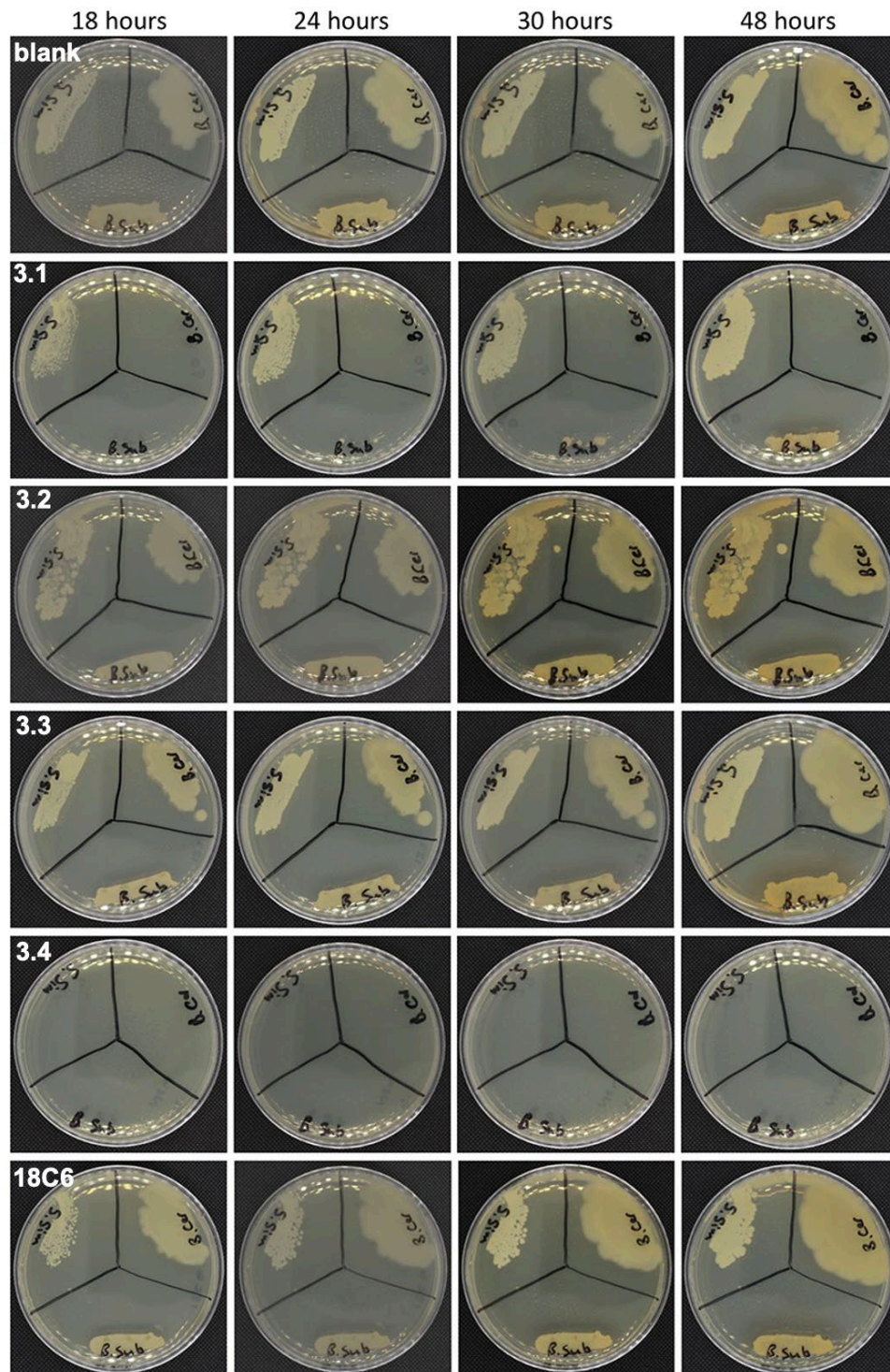


Figure 3.9. Bacterial selectivity of **3.1-3.4** and 18-crown-6 (biological repeat 1). Bacterial growth was monitored for 24 h at 35 °C on a Müller-Hinton agar plate containing 50 µL of a 25 mM DMSO stock of **3.1**, **3.2**, **3.3**, **3.4** and 18-crown-6. Blank contained 300 µL DMSO in the agar plate. All plates are photographed so that the *B. cereus* section is on the right, the *B. subtilis* section is on the bottom, and the *S. simulans* section is on the left of the agar plate.

The antibacterial activity of **3.1** against *B. cereus* was subsequently investigated in more detail. *B. cereus* is a common cause of foodborne illness and is closely related to the bioterrorism agent *B. anthracis*, making it a pathogen of interest.^{164,165} The minimum inhibitory concentration (MIC) of compounds **3.1-3.4** against *B. cereus* was determined using standard broth microdilution methods (**Appendix B**).¹⁶⁶ Compound **3.1** showed an MIC value of 25-30 μM , comparable to the MIC value obtained for the known PE-targeting peptide duramycin (MIC $\sim 32 \mu\text{M}$, **Appendix B**). Consistent with our previous findings, compounds **3.2** and **3.3** did not have any effect on the growth of *B. cereus* (MIC $> 100\mu\text{M}$). Compound **3.4** also exhibited a lower MIC than **3.1** (MIC = 6.25 μM), which correlates to the screening assay (**Figure 3.9**). Imaging of *B. cereus* after treatment of compound **3.1** and **3.4** also suggested that these compounds acted via different mechanisms (**Appendix B**). Compound **3.1** caused increased elongation or chaining of the bacterial cells (similar to duramycin, **Figure 3.10**) while **3.4** did not exhibit the same morphological changes. This interesting difference led us to investigate the potent antibacterial activity of **3.4** in more detail in **Chapter 4**.

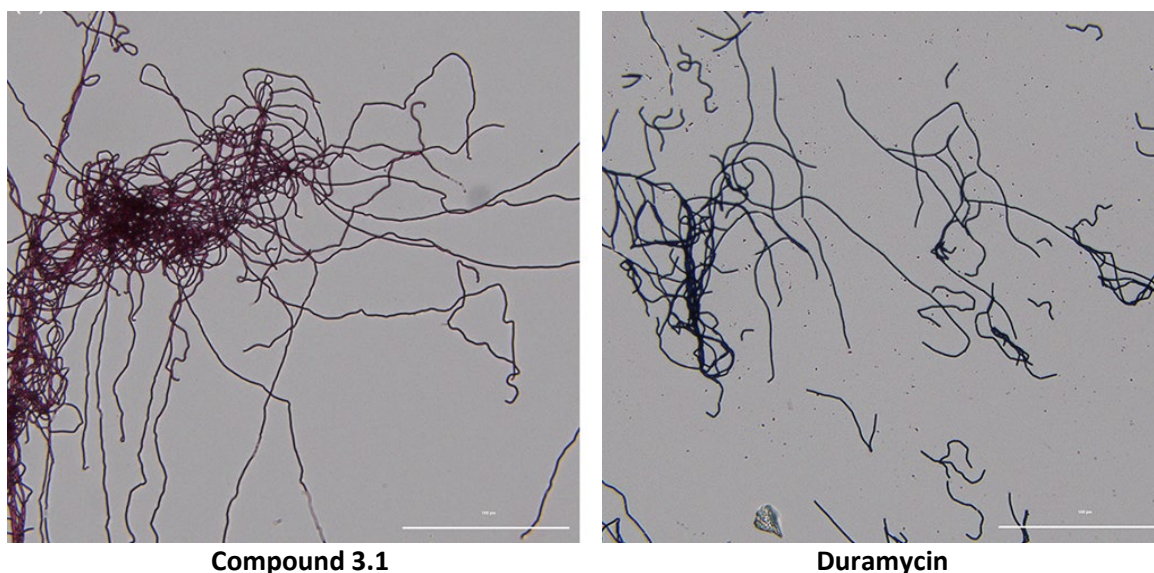


Figure 3.10: similarities in *B. cereus* morphology after incubation with compound **3.4** (25 μM) and **duramycin** (64 μM) at their MIC concentrations. Image obtained after 1:10 dilution in Müller-Hinton broth and Gram staining using a BioTek Cytation 5 Cell Imaging Multi-Mode Reader (40x objective, Brightfield). Scale bar represents 100 μm .

Next, we investigated the ability of **3.1** to cause membrane depolarization of *B. cereus* using the voltage-sensitive dye, 3,3'-dipropylthiadicarbocyanide [Disc₃(5)].¹⁶⁷ This cationic membrane-permeable fluorophore accumulates in polarized cells, where it self-quenches. When the membrane potential is dissipated, the dye is released into the medium and de-quenched, which can be followed by a fluorometric assay (**Figure 3.11, a**). Alternatively, the depolarization event can also be studied using fluorescence imaging (**Figure 3.11, b**). In this case, cells that are polarized show a pronounced red fluorescence due to the accumulation of Disc₃(5), whereas depolarized cells do not show fluorescence. Gramicidin was used as a positive control known to cause membrane depolarization, and clindamycin was used as a negative control because it targets the ribosome rather than the bacterial membrane.¹⁶⁸⁻¹⁶⁹

At 25 μM (1xMIC), **3.1** caused partial depolarization of *B. cereus*. Full depolarization was seen at 40 μM (1.6xMIC) and 250 μM (10xMIC). Depolarization occurs when the ionic gradient of the membrane is interrupted. This is common in membrane-targeting antibiotics.³² The ability of **3.1** to cause depolarization in *B. cereus* correlates with binding to PE in bacterial membranes.

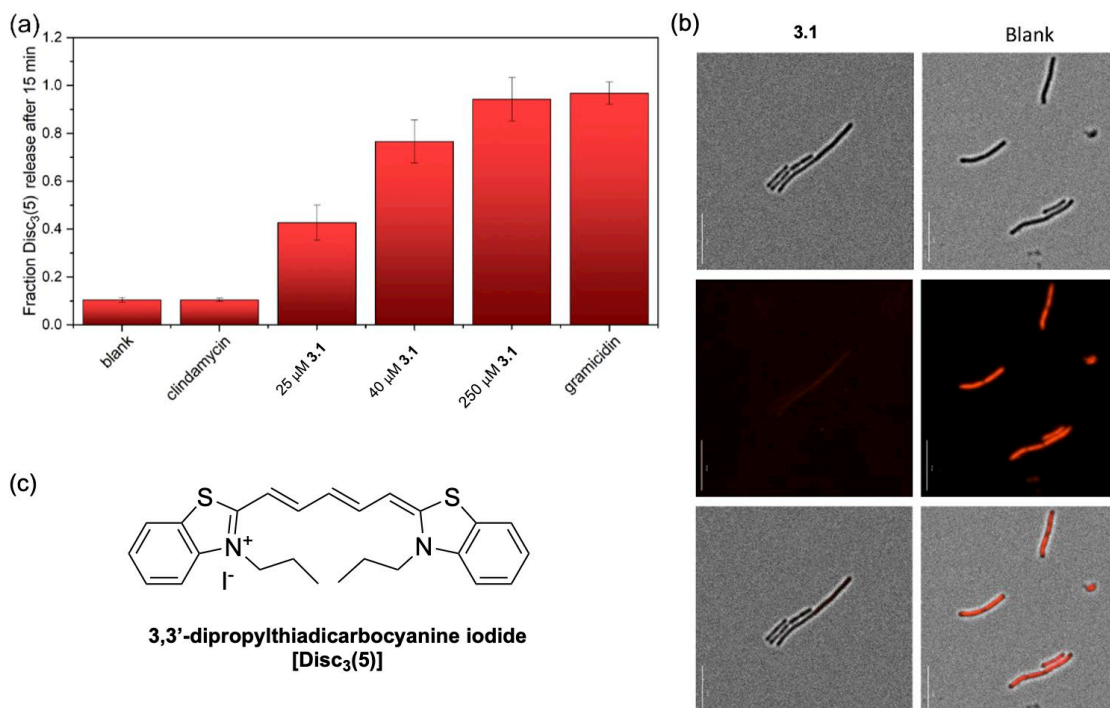


Figure 3.11: Membrane depolarization of *B. cereus* by **3.1** measured using $\text{Disc}_3(5)$. (a) Fraction of $\text{Disc}_3(5)$ released after 15 minutes incubation with clindamycin (negative control, 1 $\mu\text{g}/\text{mL}$, 1xMIC), 25 μM **3.1** (1xMIC), 40 μM **3.1** (1.6xMIC), 250 μM **3.1** (10xMIC) or gramicidin (positive control, 1.25 μM , 1xMIC). Data is the average of 2 biological x 2 technical repeats and error bars represent standard deviations. (b) Brightfield (top) and fluorescence (middle) and overlay (bottom) imaging of *B. cereus* incubated for 15 minutes with 4% DMSO (blank) or 250 μM **3.1** (10xMIC). Absence of fluorescence indicates that the cells are depolarized. Scale bars represent 10 μm . (c) Chemical structure of the membrane permeable dye, 3,3'-dipropylthiadicyanocyanine iodide [$\text{Disc}_3(5)$].

Lastly, we investigated the bactericidal activity of **3.1** since membrane-active antibiotics are normally bactericidal rather than bacteriostatic.^{5, 170} Bacteriostatic refers to antibiotics that inhibit growth of the bacteria, while bactericidal kill bacteria, thus limiting the occurrence of resistance. The minimum bactericidal concentration (MBC), defined as the lowest concentration needed to kill 99.9% of bacteria, was 35-40 μM for **3.1**, which is only slightly higher than its MIC value (25-30 μM) (**Appendix B**). This suggests that compound **3.1** has bactericidal activity and further confirms a mode of action that involves the bacterial membrane.

3.3 Conclusions

In this chapter, we have identified a new crown ether urea derivative (**3.1**) that is able to selectively bind to the bacterial lipid PE over the mammalian lipid PC in both organic solution and in liposomes. This compound functions as a bactericidal agent against *B. cereus* with an MIC value of 25-30 μM and causes membrane depolarization in this bacterium. The other urea and crown ether compounds did not have the same affinity for PE. This demonstrates that the 18-crown-6 and urea group are both required for strong PE headgroup binding and a rigid linker is needed between the two to achieve the right conformation. Future work should focus on other phosphate binding molecules that can have antibacterial activity, as well as analogues of **3.1** to determine structure-activity relationships and lower the MIC values.

CHAPTER 4

IDENTIFICATION OF THE MECHANISM OF ACTION FOR UREA-BASED ANTIBIOTICS USING BACTERIAL CYTOLOGICAL PROFILING

4.1 Introduction

Bacterial cytological profiling (BCP) is used in this chapter to identify the mechanism of action (MOA) for a urea-based antibiotic with unknown MOA identified in **Chapter 3** (compound **3.4**). BCP is a method to classify the effects of antibiotics using fluorescent staining, microscopy, and statistical analysis of image data. Bacteria are stained with fluorescent dyes that allow visualization of the cell membrane (FM4-64), nucleoid (4'-6-diamidino-2-phenylindole [DAPI]), and membrane permeability (Sytox Green). Morphological changes in the cells can be identified based on the shape, location, and fluorescence intensity generated by fluorescence microscopy. Computational image processing allows large sample sizes to be processed in a relatively short amount of time. This is highly beneficial for future drug design, since one of the most significant hurdles is identifying the mechanism of action (MOA). This chapter explores the steps for optimizing

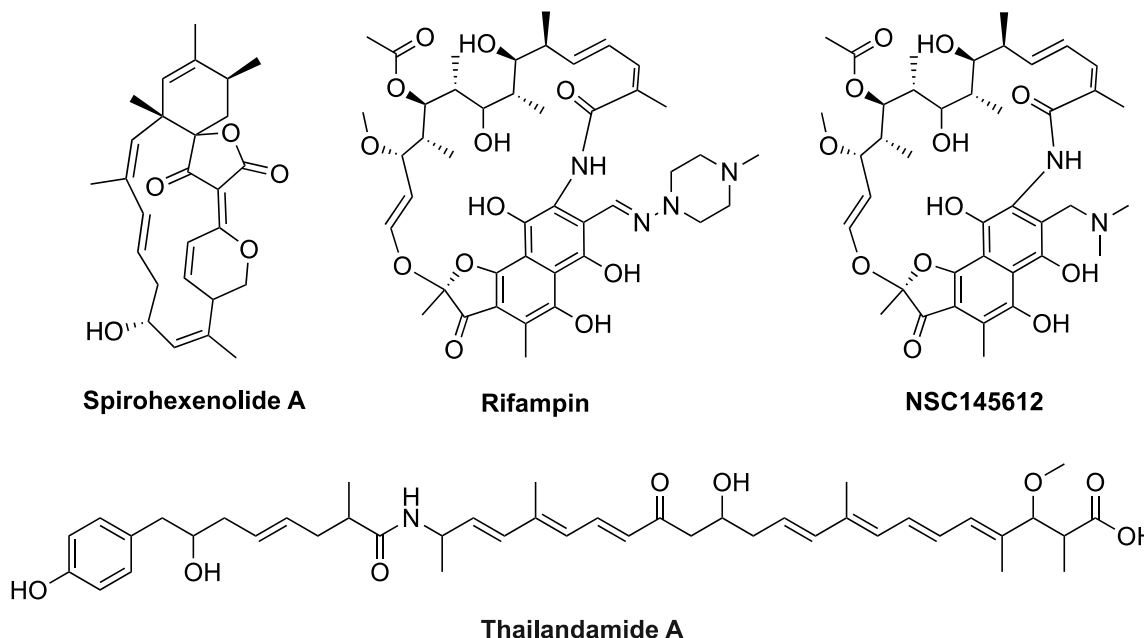
BCP analysis: careful selection of bacteria, dyes, microscopes, filters, processing software, and known antibiotics; the data collected, and the correlation of the novel compounds with known MOA.

4.1.1 Development of BCP

Bacterial cytological profiling is an image-based profiling assay that allows rapid categorizing of an antibiotic with an unknown MOA based on early morphological changes. Some of these changes can be seen within only 30 minutes of incubation (e.g., nucleoid decondensation, membrane lysis), while other changes only manifest after longer incubation times. After 2 or 5 hours of incubation with an antibiotic there is enough variability to separate antibiotics into different classes based on their MOA. Bacterial cytological profiling was developed by Nonejuie *et al.* in 2013 at UC San Diego. Image profiles were generated from 41 antibiotics belonging to 26 different MOA classes using a membrane-permeable *E. coli* strain (*lptD4213*).^{11, 171} Antibiotics that normally do not work on *E. coli* could be tested because of the increased permeability and high concentration of antibiotic treatments (5x the MIC). This produced a classification system that could determine the correct MOA in double-blind studies and separate different targets within the same class of antibiotics when tested together. They also identified the natural product **Spirohexenolide A (Scheme 4.1)** as a membrane active antibiotic.

Rapid screening by BCP allows researchers to test larger libraries of compounds and identify new antibiotics with unique MOAs. **NCS145612 (Scheme 4.1)** was discovered in a screening of 64 compounds from the National Cancer Institute's Developmental Screening Program. It had a promising minimum inhibitory concentration (MIC) of 25 μ M

against *A. baumannii*, a Gram-negative pathogen that is becoming increasingly worrisome in hospital settings.¹⁷² The use of BCP demonstrated that **NCS145612** inhibits growth via targeting RNA transcriptase, similar to **Rifampin**. This is not surprising given the similarities in chemical structure (**Scheme 4.1**).¹⁷²



Scheme 4.1: Some antibiotics that have been used in bacterial cytological profiling studies.

BCP can also be used in combination with genetic profiling to identify novel targets. **Thailandamide A** (**Scheme 4.1**) is a linear polyene natural product produced by the Gram-negative soil bacteria *Burkholderia thailandensis*, that exhibits antibiotic activity (MIC ~10 μ M) against *B. subtilis* and *S. aureus*. Previous work had been unsuccessful in identifying the MOA of **thailandamide A**, but BCP revealed a unique pathway not represented by common antibiotics.¹⁷³⁻¹⁷⁴ Genetic identification of mutant strains of *B. subtilis* led researchers to identify a new class of fatty acid biosynthesis

antibiotics that inhibit bacterial growth by targeting acetyl-CoA carboxylase (the first step in fatty acid biosynthesis).¹⁷⁴ This shows the adaptability of bacterial cytological profiling to aid in drug development.

Larger bacteria like *E. coli* and *B. subtilis* have been the most widely used in BCP assays because they are easier to image, but over 20 Gram-positive and Gram-negative bacteria have been adapted in academic studies.^{175 176 177 178} Sridhar *et al.* developed an assay for *S. aureus*, *K. pneumoniae*, and *S. enterica* imaging in 96-well plates and some pharmaceutical companies are adapting their own assays for high throughput screening.^{176 179 176, 180} Other applications of bacterial cytological profiling include rapid susceptibility testing and the detection of early morphological changes below the MIC value. Treatment of clinical isolates of *S. aureus* with daptomycin induced physical changes that identified methicillin resistant strains in under 2 hours with 100% accuracy.¹⁷⁸ These examples demonstrate the reliability, speed, and accuracy of BCP methods. As more researchers and pharmaceutical companies adopt this technology, the MOA libraries will improve, allowing for more applications and discoveries.

4.1.2 BCP workflow

The BCP workflow used in this chapter is outlined in **Figure 4.1**. The determination of a MOA requires three key steps: image generation, image analysis and statistical analysis. Image generation includes the choice of antibiotics and optimization of imaging techniques (cell fixation and fluorescence staining). Image analysis generates quantitative data by creating measurable objects from images. Statistical analysis is used to extract

the most relevant features to separate the antibiotic classes and classify the antibiotic with unknown MOA into one of the known profiles. The methods used will be discussed below in general terms to guide the reader through the data interpretation in **Section 4.3**.

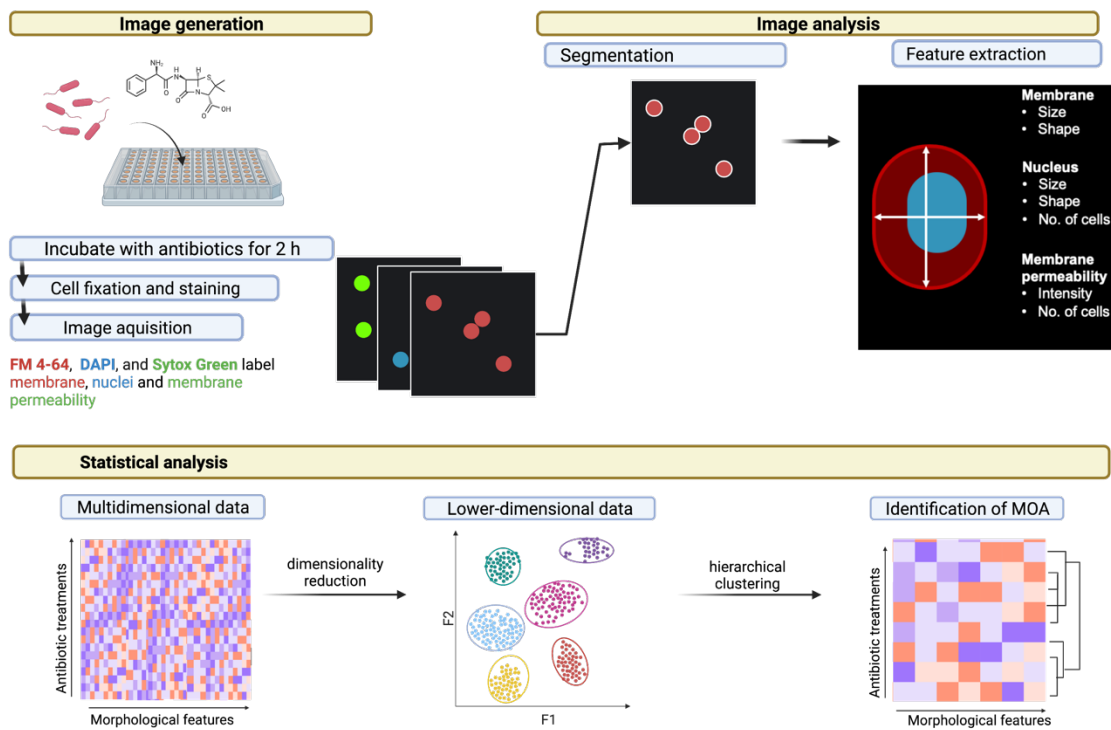


Figure 4.1: Schematic overview of the bacterial cytological profiling (BCP) assay performed in this study.

4.1.2.1 Cell fixation and staining

Before imaging, bacteria must be immobilized (fixation) and stained with fluorescent probes for visualization. Fixation can be achieved through specific coatings applied to the image plate and/or the use of solvents. It is important to optimize the fixation method for the specific bacteria and strain used.^{176, 181} Issues with bacterial adhesion could result in large clumping (only stuck in certain areas, non-uniform coating)

or too few to analyze (poor adhesion). Both cases diminish image quality and introduce downstream error.

Staining of bacteria with fluorescent dyes allows visualization of the bacteria with a confocal fluorescence microscope. Fluorescent dyes are selected based on their excitation (ex.) and emission (em.) wavelengths (λ). The stains must have minimal autofluorescence (i.e., low fluorescence in aqueous environments) and bind specifically to the given target. Non-selective or off-target fluorescence can reduce clarity. The three fluorophores typically used in BCP are **DAPI, Sytox Green (SG), and FM 4-64, which exhibit blue ($\lambda_{em} = 457$ nm), green ($\lambda_{em} = 523$ nm), or red ($\lambda_{em} = 640$ nm) fluorescence respectively, so that the emission does not overlap.**¹¹ The excitation (dashed lines) and emission spectra (solid lines) for each fluorophore is simplified in **Figure 4.2**. Sytox Green and DAPI both stain DNA to measure the density and chromosome architecture of bacteria. DAPI is a membrane-permeable fluorophore that preferentially coordinates to the minor groove in DNA.¹⁸²⁻¹⁸³ DAPI-staining can visualize changes in DNA-packing (size, shape) or density (intensity).¹⁸⁴ Sytox Green (SG) is a membrane impermeable stain that exhibits green fluorescence in the presence of DNA. The increase of SG intensity is proportional to the amount of membrane damage caused by an antibiotic.¹⁸⁵ BCP uses the two nucleic acid stains together to determine the amount of cell lysis via the intensity of SG or the ratio of SG/DAPI stained nuclei.^{11, 184} FM 4-64 is an amphiphilic styryl fluorophore used to visualize bacterial membranes. FM 4-64 consists of a polymethine fluorophore sandwiched between a hydrophilic tail and cationic headgroup. The hydrophobic headgroup reduces membrane insertion so that the outer membrane

accumulates the fluorescent dye.¹⁸⁶ FM 4-64 exhibits red fluorescence and allows for measurements of bacterial cell size and shape. When combined, the fluorescent probes can identify unique changes in bacterial cell morphology that reflect the specific MOA.

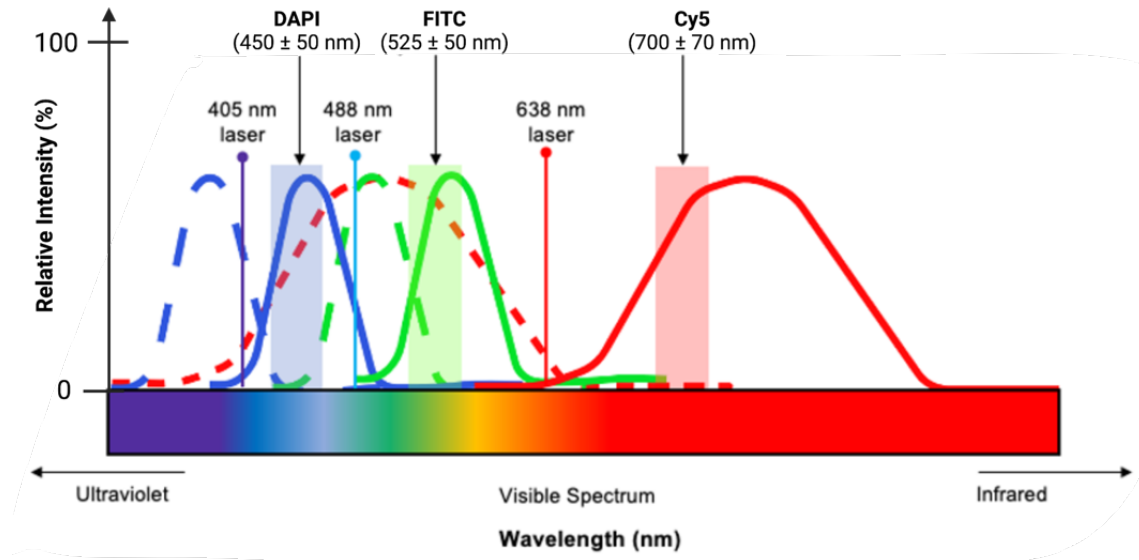


Figure 4.2: Simplified graphs for DAPI, Sytox Green, and FM 4-64 excitation (dashed line) and emission (solid line) spectra. Sequential scanning required the use of three separate excitation sources (lasers) and three emission filters (DAPI, FITC, and Cy5). Settings listed are specific to the Nikon A1 confocal microscope at Tulane University. Adapted from ThermoFisher.¹⁸⁷

4.1.2.2 Cell imaging

Fluorescence confocal microscopy is widely used in biomedical and materials science because of its adaptability to different fluorophores and high contrast compared to traditional microscopes.^{179-180, 188} Confocal microscopy uses lasers as light source and is commonly employed in fluorescence imaging because it can filter out unwanted background light through an adjustable pinhole and emission filter.¹⁸⁹ Fluorescent confocal microscopy follows a similar format to any spectrometer. First, the fluorophore

is excited by a specific, higher energy wavelength. Emission of a weaker, longer wavelength is separated from background noise by a dichroic mirror and emission filter before reaching the detector.¹⁸⁹ High resolution images are obtained in confocal microscopy because the incoming excitation light source is finely tuned by the microscope's objective. The laser is focused on a defined spot at a specific depth within the sample to minimize background fluorescence from out-of-focus areas.¹⁸⁹ The emission filters specific to each channel of the confocal microscope at Tulane University are listed in **Figure 4.2**. The DAPI, FITC, and Cy5 channels were used for DAPI, Sytox Green, and FM 4-64 stained images, respectively. The channel names are arbitrary and based on common fluorophores. One channel is used for each fluorophore, resulting in 3 different images. The microscope can be programmed to image sequentially so that there is minimal overlap of emission for each fluorophore.

Even with high-resolution techniques like confocal microscopy, it is much harder to image bacteria than eukaryotic cells. Bacteria are much smaller and require high magnification to capture variation at the single-cell level. Imaging errors should be minimized by optimizing fixation and staining techniques as well as keeping the microscope parameters consistent between experiments.^{184 190}

4.1.2.3 Image analysis and statistical analysis

Segmentation

Segmentation is the process of generating computational data from each image so that features of the bacteria can be analyzed. Objects in this study refer to the nucleoids (identified by DAPI) or membranes (identified by FM 4-64) of individual

bacteria. Segmentation parameters define how the software recognizes cells compared to background noise or neighboring cells.¹⁹¹ Segmentation algorithms typically assume a circular object.¹⁹²⁻¹⁹³ This means that rod-shaped bacteria are less accurately separated from a growing neighbor.¹⁹¹ CellProfiler™ is an automated image analysis software that allows the user to optimize their own segmentation parameters.¹⁹⁴ Segmentation can be improved by creating a robust model and removing any obvious outliers before further analysis. A robust model is one that limits over- or under-segmentation in all images for each object. First, the segmentation parameters for each channel must be kept constant between antibiotic treatments and biological replicates. This ensures reproducibility and non-bias results.¹⁹¹ Second, proper segmentation can be achieved using size and intensity features. Over-segmentation occurs when there is too much separation or splitting of the image during object detection.¹⁹³ This is usually easier to fix because you can increase the size of the object filter. Under-segmentation is when the software is unable to identify the boundary between two cells, so it combines them as one object. Chaining in *B. subtilis* makes identification of the individual bacteria difficult. However, using the size of the membrane and intensity of the membrane stain as a guiding feature, CellProfiler™ has been shown to accurately classify cells.¹⁹⁴

Linear Discriminate Analysis (LDA)

Image analysis generates multidimensional data that is difficult to rationalize on an (x,y) or (x,y,z) plot. To analyze large, complex data sets it is common to exploit dimensionality reduction techniques that allow better visualization of trends and errors between experiments (**Figure 4.3**). Our study uses dimensionality reduction to identify

important trends in bacterial morphology between antibiotic treatments within different MOA targets. Optimal separation between different antibiotic targets leads to more precise classification of the unknown MOA.

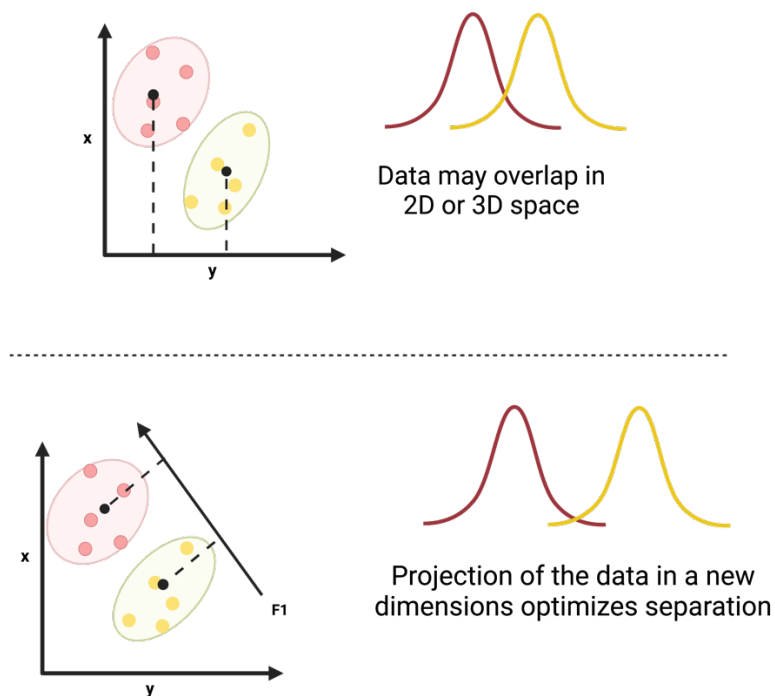


Figure 4.3: A simplified representation of how dimensionality reduction using linear discriminant analysis (LDA) allows better understanding of trends within a dataset.

Linear transformation is a dimensionality reduction technique used to simplify multidimensional data onto a 2D or 3D space. Two of the most common techniques are principal component analysis (PCA) and linear discriminant analysis (LDA).¹⁹² The key differences between the two are that PCA is used to optimize the separation between all variables (antibiotics) and LDA optimizes separation between classes of variables while limiting the in-class disparity. To optimize separation of the MOA classes, an eigenvector

(discriminant factor, F1) is drawn to define a new dimension which segregates the cell measurement data (variables) into discrete MOA classes (**Figure 4.3**). Data is transformed onto a simple linear plot with the distance of each datapoint summarized by an eigenvalue. The eigenvalue is a positive or negative value that is used to calculate the contribution of each variable to the new axis (F1). In LDA, the average of each antibiotic class cell measurement should be statistically significant from the average mean of the data set. Any variable that does not differ between antibiotic targets can be removed because it will not contribute to the final classification of the unknown MOA's profile.

Clustering

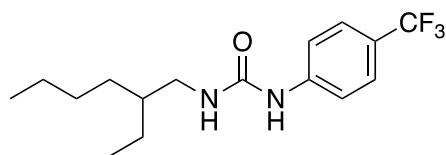
In LDA, centroids are used to visualize the relationship between different classes of antibiotics on an (x, y) plane. This is important for validation of the LDA model and optimizing the distance between class and within-class means. However, we need to use more complex data clustering to assign the unknown MOA to the known antibiotic profiles. Euclidian distance clustering is a method of grouping variables by their separation within a three dimensional (Euclidian) space (x,y,z). We use this to calculate the relationship between two antibiotic treatments in connection with the rest of the dataset.¹⁹² Agglomerative hierarchical clustering (AHC) is an approach commonly used in morphological profiling that creates a dendrogram to show the relationships between bacteria in different environments.¹⁹² Agglomerative clustering begins with the individual groups of MOA classes, and combines them until all are connected under a single node in the dendrogram. In a dendrogram, the smallest clusters in height are the most closely

related. This means that the distance between each node connection corresponds to the relationship of one cluster to another. If clustering of the new antibiotic is not obvious, this could mean that the compound is acting on a novel target or that different antibiotics should be selected for future analysis. Either way, it is a highly useful tool in classification of new drugs and visualizing the relationships between antibiotic profiles.

4.2 Results and Discussion

4.2.1 MIC determination of potential novel antibiotics

Compound **3.4** was designed as a control in **Chapter 3** for PE-binding, but exhibited broad spectrum activity against Gram-positive bacteria with no indication of lipid recognition (**Figure 4.4**).¹⁹⁵ Additionally, studies conducted by Dr. Hassan Gneid also indicated low-hemolytic activity (**Appendix C**).¹⁹⁶ Hemolysis is an important indication of toxicity, data shown in **Figure 4.4** represents the concentration needed to achieve 50% hemolysis of human red blood cells (HC₅₀). Since our studies indicated that **3.4** was not acting through membrane recognition, we wanted to use BCP to identify the MOA.

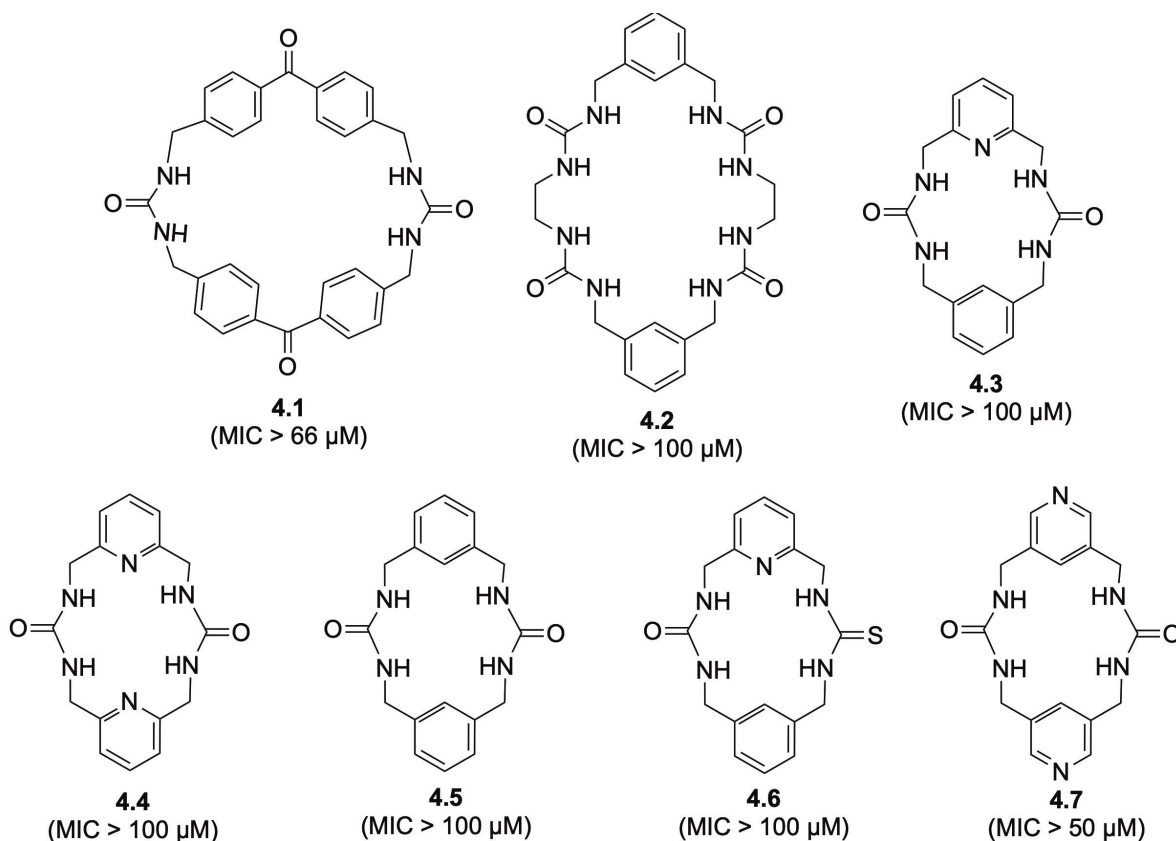


3.4

Antibiotic activity	
Bacteria	MIC (μM)
<i>B. cereus</i>	6
<i>B. subtilis</i>	1.5
<i>S. aureus</i>	1.5
<i>E. coli</i>	> 100
Hemolytic activity	
HC ₅₀	> 400 μM

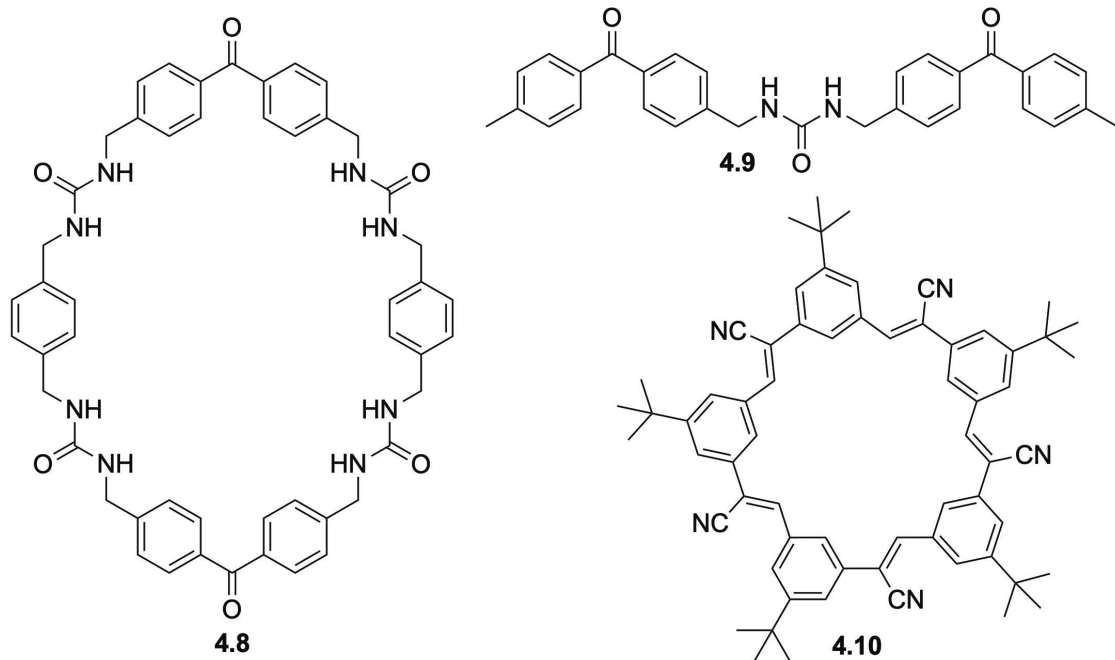
Figure 4.4: Antibiotic activity and structure of compound **3.4**.

In addition, we wanted to test other urea molecules to see if they would exert similar antibiotic activity. Urea-based compounds **4.1-4.9** were obtained from Linda Shimizu to include in antibacterial and MOA studies.¹⁹⁷⁻²⁰¹ We also wanted to test the activity of cyanostar **4.10** (received from Amar Flood) due to its strong binding to phosphate species.⁵⁷ Unfortunately, none of the compounds received from collaborators indicated any antibiotic activity against *B. subtilis* or *S. aureus* in broth dilution minimum inhibitory concentration (MIC) studies (**Scheme 4.2** and **4.3**). Antibiotic susceptibility studies were conducted with *B. cereus* (ATC 11778) or *S. aureus* (ATC 25923) to determine if the ureas would display similar antibiotic activity to compound **3.4**. This requires the antibiotic to be soluble in a solvent that is miscible with the aqueous solutions used for bacterial testing. Only 7 compounds were soluble enough in DMSO (**4.2-4.6**) or DMSO/CH₃CN mixtures (**4.1** and **4.7**) to obtain MIC values. The MIC values listed in **Scheme 4.2** correspond to the highest concentration tested, implying that the macrocycles displayed no measurable activity against Gram-positive bacteria.



Scheme 4.2: Compounds received from Linda Shimizu's lab. The MIC values listed were the highest concentrations able to be tested.

Compounds **4.8-4.10** were unable to be tested due to solubility issues (**Scheme 4.3**). Compounds **4.8** and **4.9** were only available in limited quantities, so solubility was only tested in DMSO or DMSO/ CH_3CN mixtures. We tried to dissolve the cyanostar (**4.10**) in phosphate buffered saline (PBS), DMSO, acetonitrile, and mixtures of these solvents but it was not possible to obtain a homogenous solution for antibiotic testing.



Scheme 4.3: Compounds received from Linda Shimizu and Timothy Glass that were unable to be tested for antibiotic activity due to solubility issues.

Although these findings are inconclusive, urea macrocycles may still be a viable option for future antibiotic development. Pillararenes, cyclodextrins and larger cavity molecules have shown broad-spectrum antibiotic effects. However, many of these molecules contain highly cationic regions to mimic antimicrobial peptides.²⁰² Additionally, the macrocycles tested have all shown some type of molecular stacking or self-assembly which can form pores in bacterial membranes but also create solubility issues.^{197-198, 201, 203-205} As none of the other urea-based compounds showed sufficient antibacterial activity, compound **3.4** was the only one used throughout the BCP assay.

4.2.2 Selection of antibiotics with known MOA

Before we can begin optimizing the imaging parameters, we need to select the antibiotics with known MOA and verify their MIC with the specific bacterial strain and culture method. Six antibiotics from five different target classes were incubated with *B. subtilis* to create 5 distinct MOA profiles. *B. subtilis* was chosen because of large size, because it has been previously used in BCP assays, and because our antibiotic with unknown MOA (**3.4**) had shown activity against this Gram-positive organism (**Figure 4.4**).^{195 184} Target classes included: folate synthesis (FS), protein synthesis (PS), ribonucleic acid (RNA), membrane (MEM), and cell wall synthesis (CW). Expected changes in morphology based on previous BCP studies are shown in **Figure 4.5**. Two cell-wall targeting antibiotics, phosphomycin and vancomycin, were chosen because they impart very different changes to the cell phenotype.^{11, 184} Vancomycin physically blocks cell wall synthesis by binding to the growing peptidoglycan chain. This leads to minimal changes in the cell size. Phosphomycin targets the enolpyruvate transferase MurA enzyme within bacteria and creates mis-regulation during cell wall synthesis so that cells become elongated. Phenylthiazole-substituted aminoguanidines have previously shown cell wall targeting activity against *E. faecalis*.¹⁷⁵ Since guanidines are also used in phosphate recognition, we wanted to include both extremes in morphology that can be induced by cell wall-targeting antibiotics to ensure accurate classification of compound **3.4**.

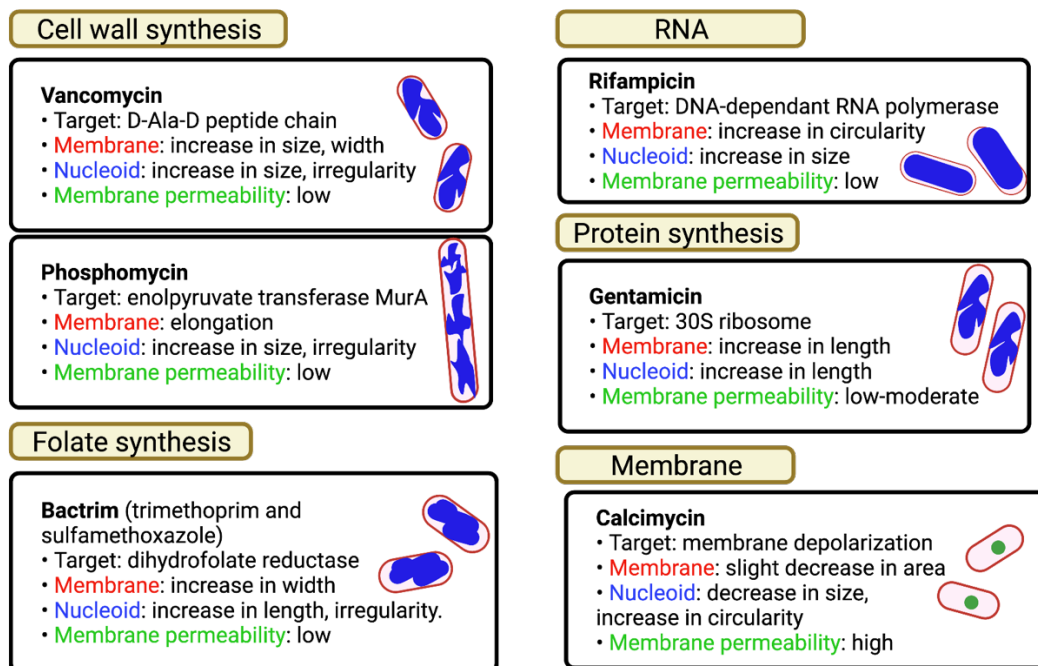


Figure 4.5: Graphical depiction of the expected morphology for bacteria after treatment with the known antibiotics used in this study.^{11, 184, 206-207}

The MIC value for each antibiotic was determined using the broth microdilution method and visual inspection (**Table 4.1**). MIC values are based on 3 biological repeats, using untreated (DMSO, broth) and clindamycin controls. Compounds were dissolved in DMSO or sterile cation-adjusted Müller-Hinton broth (MH2), as listed in **Table 4.1**. Overall, the MIC values obtained were consistent with those reported in previous BCP studies.^{11, 184}

Table 4.1: MIC values and abbreviations for antibiotics used within the BCP assay.

Antibiotic	MOA	MIC ($\mu\text{g/mL}$)	Solvent
Phosphomycin	CW	250	MH2
Vancomycin	CW	0.05	DMSO
Bactrim	FS	1500	MH2
Rifampicin	RNA	0.08	DMSO
Gentamicin	PS	10	MH2
Compound 3.4	UNK	0.5	DMSO
Calcimycin	MEM	0.01	DMSO

4.2.3 Cell fixation and staining

Next, we determined the optimal parameters for cell fixation, staining, and incubation. The full procedure is given in **Chapter 5** (Materials and Methods), which is a modified version of a high throughput method developed by Sridhar *et al.*¹⁷⁶ To begin, image quality 96-well plates were incubated with a vitronectin coating prior to the assay. This glycoprotein matrix assists in cell adhesion to the 96-well plate.¹⁸⁸ Next, *B. subtilis* bacteria were incubated for 2 hours with antibiotic at 5xMIC. Cells were washed with phosphate buffered saline (PBS), incubated with 4% paraformaldehyde (to ensure cell death and preserve features), washed again with PBS, and incubated with 50 μL of dye mix (5 $\mu\text{g/mL}$ DAPI, 2.5 μM Sytox Green, 10 $\mu\text{g/mL}$ FM4-64 in Hank's Balanced Salt Solution ([HBSS]) per well for 45 minutes in the dark at 25 $^{\circ}\text{C}$.^{184, 188} Finally, the 96-well plates were imaged immediately and kept in a dark environment to avoid photobleaching.

4.2.4 Cell imaging

Single-cell imaging was performed using a Nikon A1 confocal microscope with consecutive DAPI, FITC, and Cy5 lasers using a 40x oil objective. Metadata from the microscope is listed in **Appendix C**. Magnification settings and intensity parameters for DAPI and Sytox Green stained cells (DAPI and FITC laser power) were kept constant throughout all three repeats. Raw images were imported directly to CellProfiler™, where standardized image correction was applied using the “EnhanceOrSuppressFeatures” model to increase resolution (**Figure 4.6**).

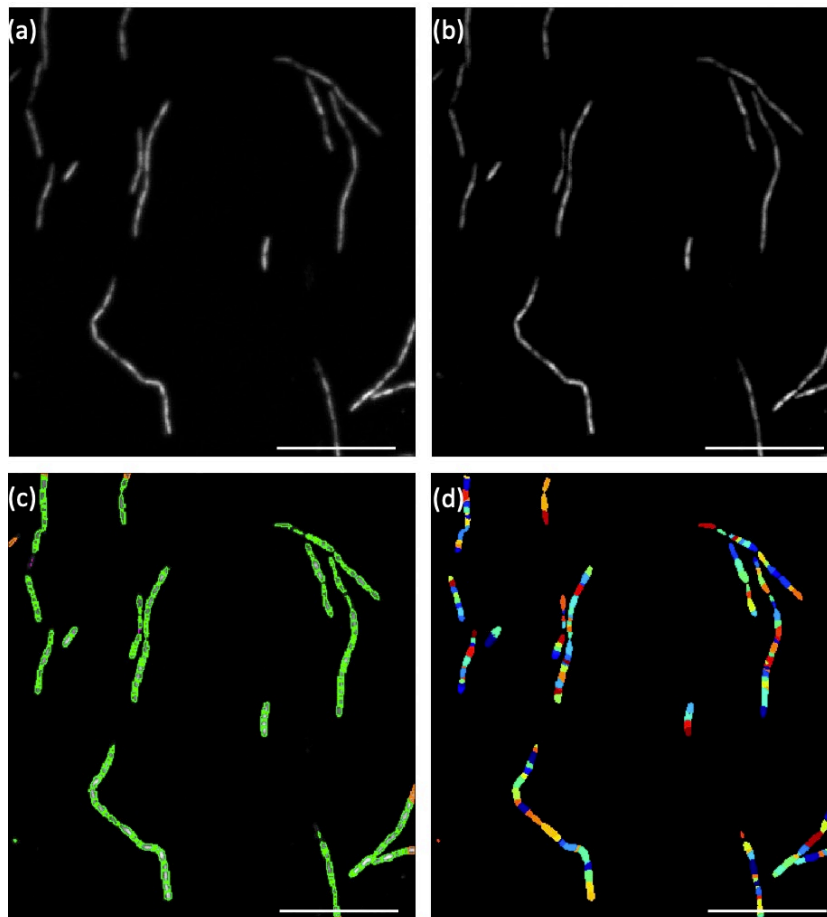


Figure 4.6: The workflow of image analysis using CellProfilerTM. Images shown are of compound **3.4** treated *B. subtilis* stained with DAPI in the DAPI channel. a) cropped image, b) enhanced image, c) object outlines (segmentation), d) object selection. Scale bar = 24 μm .

Intensity measurements used in the analysis (DAPI, Sytox Green stained nuclei) were obtained from non-corrected images, while morphological measurements used the corrected images. Single channel and overlaid images are shown in **Figure 4.7**. Images shown in **Figure 4.7** are optimized for clarity using Fiji v2.3.0.²⁰⁸ A review of the morphological changes of the bacterial features shows a positive correlation between membrane targeting calcimycin treated cells and compound **3.4**. These treatments showed the highest amount of Sytox Green stained cells indicating that compound **3.4** is likely acting through a membrane-active pathway.

All antibiotic treatments caused some increase in the membrane area. Cell elongation is a common response to environmental stress because larger cells are more difficult for predators (protozoa, neutrophils) to ingest.^{209 210 206} Phosphomycin-treated cells exhibit the largest increase in membrane length and eccentricity (elongated-ness). Elongation in rod-shaped bacteria primarily occurs in response to mis-regulation during cell wall synthesis.²⁰⁶ Internal-targeting cell wall antibiotics cause the bacteria to produce peptidoglycan for their lateral rather than the septal cell wall which elongate the cells.²⁰⁶

¹¹ More subtle changes in the membrane length were seen in rifampicin, calcimycin and compound **3.4** treated cells (**Figure 4.7**). Calcimycin also displays a reduction in cell width, creating more rod-shaped cells compared to the DMSO control. Bactrim, vancomycin, and gentamicin treated cells showed minimal increases in membrane area and more circularity compared to other antibiotic treatments.

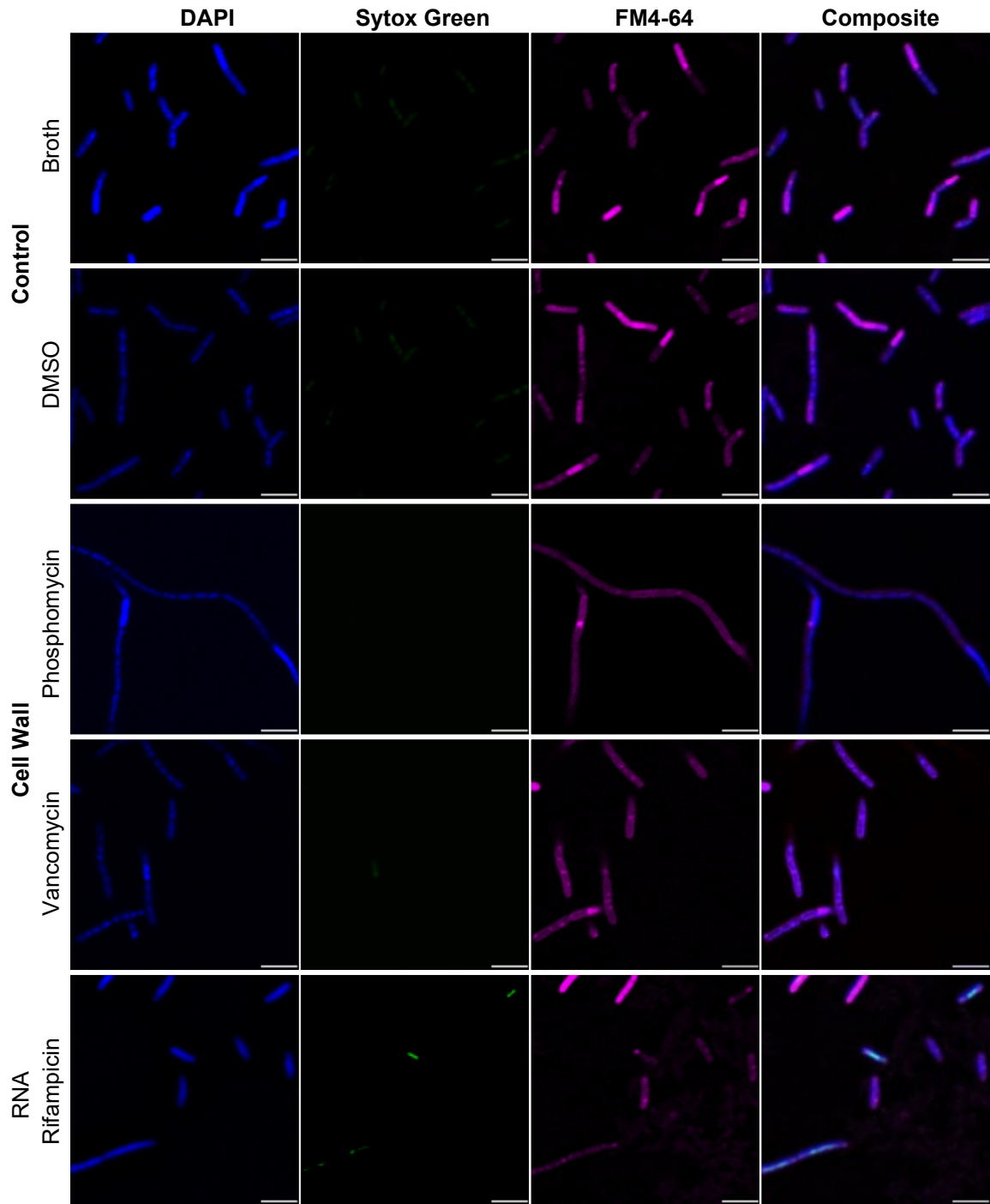


Figure 4.7: Images taken after 2 h of incubation with the listed antibiotic, DMSO or broth. From left: DAPI, Sytox Green, and FM4-64 stained cells. Sytox Green is used to visualize membrane lysis, so no cells are present when the membrane is intact. Brightness was enhanced for clarity using Fiji, scale bar represents 5 μm .

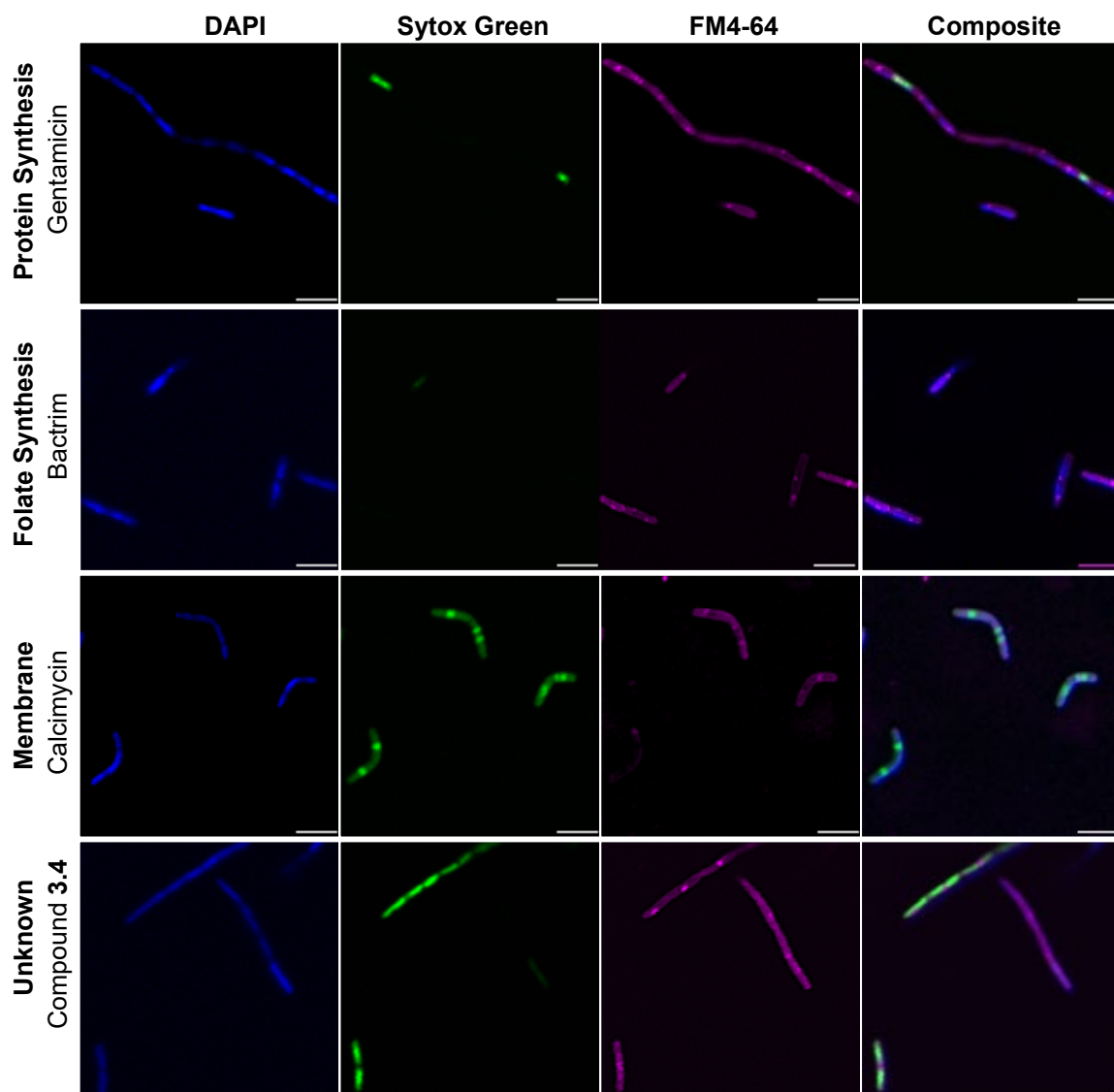


Figure 4.7 (continued): Images taken after 2 h of incubation with the listed antibiotic. From left: DAPI, Sytox Green, and FM4-64 stained cells. Sytox Green is used to visualize membrane lysis, so no cells are present when the membrane is intact. Brightness was enhanced for clarity using Fiji, scale bar represents 5 μm .

Changes in DNA packing can be seen by the intensity and morphology of DAPI stained cells. Rifampicin treated cells have been shown to exhibit rapid decondensation, which refers to the un-packing of DNA within the nucleoid. This causes a slight increase in the DAPI area as it expands within the membrane (**Figure 4.7**).^{211 184 11} Vancomycin and phosphomycin express a higher nucleoid area but with more irregular packing of DNA.¹⁸⁴¹¹ This packing results in segmented nucleoids spread out within the cell that is typical to cell wall targeting antibiotics. Bactrim treated cells also had higher irregularity. The DAPI stained area looks almost oval shaped, with higher nucleoid density in the center of the cell. Compound **3.4** induced more rod-shaped nuclei, seen by an increase in DAPI length and decrease in circularity. Gentamicin and calcimycin treatments exhibit a slight decrease in the size of the DAPI-stained area compared to controls. Calcimycin-treated bacteria also exhibited a higher DAPI intensity in tightly packed, more circular nucleoids compared to the DMSO control.

Increased membrane permeability reflects higher intensities of Sytox Green in the nucleoid. Calcimycin is a membrane active antibiotic that causes depolarization and pore formation through Ca^{2+} channels. Depolarization of the membrane leads to increased permeability which allows Sytox Green uptake. Other treatments also displayed an increase in SG uptake, because it is common to see a decrease in membrane integrity as a downstream effect from other targets.^{11, 212} For example, when gentamicin blocks protein synthesis, it promotes mistranslation and impacts membrane permeability.¹¹ Cell wall targeting antibiotics have also shown membrane lysing to a lesser extent, but phosphomycin and vancomycin treated cells exhibited little to no SG uptake in this

study.¹⁸⁴ Compound **3.4** appears to accumulate a substantial amount of Sytox Green (SG), almost to the extent of calcimycin. These results show that this urea-based antibiotic is likely acting through a membrane-active MOA. However, compound **3.4** does not display the same shrinkage of the nucleoid as displayed in the calcimycin treated cells, but this is likely specific to the cation transport mechanism of calcimycin. Many other membrane-active antibiotics display more subtle changes in DAPI, as seen in compound **3.4**.¹¹ The initial imaging suggests that compound **3.4** is a membrane-targeting antibiotic, but quantitative analysis discussed below will confirm these findings.

4.2.5 Statistical image analysis

Cell objects (nucleoids, membranes) created by CellProfiler were measured by the “MeasureObjectSizeShape” module and data was exported to Excel. Object intensity was measured for both DAPI and Sytox Green stained nucleoids using the “MeasureObjectIntensity” module. A description of the calculated parameters are given in **Table 4.2**, and the obtained measurements for each antibiotic is given in **Table 4.3**. Where treatments did not affect membrane permeability, SG intensity is statistically represented with zero values. The data reflects three biological repeats where a minimum of 50 bacteria were analyzed per well. This results in $n \geq 150$ for DAPI and FM 4-64 parameters. The parameters selected by CellProfiler™ follow previous work by Lamsa *et al.* which define object size, shape and intensity measurements.¹⁸⁴ Linear discriminant analysis was performed using the Addinsoft XLSTAT 2022.2.1 plugin (Student Version) in Microsoft Excel 16.60 for Mac.

Table 4.2: Description of parameters (adapted from CellProfiler™)¹⁹⁴

Parameters that describe an object's size	
Area	Area of the object calculated by the number of pixels in the object (μm^2)
Length	Length (μm) of the major axis of the ellipse that has the same normalized second central moments as the region.
Width	Width (μm) of the minor axis of the ellipse that has the same normalized second central moments as the region.
Fret Diameter	The distance (μm) between two parallel lines tangent on either side of the object.
Perimeter	The distance around the boundary of the object (μm)
Convex area	The number of pixels within the area of a convex polygon drawn around the object (μm^2)
Circularity	
Form Factor	Calculated as $4*\pi*Area/Perimeter^2$. Equals 1 for a perfectly circular object.
Eccentricity	The elongated-ness of the object calculated by the ratio of the distance between the foci of the ellipse and its major axis length. Values range from 0-1, where 0 is a circle and 1 is a straight line.
Irregularity	
Extent	The proportion of the pixels in the bounding box that area also in the region. Computed as the area/volume of the object divided by the area/volume of the bounding box. Cells will have larger extents if they occupy the box more or, have less protrusions/irregularities.
Compactness	A filled circle will have a compactness of 1, irregular objects or objects with holes have a value greater than 1. Calculated as $Perimeter^2/4*\pi*Area$, related to form factor.
Intensity	
Intensity	The sum of the pixel intensities within an object, measured by the "Integrated Intensity" object.

Table 4.3: Median values obtained from CellProfiler™ object measurements. Data shown below is the median value calculated for the entire dataset (three biological repeats, $n \geq 150$ cells (except for Sytox Green Intensity)). Standard deviation represents the variation between the entire population.

	<u>Membrane Area</u> (μm)	<u>Membrane Length</u> (μm)	<u>Membrane Width</u> (μm)	<u>DAPI Area</u> (μm^2)
DMSO	8.280 \pm 3.940	1.930 \pm 0.639	1.347 \pm 0.259	6.960 \pm 3.299
Untreated	7.440 \pm 2.164	1.869 \pm 0.416	1.259 \pm 0.197	7.440 \pm 2.137
Phosphomycin	19.200 \pm 8.495	4.329 \pm 1.571	1.439 \pm 0.236	10.560 \pm 2.649
Vancomycin	10.800 \pm 2.956	2.314 \pm 0.652	1.397 \pm 0.265	9.600 \pm 1.578
Bactrim	8.160 \pm 3.471	2.001 \pm 0.648	1.297 \pm 0.258	7.440 \pm 3.305
Calcimycin	10.800 \pm 3.179	2.643 \pm 0.795	1.278 \pm 0.250	6.960 \pm 2.589
Gentamicin	9.120 \pm 3.259	2.435 \pm 0.616	1.253 \pm 0.289	6.480 \pm 1.896
Rifampicin	11.040 \pm 3.545	2.659 \pm 0.813	1.369 \pm 0.214	8.400 \pm 3.368
Compound 3.4	12.240 \pm 3.753	2.761 \pm 0.785	1.401 \pm 0.235	7.200 \pm 2.576
	<u>DAPI Convex Area</u> (μm^2)	<u>Membrane Max Fret Diameter</u> (μm)	<u>Membrane Min Fret Diameter</u> (μm)	<u>Membrane Perimeter</u> (μm)
DMSO	7.800 \pm 3.717	1.828 \pm 0.622	1.181 \pm 0.261	4.966 \pm 1.522
Untreated	7.920 \pm 2.405	1.731 \pm 0.373	1.008 \pm 0.185	4.618 \pm 0.895
Phosphomycin	12.240 \pm 3.019	3.994 \pm 1.444	1.347 \pm 0.255	9.941 \pm 3.104
Vancomycin	10.560 \pm 1.816	2.264 \pm 0.588	1.358 \pm 0.248	5.993 \pm 1.203
Bactrim	8.400 \pm 3.645	1.874 \pm 0.603	1.138 \pm 0.246	5.016 \pm 1.385
Calcimycin	7.440 \pm 2.910	2.448 \pm 0.683	1.164 \pm 0.218	6.216 \pm 1.617
Gentamicin	7.200 \pm 2.102	2.213 \pm 0.550	1.064 \pm 0.285	5.645 \pm 1.323
Rifampicin	9.360 \pm 3.759	2.448 \pm 0.727	1.195 \pm 0.198	6.303 \pm 1.451
Compound 3.4	8.160 \pm 2.971	2.471 \pm 0.816	1.200 \pm 0.292	6.526 \pm 1.786
	<u>DAPI Length</u> (μm)	<u>DAPI Width</u> (μm)	<u>DAPI Max Fret Diameter</u> (μm)	<u>DAPI Min Fret Diameter</u> (μm)
DMSO	1.713 \pm 0.589	1.249 \pm 0.226	1.610 \pm 0.568	1.050 \pm 0.215
Untreated	1.852 \pm 0.421	1.239 \pm 0.203	1.731 \pm 0.383	0.960 \pm 0.195
Phosphomycin	2.222 \pm 0.361	1.557 \pm 0.268	2.173 \pm 0.378	1.362 \pm 0.257
Vancomycin	2.079 \pm 0.224	1.525 \pm 0.195	1.935 \pm 0.231	1.358 \pm 0.195
Bactrim	1.906 \pm 0.510	1.292 \pm 0.309	1.697 \pm 0.478	1.138 \pm 0.297
Calcimycin	1.826 \pm 0.434	1.246 \pm 0.276	1.731 \pm 0.419	1.018 \pm 0.262
Gentamicin	1.706 \pm 0.429	1.210 \pm 0.210	1.657 \pm 0.324	1.102 \pm 0.350
Rifampicin	2.141 \pm 0.601	1.309 \pm 0.297	1.979 \pm 0.557	1.152 \pm 0.285
Compound 3.4	1.840 \pm 0.562	1.233 \pm 0.205	1.747 \pm 0.501	0.960 \pm 0.237

Table 4.3 (continued): Median values obtained from CellProfiler™ object measurements. Data shown below is the median value calculated for the entire dataset (three biological repeats, $n \geq 150$ cells (except for Sytox Green Intensity)). Standard deviation represents the variation between the entire population.

	<u>DAPI Perimeter</u> (μm)	<u>DAPI Form Factor</u>	<u>Membrane Form Factor</u>	<u>Membrane Eccentricity</u>
DMSO	4.548 \pm 1.350	1.064 \pm 0.168	1.014 \pm 0.160	0.723 \pm 0.135
Untreated	4.577 \pm 0.922	1.065 \pm 0.144	1.058 \pm 0.129	0.746 \pm 0.156
Phosphomycin	5.923 \pm 0.931	0.930 \pm 0.112	0.626 \pm 0.159	0.946 \pm 0.067
Vancomycin	5.455 \pm 0.521	0.982 \pm 0.090	0.936 \pm 0.137	0.802 \pm 0.153
Bactrim	4.676 \pm 1.276	0.994 \pm 0.168	0.975 \pm 0.162	0.761 \pm 0.166
Calcimycin	4.718 \pm 1.083	1.006 \pm 0.194	0.845 \pm 0.187	0.872 \pm 0.115
Gentamicin	4.395 \pm 0.796	0.968 \pm 0.201	0.905 \pm 0.170	0.856 \pm 0.129
Rifampicin	5.215 \pm 1.335	0.967 \pm 0.176	0.867 \pm 0.161	0.861 \pm 0.130
Compound 3.4	4.776 \pm 1.142	1.008 \pm 0.159	0.861 \pm 0.153	0.863 \pm 0.128
	<u>DAPI Extent</u>	<u>Membrane Extent</u>	<u>DAPI Compactness</u>	<u>DAPI Eccentricity</u>
DMSO	0.690 \pm 0.103	0.677 \pm 0.102	0.940 \pm 0.163	0.675 \pm 0.178
Untreated	0.714 \pm 0.111	0.714 \pm 0.112	0.939 \pm 0.141	0.736 \pm 0.156
Phosphomycin	0.625 \pm 0.095	0.495 \pm 0.134	1.075 \pm 0.139	0.688 \pm 0.148
Vancomycin	0.625 \pm 0.092	0.625 \pm 0.109	1.018 \pm 0.103	0.673 \pm 0.138
Bactrim	0.646 \pm 0.108	0.667 \pm 0.117	1.006 \pm 0.183	0.727 \pm 0.169
Calcimycin	0.667 \pm 0.109	0.625 \pm 0.115	0.994 \pm 0.148	0.707 \pm 0.178
Gentamicin	0.643 \pm 1.397	0.600 \pm 0.129	0.955 \pm 0.129	0.710 \pm 0.142
Rifampicin	0.644 \pm 0.107	0.639 \pm 0.120	1.034 \pm 0.189	0.794 \pm 0.137
Compound 3.4	0.667 \pm 0.116	0.643 \pm 0.151	0.992 \pm 0.186	0.740 \pm 0.152
	<u>Membrane Compactness</u>	<u>DAPI Intensity</u>	<u>Sytox Green Intensity</u>	
DMSO	0.986 \pm 0.169	0.333 \pm 0.199	0.037 \pm 0.084	
Untreated	0.945 \pm 0.134	0.263 \pm 0.251	0.000 \pm 0.104	
Phosphomycin	1.599 \pm 0.417	0.060 \pm 0.168	0.000 \pm 0.175	
Vancomycin	1.068 \pm 0.209	0.179 \pm 0.101	0.000 \pm 0.064	
Bactrim	1.025 \pm 0.187	0.044 \pm 0.052	0.181 \pm 0.309	
Calcimycin	1.184 \pm 0.419	0.173 \pm 0.275	0.867 \pm 0.158	
Gentamicin	1.105 \pm 0.210	0.068 \pm 0.035	0.249 \pm 0.134	
Rifampicin	1.153 \pm 0.236	0.111 \pm 0.266	0.000 \pm 0.159	
Compound 3.4	1.161 \pm 0.255	0.039 \pm 0.210	0.441 \pm 0.230	

Linear discriminant analysis was used to determine the best parameters that delineates the MOA classes. In LDA, eigenvalues are computed for each variable (cell measurement) by dividing the deviation between classes by the within-class variation.^{192, 213} Not all the variation is reflected in one grouping of eigenvalues, so multiple iterations are used to summarize the data. Each discriminant factor (F1-F6) represents some part of the variance in the data set. This is shown in the Scree plot (**Figure 4.8**). Eigenvalues for all measurements are listed in **Table 4.4**. Any parameter with eigenvalues <0.1 was removed before the final analysis because it would not accurately represent the variance between antibiotic classes. These factors were considered redundant and removed from the dataset.

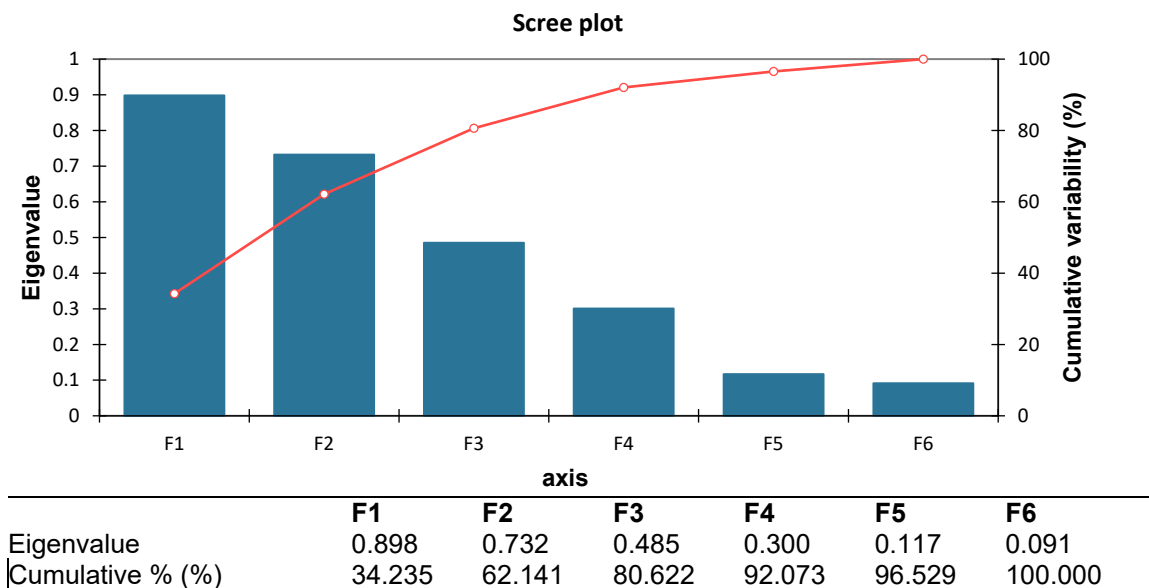


Figure 4.8: Graphs generated by XLSTAT to explain the variation in cell measurements between antibiotic MOA classes. The Scree plot shows the cumulative variation between each axis drawn in LDA. The table of eigenvalues are listed below for clarity.

Table 4.4: Table of eigenvalues for the cell measurement parameters used in linear discriminant analysis.

	F1	F2	F3	F4	F5	F6
Membrane Area	1.294	-0.375	-1.605	3.097	0.061	0.640
Membrane Compactness	0.844	-0.181	-0.691	2.118	0.853	0.298
Membrane Eccentricity	-0.407	0.371	-0.174	-0.370	0.491	-0.407
Membrane Extent	-0.124	-0.105	0.251	0.028	-0.283	0.185
Membrane Form Factor	0.753	-0.453	-0.081	0.209	0.685	0.482
Membrane Length	-2.202	1.433	0.868	-0.946	2.115	1.377
Membrane Max Feret Diameter	1.595	0.260	0.097	-0.244	-1.416	-3.182
Membrane Min Feret Diameter	0.318	0.226	0.204	0.017	-0.075	0.267
Membrane Width	-1.047	0.879	0.037	-0.494	0.698	-0.888
Membrane Perimeter	-0.241	-1.478	1.305	-3.572	-1.010	1.692
DAPI Area	-0.211	-0.492	-0.375	0.264	-0.130	-1.539
DAPI Compactness	0.382	0.587	0.216	0.420	-0.403	-0.703
DAPI Convex Area	-0.709	0.435	0.172	0.834	-1.008	-0.956
DAPI Eccentricity	0.495	0.372	0.015	-0.168	-0.100	0.545
DAPI Extent	-0.035	-0.195	0.026	-0.067	-0.093	0.193
DAPI Form Factor	0.493	0.358	0.632	0.241	0.147	-0.501
DAPI Length	0.752	-0.720	0.979	0.738	0.011	-0.022
DAPI Max Feret Diameter	-0.180	0.281	-0.416	-1.444	0.578	0.290
DAPI Min Feret Diameter	1.006	-0.631	-0.132	1.374	0.960	-1.053
DAPI Width	0.527	1.227	0.206	-1.074	-0.424	2.480
DAPI Perimeter	-0.016	-0.065	-0.063	-0.155	0.415	1.166
DAPI Intensity	0.008	-0.507	0.508	-0.165	0.634	-0.091
Sytox Intensity	-0.671	0.335	0.222	0.552	0.181	-0.042

Validation of the cell measurements used to separate the MOA classes are summarized by the following graphs. A Scree plot (**Figure 4.8**) summarizes the contributions of each factor to the total variance. Factors F1-F4 contain more than 90%

of the variation so they can be used to summarize the relationship between different antibiotics. Next, a variable plot (**Figure 4.9**) shows the first two discriminant functions (F1, F2) that summarize 62% of the variation in the dataset. Larger eigenvalues in a variable plot correspond to a higher contribution of that variable to the clustering of antibiotics for the axis.

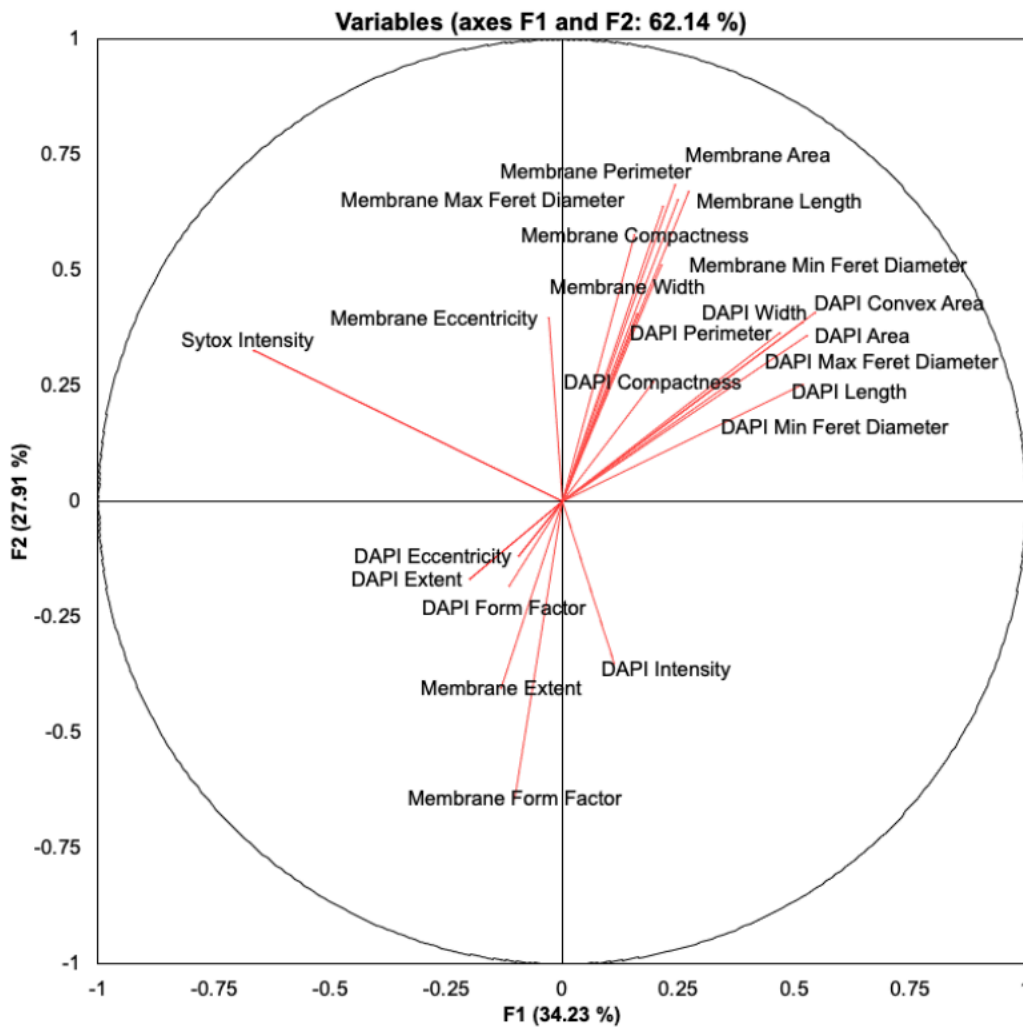


Figure 4.9: Graphs generated by XLSTAT to explain the variation in cell measurements between antibiotic MOA classes. The variable plot summarizes the contribution of cell measurements to the separation of the different antibiotic MOA classes.

Proper classification of compound **3.4** is dependent on minimal overlap between the confidence ellipses of the antibiotics with known MOA. Centroids plotted on different axes represent the mean distribution of each MOA class and the confidence ellipses include 95% of the variation within the class (**Figure 4.10**). Confusion matrices validate the model by predicting the assignment of an unclassified training sample to a MOA class. This means that outliers in the overlapping areas of a MOA centroid may be mis-categorized. Our confusion matrix was validated by correctly identifying the MOA for 79% of the randomly chosen samples (**Table 4.5**). The highest error was seen in protein synthesis and RNA antibiotics (~50% correct) but all other classes showed > 85% correct for the training sample. Protein synthesis and RNA antibiotics showed more subtle changes in their morphology leading to greater overlap between the classes and lower confidence.

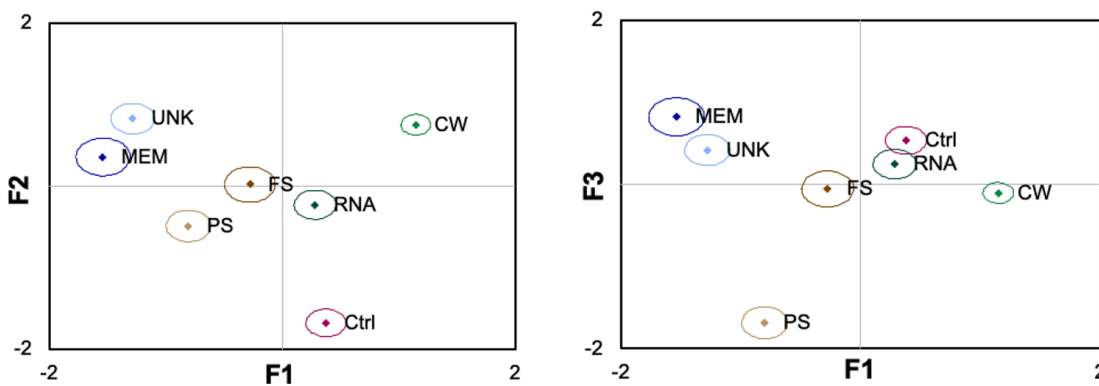


Figure 4.10: Centroids and confidence ellipses generated by XLSTAT. Centroids represent 95% confidence of assignment to the antibiotic class. Data shown is representative of 3 biological repeats ($n \geq 150$). Centroids were generated using discriminant functions F1 and F2 (left) or F1 and F3 (right), diamonds represent mean values for each centroid. Confidence ellipses represent 95% of the spread of the data within the class.

Table 4.5: Confusion matrix for the training sample generated by XLSTAT.

from \ to	CW	Ctrl	FS	MEM	PS	RNA	UNK	Total	% correct
CW	412	16	12	0	0	16	18	474	86.92%
Ctrl	0	258	0	0	0	6	0	264	97.73%
FS	6	8	142	0	0	0	6	162	87.65%
MEM	0	0	2	126	0	0	16	144	87.50%
PS	8	4	42	2	106	2	44	208	50.96%
RNA	46	26	10	6	2	126	24	240	52.50%
UNK	2	0	12	6	2	2	192	216	88.89%
Total	474	312	220	140	110	152	300	1708	79.74%

The heatmap in **Figure 4.11** shows the mean values of the centroids generated by correlations of F1-F4 and the dendrogram relates them in Euclidean space through agglomerative hierarchical clustering. Clustering of the antibiotic classes show that compound **3.4** is most similar to the membrane targeting antibiotic calcimycin. The heatmap clearly shows this relationship, just as the centroid plots do in **Figure 4.10**. There is less similarity in **3.4** and calcimycin in the fourth discriminant function (F4), which is seen by the heatmap in **Figure 4.11**. This is expected because the two bacterial treatments did not exhibit identical changes in morphology. Calcimycin treated cells have a distinctly circular small nuclei specific to the Ca²⁺ transport mechanism, which is not expected in **3.4**.¹¹ Gentamicin also noticeably shows a strong similarity with the membrane-targeting antibiotics in F1, presumably because of its higher Sytox Green intensity compared to other treatments.

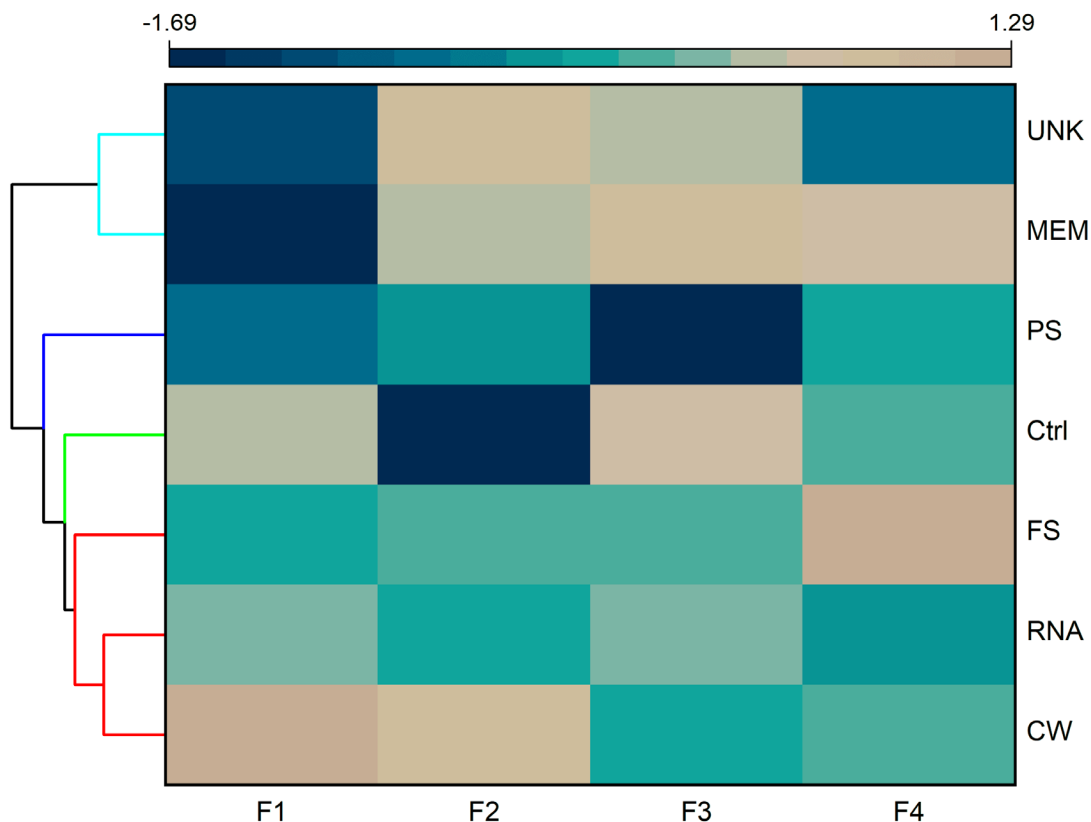


Figure 4.11: Agglomerative hierarchical clustering graph showing the heat map (centroids from F1-F4) and dendrogram of the relationship in a 4-dimensional Euclidean space. The height of the dendrogram represents the relationship between clusters, with higher branching being further apart.

The dendrogram shows specific separation of compound **3.4** and calcimycin from the other antibiotics, seen by the distinct clustering in Figure 4.11. The height of the dendrogram before it reaches a node is proportional to the relationship between the two classes. This means that the cluster of CW, RNA and FS seen by the second red hierarchical cluster is closely related to the untreated antibiotics (black node, **Figure 4.11**). Cell wall targeting antibiotics are far from compound **3.4** because of the elongation and irregular nucleoid. The control compounds and RNA-active clusters overlap because of the subtle

changes in morphology. The unknown (**3.4**) clusters closest to the membrane active antibiotics due to its high Sytox Green intensity and membrane shape. However, the molecule is unlikely to act in the same way as the Ca^{2+} ionophore calcimycin given the difference in nucleoid size. This is not completely surprising, as compound **3.4** does not have an obvious binding site for cations such as Ca^{2+} . However, it does contain a urea functionality that is known to bind to anions. As we already ruled out the ability of **3.4** to bind to the lipid headgroups in the membrane (**Chapter 3**), another possible membrane-related mechanism could be transmembrane anion transport.

4.2.6 Anion transport studies

Bacterial cytological profiling suggested that compound **3.4** exhibits a membrane-based mechanism, but it was unlike the Ca^{2+} transport mechanism of calcimycin. Previously, we found that compound **3.4** does not interact with membrane phospholipids, but ureas are well-known for their chloride transport ability.¹⁵⁰ Ureas can facilitate chloride transport by creating synthetic channel membranes or acting as ion carriers.¹⁵⁰ In fact, previous work has suggested that tris-thiourea *tren*-based chloride transporters exert antibiotic activity in *S. aureus* through chloride transport.²¹⁴ Anion transport across the membrane would lead to a change in membrane polarization/leakage similar to calcimycin, but the exact morphological changes have never been documented. To test this hypothesis, we performed liposome-based chloride transport assays with compound **3.4** (**Figure 4.12**).

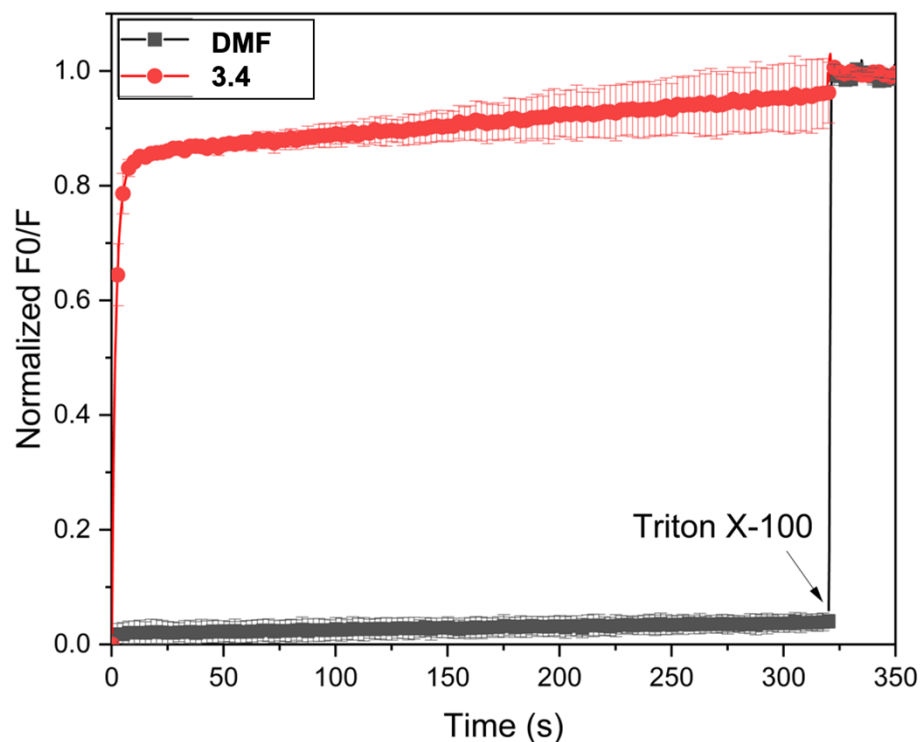


Figure 4.12: Chloridetransport mediated by compound **3.4** across 100 nm 7:3 eggPC:cholesterol LUVs loaded with 1 mM lucigenin, 222 mM NaNO₃, 10 mM HEPES buffer at pH 7.4, and suspended in a solution of 25 mM NaCl, 222 mM NaNO₃, 10 mM HEPES buffer at pH 7.4. Compound **3.4** was added at a concentration of 5 mol% (with respect to total lipid (eggPC+cholesterol)). Results are the average of 2 repeats and error bars represent standard deviations. DMF was used as a blank run (no transporter added) to assess background permeability.

Chloride transport by compound **3.4** was measured using a standard lucigenin quenching assay with the help of Rayhanus Salam.²¹⁵ Lucigenin is a non-selective anion sensor, whose fluorescence is quenched in the presence of certain anions (mostly halide anions such as Cl⁻). In this assay, large unilamellar vesicles (LUVs) (100 nm, 70% PC 30% cholesterol) encapsulating 1 mM lucigenin, 10 mM HEPES buffer at pH = 7.4 and 222 mM NaNO₃ were suspended in a lucigenin-free solution containing 10 mM HEPES buffer at pH = 7.4 and 222 mM NaNO₃ (3 mL total volume in fluorescence cuvette equipped with a stir

bar). Then, 3.75 μL of compound **3.4** in DMF (5 mol% with respect to total lipid) or DMF as a negative control to the vesicles. To start the transport experiment, 37.5 μL NaCl (1 M) was added to achieve a final concentration of 25 mM NaCl and 0.5 mM lipid in the cuvette. The fluorescence intensity ($\lambda_{\text{ex}} = 430 \text{ nm}$, $\lambda_{\text{em}} = 505 \text{ nm}$) was measured for 350 s. At time $t = 320 \text{ s}$, detergent (37.5 μL of 10% Triton X-100) was added to fully lyse the membrane and observe maximum quenching. The data is shown as F_0/F , because this value is linearly correlated with chloride concentration (F_0 is the fluorescence intensity at the beginning of the measurement), normalized for the maximum value of F_0/F obtained upon the addition of detergent. Compound **3.4** exhibited excellent chloride transport ability (**Figure 4.12**), which follows the previous results that it acts as a membrane-active antibiotic.

4.3 Conclusion

In this study, we employed the statistical power of bacterial cytological profiling to identify a urea-based antibiotic as a membrane-targeting antibiotic. Previous work has shown that **3.4** is not likely to interact with the phospholipid bilayer and the lack of nuclear decondensation in this study shows that it is not targeting the cell wall. In addition, if **3.4** were acting through other intracellular mechanisms, we would see alternative changes in nuclear morphology or lower Sytox Green permeated cells. Urea-based receptors have been studied in supramolecular chemistry extensively for their anion binding ability. It is likely that **3.4** is causing membrane depolarization through an anion transport mechanism, which would lead to increased permeability. Future work

should continue to test different supramolecular molecules for antibiotic activity and develop a larger imaging library for unique ion-transport mechanisms.

CHAPTER 5

MATERIALS AND METHODS

5.1 General

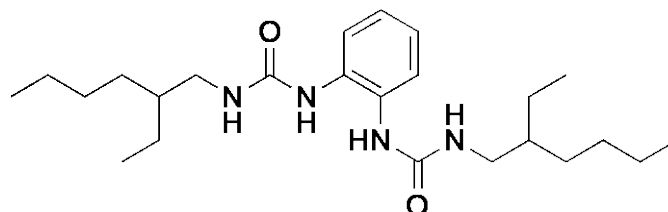
Compound names are those generated by Chemdraw 16.0.1.4 following IUPAC nomenclature. Solvents, reagents and inorganic salt were purchased by Sigma Aldrich, TCI, or Alpha Aesar and used without further purification. Reactions were performed under an inert Ar atmosphere in oven-dried glassware. Flash column chromatography was carried out using SiliaFlash P60 (40-63 μm , 230-400 mesh). Thin-layer chromatography was carried out using silica gel TLC plates with fluorescent indicator, visualized under UV light (254 nm) or by staining with ninhydrin or permanganate solutions. ^1H NMR and ^{13}C NMR spectra were collected on a Bruker 500 MHz NMR, Varian Unity Inova 400 MHz or a Bruker Avance 300 MHz spectrometer. ^{13}C NMR spectra were collected proton decoupled. Mestrenova was used for NMR visualization. Chemical shifts (δ) are reported in parts per million (ppm) and calibrated to the residual solvent peak in CDCl_3 ($\delta = 7.26$ (^1H) and 77.2 ppm (^{13}C)) or $\text{DMSO}-d_6$ ($\delta = 2.50$ (^1H) and 39.5 ppm (^{13}C)). Coupling constants (J) are given in Hertz (Hz). The following abbreviations are used for spin multiplicity: s = singlet, d = doublet, h = heptet, m = multiplet, br. = broad. Infrared (IR) spectra were

recorded on a Nexus 670 Avatar FTIR spectrometer; only selected maximum absorbances (ν_{\max}) of the most intense peaks are reported (cm^{-1}). Electron spray ionization (ESI) mass spectra were recorded on a Bruker micrOTOF. Elemental analysis was conducted by *Midwest Laboratories, Inc.* The lipids 14:0 CDL (1',3'-bis[1,2-dimyristoyl-*sn*-glycero-3-phospho]-glycerol), POPE (1-palmitoyl-2-oleoyl-*sn*-glycero-3-phosphoethanolamine), POPC (1-palmitoyl-2-oleoyl-glycero-3-phosphocholine), DOPE (1,2-dioleoyl-*sn*-glycero-3-phosphoethanolamine), DOPC (1,2-dioleoyl-*sn*-glycero-3-phosphocholine), BODIPY-CDL (1,1',2,2'-tetraoleoyl cardiolipin [4-(dipyrrrometheneboron difluoride)butanoyl]), 18:1-6:0 NBD-PE (1-oleoyl-2-(6-((7-nitro-2-1,3-benzoxadiazol-4-yl)amino)hexanoyl)-*sn*-glycero-3-phosphoethanolamine), and 18:1-6:0 NBD-PC (1-oleoyl-2-(6-((7-nitro-2-1,3-benzoxadiazol-4-yl)amino)hexanoyl)-*sn*-glycero-3-phosphocholine) were purchased from *Avanti Polar Lipids, Inc.* Molecular modelling was performed using the Molecular Operating Environment (MOE) software version 2018.01. Fluorescence spectra and kinetic studies were performed on an Agilent Cary Eclipse fluorescence spectrophotometer equipped with stirring function and Peltier temperature controller. 3 mL macrocuvettes were used and all solutions were stirred using a cuvette stir bar (Sigma-Aldrich #Z363545). Bacterial growth curves were performed using a BioTek Cytation 5 Cell Imaging Multi-Mode Reader. Bacteria images were captured using the BioTek Cytation 5 or Nikon Eclipse Ti A1 confocal microscope equipped with a 40x/0.95 oil objective and 96-well plate adapter.

5.2 Synthesis and characterization

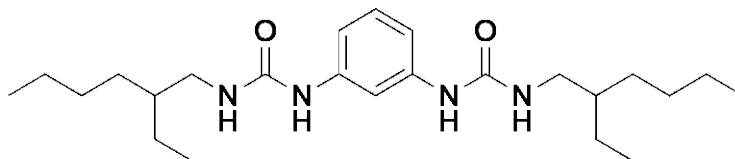
5.2.1 Synthesis and characterization of novel compounds in Chapter 2

1,1'-(1,2-phenylene)bis(3-(2-ethylhexyl)urea), 2.1.



2-ethyl-hexyl isocyanate (854 μL , 756 mg, 4.8 mmol, 2 eq.) was added to *o*-phenylenediamine (264 mg, 2.4 mmol, 1 eq) dissolved in 10 mL DCM and stirred overnight. The oily product was purified using a silica column (100% DCM) (350 mg, 0.8 mmol, 35% yield). ^1H NMR (400 MHz, $\text{DMSO-}d_6$, 298 K, ppm) δ 7.73 (s, 2H), 7.51 – 7.41 (m, 2H), 6.98 – 6.88 (m, 2H), 6.42 (t, $J = 5.7$ Hz, 2H), 3.21 – 2.78 (m, 4H), 1.41 – 1.18 (m, 18H), 0.94 – 0.76 (m, 12H). ^{13}C NMR (101 MHz, $\text{DMSO-}d_6$, 298 K, ppm) δ 156.5, 132.0, 123.8, 123.5, 42.5, 39.7, 30.9, 28.9, 24.1, 23.0, 14.5, 11.2. IR (neat): ν (cm^{-1}) = 3276, 2940, 2867, 1634, 1553, 1451, 1256, 752, 623. HRMS (ESI) $\text{C}_{24}\text{H}_{43}\text{N}_4\text{O}_2$ [$\text{M}+\text{H}^+$], m/z (calculated) = 419.3386, observed = 419.3384.

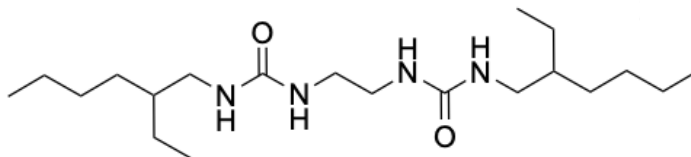
1,1'-(1,3-phenylene)bis(3-(2-ethylhexyl)urea), 2. 2.



2-ethylhexyl isocyanate (836 μL , 742 mg, 4.8 mmol, 2 eq.) was added to *m*-phenylenediamine (258 mg, 2.4 mmol, 1 eq.) dissolved in 10 mL DCM and stirred

overnight. The oily product was purified using a silica column (eluent: 10% MeOH in DCM) to yield **2.2** as a brown oil (430 mg, 1 mmol, 43% yield). ^1H NMR (300 MHz, CDCl_3 , 298 K, ppm) δ 7.50 (s, 2H), 7.26 – 7.10 (m, 1H), 7.10 – 6.47 (m, 3H), 5.58 (s, 1H), 3.50 – 2.77 (m, 4H), 1.40 – 1.22 (m, 18H), 0.95 – 0.83 (m, 12H). ^{13}C NMR (101 MHz, CDCl_3 , 298 K, ppm) δ 157.4, 139.4, 129.1, 120.4, 117.0, 43.4, 39.9, 29.7, 29.0, 24.2, 23.1, 14.1, 10.8. IR (neat): ν (cm^{-1}) = 3345, 2929, 2850, 1639, 1553, 1240, 623. HRMS (ESI) $\text{C}_{24}\text{H}_{43}\text{N}_4\text{O}_2$ [$\text{M}+\text{H}^+$], m/z (calculated) = 419.3386, observed = 419.3384.

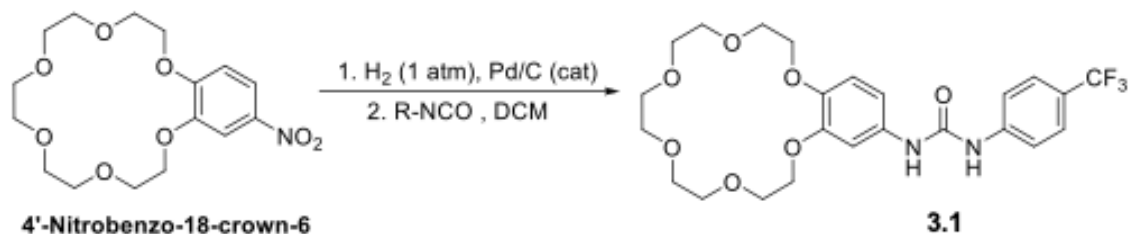
1,1'-(ethane-1,2-diyl)bis(3-(2-ethylhexyl)urea), 2.3.



Ethylenediamine (300 μL , 269 mg, 0.7 mmol, 1 eq.) was mixed with 10 mL pyridine before adding 2-ethylhexyl isocyanate (254 μL , 225 mg, 1.4 mmol, 2 eq.), and allowed to stir for 24 hours under N_2 atmosphere. The final product, **2.3**, was obtained through recrystallization in dichloromethane to yield a white solid (181.6 mg, 0.49 mmol, 70% yield). ^1H NMR (400 MHz, CDCl_3 , 298 K, ppm) δ 6.36 (s, 2H), 5.60 (s, 2H), 3.21 (s, 4H), 3.05 (m, 4H), 1.40 – 1.19 (m, 18H), 0.92 – 0.76 (m, 12H). ^{13}C NMR (101 MHz, CDCl_3 , 298 K, ppm) δ 160.0, 43.4, 40.9, 40.0, 31.0, 29.1, 24.2, 23.2, 14.2, 11.0. IR (neat): ν (cm^{-1}) = 3334, 2957, 2925, 2854, 2361, 1623, 1569, 1268, 618. HRMS (ESI) $\text{C}_{20}\text{H}_{42}\text{N}_4\text{O}_2\text{Na}^+$ [$\text{M}+\text{Na}^+$], m/z (calculated) = 393.3206, observed = 393.3206.

5.2.2 Synthesis and characterization of novel compounds in Chapter 3

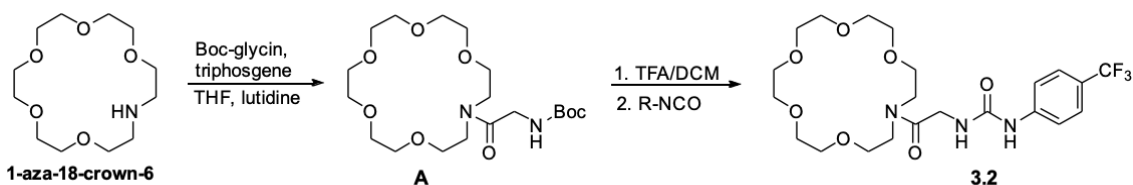
1-(2,3,5,6,8,9,11,12,14,15-decahydrobenzo[*b*][1,4,7,10,13,16]hexaoxacyclo-octadecin-18-yl)-3-(4-(trifluoromethyl)phenyl)urea, **3.1**.



4'-Nitrobenzo-18-crown-6 (300 mg, 0.84 mmol, 1 eq) was dissolved in MeOH (5 mL) and a catalytic amount of Pd/C was added. The mixture was degassed, put under a hydrogen atmosphere (1 atm) and allowed to stir for 12 h at room temperature. The solution was filtered over Celite to remove Pd/C, washed with MeOH and subsequently concentrated using a rotary evaporator. The resulting pale pink liquid was dried overnight under high vacuum to remove all residual MeOH. To the obtained dried aniline derivative was added DCM (5 mL) and 1-isocyanato-4-(trifluoromethyl)benzene (467 mg, 2.5 mmol, 3 eq) and the mixture was refluxed for 3 days under Ar atmosphere. The crude mixture was concentrated *in vacuo* and the obtained pale pink oil was subsequently purified by column chromatography (silica, solvent gradient of 0% to 10% MeOH in DCM) to yield **3.1** as an off-white solid (410 mg, 0.796 mmol, 95% yield). ^1H NMR (300 MHz, CDCl_3 , 298 K, ppm) δ 8.40 (br. s, 1H), 7.95 (br. s, 1H), 7.57 (d, $J = 8.5$ Hz, 2H), 7.46 (d, $J = 8.5$ Hz, 2H), 6.99 (d, $J = 2.4$ Hz, 1H), 6.71 (m, 1H), 6.57 (d, $J = 8.6$ Hz, 1H), 4.06 – 3.95 (m, 4H), 3.88 – 3.79 (m, 4H), 3.78 – 3.66 (m, 12H). ^{13}C NMR (101 MHz, CDCl_3 , 298 K, ppm) δ 153.6, 148.5, 144.3, 142.8,

132.6, 126.1 (q, $^3J_{CF} = 3.9$ Hz), 124.5 (q, $^1J_{CF} = 271.4$ Hz), 123.8 (q, $^2J_{CF} = 32.6$ Hz), 118.4, 113.8, 113.0, 106.7, 70.8, 70.7, 70.6, 70.5, 70.4 (presumable 2xC), 69.7, 69.5, 68.9, 68.2. IR (neat): ν (cm $^{-1}$) = 3317, 3295, 2911, 2875, 2875, 1648, 1603, 1554, 1514, 1409, 1329, 1242, 1236, 1183, 1130, 1110, 1108, 1070, 841. MS (ESI) $m/z = 537$ [M+Na] $^+$. Elemental analysis calcd for C $_{24}$ H $_{29}$ F $_3$ N $_2$ O $_7$: C 56.03, H 5.68, N 5.44, found: C 55.42, H 5.69, N 5.25.

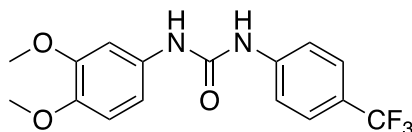
1-(2-(1,4,7,10,13-pentaoxa-16-azacyclooctadecan-16-yl)-2-oxoethyl)-3-(4(trifluoromethyl)phenyl)urea, 3.2.



Boc-protected crown ether analog **A** was synthesized from 1-aza-18-crown-6 (170.9 mg, 0.65 mmol, 1 eq) according to a modified literature procedure.²¹⁶ The obtained Boc-protected intermediate **A** was dissolved in 30 mL 1:2 TFA:DCM and stirred at room temperature overnight. The reaction mixture was concentrated using a rotary evaporator to remove the solvents and left to dry under high vacuum for 24 hours. 1-isocyanato-4-(trifluoromethyl)benzene (0.3 mL, 2.1 mmol, 3.2 eq) was added to the Boc-deprotected oil in 95:5 DCM:pyridine (10 mL) and the resulting mixture was refluxed overnight. This crude mixture was concentrated *in vacuo* and the oily product was subsequently purified by column chromatography (silica, solvent gradient of 0% to 10% MeOH in DCM) to yield **3.2** as a pale yellow/brown oil (96.9 mg, 0.19 mmol, 29% yield). ^1H NMR (300 MHz, CDCl $_3$, 298 K, ppm) δ 8.74 (br. s, 1H), 7.42 (d, $J = 8.5$ Hz, 2H), 7.31 (d, $J = 8.5$ Hz, 2H), 6.86 (br. s,

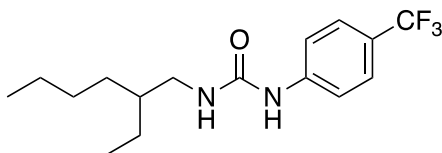
1H), 4.19 (d, $J = 4.7$ Hz, 2H), 3.77 – 3.54 (m, 24H). ^{13}C NMR (101 MHz, CDCl_3 , 298 K, ppm) δ 171.2, 156.1, 143.2, 125.8 (q, $^3J_{\text{CF}} = 3.4$ Hz), 124.6 (q, $^1J_{\text{CF}} = 270.9$ Hz), 123.3 (q, $^2J_{\text{CF}} = 32.5$ Hz), 118.1, 70.8 (2 peaks), 70.4, 70.2 (multiple C's), 70.1 (2 peaks), 69.7 (2 peaks), 48.7, 47.1, 42.1. IR (neat): ν (cm^{-1}) = 3750, 3628, 3301, 3009, 2868, 2360, 2341, 1652, 1557, 1324, 1216, 1112. MS (ESI) $m/z = 530$ $[\text{M}+\text{Na}]^+$. Elemental analysis calcd for $\text{C}_{22}\text{H}_{32}\text{F}_3\text{N}_3\text{O}_7$: C 52.07, H 6.36, N 8.28, found: C 51.83, H 6.26, N 8.10.

1-(3,4-dimethoxyphenyl)-3-(4-(trifluoromethyl)phenyl)urea, 3.3.



1-Isocyanato-4-(trifluoromethyl)benzene (150 μL , 1.0 mmol, 4.4 eq) and 2,4-(dimethoxy)aniline (36.6 mg, 0.24 mmol, 1 eq) were dissolved in DCM (3 mL) and the resulting mixture was stirred overnight. The resulting precipitate was filtered and washed with DCM to yield **3.3** as a white solid (74.8 mg, 0.22 mmol, 92% yield). ^1H NMR (400 MHz, $\text{DMSO}-d_6$, 298 K, ppm) δ 9.02 (s, 1H), 8.64 (s, 1H), 7.70 – 7.58 (m, 4H), 7.21 (s, 1H), 6.92 – 6.85 (m, 2H), 3.74 (s, 3H), 3.71 (s, 3H). ^{13}C NMR (101 MHz, $\text{DMSO}-d_6$, 298 K, ppm) δ 152.4, 148.8, 144.3, 143.6, 133.8, 126.1 (q, $^3J_{\text{CF}} = 4.0$ Hz), 124.6 (q, $^1J_{\text{CF}} = 270.7$ Hz), 121.6 (q, $^2J_{\text{CF}} = 32.2$ Hz), 117.8, 112.4, 110.5, 104.1, 55.8, 55.4. IR (neat): ν (cm^{-1}) = 3321, 2935, 2857, 1705, 1650, 1512, 1322, 1122, 1158, 1021, 1068. MS (ESI) $m/z = 341$ $[\text{M}+\text{H}]^+$. Elemental analysis calcd for $\text{C}_{16}\text{H}_{15}\text{F}_3\text{N}_2\text{O}_3$: C 56.47, H 4.44, N 8.23, found: C 56.26, H 4.46, N 8.49.

1-(2-ethylhexyl)-3-(4-(trifluoromethyl)phenyl)urea, **3.4**.



4-(Trifluoromethyl)aniline (300 μ L, 2.4 mmol, 1 eq) and 2-ethylhexyl isocyanate (1 mL, 5.7 mmol, 2.4 eq) were added to 10 mL DCM and refluxed for 3 days. The crude mixture was concentrated using a rotary evaporator and the obtained oil was subsequently purified by column chromatography (silica, 10% MeOH in DCM) to yield **3.4** as a colorless oil (720 mg, 2.27 mmol, 95% yield). ^1H NMR (400 MHz, CDCl_3 , 298 K, ppm) δ 7.76 (br. s, 1H), 7.45 (d, $J = 8.6$ Hz, 2H), 7.38 (d, $J = 8.6$ Hz, 2H), 5.57 (br. s, 1H), 3.25 – 3.06 (m, 2H), 1.38 (h, $J = 6.0$ Hz, 1H), 1.30 – 1.17 (m, 8H), 0.91 – 0.75 (m, 6H). ^{13}C NMR (101 MHz, CDCl_3 , 298 K, ppm) δ 156.3, 142.4, 126.4 (q, $^3J_{\text{CF}} = 3.9$ Hz), 124.7 (q, $^2J_{\text{CF}} = 32.8$ Hz), 124.3 (q, $^1J_{\text{CF}} = 271.4$ Hz), 118.8, 43.3, 39.7, 31.0, 29.0, 24.2, 23.1, 14.1, 10.9. IR (neat): ν (cm^{-1}) = 3344, 2960, 2930, 1651, 1601, 1559, 1560, 1320, 1183, 1158, 1070, 1015, 839. MS (ESI) $m/z = 317$ $[\text{M}+\text{H}]^+$. Elemental analysis calcd for $\text{C}_{16}\text{H}_{23}\text{F}_3\text{N}_2\text{O}_7$: C 60.74, H 7.33, N 8.85, found: C 60.70, H 7.28, N 8.92.

5.3 ^1H NMR titrations

^1H NMR titrations were performed using a Bruker 500 MHz or Bruker 300 MHz instrument. Both host and guest were dried under high vacuum for 12 hours before each titration. For each titration, the concentration of the host was kept constant upon each addition of guest and ^1H NMR spectra were recorded after each addition. The downfield

shift in the urea N-H peaks was determined using MestreNova, and these values were used to calculate association constants (K_a) using the online tool BindFit.¹⁵²

5.3.1 *Cardiolipin binding*

Cardiolipin 14:0 (Avanti #750332) was investigated as a potential bacterial lipid target for the bis-urea molecules in **Chapter 2**. We speculated that the sodium ion bound to CDL was creating solubility issues, so the CDL-2Na⁺ was exchanged for 2TBA⁺. To achieve this, Cardiolipin 14:0 (Avanti #750332, ~ 20 mg) was dissolved in 20 mL of 1:1 CHCl₃:MeOH and added slowly to an ion exchange column (BioTage Isolute[®] SCX). The protonated lipid was diluted in MilliQ water to 50 mL so that the pH could be accurately recorded during the addition of TBA-OH. After 2 eq. TBA-OH was added dropwise (pH = 7), the CDL-TBA₂ complex was lyophilized for 3 days to yield a fluffy white powder that could be used in ¹H NMR titrations.

Binding studies were performed in 0.5% MilliQ H₂O:95.5% DMSO-*d*₆ using lipids (14:0 CDL-2TBA, or POPC) as guests. A 1 mM solution of host was used as the starting point, to which aliquots of a solution containing 15 mM guest and 1 mM host were added using a Hamilton gas-tight syringe (this procedure ensures that the host concentration remains constant throughout the titration). Solubility issues limited any increase in host or guest concentration. The instrument was locked to DMSO-*d*₆ and the downfield shift in the urea N-H peaks was determined using MestreNova. Titrations showed no measurable binding for any of the bis-urea compounds, so binding constants were unable to be obtained.

5.3.2 Zwitterionic lipid binding

A ternary mixture consisting of 0.5% Milli-Q H₂O, 24.5% DMSO-*d*₆ and 75% CDCl₃ was used to ensure adequate solubility of both the host and the guest in the same solvent system. Titrations were performed using a 5 mM solution of host as the starting point, to which aliquots of a solution containing 35 mM guest and 5 mM host were added using a Hamilton gas-tight syringe (this procedure ensures that the host concentration remains constant throughout the titration). The instrument was locked to DMSO-*d*₆, but data was referenced to CDCl₃ ($\delta = 7.26$ ppm). In the case of the urea-containing compounds (**3.1**, **3.2**, **3.3**, **3.4**), the ureas were used as the host and the lipids were used as guest. The downfield shift in the urea N-H peaks was determined using MestreNova, and these values were used to calculate association constants (K_a) using the online tool BindFit¹⁵² assuming a 1:1 stoichiometry for binding. For the crown ether, the binding event could only be studied using the lipid (POPE) as the host and 18-crown-6 as the guest. In this case, the upfield shift of the POPE-NH₃⁺ peak was determined using MestreNova, and these values were used to calculate association constants (K_a) using the online tool BindFit. All titrations were repeated a minimum of 3 times, and association constants are given as the average of these 3 repeats with errors representing standard deviations. Lipids purchased from *Avanti Polar Lipids, Inc* were used in powder form for all titrations: POPC (#850457) & POPE (#850757).

5.4 Computational modeling

All computer modelling was performed using Molecular Operating Environment™ version 2018:01 (MOE) and conformational analysis employed an MMFF94x force field with an implicit 75:25 chloroform:DMSO solvent model to mimic the conditions used during the ¹H NMR titrations (generalized Born solvation model, dielectric constant exterior 15.28 (4.81 for chloroform and 46.7 for DMSO, so approximately $0.75 \times 4.81 + 0.25 \times 46.7 = 15.28$)). Structures were first generally energy minimized, followed by a LowModeMD conformational search of various possible low-energy conformers (Rejection Limit: 100, Iteration Limit: 10,000, RMS Gradient: 0.005, MM Iteration Limit: 500, RMSD Limit: 0.25, Energy Window: 7, Conformation Limit: 10,000, enforce chair conformation and do not allow amide bond rotation).

5.5 Liposome-based assays

5.5.1 *Cardiolipin binding in Triton X-100 micelles*

We used Triton X-100 micelles containing TopFluor® (BODIPY) fluorescently labeled CDL (Avanti Polar Lipids #810286).¹²³ Binding can be measured by changes in the fluorescence intensity of the BODIPY dye upon the addition of compound or DMSO (blank). To make the micelles, NBD-CDL was added to a round bottom flask and dissolved in CHCl₃. A lipid film was formed by removing the solvent on a rotary evaporator. After drying overnight, a solution of Triton X-100 in MilliQ (2.5 mM) was added to the lipid film so that the concentration of NBD-CDL was 0.4 mol%. NBD-CDL in Triton X-100. The

solution was vortexed to remove all lipid from the walls of the round bottom flask. The cloudy solution was added to a cuvette to stir the solution more rapidly, but after 24-hours it remained heterogenous and unable to generate any usable data.

5.5.2 NAO displacement assay

Liposomes were prepared by dissolving a lipid mixture (7:3 POPE:CDL, 5 mg/mL) in 2:1 CHCl₃:CH₃OH, followed by solvent removal using a rotary evaporator. The lipid film was dried further on high vacuum for at least 5 hours prior to use. The lipid film was hydrated with buffer (10 mM Tris-HCl, pH 7.4) and vortexed until all the lipid was removed from the round bottom flask. The resulting suspension was subjected to 9 freeze-thaw cycles, alternating between submersion in liquid nitrogen followed by thawing in mildly warm water. The lipid suspension was allowed to rest at room temperature for 30 minutes before extruding 25 times through a 100 nm polycarbonate membrane (*Nucleopore*) using the Avanti mini extruder set (*Avanti Polar Lipids, Inc.*) to create a stock lipid solution. For each measurement, the concentrated liposome stock was diluted in Tris-HCl buffer solution (10 mM, pH 7.4) to achieve a final lipid concentration of 5 μM. In each run 3 mL of the liposome stock was added to a cuvette with a stir bar for adequate mixing.

Prior to the assay, the optimal concentration of NAO to be added to the liposomes was determined by a self-quenching titration of NAO into the liposome solution (excitation wavelength = 488 nm, emission wavelength = 520 nm). For the assay, 2.5 μL of NAO (3 mM) dissolved in EtOH was added to the liposomes to yield 2.75 μM NAO (>2

eq NAO per CDL) in the cuvette. Compounds were dissolved in EtOH (3 mM, 15 mM and 30 mM stocks), so that a variety of concentrations could be tested without exceeding a maximum addition of 4 μ L of ethanol. Fluorescence measurements were taken after a short period of mixing (< 5 mins) to allow displacement of the NAO. The change in fluorescence was measured in triplicate for each compound along with ethanol controls (excitation wavelength = 488 nm, emission wavelength = 520 nm).

5.5.3 Fluorescence titrations with POPC and POPE

To determine the interaction between the hosts and PE lipids that are part of a bilayer (membrane), we performed fluorescence titrations whereby aliquots of the hosts in DMSO were added to an aqueous solution of 100 nm large unilamellar vesicles (LUVs) containing NBD-labelled lipids (*Avanti Polar Lipids*, #810130 for NBD-PE and # 810153 for NBD-PC). Due to the inability of pure POPE to form stable liposomes, a mixture of 1:1 POPE:POPC was used. The titrations were thus performed with either 100 nm POPC LUVs containing 1 mol% NBD-PC, or 100 nm 1:1 POPE:POPC LUVs containing 1 mol% NBD-PE.

To prepare the LUVs, the unlabeled lipids were weighed out in a small (25 mL) round bottom flask, and 1 mol% NBD-labelled lipid was added from a 1 mg/mL stock in chloroform (mol% with respect to total unlabeled lipid). The lipids were subsequently dissolved in chloroform to generate a homogenous mixture. The chloroform was removed via a rotary evaporator and the lipid mixture was further dried overnight under high vacuum. The lipid film was hydrated with Tris buffer (10 mM Tris, 150 mM NaCl, pH 7.4) and vortexed until all lipid was in suspension. The resulting suspension was subjected to

11 freeze-thaw cycles, alternating between submersion in liquid nitrogen followed by thawing in mildly warm water. The lipid suspension was allowed to rest at room temperature for 30 minutes before extruding 35 times through a 100 nm polycarbonate membrane (*Nucleopore*) using the Avanti mini extruder set (*Avanti Polar Lipids, Inc.*).

For each titration, the lipid stock solution was diluted with Tris buffer to obtain 2.5 mL of a 25 μ M lipid solution in a fluorescence cuvette. The emission spectrum was measured using an Agilent Cary Eclipse fluorescence spectrophotometer (excitation wavelength = 470 nm). Aliquots of the hosts in DMSO (10 mM stock) were added and the emission spectrum was obtained upon each addition. A cuvette stir bar was added to achieve adequate mixing upon each addition. The final addition corresponded to 105-120 μ M hosts and a total volume of 25-30 μ L DMSO. A control experiment where the same volume of neat DMSO was added was also performed. For the spectra, fluorescence intensity was normalized by dividing the fluorescence intensity at every wavelength by the fluorescence intensity at 530 nm prior to the addition of compound (maximum fluorescence).

Where there was a significant change in fluorescence intensity, a Stern-Volmer analysis was performed. F_0/F values, whereby F_0 is the intensity at 530 nm before the addition of host and F is the intensity at 530 nm upon each addition, were plotted against the concentration of host and a linear fit was performed using OriginPro 2018. The titrations were repeated a minimum of 3 times (independent repeats), and the Stern-Volmer constant was calculated for each repeat and subsequently averaged.

5.5.4 Lipid flip-flop assay

To obtain additional evidence for the interaction of the hosts with PE lipids in membranes, we performed lipid flip-flop experiments.⁸² The experiments were performed using DOPC liposomes containing either NBD-PE or NBD-PC in the outer leaflet. To mimic bacterial membranes, we also performed the experiments using 7:3 DOPE:DOPG liposomes containing either NBD-PE or NBD-PC.²¹⁷ However the significant fluorescence quenching of the NBD-labelled lipids by the hosts in PE liposomes led to interference with the flip-flop assay in the case of DOPE:DOPG liposomes.

To prepare the liposomes (100 nm LUVs), aliquots of the appropriate lipid stock solution in chloroform (DOPC or 7:3 DOPE:DOPG) was transferred to a small round bottom flask and dried via rotary evaporation. The lipid film was dried further on high vacuum for at least 5 hours prior to use. The lipid film was hydrated with buffer (5 mM HEPES, 100 mM NaCl, pH 7.4) and vortexed until all the lipid was removed from the round bottom flask. The resulting suspension was subjected to 9 freeze-thaw cycles, alternating between submersion in liquid nitrogen followed by thawing in mildly warm water. The lipid suspension was allowed to rest at room temperature for 30 minutes before extruding 25 times through a 100 nm polycarbonate membrane (*Nucleopore*) using the Avanti mini extruder set (*Avanti Polar Lipids, Inc.*) to create a stock lipid solution.

For the flip-flop assay, the lipid solution was diluted in buffer (5 mM HEPES, 100 mM NaCl, pH 7.4) to achieve 35 mL of 25 μ M lipid in a small glass beaker with stir bar. An ethanol solution of NBD-labelled PE or PC lipid was added to achieve a final concentration of 0.25 μ M NBD-PE or NBD-PC (1 mol%) in the outer leaflet of the membrane (exo lipid).

After 1 minute of stirring, 3 mL of the solution was transferred to measure the initial percentage of *exo* NBD-lipid. To the remaining 32 mL solution was added 32 μ L of a DMSO solution of the host and a timer was started. At certain time intervals, 3 mL of the solution was transferred to a cuvette to determine the percentage of *exo* NBD-labelled lipid. To determine %*exo* NBD-lipid, a 200 s kinetic fluorescence experiment was performed on the 3 mL samples using an Agilent Cary Eclipse fluorescence spectrophotometer (excitation wavelength = 470 nm, emission wavelength = 530 nm). In this kinetic assay, 180 μ L of a dithionite solution (1 M sodium dithionite, 10 mM Tris, pH 10) was added to reduce the nitro group of the NBD-labelled lipid after 50 s, and 180 μ L of 10% Triton X-100 was added to lyse the liposomes after 150 s (complete quenching of fluorescence should occur upon the addition of Triton X-100, because all NBD-labelled lipids should become available for reduction by dithionite). We found that the dithionite solution degraded rapidly and was therefore prepared fresh every hour. The %*exo* NBD-lipid is given by (where F_i is the fluorescence intensity just before the addition of dithionite and F_f is the intensity just before the addition of Triton X-100):

$$\% \textit{exo lipid} = \frac{F_i - F_f}{F_i}$$

The data at each time point was further converted to % lipid flipped, by subtracting the %*exo* lipid at any given time, by the %*exo* lipid at time $t = 0$ min (before addition of host).

5.5.5 Calcein leakage assay

100 nm 1:1 POPE:POPC large unilamellar vesicles (LUVs) were formed by transferring an aliquot of the lipid stock solution in chloroform to a small round bottom flask. A lipid film was formed by removal of the chloroform solvent on a rotary evaporator and dried further on high vacuum for at least 5 hours prior to use. The lipid film was hydrated with the internal solution (70 mM calcein, 150 mM NaCl, 10 mM Tris buffer, pH 7.4) and vortexed until all lipid was removed from the glass walls of the round bottom flask. The resulting suspension was subjected to 9 freeze-thaw cycles, alternating between submersion in liquid nitrogen followed by thawing in mildly warm water. The lipid suspension was allowed to rest at room temperature for 30 minutes before extruding 25 times through a 100 nm polycarbonate membrane (*Nucleopore*) using the Avanti mini extruder set (*Avanti Polar Lipids, Inc.*). The resulting uniform LUVs were separated from the unencapsulated calcein by size exclusion chromatography using a Sephadex column (G-50, medium).

For each measurement, the obtained concentrated stock liposome solution was diluted in external buffer (150 mM NaCl, 10 mM Tris buffer, pH 7.4) to afford 3 mL of a final lipid concentration of 10 μ M in a cuvette. A cuvette stir bar was added and a 14-minute kinetic fluorescence experiment was performed using an Agilent Cary Eclipse fluorescence spectrophotometer (excitation wavelength = 490 nm, emission wavelength = 520 nm). In this kinetic assay, 30 μ L of a 10 mM DMSO stock solution of the host was added after 1.5 min (resulting in a final host concentration of 100 μ M), and 30 μ L of 10% Triton X-100 was added to lyse the liposomes after 11.5 min. The percent calcein release

is given by (where F_0 is the fluorescence intensity before the addition of host ($t = 0$ min), F is the intensity at any given time and F_F is the intensity after the addition of Triton X-100 (final data point)):

$$\% \text{ calcein release} = \frac{F - F_0}{F_F - F_0} \cdot 100\%$$

5.5.6 Anion transport assay

In **Chapter 4**, a standard transmembrane transport study was used to determine if **3.4** exerts antibacterial activity via a transmembrane anion transport mechanism.²¹⁵ 100 nm liposomes (7:3 EggPC:cholesterol) were formed by transferring an aliquot of a lipid stock solution in chloroform to a small round bottom flask, followed by drying via rotary evaporation. The lipid film was dried further on high vacuum for at least 5 hours prior to use. The lipid film was hydrated with the internal solution (1 mM lucigenin, 222 mM NaNO₃, 10 mM HEPES buffer at pH 7.4) and vortexed for about 5 minutes. The resulting suspension was subjected to seven freeze-thaw cycles, alternating between submersion in liquid nitrogen followed by thawing in mildly warm water. The lipid suspension was allowed to rest at room temperature for 30 minutes before extruding 27 times through a 100 nm polycarbonate membrane (*Nucleopore*) using the Avanti mini extruder set (*Avanti Polar Lipids, Inc.*). The resulting uniform large unilamellar vesicles (LUVs) were separated from the unencapsulated lucigenin by size exclusion chromatography using a Sephadex column (G-50, medium), and diluted in external buffer (222 mM NaNO₃, 10 mM HEPES buffer at pH 7.4) to achieve a final lipid concentration of 0.5 mM lipid.

To start the anion transport experiment, the lucigenin-loaded liposomes (0.5 mM lipid) were transferred to a 3 mL fluorescence cuvette and a small cuvette stir bar was added. The cuvette was placed in the fluorometer and stirring was started at maximum speed (stirring continued throughout the experiment). 10 Seconds before the start of the kinetic run, 7.5 μ L DMF or a DMF stock solution of compound **3.4** was added to the liposomes to achieve a final concentration of **3.4** of 5 mol% with respect to total lipid concentration. At time $t = 0$ s, the kinetic run was started by the addition of 75 μ L NaCl solution to achieve a final concentration of 25 mM NaCl, and the fluorescence intensity at 505 nm (excitation 430 nm) was measured for 400 s. At time $t = 320$ s, detergent (75 μ L of 10% Triton X-100) was added to fully lyse the membrane and estimate the quality of the liposomes. The obtained kinetic run was subsequently converted to 'normalized F_0/F ', using the following equation (where F is the fluorescence intensity at any time, F_{final} is the fluorescence intensity after adding Triton X-100, and F_0 is the fluorescence intensity at time $t = 0$ s:

$$\text{Normalized } \frac{F_0}{F} = \frac{\frac{F_0}{F} - \frac{F_0}{F_0}}{\frac{F_0}{F_{final}} - \frac{F_0}{F_0}} = \frac{\frac{F_0}{F} - 1}{\frac{F_0}{F_{final}} - 1}$$

The calculation is valid because of the linear correlation between lucigenin quenching (F_0/F) and NaCl concentration. By taking the value upon addition of Triton X-100 (F_{final}) as a reference point, the data is normalized and the error between experiments is reduced. By subtracting 1 in the formula, we ensure that values start at 0 and reach a maximum value of 1. The 'normalized F_0/F ' data of 2 independent experiments conducted with 2 different sets of liposomes was averaged and the standard deviations were calculated.

5.6 Hemolysis

Hemolysis can determine if a potential antibiotic will cause lysis of human erythrocytes. The EC₅₀ value represents the concentration of a drug that causes 50% hemolysis. We calculated the EC₅₀ for compounds **3.1** and **3.4** cells based on a previous study designed for antimicrobial peptides.¹⁹⁶ To begin, Single donor human blood cells were washed twice and diluted to 2.5 x 10⁷ cells/mL in a solution of 4% DMSO in PBS buffer (1x). Compounds were added in various concentrations from serial dilutions (100-400 μM) of DMSO stocks (25 μM) based on MIC values. Duramycin was tested at lower concentrations (0.001-10 μM) to compare the antimicrobial peptide to the compounds. Triton X-100 (1%) was used as a positive control and 4% DMSO PBS buffer was used as a negative control. The plates were sealed with a protective film to prevent evaporation and incubated for 1 hour at 37°C. After incubation, the 96 well plates were centrifuged at 3900 rpm for 5 min. 50 μL of each well's supernatant was then carefully transferred to a new 96 well plate, which was then centrifuged to remove any bubbles. The absorbance of the supernatant was measured at 414 nm. The percent of hemolysis was calculated by:

$$\% \text{ Hemolysis} = \frac{\text{Abs}(\text{Sample}) - \text{Abs}(\text{Neg})}{\text{Abs}(\text{Pos}) - \text{Abs}(\text{Neg})} \times 100$$

Where Abs(Sample) is each sample's absorption at 414 nm, Abs(Neg) is the negative control's average absorbance at 414 nm, and Abs(Pos) is the positive control's average absorption at 414 nm. The % hemolysis values were input into OriginPro 2018b (b9.5.5.409 (Academic)) and fitted with the DoseResp model with the maximum value set at 100% to determine HC50 from the inflection point.¹⁹⁶

5.7 Bacterial Assays

5.7.1 Minimum Inhibitory Concentration (MIC) studies

The minimum inhibitory concentration (MIC) against different bacteria was determined using the broth microdilution method recommended by the Clinical and Laboratory Standards Institute.²¹⁸ Bacterial strains (*B. cereus* (ATCC 117781), *B. subtilis* (ATCC 6051), *S. aureus* (ATCC 25923), *E. faecalis* (ATCC 29242), *E. coli* (ATCC 25922), and *P. aeruginosa* (ATCC 27853) were obtained from the American Type Culture Collection and stored in glycerol stocks at -80 °C. For each experiment, a small amount of the glycerol stock was streaked onto a Müller-Hinton agar plate (Sigma-Aldrich #70191) and the agar plate was incubated for 18-24 hours at 35 °C. The obtained colonies were aseptically transferred into sterile cation-adjusted Müller-Hinton broth (Sigma-Aldrich #90922) and vortex briefly. Colonies were added until the inoculum solution achieved an OD₆₀₀ value corresponding to 1 x 10⁸ CFU/mL. OD₆₀₀ values were determined using a Biowave CO8000 Cell Density meter and 17x100 mm polystyrene culture tubes (VWR #60818-703). The inoculum was subsequently diluted to 5 x 10⁵ CFU/mL in sterile cation-adjusted Müller-Hinton broth.

In **Chapter 3**, compounds were dissolved in DMSO for solubility reasons. In each experiment a solvent control and bacterial viability control (known antibiotic) were run along with the other treatments. Compounds and controls (8 µL) were added to a non-tissue culture treated 96-well plate (Falcon #351172) followed by 192 µL of the bacteria inoculum so that the final concentration of DMSO did not exceed 4% v/v. Finally, the 96-well plate was covered with a Breathe-Easy sealing membrane (Sigma-Aldrich # Z380059)

before incubation. The optical density at 600 nm (OD_{600}) was subsequently measured for 24 hours using a BioTek Cytation 5 Cell Imaging Multi-Mode Reader (35 °C, absorbance measurement at 600 nm, orbital shaking (shaking every 10 minutes, for 1 min at 548 rpm (2 mm))). The MIC value was defined as the minimum concentration of compound that resulted in complete inhibition of bacterial growth over the full 24 hours. We also tried to obtain an MIC value against *B. cereus* for the known PE-binding antibiotic duramycin, but faced problems with repeatability.^{219 100} For all concentrations investigated, duramycin caused a delay in bacterial growth. However, full inhibition of bacterial growth was only seen for most repeats at 32 μ M and 64 μ M and all repeats at 128 μ M duramycin.

In **Chapter 4**, the MIC values of compounds **4.1-4.10** and six known antibiotics were optimized for *B. subtilis* in cation-adjusted Müller Hinton broth (MH2). Antibiotics were dissolved in DMSO (rifampicin (Alfa Aesar #J60836-03), calcimycin (Sigma-Aldrich #21186) vancomycin (Sigma-Aldrich #1709007)), or MH2 (phosphomycin (Sigma-Aldrich #P5396), gentamicin (Sigma-Aldrich #G1264), Bactrim). Compounds and controls (8 μ L) were added to a non-tissue culture treated 96-well plate (Falcon #351172) followed by 192 μ L of the bacteria inoculum so that the final concentration of DMSO did not exceed 4% v/v. Finally, the 96-well plate was covered with a Breathe-Easy sealing membrane (Sigma-Aldrich # Z380059) and incubated for 24 h at 35 °C without shaking. The MIC was determined visually after 24 h in the incubator. The lack of bacterial growth could be seen by the clarity of the well and clindamycin controls were used as a reference.

5.7.2 Bactericidal activity assay

The minimum bactericidal concentration (MBC) was determined using the method suggested by the Clinical and Laboratory Standards Institute. In brief, at the end of the MIC determination (see previous section), 100 μ L of the *B. cereus* culture obtained after 24 h incubation with various concentrations of compound **3.1** was streaked onto a Müller-Hinton agar plate (Sigma-Aldrich #70191) and the agar plate was incubated for 18-24 hours at 35 °C. The colonies were counted to determine the final CFU/mL after 24 h incubation. This final CFU/mL was compared with the initial CFU/mL at the start of the 24 h incubation (typically 5×10^5 CFU/mL, but this was determined experimentally each time) to calculate the percentage of bacteria that were killed. Bactericidal activity is defined as the ability to kill 99.9% of bacteria.

5.7.3 Imaging studies in Chapter 2

To investigate morphological changes in *B. cereus* induced by compounds **3.1**, we performed live imaging and Gram staining. For the live imaging, 10 μ L of the *B. cereus* cultures obtained by 24 h incubation with various concentrations of compounds **3.1-3.4** and **18C6** was transferred to a 96-well plate with glass bottom suitable for microscopy (Greiner Bio-one #655892) and diluted with 90 μ L Müller-Hinton broth. The 96-well plate was subsequently centrifuged for 1 minute at 3000 rpm using an Eppendorf Centrifuge 5810 to ensure that all bacteria are in a single optical plane at the bottom of the 96-well plate. The bacteria were then imaged using a BioTek Cytation 5 Cell Imaging Multi-Mode Reader (40x or 60x objective, Brightfield).

For the Gram-staining, 5 μ L of the *B. cereus* culture obtained by 24 h incubation with various concentrations of compounds **3.1-3.4** and **18C6** was transferred onto a Polysine microscope adhesion slide (ThermoScientific #P4981-001) and stained using a Gram stain kit (Fischer Scientific #ES800). The slides were subsequently visualized using a BioTek Cytation 5 Cell Imaging Multi-Mode Reader (40x or 60x objective, Brightfield) or an Amscope Quintuple Plan Infinity Kohler Laboratory Trinocular Compound Microscope (100x oil objective, Brightfield).

5.7.4 Membrane depolarization assay

A membrane depolarization assay was performed using the dye Disc₃(5) (3,3'-dipropylthiadicarbocyanine iodide), according to the method by te Winkel *et al.*¹⁶⁷ optimized for *B. cereus*. The MIC values for the negative control clindamycin (1 μ g/mL) and positive control gramicidin (1.25 μ M) against *B. cereus* were initially determined, as described above for the other compounds.

For each experiment, a small amount of the *B. cereus* glycerol stock was streaked onto a Müller-Hinton agar plate (Sigma-Aldrich #70191) and the agar plate was incubated for 18-24 hours at 35 °C. The obtained colonies were aseptically transferred into sterile cation-adjusted Müller-Hinton broth (Sigma-Aldrich #90922) and diluted to OD₆₀₀ = 0.1. The bacteria were subsequently incubated at 35 °C until they reached mid-logarithmic phase (typically OD₆₀₀ = 0.5-0.6). The cultures were then centrifuged at 3000 rpm for 5 mins and the pellets were re-suspended and diluted in Müller-Hinton broth supplemented with 0.5 mg/mL BSA (bovine serum albumin) to OD₆₀₀ = 0.1.

For the measurements at 1xMIC and 1.6xMIC, 172 μL of the diluted cells were transferred to a fluorescence 96-well plate (sterile, black, flat-bottom, polystyrene microplate from Brand #7816668) and the fluorescence intensity was followed for 3 minutes to obtain values for background fluorescence. After obtaining a baseline, 8 μL DiSC₃(5) dissolved in DMSO was added to each well to a final concentration of 1 μM DiSC₃(5) and 4% DMSO, and the fluorescence intensity was measured for another 15 minutes. At this point, 20 μL of stock solutions of **3.1** and control antibiotics (dissolved to 10x the desired concentration in Müller-Hinton broth with 4% DMSO) were added and the fluorescence was measured for 1 hour. All fluorescence measurements were performed using a BioTek Cytation 5 Cell Imaging Multi-Mode Reader (35 °C, excitation at 610 nm and emission at 660 nm, time intervals of 23 seconds, orbital shaking (5 seconds at 548 rpm (2 mm) before each measurement). As a control, the measurements were also conducted on Müller-Hinton broth supplemented with 0.5 mg/mL BSA (bovine serum albumin) that did not contain any bacteria.

For the measurements at 10xMIC, the procedure was altered due to the limited solubility of the crown ether compounds. In this case, 193 μL of the diluted cells were transferred to a fluorescence 96-well plate (sterile, black, flat-bottom, polystyrene microplate from Brand #7816668) and the fluorescence was followed for 3 minutes to obtain values for background fluorescence. After obtaining a baseline, 2 μL DiSC₃(5) dissolved in DMSO was added to each well to a final concentration of 1 μM DiSC₃(5) and 1% DMSO, and the fluorescence intensity was measured for another 15 minutes. At this point, 5 μL of stock DMSO solutions of **3.1** and control antibiotics were added and the

fluorescence was measured for 1 hour. All fluorescence measurements were performed using a BioTek Cytation 5 Cell Imaging Multi-Mode Reader (35 °C, excitation at 610 nm and emission at 660 nm, time intervals of 23 seconds, orbital shaking (5 seconds at 548 rpm (2 mm) before each measurement). As a control, the measurements were also conducted on Müller-Hinton broth supplemented with 0.5 mg/mL BSA (bovine serum albumin) that did not contain any bacteria.

To convert the raw fluorescence data to fraction of Disc₃(5) released, we used the fact that Disc₃(5) accumulates into polarized cells and self-quenches. Therefore, the highest possible fluorescence that can be measured, should correspond to the values obtained for the control experiments without bacteria. In these control experiment, the procedure described above (3 minutes background fluorescence, followed by addition of Disc₃(5), followed by the addition of compound) was repeated using Müller-Hinton broth supplemented with 0.5 mg/mL BSA (bovine serum albumin) that did not contain any bacteria. By calculating the fraction Disc₃(5) release this way, any potential artifacts due to differences in DMSO content, slow stirring or other interferences can be removed. Full depolarization should correspond to a fraction Disc₃(5) release of 1.0, as is seen for the positive control gramicidin.

$$\text{fraction Disc}_3(5) \text{ release} = \frac{\text{Fluorescence intensity in the presence of } B. \text{cereus}}{\text{Fluorescence intensity in the absence of } B. \text{cereus}}$$

For imaging of cell depolarization, the membrane depolarization assay described above was stopped after 15 minutes or 1 hour, and 2 µL of the bacterial solution was transferred to a microscopy cover glass and a 1% agarose gel was put on top of the solution to immobilize the bacteria. Images were taken using a BioTek Cytation 5 Cell

Imaging Multi-Mode Reader, with the Texas Red filter set for fluorescence images. All fluorescence images were taken using the same exposure settings (LED intensity = 7, Shutter Speed MS = 1206, Camera Gain = 18). Overlays were generated using the software accompanying the BioTek Cytation 5 Cell Imaging Multi-Mode Reader.

5.7.5 BCP image collection

A high-throughput screening method was adopted to determine the mechanism of action of the unknown antibiotic.¹⁷⁶ First, a black 96-well plates with a 0.17 mm glass bottom (Cellvis) was coated with 50 μ L of 0.025 μ g/mL Vitronectin XFTM (Stem Cell Technologies #100-0763) diluted in CellAdhereTM dilution buffer (Stem Cell Technologies #07183). The plates were incubated for 1 hour at 35 °C and used within 48 h of coating (kept in the fridge if not used immediately). Directly before the assay, plates were brought to room temperature and aspirated with 50 μ L of CellAdhereTM dilution buffer by creating air bubbles in the well with the pipette before removing visible liquid.

B. subtilis (ATCC 6051) was grown in 10 mL sterile cation-adjusted Müller-Hinton broth (MH2) in polystyrene culture tubes (VWR #60818-703). *B. subtilis* was grown to exponential phase ($OD_{600} = 0.2$) and diluted 1:100 before grown to an early exponential phase ($OD_{600} = 0.15-0.19$) and used in experiments. Then 192 μ L of bacteria was added to 8 μ L of antibiotic diluted in DMSO or MH2 according to the procedure outlined in MIC studies. Plates were covered with a lid and incubated at 35 °C for 2 hours without shaking. After incubation, 150 μ L of the bacteria suspension was removed from the wells and the plates were centrifuged for 30 s at 3000 rpm. To fix cells, 100 μ L of 4% paraformaldehyde

in PBS buffer (Alpha Aesar #J60836-03) was added to the plates and incubated at room temperature for 30 minutes. The solution was removed carefully using a 100 μ L pipette. PBS (50 μ L) was added to wash the solution and removed with a 100 μ L pipette. Next, 50 μ L of dye mix (5 μ g/mL DAPI (Sigma-Aldrich #D9542), 2.5 μ M Sytox Green (Fisher Scientific #S7020), 10 μ g/mL FM4-64 (Fisher Scientific # T13320) in Hank's Balanced Salt Solution ([HBSS], Fisher Scientific #14175079) was added to each well and incubated for 45 minutes in the dark at 25 °C. Next, the 96-well plate was centrifuged at 3000 rpm for 30 s before washing with 50 μ L of PBS. The PBS wash and remaining dye solution was removed with a 100 μ L pipette so that no liquid remained. Plates were analyzed within 12 hours on an inverted Nikon Eclipse Ti A1 confocal microscope equipped with a 40x/0.95 oil objective and 96-well plate adapter. Experiments were done in triplicate with at least 50 cells analyzed per well for each treatment. The DAPI, Sytox Green, and FM4-64 dyes were imaged using DAPI, FITC, and Cy5 channels, respectively. The maximum intensity for the FITC channel was set by analyzing the intensity of nisin treated cells after a 10-minute incubation period and kept constant in all biological repeats. The maximum intensity of DAPI was determined by the DMSO or MH2 controls, and the Cy5 channel varied for each sample. Metadata containing complete information on the microscope's parameters is included in **Appendix C**.

5.7.6 BCP CellProfiler analysis

Confocal images were processed using CellProfiler™ (v4.2.1) without further image manipulation. CellProfiler™ is a machine learning software for the identification and measurement of cells and nuclei/nucleoids for image analysis.¹⁹⁴ Object selection was

performed on each channel independently. Images were cropped, enhanced, and segmented within the software before analysis. Images were cropped based on the FM4-64 channel since these had the most background noise. Cropping was done using the “Crop” module and DAPI and Sytox Green (SG) stained cells were cropped according to the FM4-64-stained image. Image enhancement allowed for automatic background subtraction and brightness adjustment using speckle enhancement in the “EnhanceOrSuppressFeatures” module. Intensity measurements for DAPI and Sytox Green stained cells were taken from images prior to any enhancement.

Next, thresholding was used to create a binary image to identify individual cells and “declump” touching objects. The “IdentifyPrimaryObject” module for each channel was set to global Otsu three class thresholding with a smoothing scale of $\sigma = 1$. The expected size of the objects was set to 2-25 px for DAPI and Sytox Green stained images and 6-60 px for FM4-46 membrane outlines. Clumped objects were separated by intensity. Most images had large amounts of bacteria chaining together or clumped side-by-side. The “DisplayObjectonImage” module generates object numbers on the raw image so that any extreme outliers could be investigated later. Measurements were generated using the “MeasureObjectSizeShape” or “MeasureIntensity” module. Many measurements from CellProfiler are generated as pixel (px) values. These values were converted to μm based on metadata from the microscope (1 px = 0.24 μm). A full description of the parameters is listed in **Chapter 4** and **Appendix C**.

5.7.7 BCP statistical analysis

CellProfiler data was exported to Excel (Version 16.60 for Mac) and any extreme outliers were removed before further processing. The data was analyzed via linear discriminant analysis (LDA) using the Addinsoft XLSTAT 2022.2.1 plugin (Student Version) in Microsoft Excel 16.60 for Mac. LDA allows for supervised training of the dataset by using “explanatory variables” to classify the antibiotics into a known MOA group. This was done by grouping the known and unknown antibiotics into six groups: CW, PS, RNA, FS, MEM, and UNK. Classification of each antibiotic to the proper MOA group was validated by a randomly generated training dataset. A confusion matrix for the training sample showed an overall 79.74% success rate of accurately assigning the antibiotic to its proper class (**Chapter 4** and **Appendix C**).

The threshold for component selection was set for 95% variation, which yielded six different axis, or “factors” (F1-F6) for each variable (cell measurement). To eliminate irrelevant data, a unidimensional test of equality was used for dimensionality reduction. Any variable with a p value <0.0001 was deemed statistically significant and others were discarded. Further calculations used F1-F4 (92% of total variation). In some cases where there were more DAPI than SG or FM4-64-stained cells, XLSTAT used the median or mode in place of missing data for the measurement. For intensity measurements of DAPI and SG-stained cells, a zero was used to show the lack of cells instead. Confidence ellipses correspond to a 95% confidence interval using the same mean values and covariance matrix as the factor scores. The dendrogram was generated based on Euclidian distance of dissimilarities using Ward’s method using Origin Labs (OriginPro 2022).

APPENDIX A

SUPPLEMENTARY INFORMATION FOR CHAPTER 2

A.1 ^1H NMR and ^{13}C NMR spectra of novel compounds

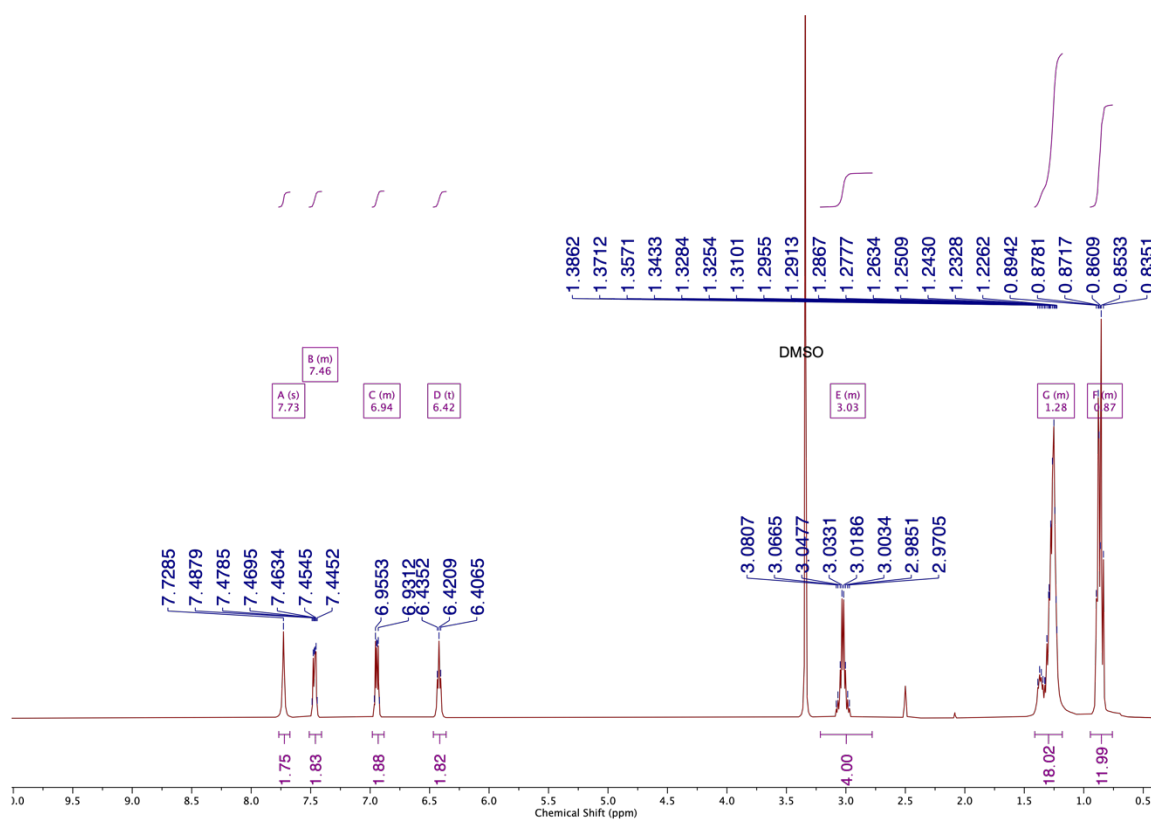


Figure A.1: ^1H NMR (300 MHz) spectrum of compound 2.1 in DMSO- d_6 at 298 K.

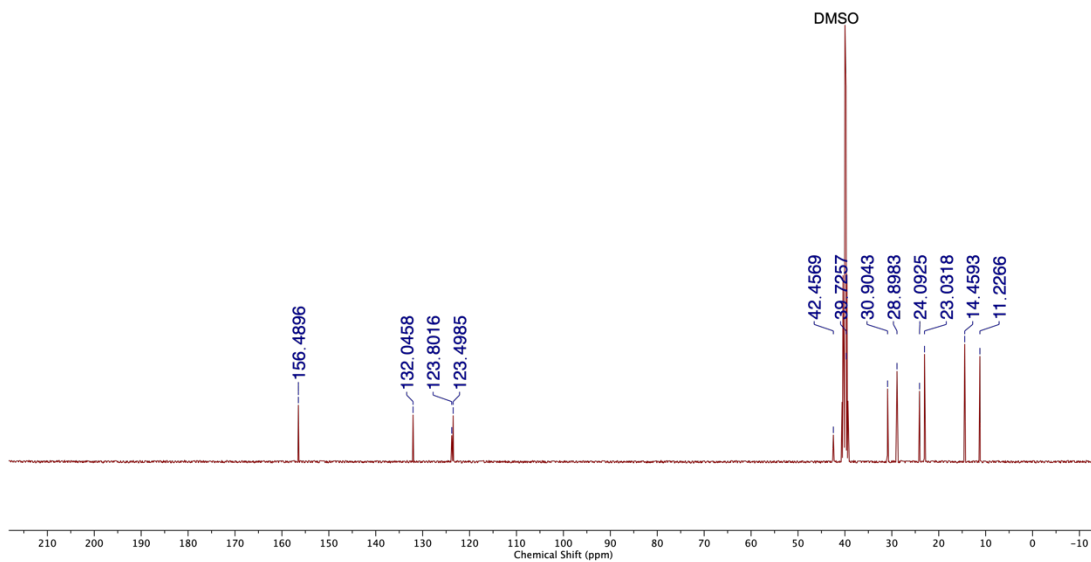


Figure A.2: ^{13}C NMR (101 MHz) spectrum of compound **2.1** in $\text{DMSO-}d_6$ at 298 K.

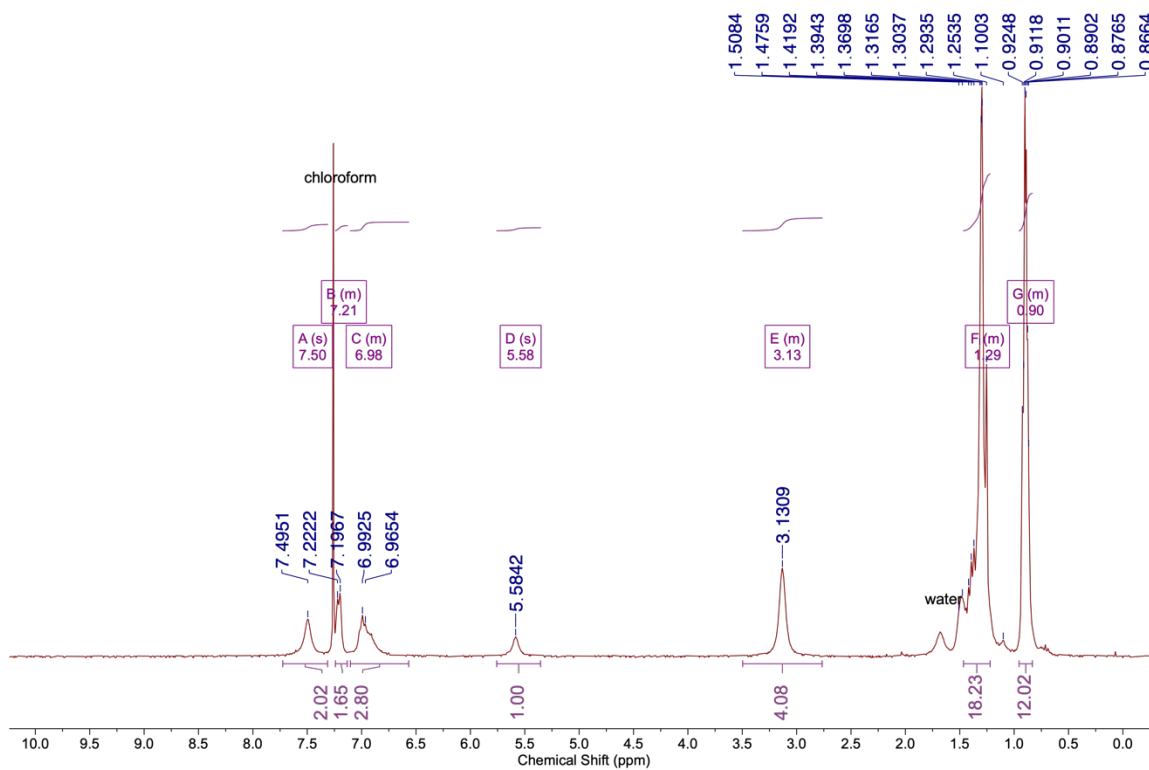


Figure A.3: ^1H NMR (300 MHz) spectrum of compound **2.2** in CDCl_3 at 298 K.

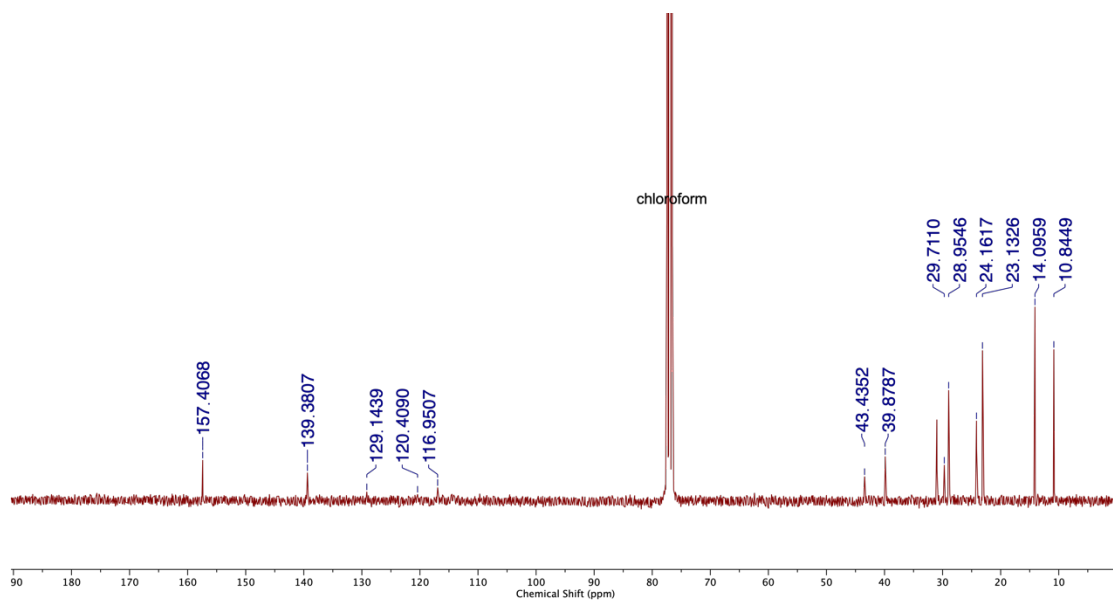


Figure A.4: ^{13}C NMR (101 MHz) spectrum of compound **2.2** in CDCl_3 at 298 K.

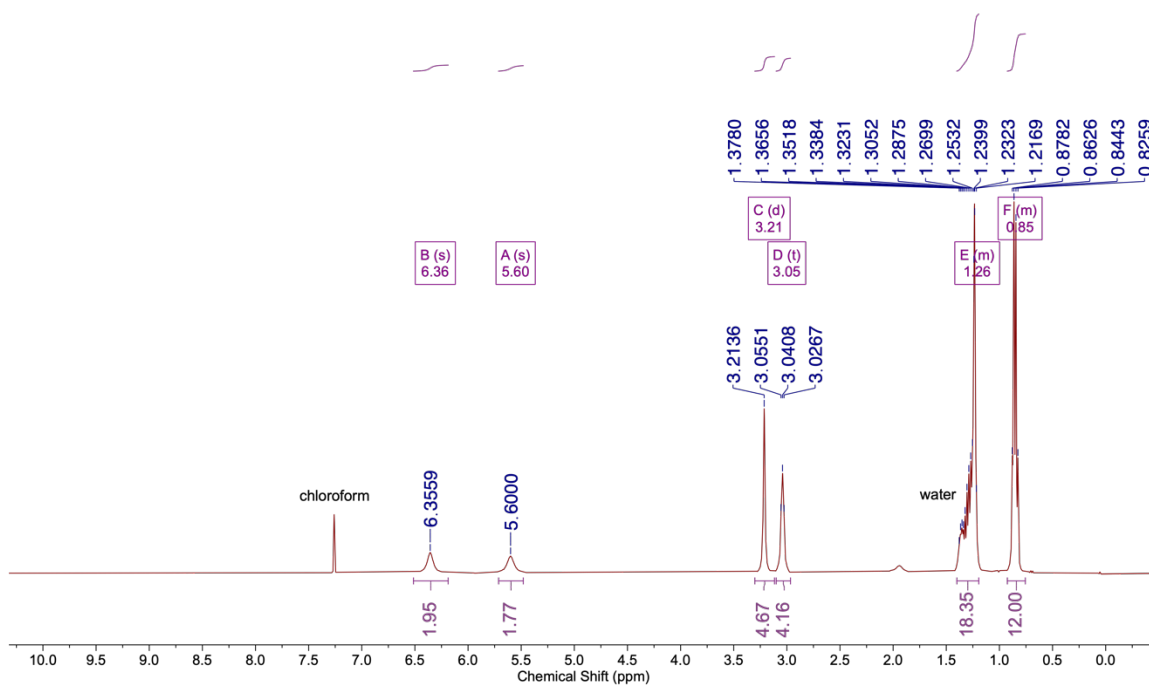


Figure A.5: ^1H NMR (300 MHz) spectrum of compound **2.3** in CDCl_3 at 298 K.

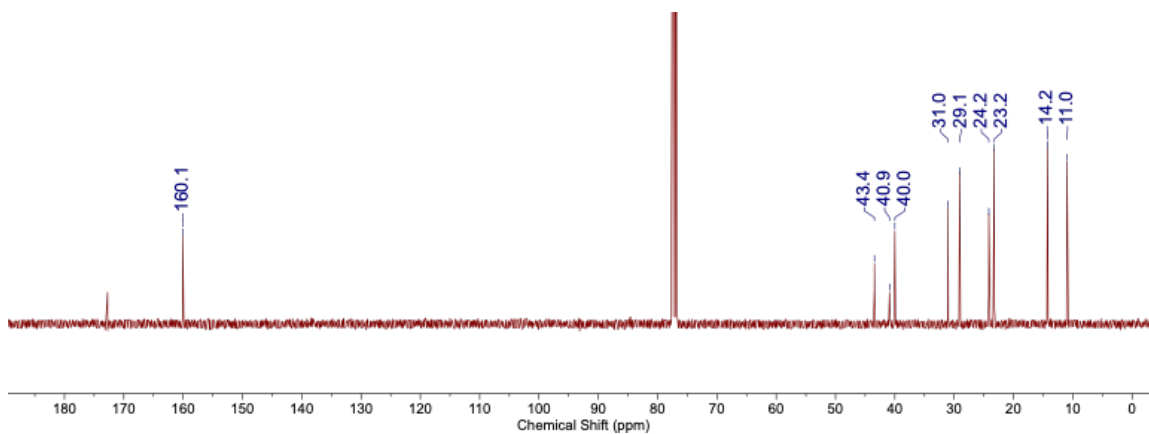


Figure A.6: ^{13}C NMR (101 MHz) spectrum of compound **2.3** in CDCl_3 at 298K.

A.2 ^1H NMR titrations

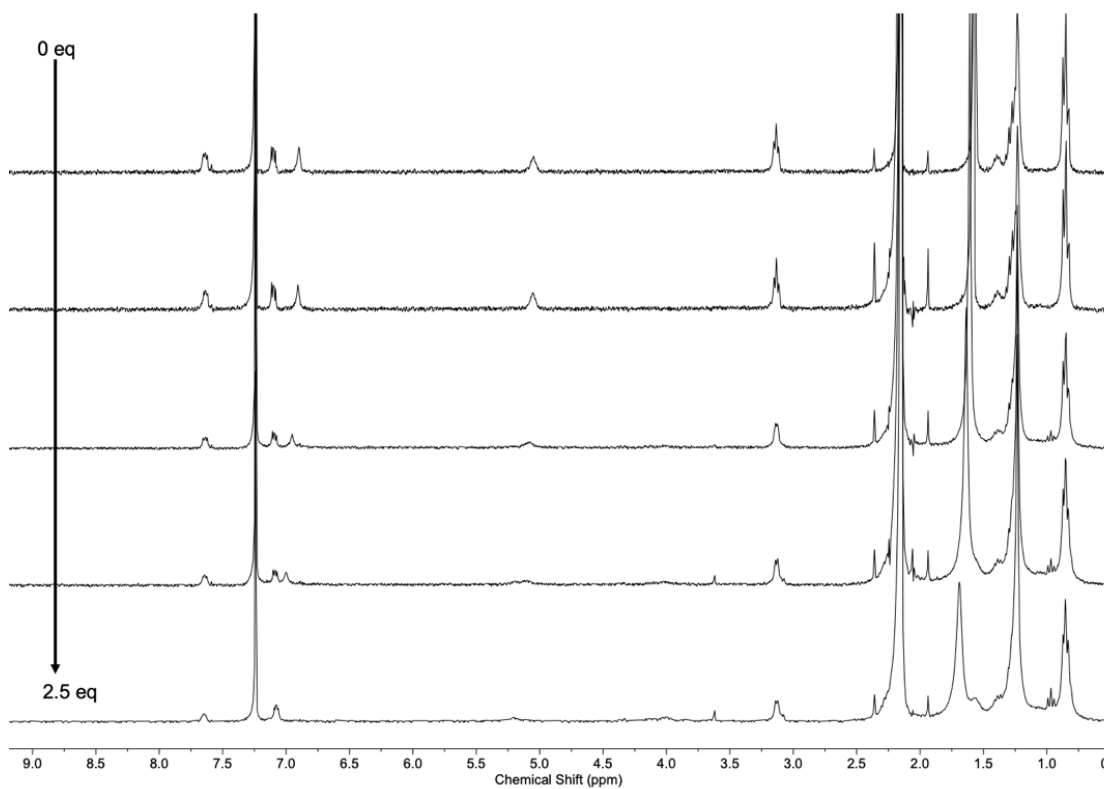


Figure A.7: ^1H NMR titration of **2.1** with CDL-TBA_2 in 0.5% Milli-Q H_2O :99.5% DMSO-d_6 at 298 K. No measurable binding was observed from urea NHs at $\delta_A = 7.64$ ppm and $\delta_B = 5.05$ ppm.

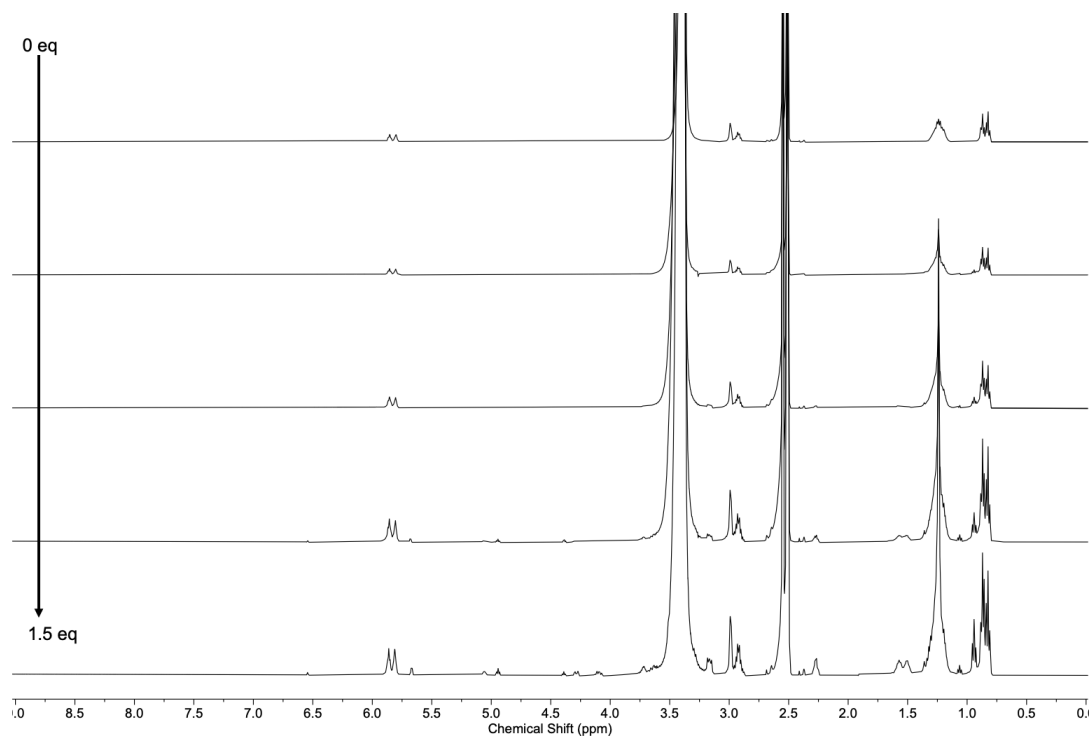


Figure A.8: ^1H NMR titration of **2.3** with CDL-TBA₂ in 0.5% Milli-Q H₂O:99.5% DMSO-d₆ at 298 K. No measurable binding was observed from urea NHs at $\delta_A = 5.85$ ppm and $\delta_B = 5.80$ ppm.

APPENDIX B

SUPPLEMENTARY INFORMATION FOR CHAPTER 3

B.1 ^1H NMR and ^{13}C NMR spectra of novel compounds

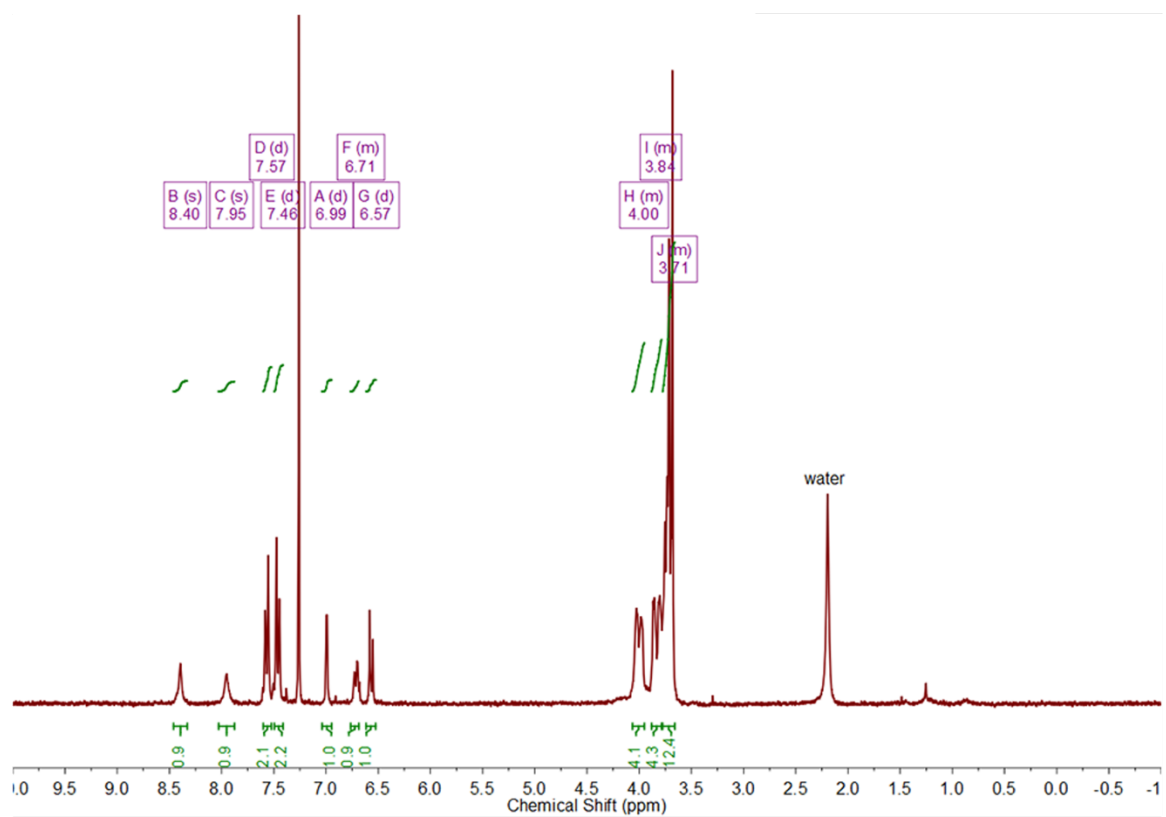


Figure B.1: ^1H NMR (300 MHz) spectrum of compound **3.1** in CDCl_3 at 298 K.

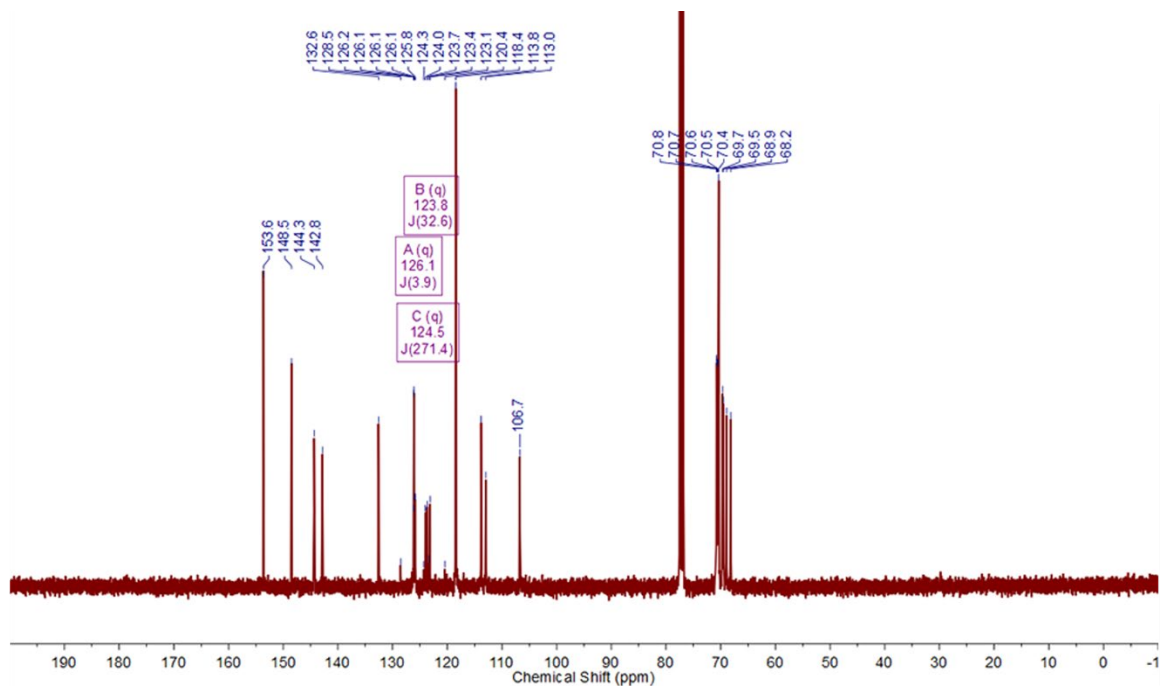


Figure B.2: ^{13}C NMR (101 MHz) spectrum of compound **3.1** in CDCl_3 at 298 K.

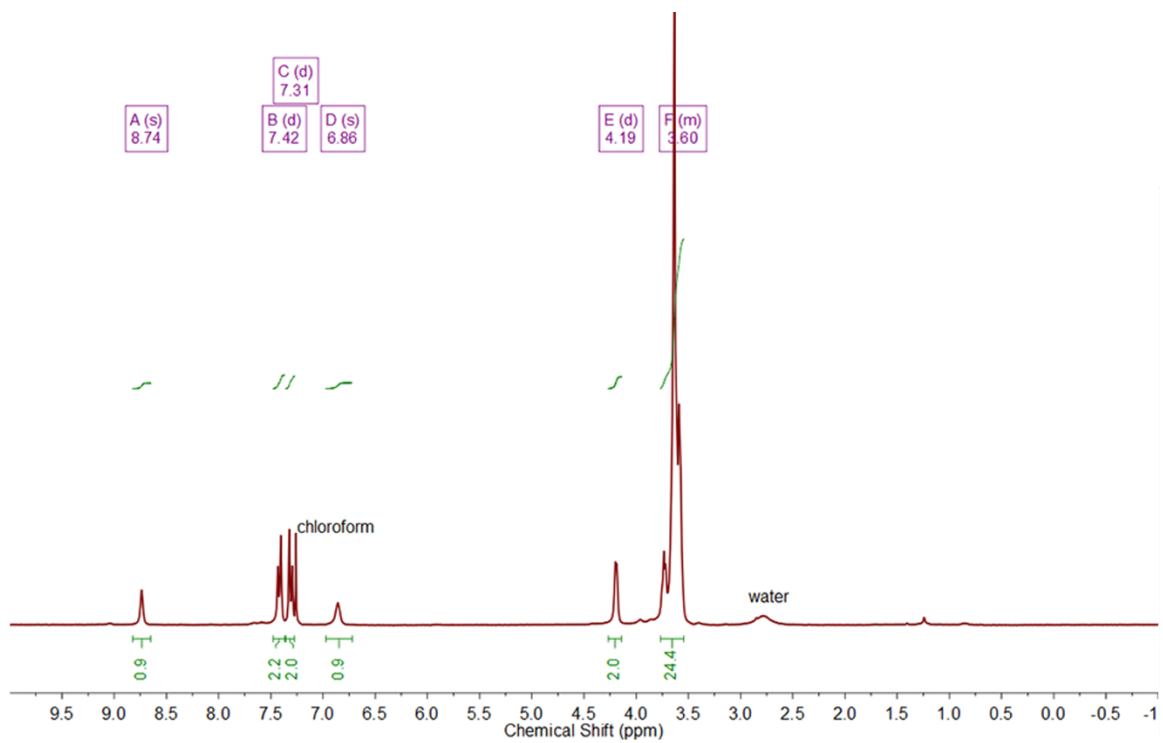


Figure B.3: ^1H NMR (300 MHz) spectrum of compound **3.1** in CDCl_3 at 298 K.

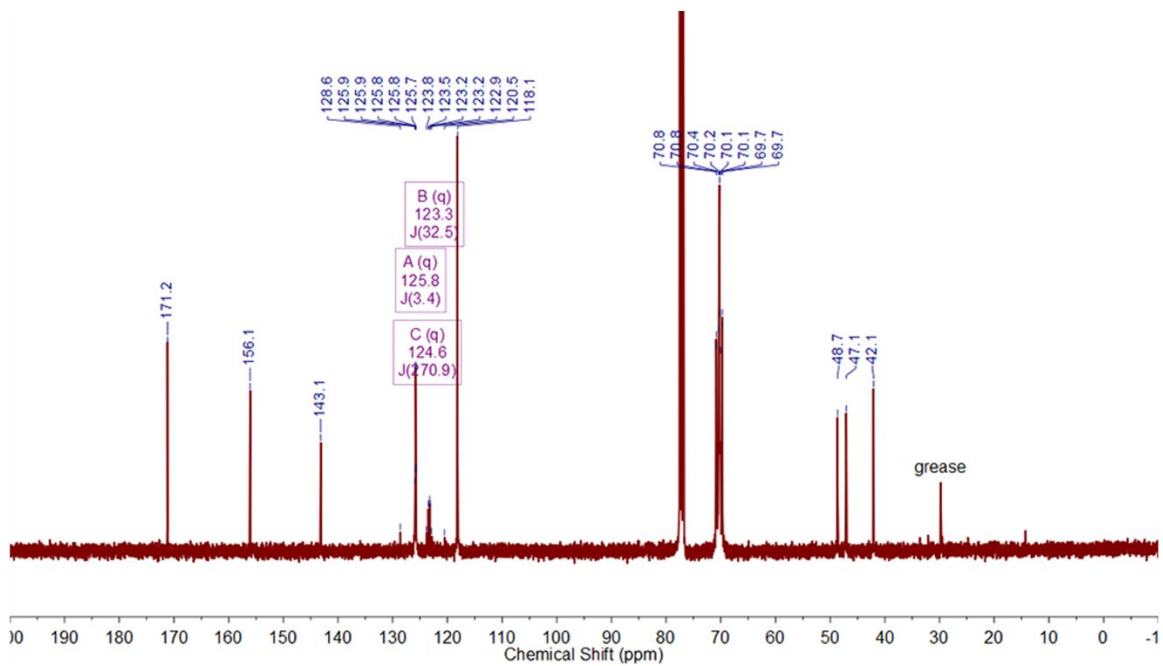


Figure B.4: ^{13}C NMR (101 MHz) spectrum of compound **3.2** in CDCl_3 at 298 K.

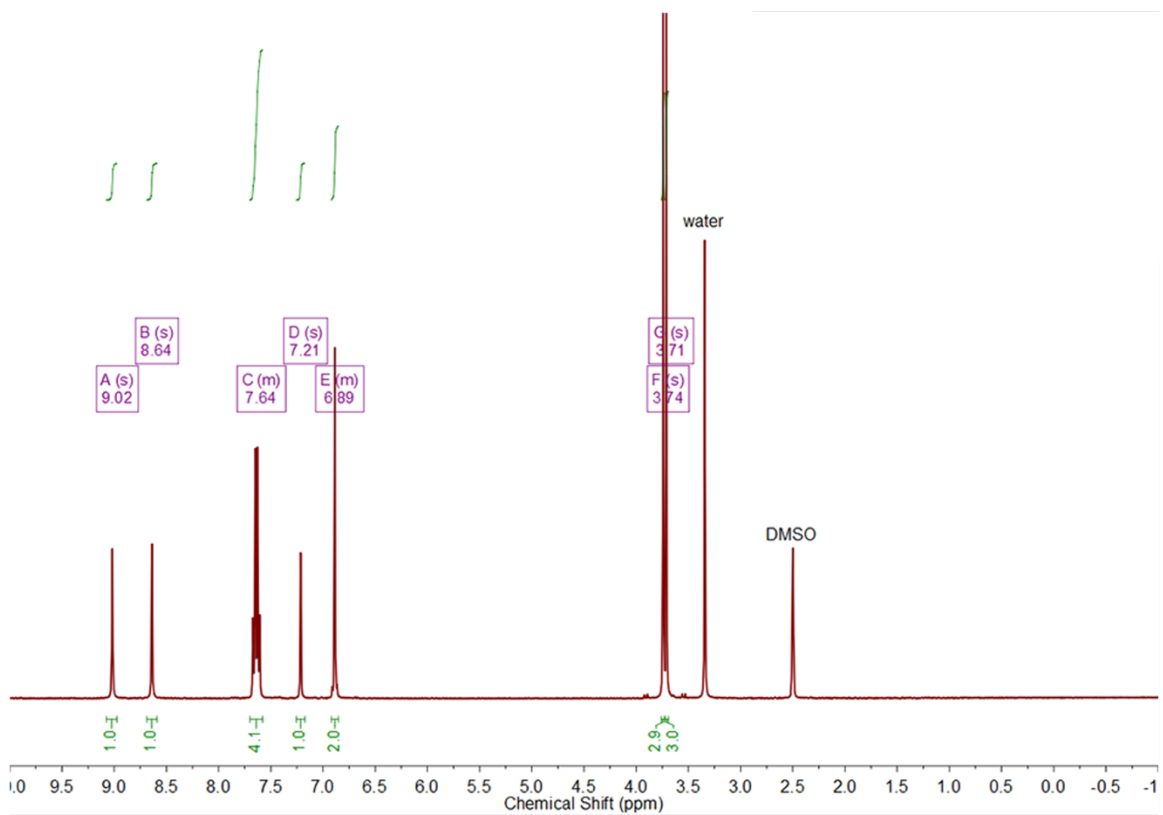


Figure B.5 ^1H NMR (400 MHz) spectrum of compound **3.3** in $\text{DMSO}-d_6$ at 298 K.

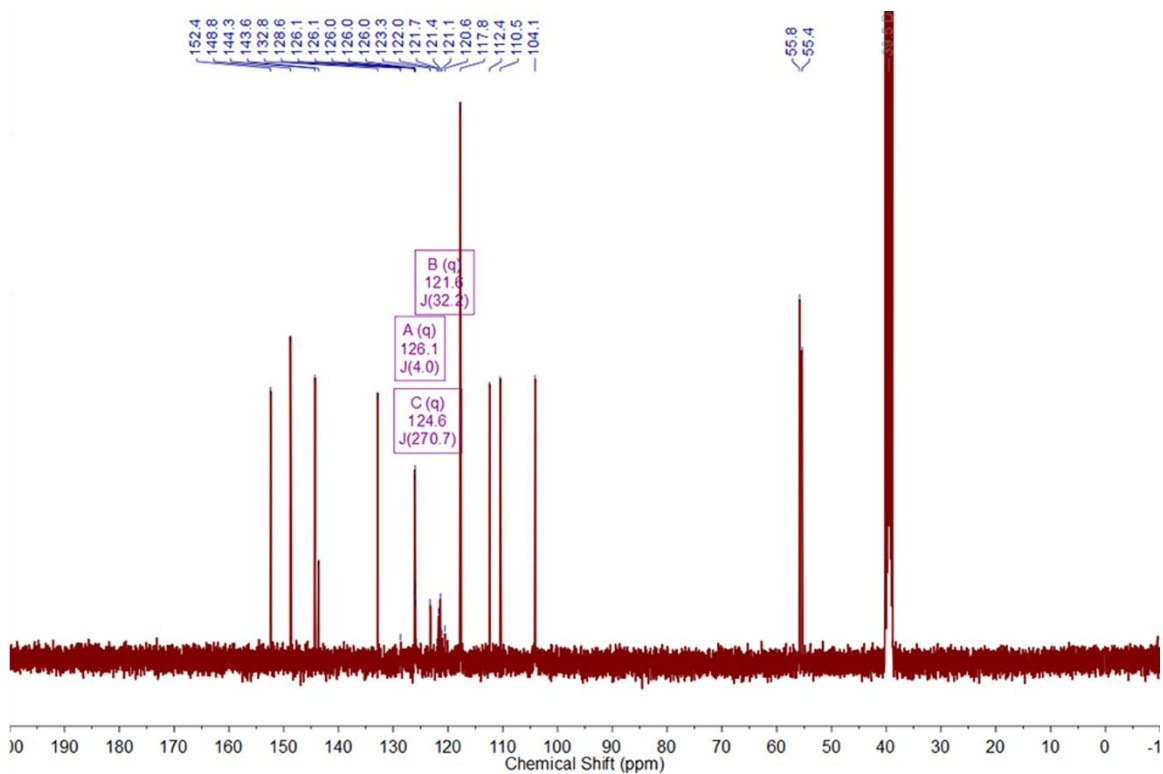


Figure B.6: ^{13}C NMR (101 MHz) spectrum of compound **3.3** in $\text{DMSO-}d_6$ at 298 K.

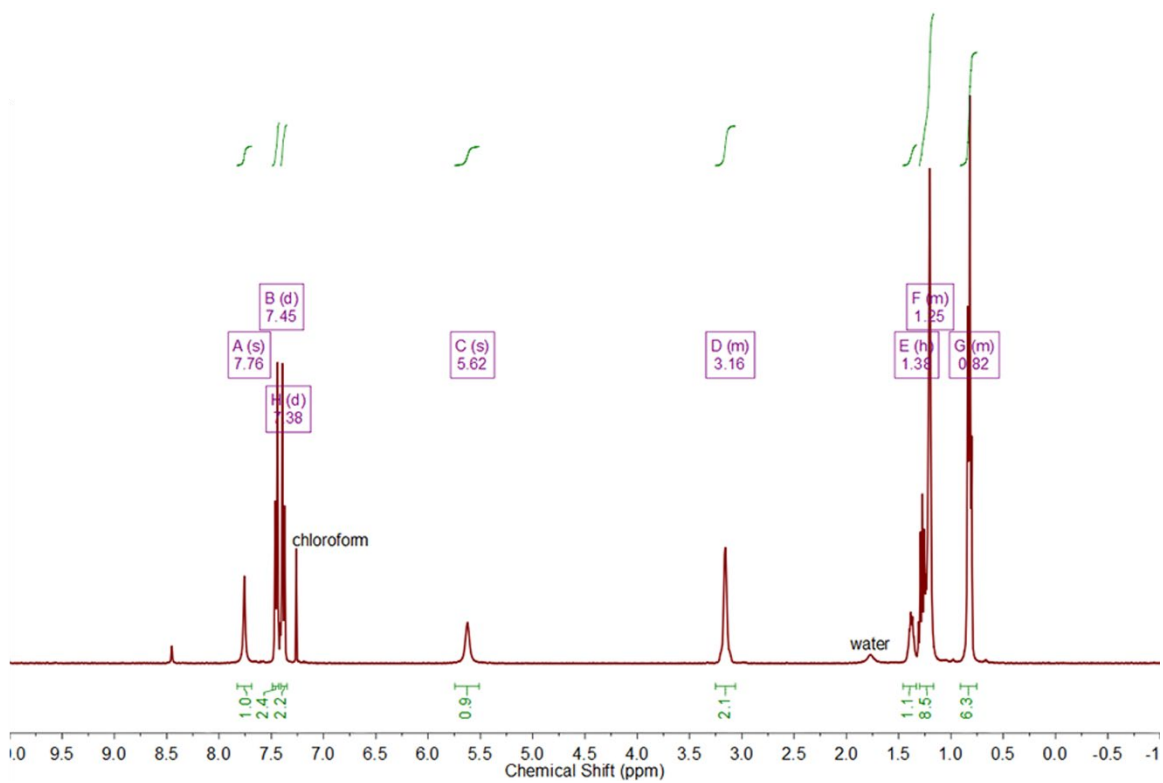


Figure B.7: ^1H NMR (300 MHz) spectrum of compound **3.4** in CDCl_3 at 298 K.

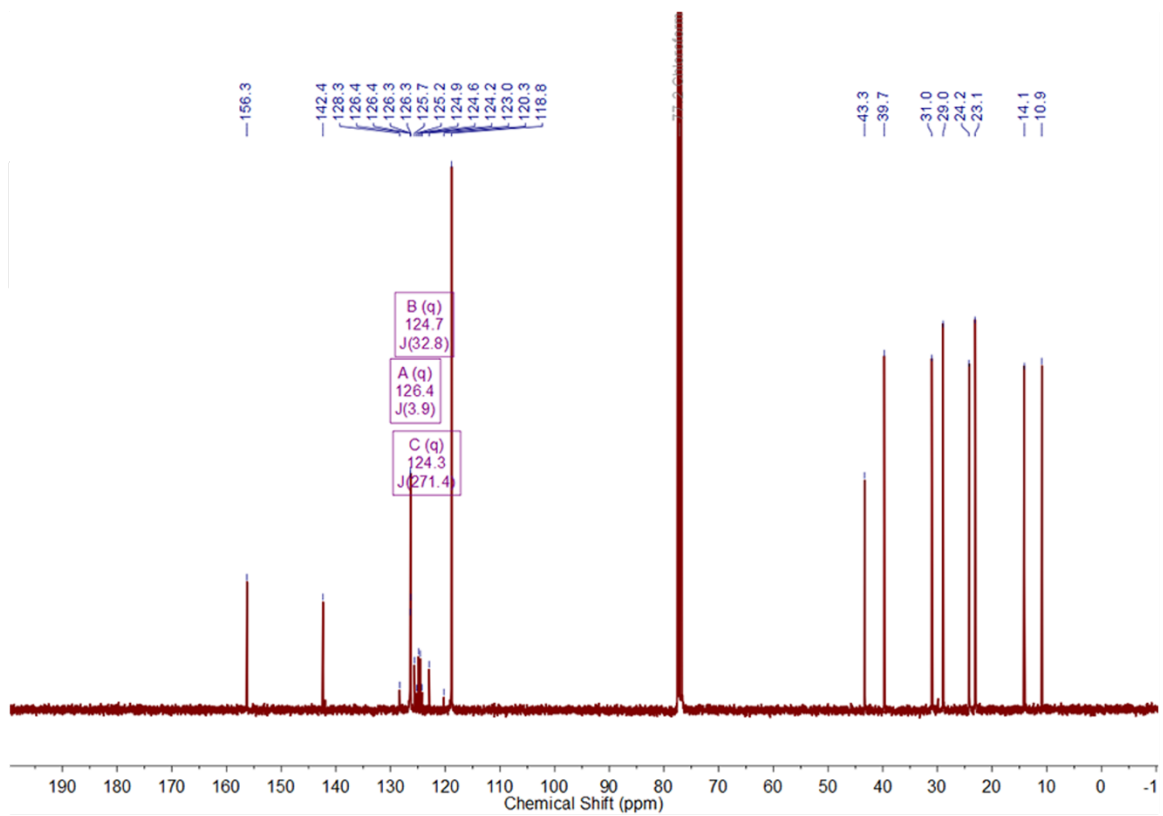


Figure B.8: ^{13}C NMR (101 MHz) spectrum of compound **3.4** in CDCl_3 at 298 K.

B.2 Binding studies with POPE and POPC

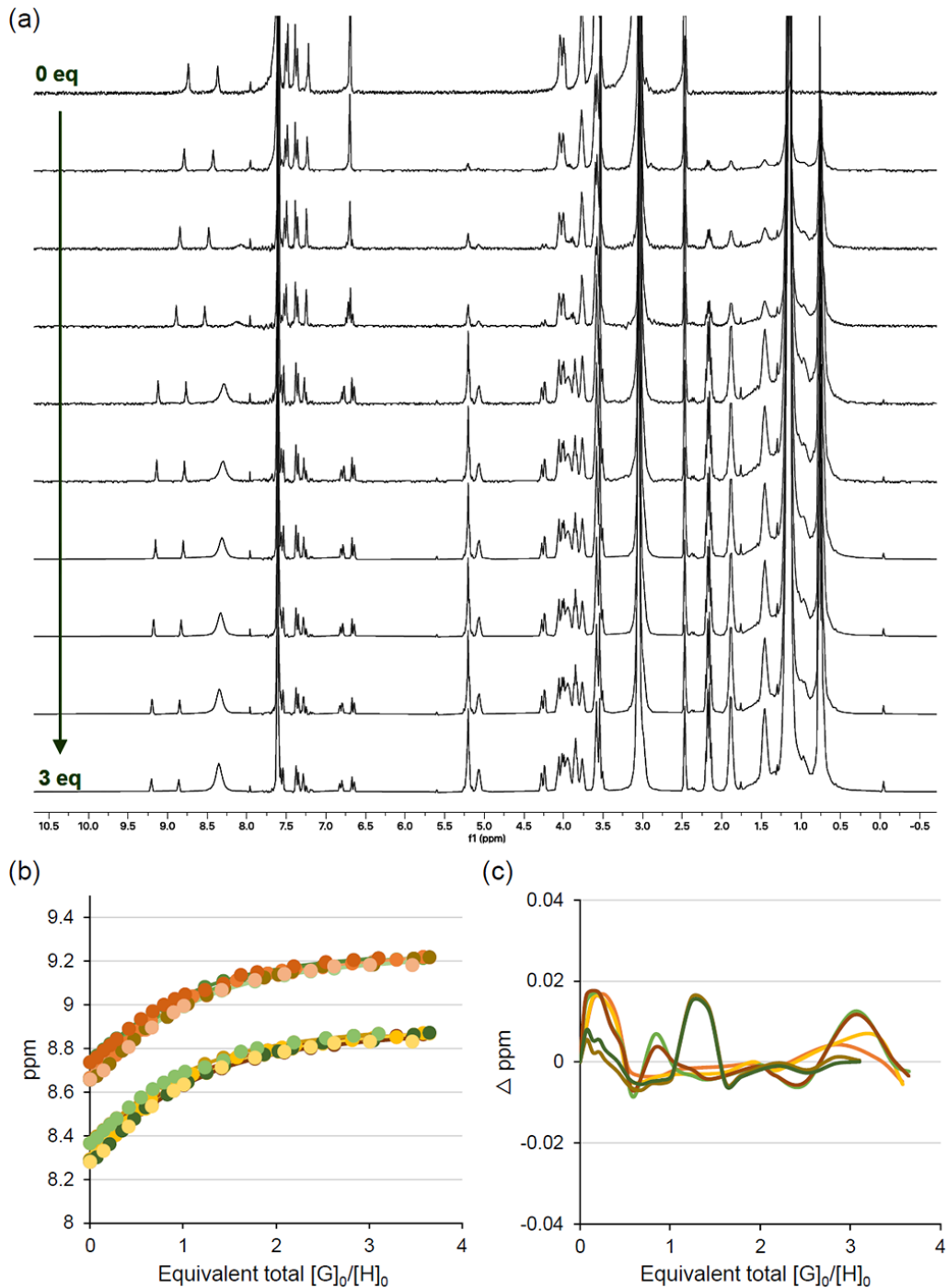


Figure B.9: ^1H NMR titration of **3.1** with POPE in 0.5% Milli-Q H_2O :24.5% $\text{DMSO}-d_6$:75% CDCl_3 at 298 K. (a) Stack plot of selected spectra of a representative titration. (b) Fitplot for the urea NHs at $\delta_A = 8.37$ ppm and $\delta_B = 8.74$ ppm using global analysis and 1:1 binding stoichiometry. Data from 3 independent repeats are overlaid. (c) Plot of the residuals for urea NHs at $\delta_A = 8.37$ ppm and $\delta_B = 8.74$ ppm using global analysis and 1:1 binding stoichiometry. Data from 3 independent repeats are overlaid.

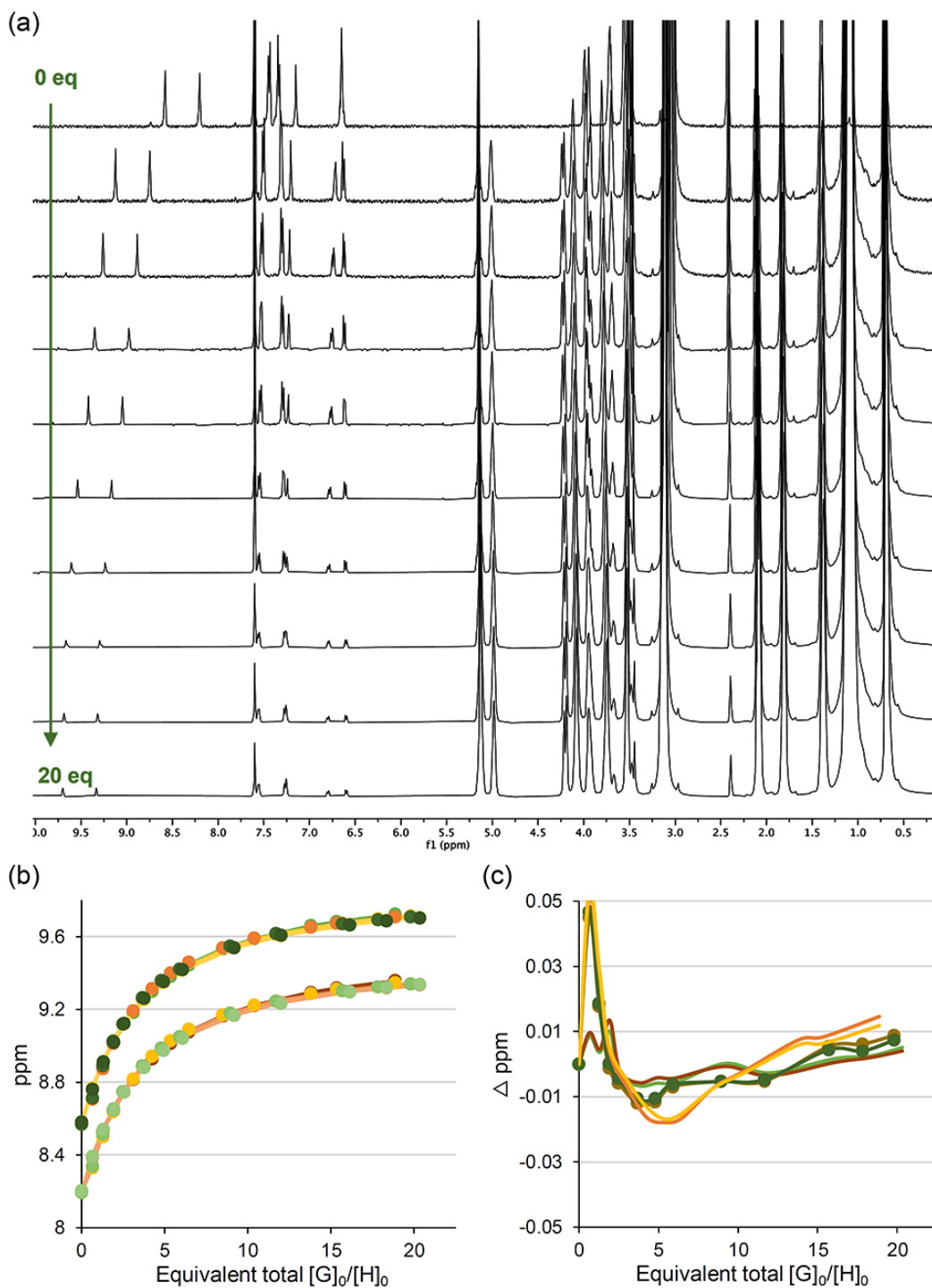


Figure B.10. ^1H NMR titration of **3.1** with POPC in 0.5% Milli-Q H_2O :24.5% DMSO-d_6 :75% CDCl_3 at 298 K. (a) Stack plot of selected spectra of a representative titration. (b) Fitplot for the urea NHs at $\delta_A = 8.37$ ppm and $\delta_B = 8.74$ ppm using global analysis and 1:1 binding stoichiometry. Data from 3 independent repeats are overlaid. (c) Plot of the residuals for urea NHs at $\delta_A = 8.37$ ppm and $\delta_B = 8.74$ ppm using global analysis and 1:1 binding stoichiometry. Data from 3 independent repeats are overlaid.

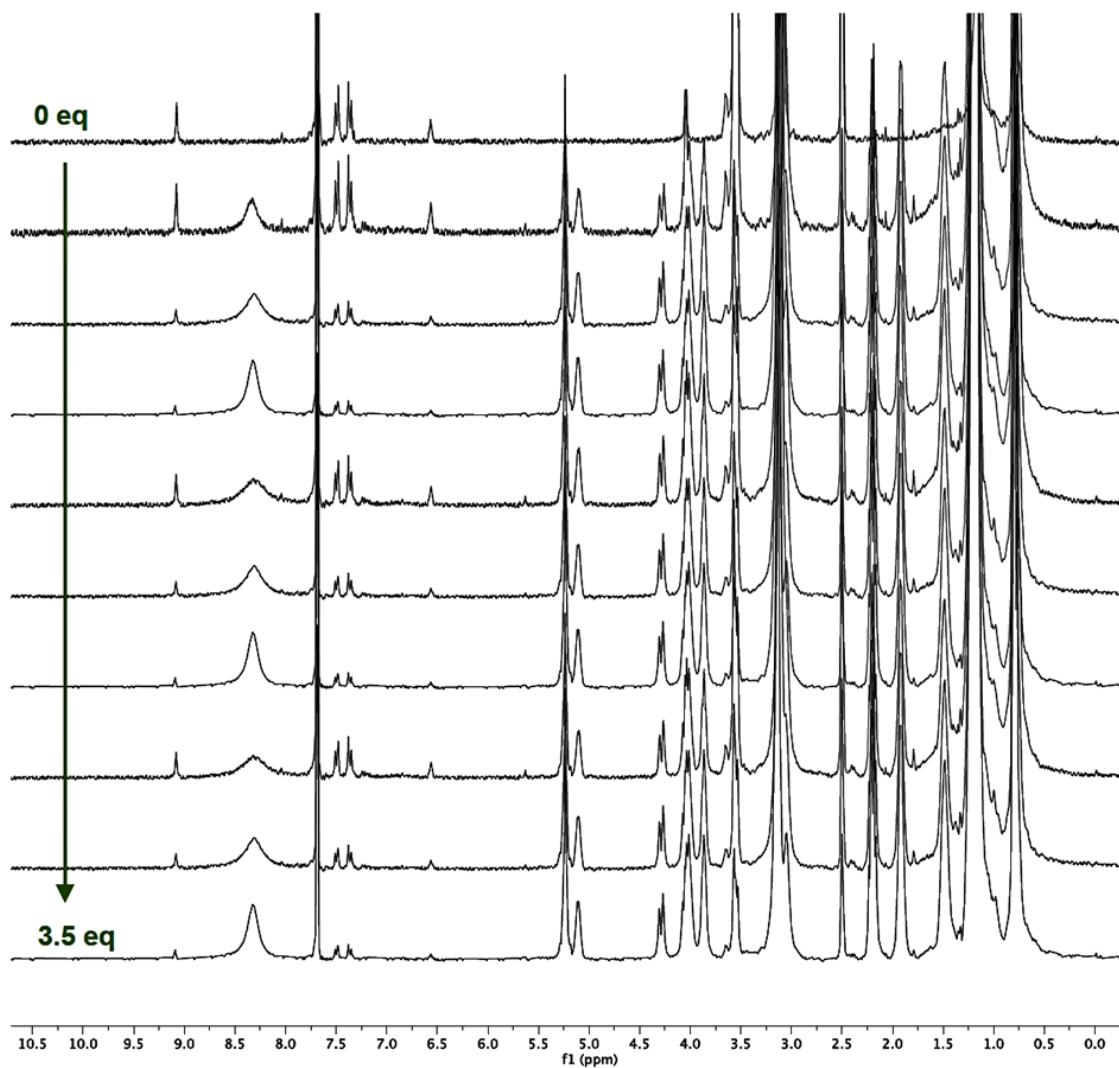


Figure B.11. Stack plot of the ¹H NMR titration of **3.2** with POPE in 0.5% Milli-Q H₂O:24.5% DMSO-*d*₆:75% CDCl₃ at 298 K. The change in chemical shift for the urea NHs is < 0.1 ppm, and we assume no binding event takes place ($K_a < 10 \text{ M}^{-1}$).

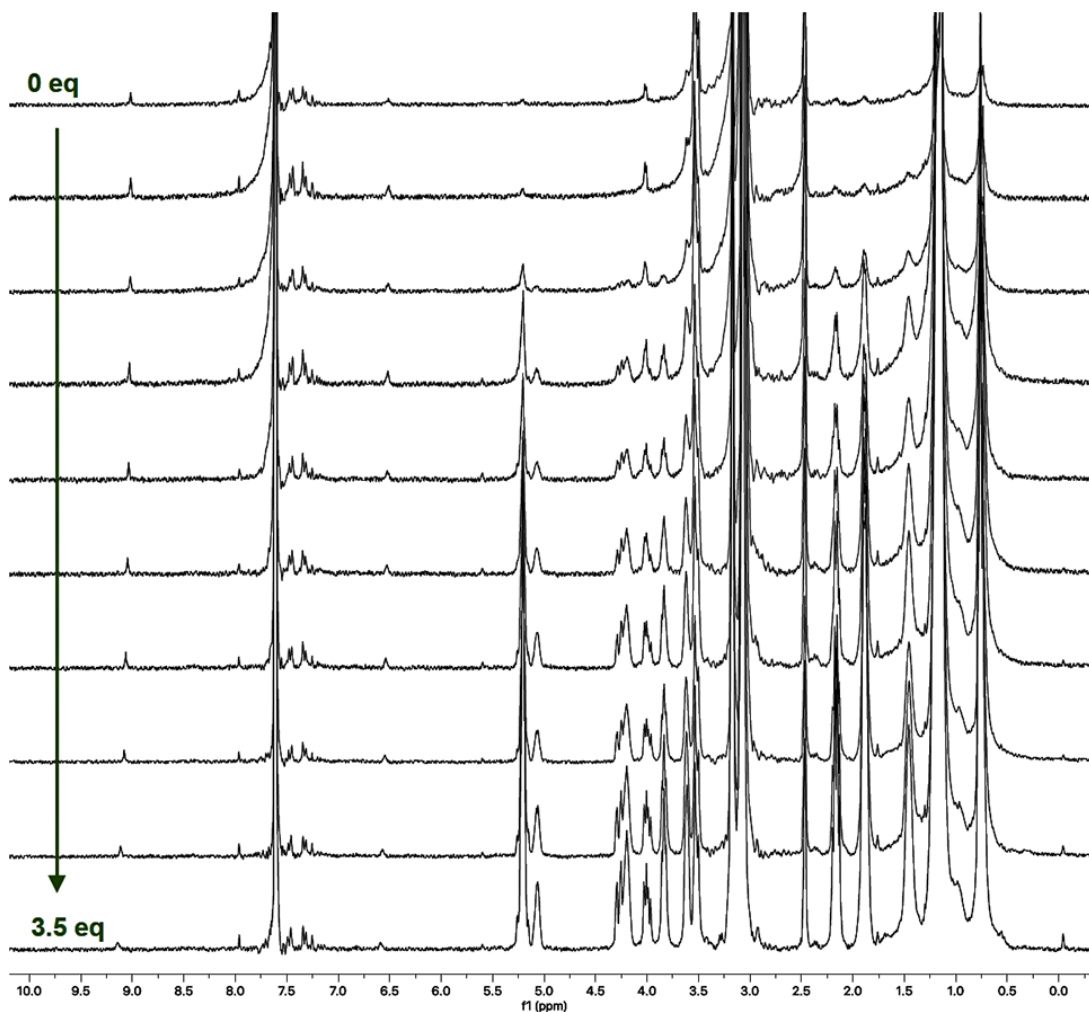


Figure B.12. Stack plot of the ^1H NMR titration of **3.2** with POPC in 0.5% Milli-Q H_2O :24.5% $\text{DMSO-}d_6$:75% CDCl_3 at 298 K. The change in chemical shift for the urea NHs is < 0.1 ppm, and we assume no binding event takes place ($K_a < 10 \text{ M}^{-1}$).

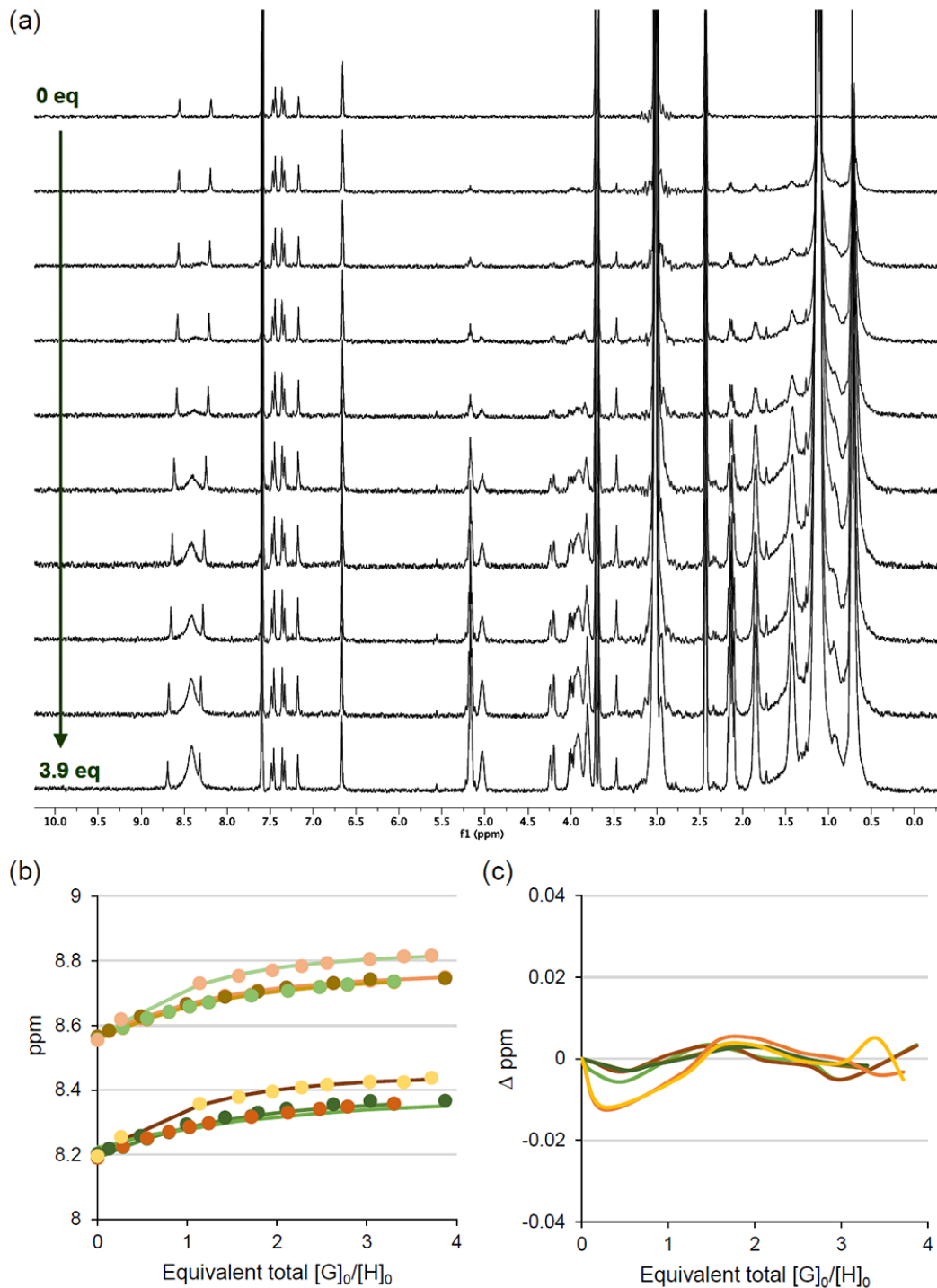


Figure B.13. ^1H NMR titration of **3.3** with POPE in 0.5% Milli-Q H_2O :24.5% $\text{DMSO-}d_6$:75% CDCl_3 at 298 K. (a) Stack plot of selected spectra of a representative titration. (b) Fitplot for the urea NHs at $\delta_A = 8.20$ ppm and $\delta_B = 8.56$ ppm using global analysis and 1:1 binding stoichiometry. Data from 3 independent repeats are overlaid. (c) Plot of the residuals for urea NHs at $\delta_A = 8.20$ ppm and $\delta_B = 8.56$ ppm using global analysis and 1:1 binding stoichiometry. Data from 3 independent repeats are overlaid.

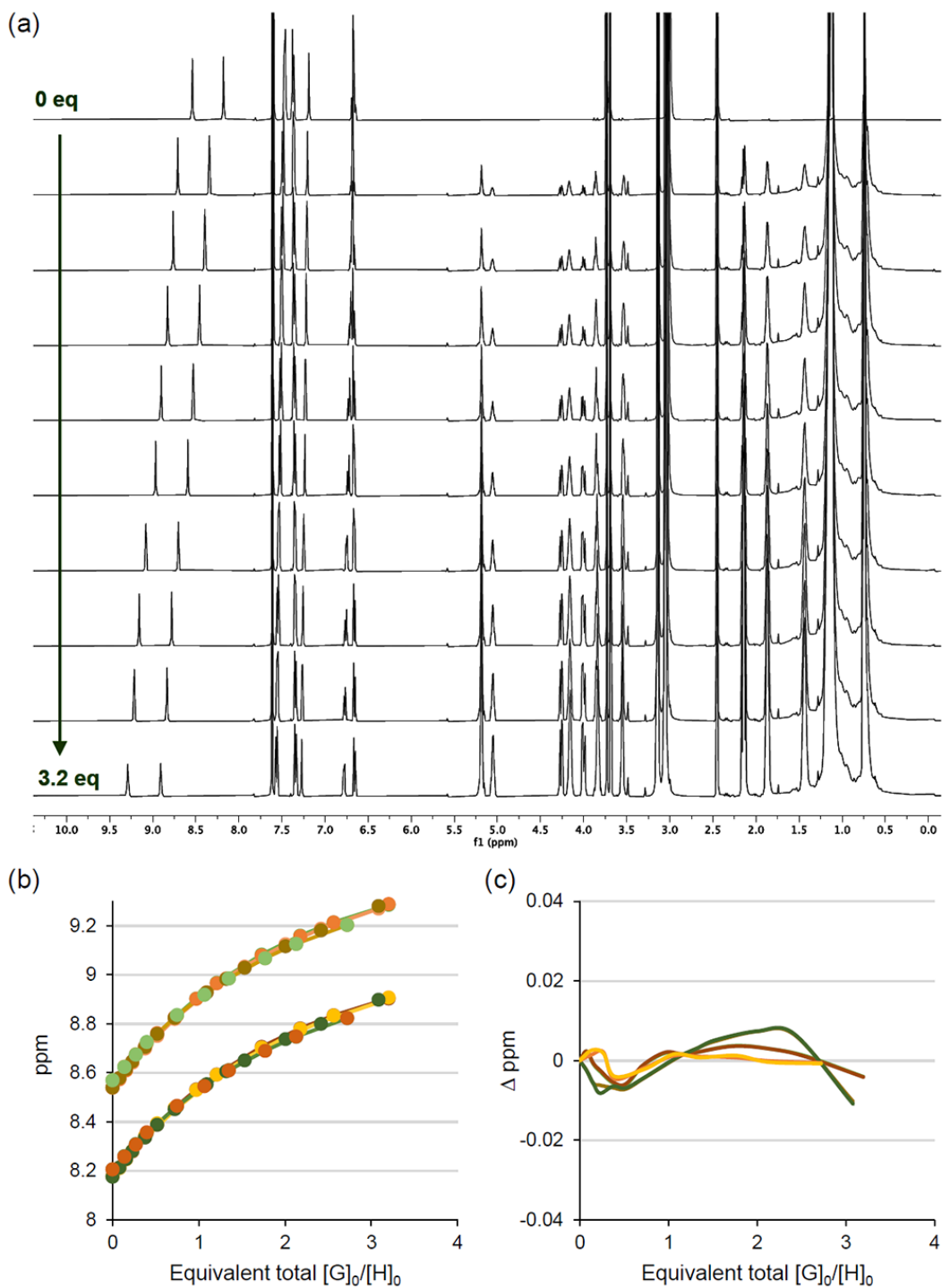


Figure B.14. ^1H NMR titration of **3.3** with POPC in 0.5% Milli-Q H_2O :24.5% $\text{DMSO-}d_6$:75% CDCl_3 at 298 K. (a) Stack plot of selected spectra of a representative titration. (b) Fitplot for the urea NHs at $\delta_A = 8.20$ ppm and $\delta_B = 8.56$ ppm using global analysis and 1:1 binding stoichiometry. Data from 3 independent repeats are overlaid. (c) Plot of the residuals for urea NHs at $\delta_A = 8.20$ ppm and $\delta_B = 8.56$ ppm using global analysis and 1:1 binding stoichiometry. Data from 3 independent repeats are overlaid.

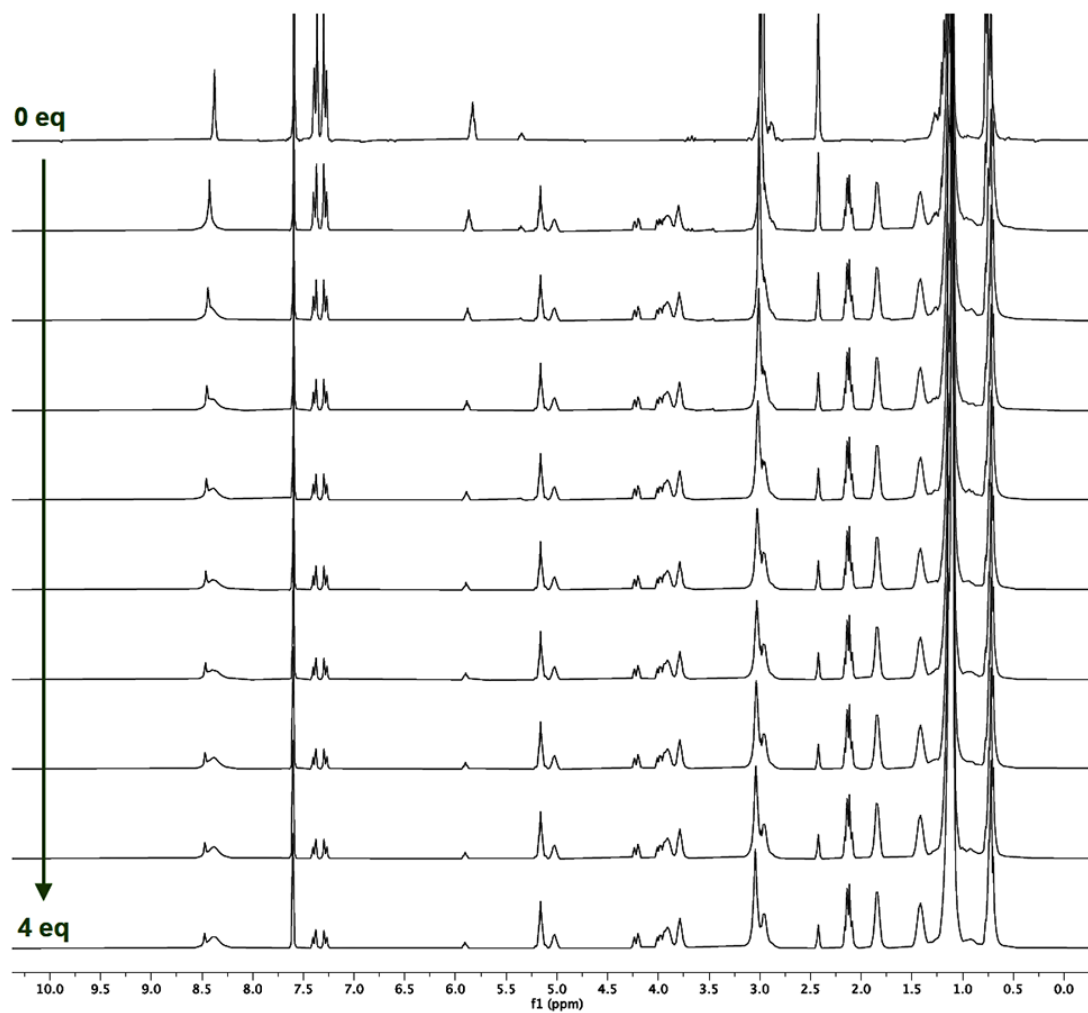


Figure B.15. Stack plot of the ^1H NMR titration of **3.4** with POPE in 0.5% Milli-Q H_2O :24.5% $\text{DMSO-}d_6$:75% CDCl_3 at 298 K. The change in chemical shift for the urea NHs is < 0.1 ppm, and we assume no binding event takes place ($K_a < 10 \text{ M}^{-1}$).

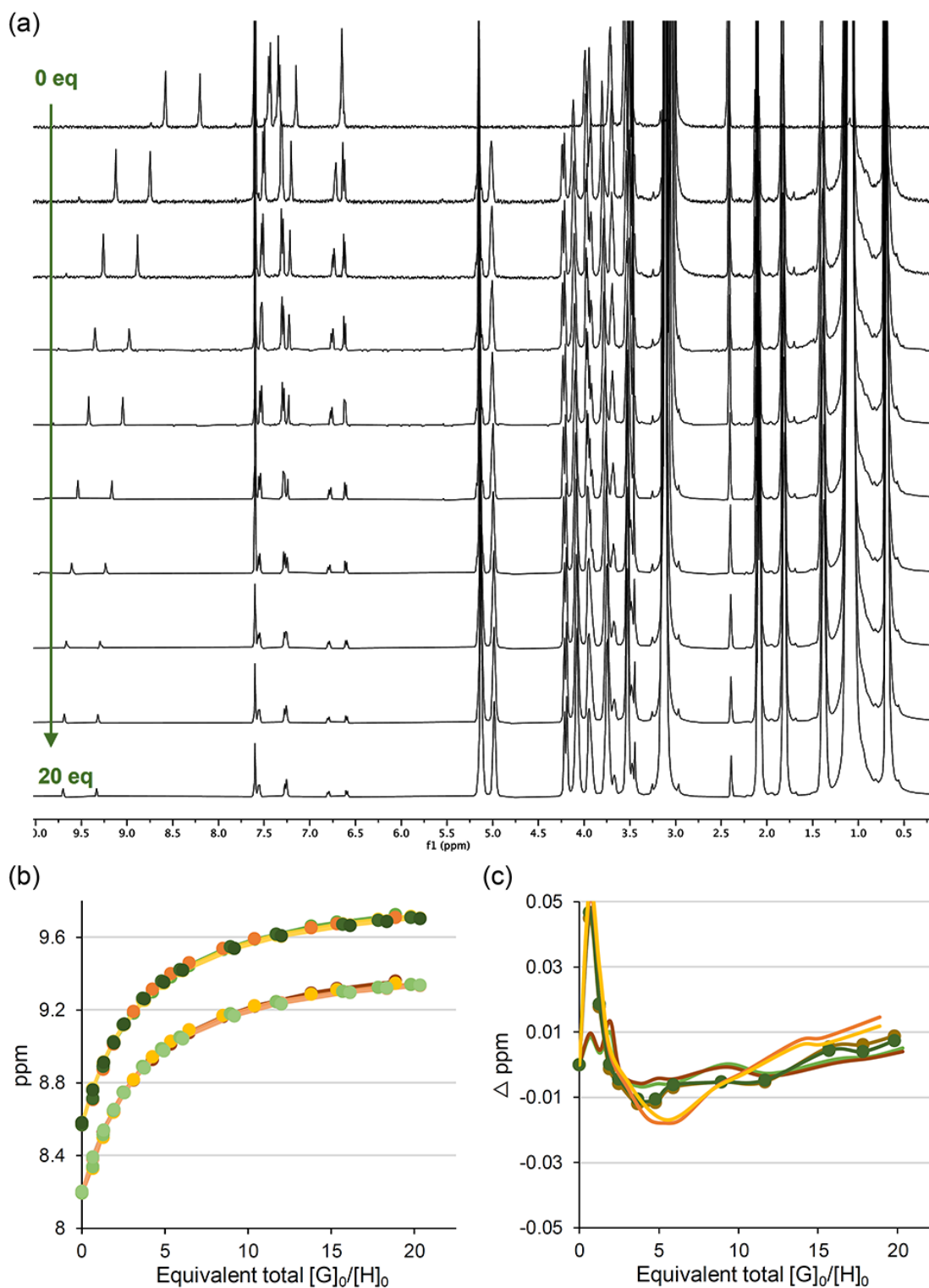


Figure B.16: ^1H NMR titration of 3.4 with POPC in 0.5% Milli-Q H_2O :24.5% $\text{DMSO}-d_6$:75% CDCl_3 at 298 K. (a) Stack plot of selected spectra of a representative titration. (b) Fitplot for the urea NHs at $\delta_A = 5.90$ ppm and $\delta_B = 8.48$ ppm using global analysis and 1:1 binding stoichiometry. Data from 3 independent repeats are overlaid. (c) Plot of the residuals for urea NHs at $\delta_A = 5.90$ ppm and $\delta_B = 8.48$ ppm using global analysis and 1:1 binding stoichiometry. Data from 3 independent repeats are overlaid.

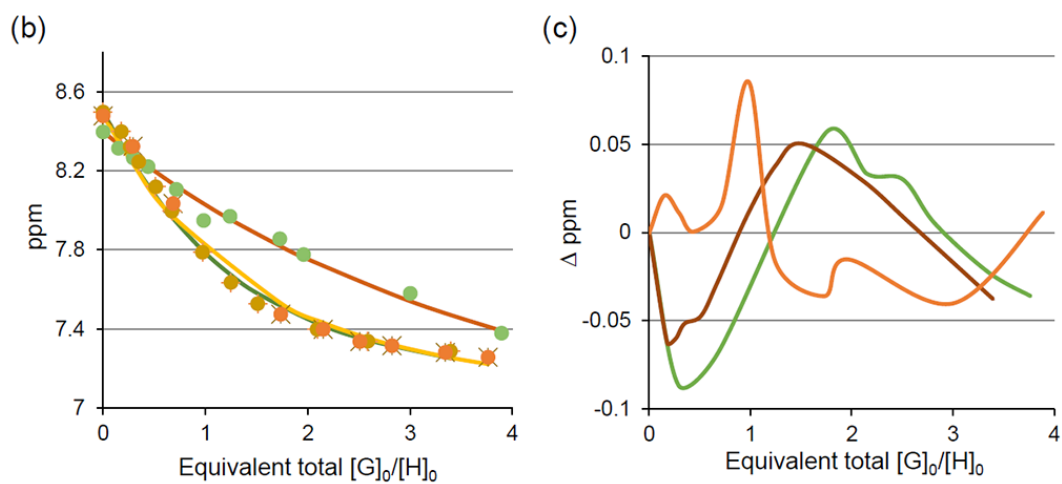
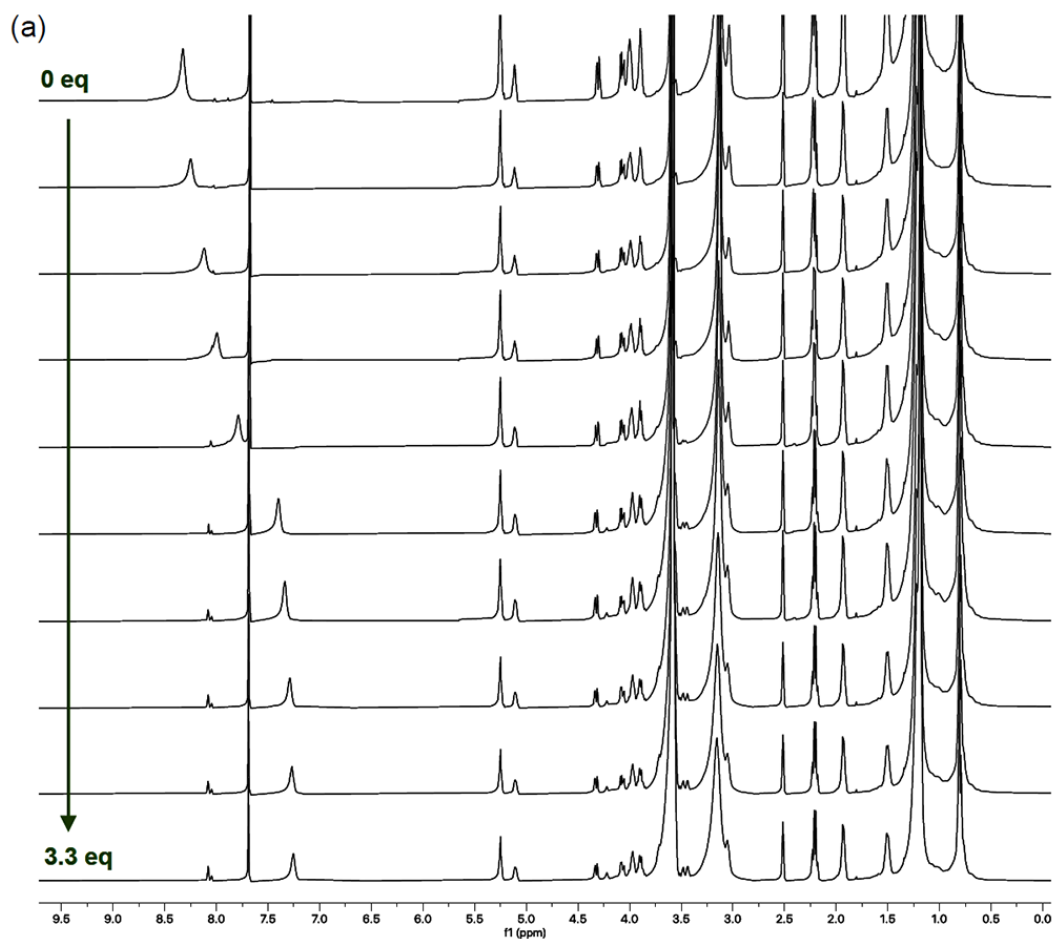


Figure B.17: ^1H NMR titration of POPE with 18-crown-6 in 0.5% Milli-Q H_2O :24.5% DMSO-d_6 :75% CDCl_3 at 298 K. (a) Stack plot of selected spectra of a representative titration. (b) Fitplot for the ammonium group of POPE at $\delta_A = 8.40$ ppm using 1:1 binding stoichiometry. Data from 3 independent repeats are overlaid. (c) Plot of the residuals for the ammonium group of POPE at $\delta_A = 8.40$ ppm. Data from 3 independent repeats are overlaid.

B.3 Fluorescence titrations with POPC and POPE

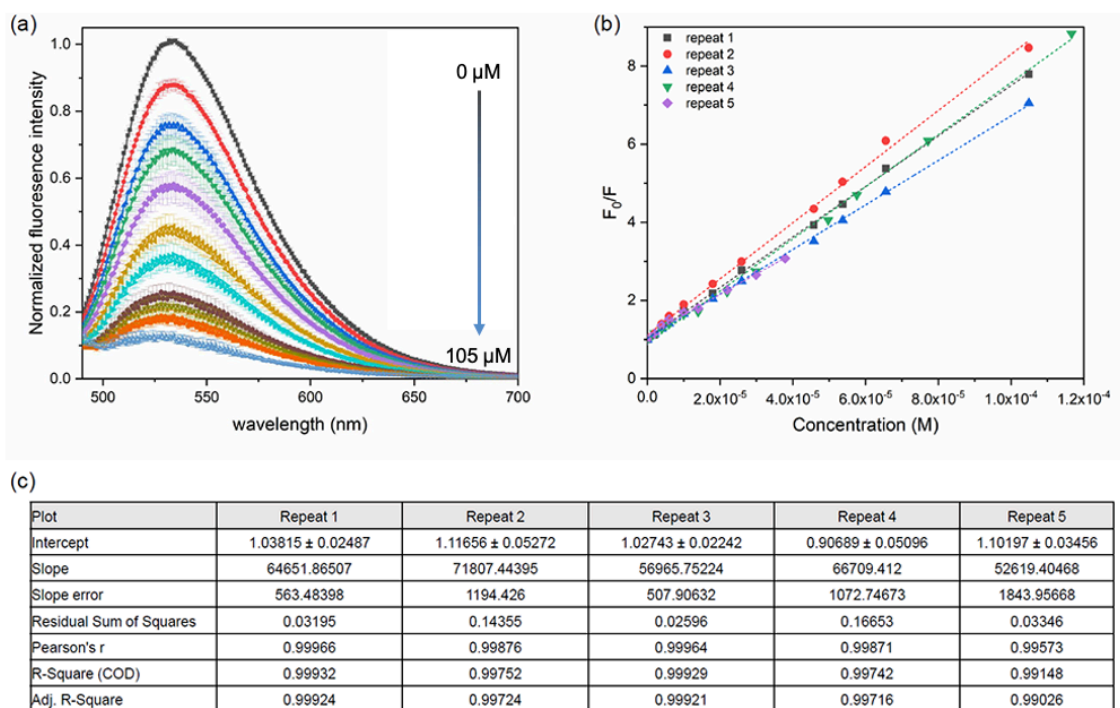


Figure B.18: Fluorescence titration of **3.1** (10 mM stock in DMSO) into a solution of 100 nm LUVs (1:1 POPC:POPE liposomes containing 1 mol% NBD-PE). Excitation wavelength = 470 nm. (a) Normalized fluorescence spectra, average of at least 2 repeats. (b) Stern-Volmer plots for all individual repeats. (c) Results of the linear fit of the Stern-Volmer plots. The slope corresponds to the Stern-Volmer constant K_{SV} .

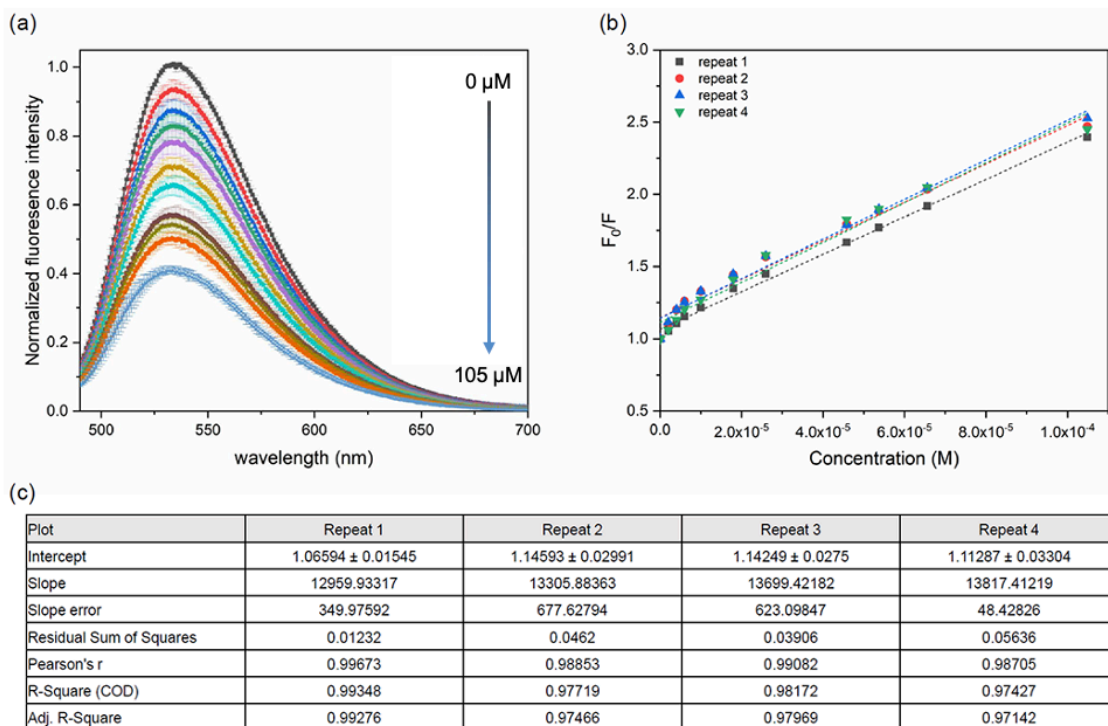


Figure B.19: Fluorescence titration of **3.1** (10 mM stock in DMSO) into a solution of 100 nm LUVs (POPC liposomes containing 1 mol% NBD-PC). Excitation wavelength = 470 nm. (a) Normalized fluorescence spectra, average of at least 2 repeats. (b) Stern-Volmer plots for all individual repeats. (c) Results of the linear fit of the Stern-Volmer plots. The slope corresponds to the Stern-Volmer constant K_{SV} .

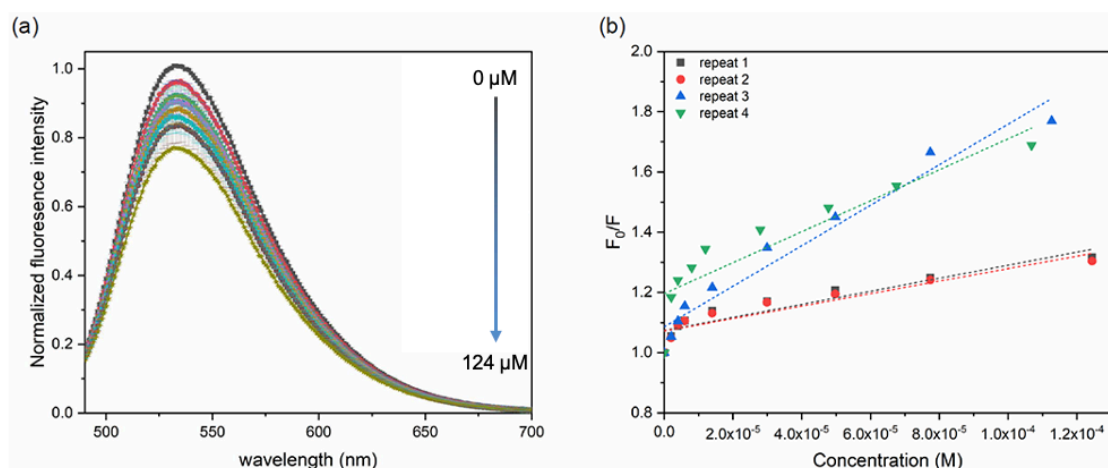


Figure B.20: Fluorescence titration of **3.2** (10 mM stock in DMSO) into a solution of 100 nm LUVs (1:1 POPC:POPE liposomes containing 1 mol% NBD-PE). Excitation wavelength = 470 nm. (a) Normalized fluorescence spectra, average of at least 2 repeats. (b) Stern-Volmer plots for all individual repeats. Linear fit resulted in R^2 values < 0.75 (no linear correlation).

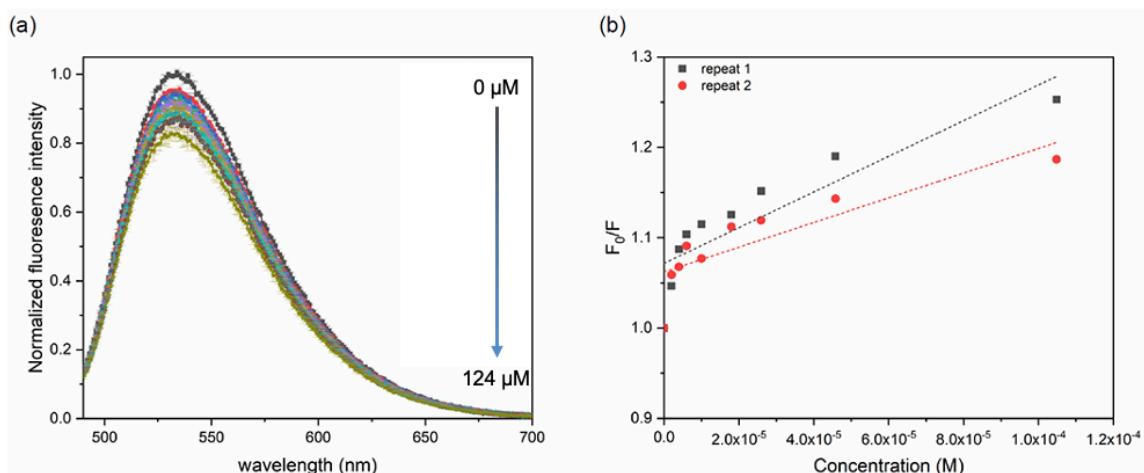


Figure B.21: Fluorescence titration of **3.2** (10 mM stock in DMSO) into a solution of 100 nm LUVs (POPC liposomes containing 1 mol% NBD-PC). Excitation wavelength = 470 nm. (a) Normalized fluorescence spectra, average of at least 2 repeats. (b) Stern-Volmer plots for all individual repeats. Linear fit resulted in R^2 values < 0.75 (no linear correlation).

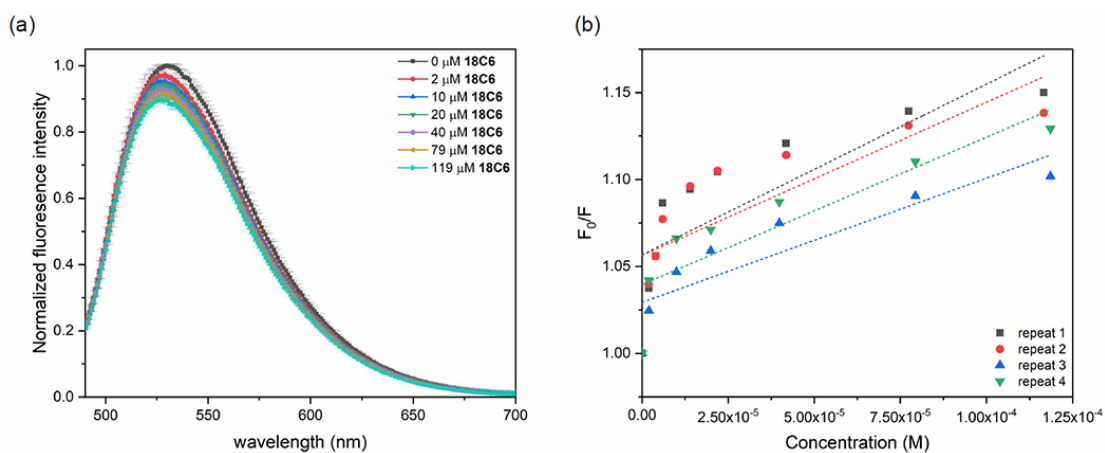


Figure B.22: Fluorescence titration of **18-crown-6** (10 mM stock in DMSO) into a solution of 100 nm LUVs (1:1 POPC:POPE liposomes containing 1 mol% NBD-PE). Excitation wavelength = 470 nm. (a) Normalized fluorescence spectra, average of at least 2 repeats. (b) Stern-Volmer plots for all individual repeats. Linear fit resulted in R^2 values < 0.75 (no linear correlation).

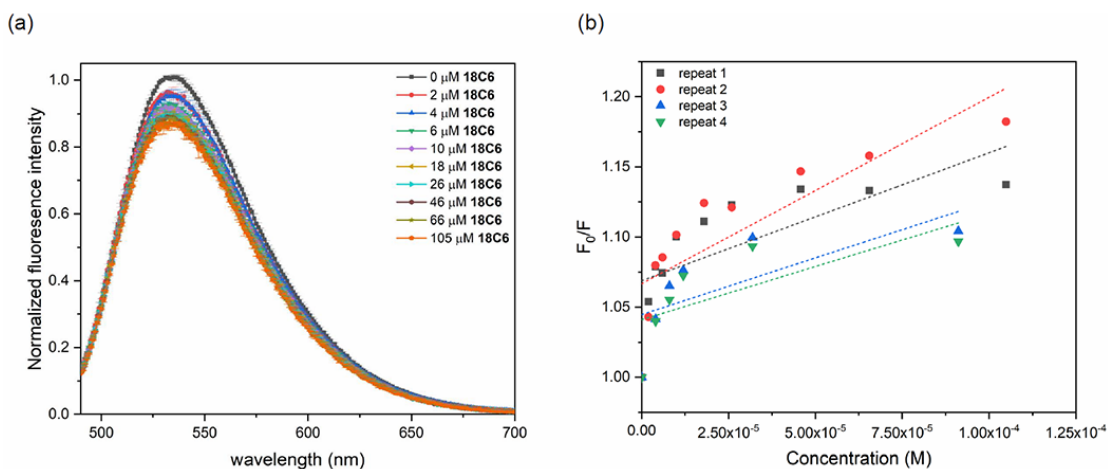


Figure B.23: Fluorescence titration of **18-crown-6** (10 mM stock in DMSO) into a solution of 100 nm LUVs (POPC liposomes containing 1 mol% NBD-PC). Excitation wavelength = 470 nm. (a) Normalized fluorescence spectra, average of at least 2 repeats. (b) Stern-Volmer plots for all individual repeats. Linear fit resulted in R^2 values < 0.75 (no linear correlation).

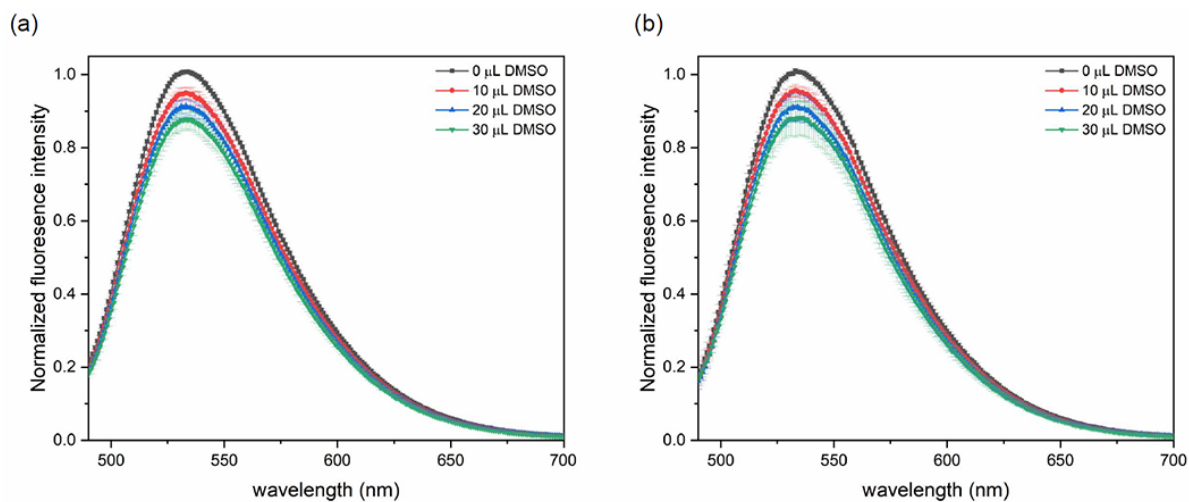


Figure B.24. Fluorescence titration of **DMSO** into a solution of 100 nm LUVs. Excitation wavelength = 470 nm. (a) 1:1 POPC:POPE liposomes containing 1 mol% NBD-PE. (b) POPC liposomes containing 1 mol% NBD-PC.

B.4 Lipid flip-flop

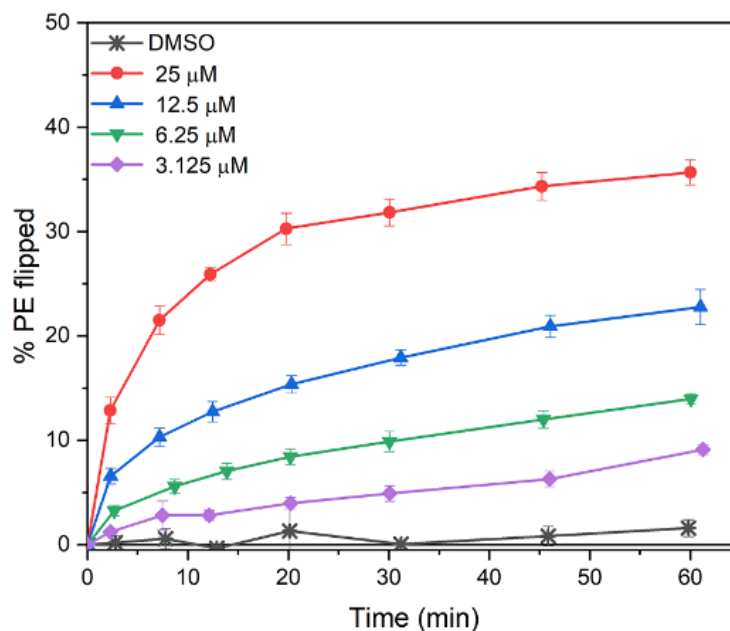


Figure B.25: Flip-flop of exo NBD-PE (1 mol%) in 100 nm DOPC large unilamellar vesicles (25 μM) mediated by various concentrations of host **3.1**. DMSO was used as a negative control. The results are the average of 2 biological x 2 technical repeats and the error bars represent standard deviations.

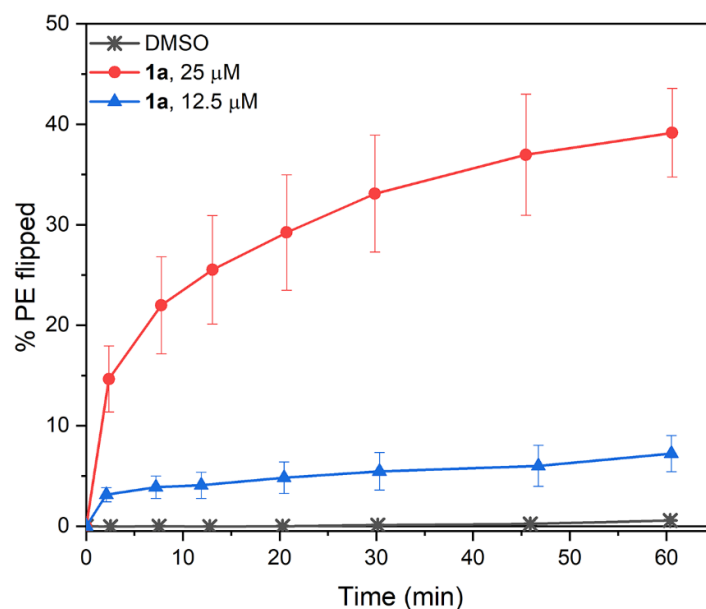


Figure B.26: Flip-flop of exo NBD-PE (1 mol%) in 100 nm 7:3 DOPE:DOPG large unilamellar vesicles (25 μM) mediated by various concentrations of hosts **3.1**. DMSO was used as a negative control. The results are the average of 2 biological x 2 technical repeats and the error bars represent standard deviations.

B.5 Bacterial selectivity assay

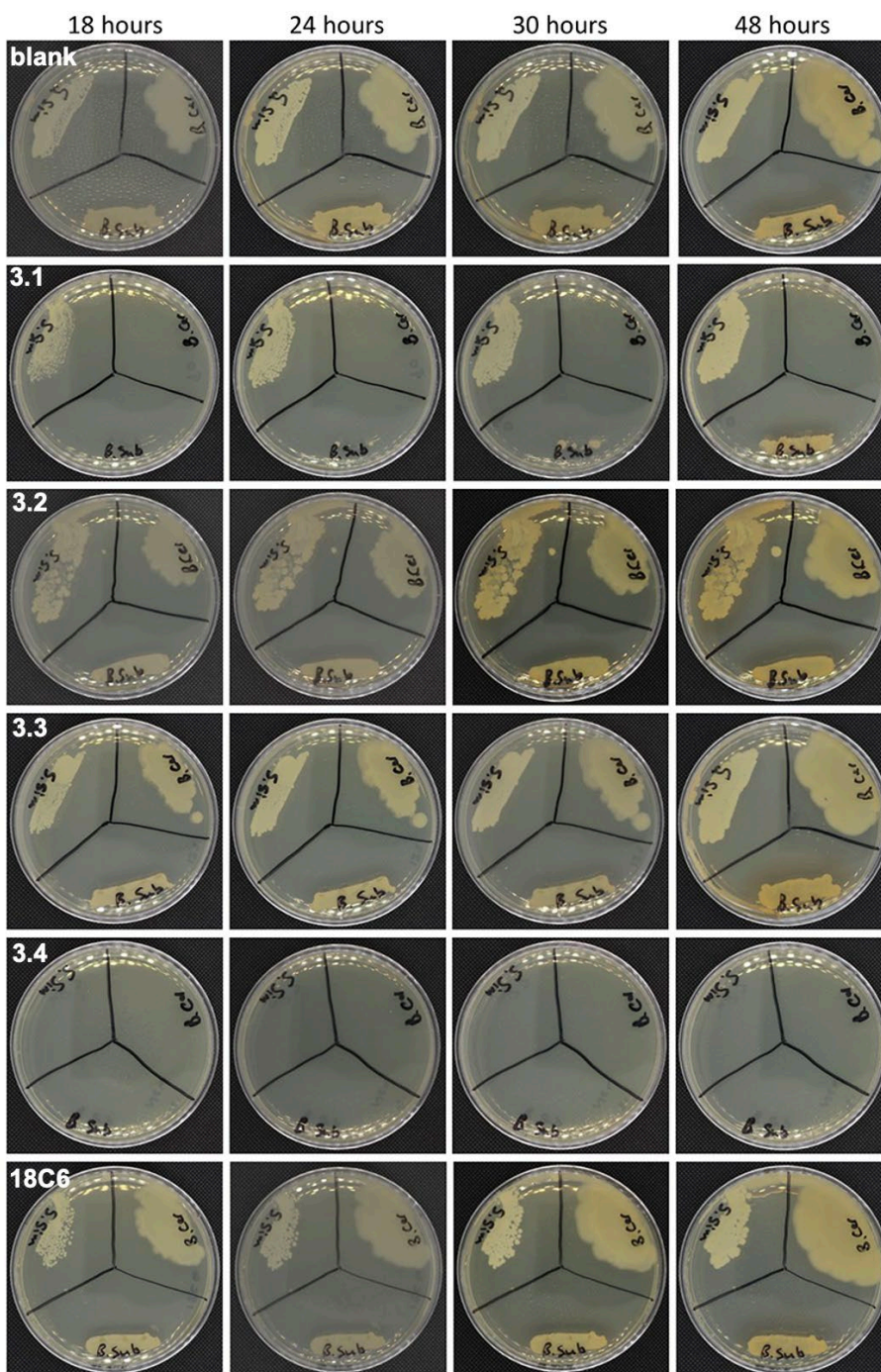


Figure B.27. Bacterial selectivity of **3.1-3.4** and 18-crown-6 (biological repeat 1). Bacterial growth was monitored for 24 h at 35 °C on a Müller-Hinton agar plate containing 50 μ L of a 25 mM DMSO stock of **3.1**, **3.2**, **3.3**, **3.4** and 18-crown-6. Blank contained 300 μ L DMSO in the agar plate. All plates are photographed so that the *B. cereus* section is on the right, the *B. subtilis* section is on the bottom, and the *S. simulans* section is on the left of the agar plate.

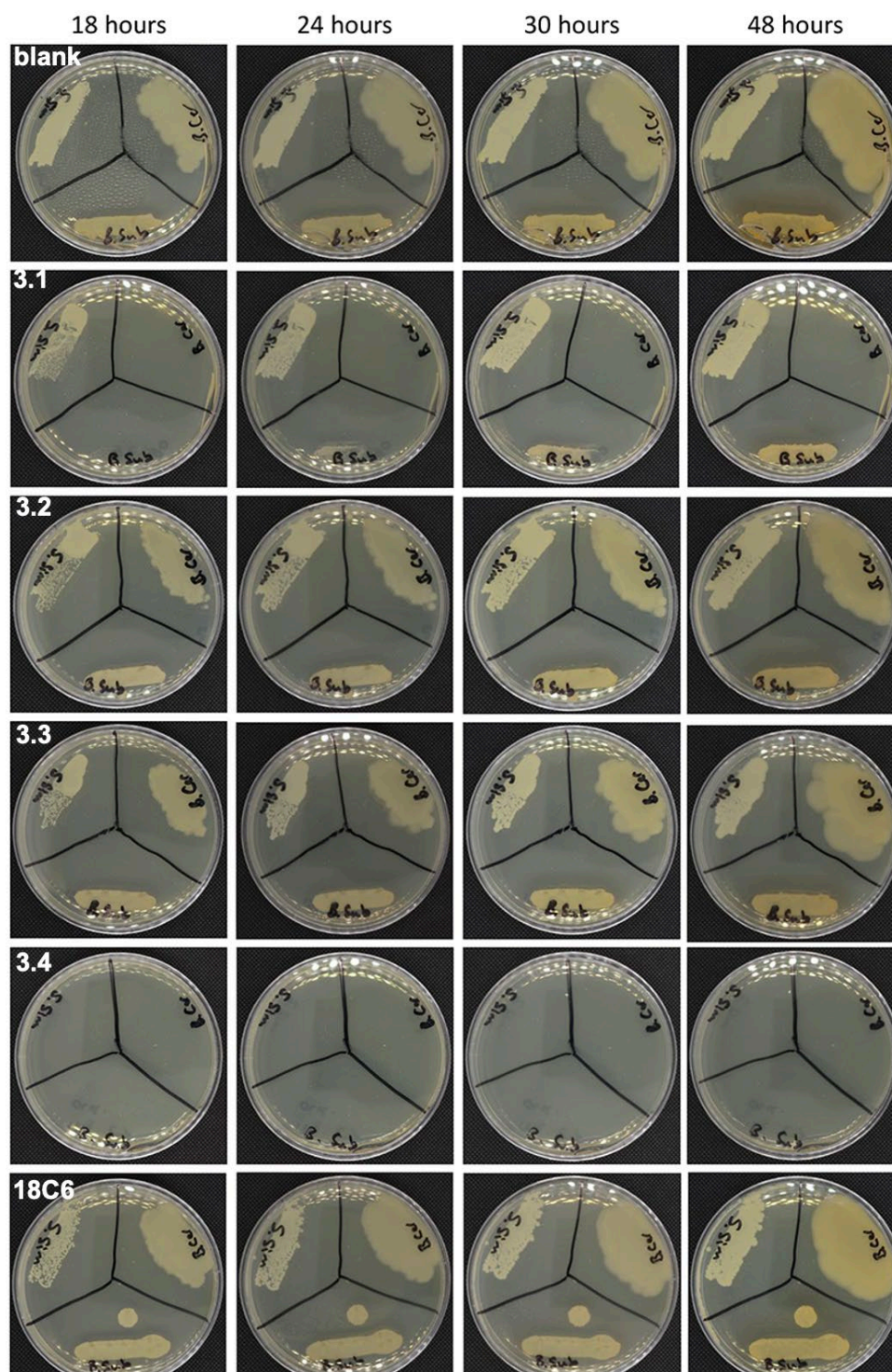


Figure B.28: Bacterial selectivity of **3.1-3.4** and 18-crown-6 (biological repeat 2). Bacterial growth was monitored for 24 h at 35 °C on a Müller-Hinton agar plate containing 50 μ L of a 25 mM DMSO stock of **3.1**, **3.2**, **3.3**, **3.4** and 18-crown-6. Blank contained 300 μ L DMSO in the agar plate. All plates are photographed so that the *B. cereus* section is on the right, the *B. subtilis* section is on the bottom, and the *S. simulans* section is on the left of the agar plate.

B.6 Growth curves from MIC studies

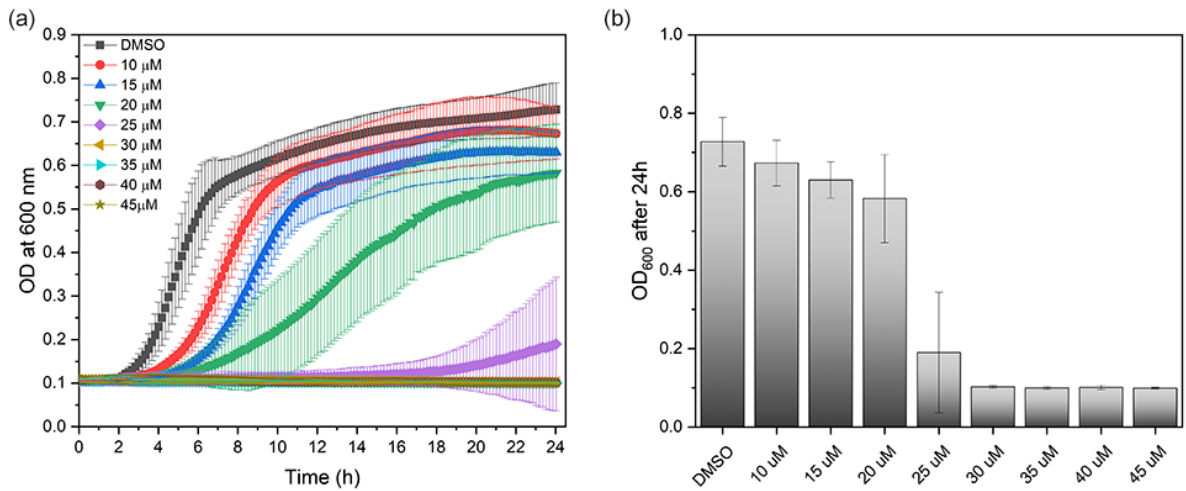


Figure B.29: MIC determination for compound **3.1**. The change in optical density at 600 nm was measured for 24 h at 35 °C to monitor the growth of *B. cereus* (starting point 5×10^5 CFU/mL) in Müller-Hinton broth containing 4% DMSO and various concentrations of compound **3.1**. DMSO was used as a negative control. The results are the average of minimum 2 biological x 2 technical repeats and the error bars represent standard deviations. (a) full growth curves. (b) Optical density (600 nm) after 24 hours incubation with various concentrations of **3.1**.

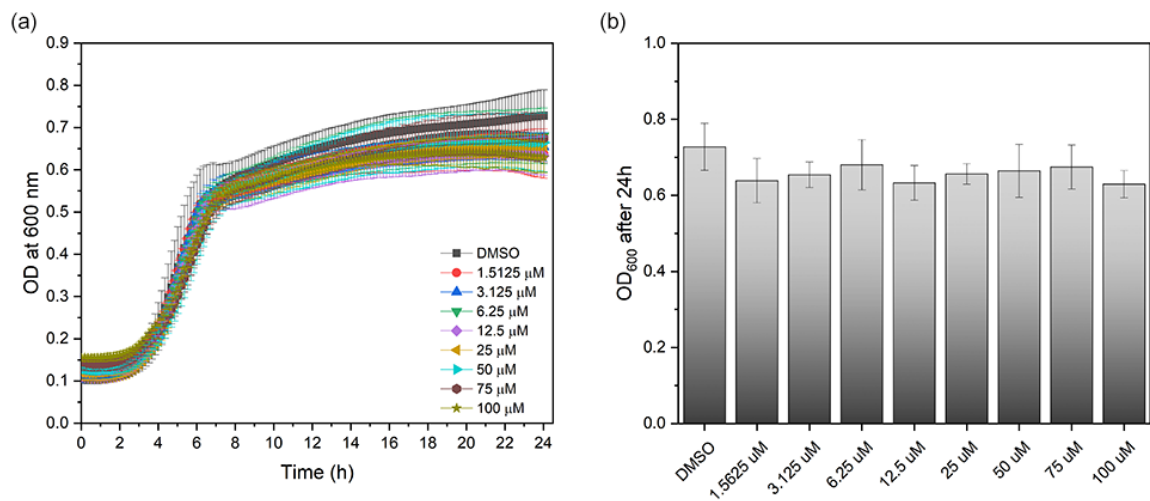


Figure B.30. MIC determination for compound **3.2**. The change in optical density at 600 nm was measured for 24 h at 35 °C to monitor the growth of *B. cereus* (starting point 5×10^5 CFU/mL) in Müller-Hinton broth containing 4% DMSO and various concentrations of compound **3.2**. DMSO was used as a negative control. The results are the average of minimum 2 biological x 2 technical repeats and the error bars represent standard deviations. (a) full growth curves. (b) Optical density (600 nm) after 24 hours incubation with various concentrations of **3.2**.

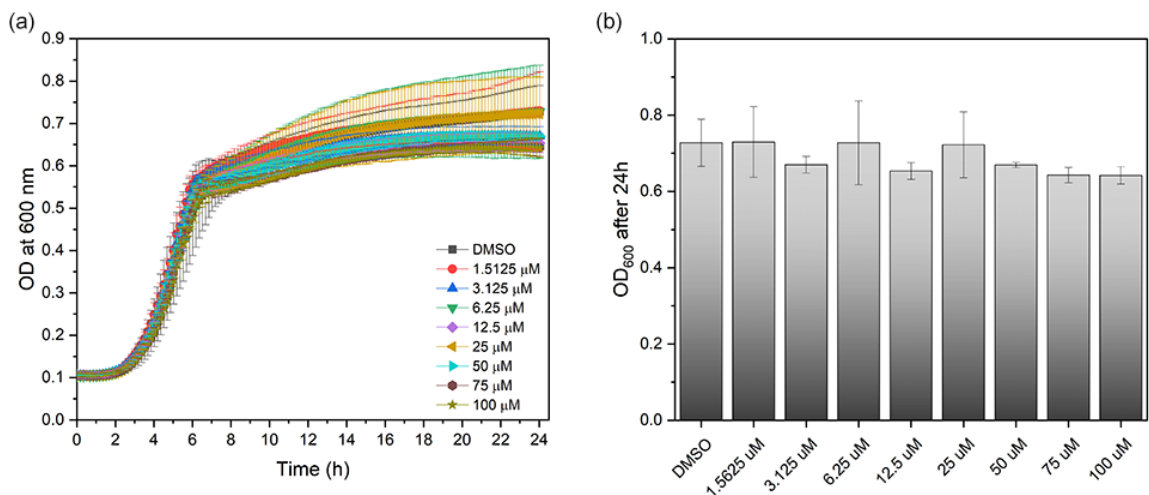


Figure B.31: MIC determination for compound **3.3**. The change in optical density at 600 nm was measured for 24 h at 35 °C to monitor the growth of *B. cereus* (starting point 5×10^5 CFU/mL) in Müller-Hinton broth containing 4% DMSO and various concentrations of compound **3.3**. DMSO was used as a negative control. The results are the average of minimum 2 biological x 2 technical repeats and the error bars represent standard deviations. (a) full growth curves. (b) Optical density (600 nm) after 24 hours incubation with various concentrations of **3.3**.

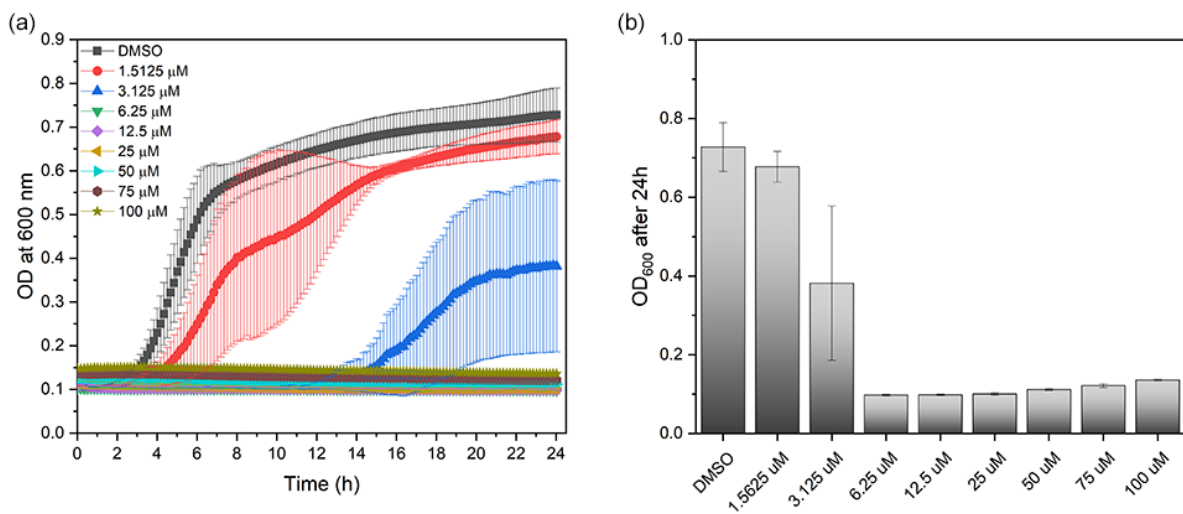


Figure B.32. MIC determination for compound **3.4**. The change in optical density at 600 nm was measured for 24 h at 35 °C to monitor the growth of *B. cereus* (starting point 5×10^5 CFU/mL) in Müller-Hinton broth containing 4% DMSO and various concentrations of compound **3.4**. DMSO was used as a negative control. The results are the average of minimum 2 biological x 2 technical repeats and the error bars represent standard deviations. (a) full growth curves. (b) Optical density (600 nm) after 24 hours incubation with various concentrations of **3.4**.

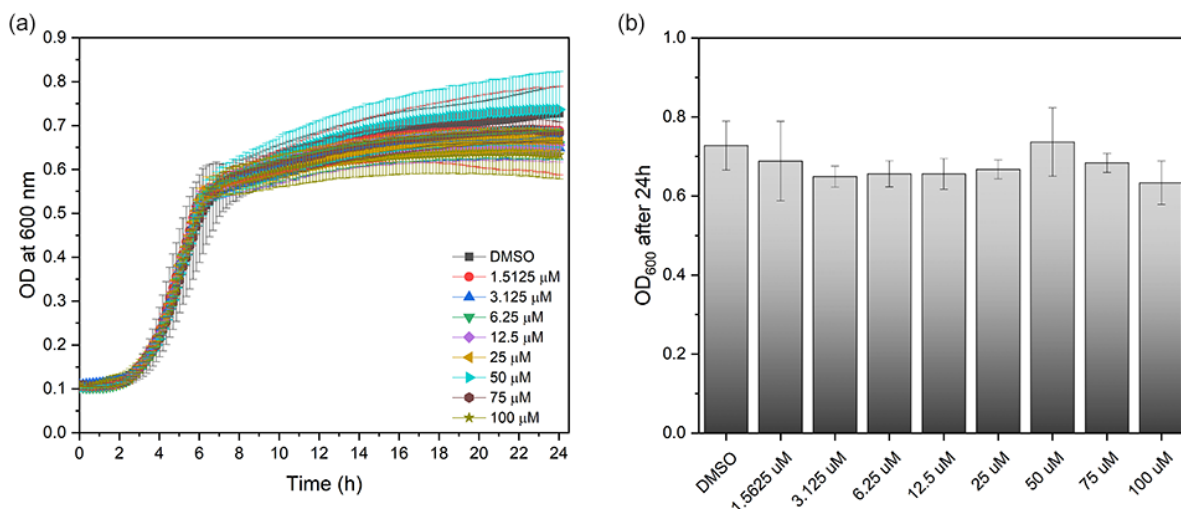


Figure B.33: MIC determination for compound **18C6**. The change in optical density at 600 nm was measured for 24 h at 35 °C to monitor the growth of *B. cereus* (starting point 5×10^5 CFU/mL) in Müller-Hinton broth containing 4% DMSO and various concentrations of compound **18C6**. DMSO was used as a negative control. The results are the average of minimum 2 biological x 2 technical repeats and the error bars represent standard deviations. (a) full growth curves. (b) Optical density (600 nm) after 24 hours incubation with various concentrations of **18C6**.

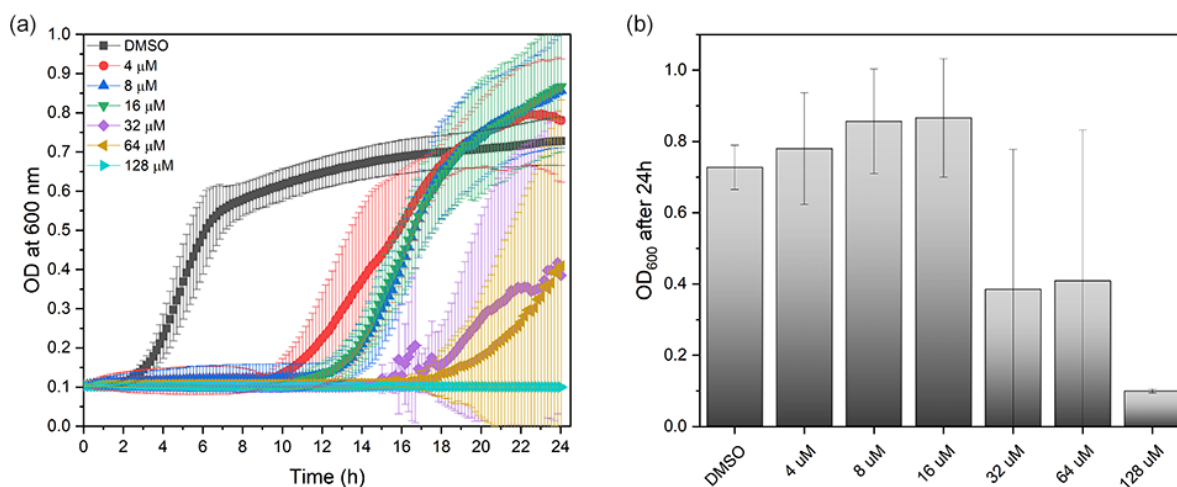


Figure B.34: MIC determination for **duramycin**. The change in optical density at 600 nm was measured for 24 h at 35 °C to monitor the growth of *B. cereus* (starting point 5×10^5 CFU/mL) in Müller-Hinton broth containing 4% DMSO and various concentrations of **duramycin**. DMSO was used as a negative control. The results are the average of minimum 2 biological x 2 technical repeats and the error bars represent standard deviations. (a) full growth curves. (b) Optical density (600 nm) after 24 hours incubation with various concentrations of **duramycin**.

B.7 Bactericidal activity

Table B.1: Bactericidal activity of compound **3.1** after 24 h incubation with *B.cereus*.

Concentration 3.1	% bacteria killed					
	Repeat 1	Repeat 2	Repeat 3	Repeat 4	Repeat 5	Repeat 6
45 μ M	100	99.9	99.8	99.9	100	100
40 μ M	100	99.9	99.8	99.9	99.8	100
35 μ M	99.9	99.7	99.3	99.7	Overgrown ^[a]	Overgrown ^[a]
30 μ M	99.9	Overgrown ^[a]	99.3	Overgrown ^[a]	Overgrown ^[a]	Overgrown ^[a]
25 μ M	n.d. ^[b]	Overgrown ^[a]	Overgrown ^[a]	Overgrown ^[a]	Overgrown ^[a]	Overgrown ^[a]

^[a] Colonies were too numerous to count. ^[b] n.d. = not determined.

B.8 Bacterial imaging with *B. cereus*

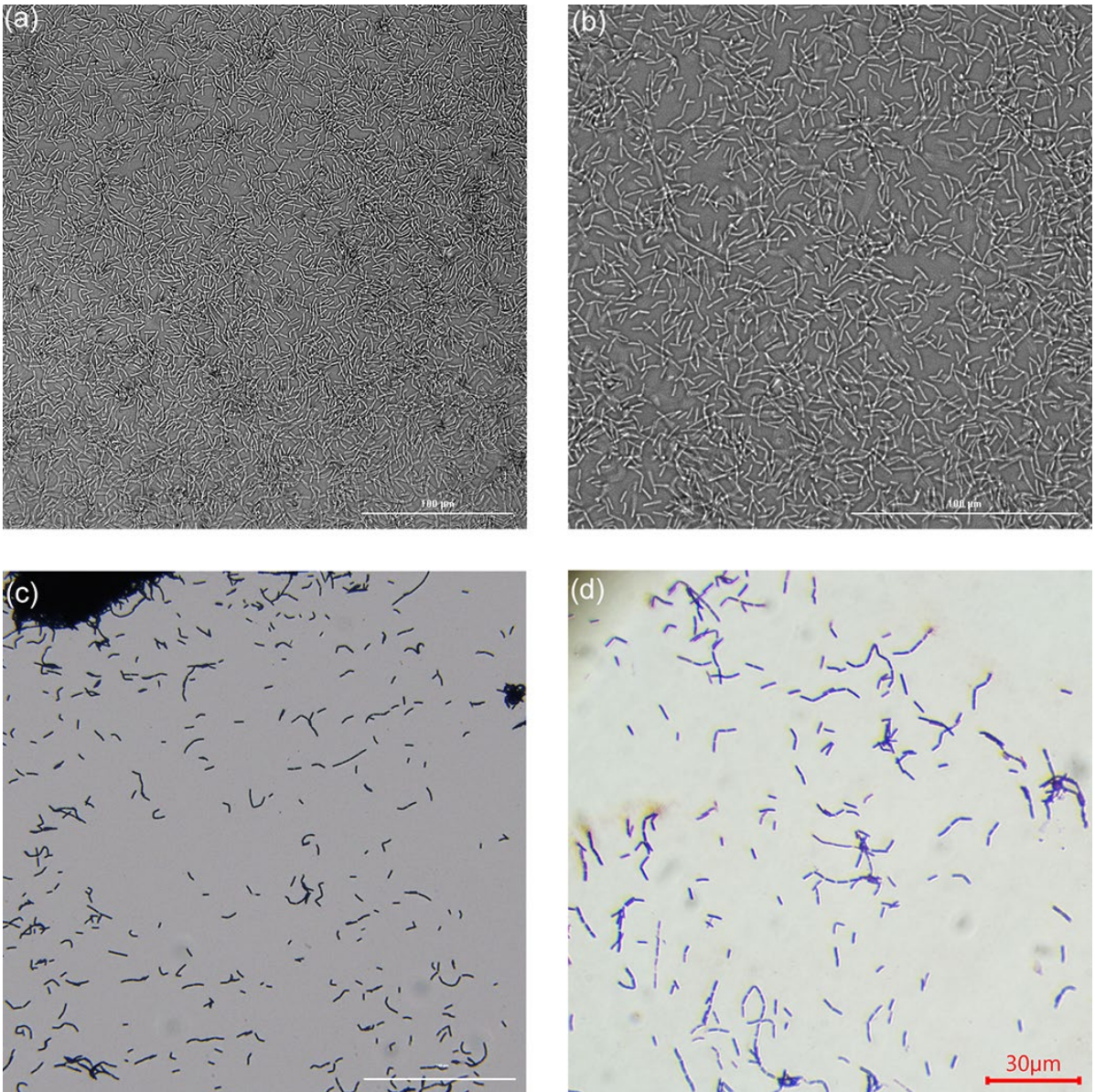


Figure B.35. Images of untreated *B. cereus* after 24 h incubation at 35 °C in Müller-Hinton broth (starting point 5×10^5 CFU/mL). (a) Image obtained after 1:10 dilution in in Müller-Hinton broth using a BioTek Cytation 5 Cell Imaging Multi-Mode Reader (40x objective, Brightfield). Scale bar represents 100 μm . (b) Image obtained after 1:10 dilution in in Müller-Hinton broth using a BioTek Cytation 5 Cell Imaging Multi-Mode Reader (60x objective, Brightfield). Scale bar represents 100 μm . (c) Image obtained after Gram staining using a BioTek Cytation 5 Cell Imaging Multi-Mode Reader (40x objective, Brightfield). Scale bar represents 100 μm . (d) Image obtained after Gram staining using an Amscope Quintuple Plan Infinity Kohler Laboratory Trinocular Compound Microscope (100x oil objective, Brightfield). Scale bar represents 30 μm .

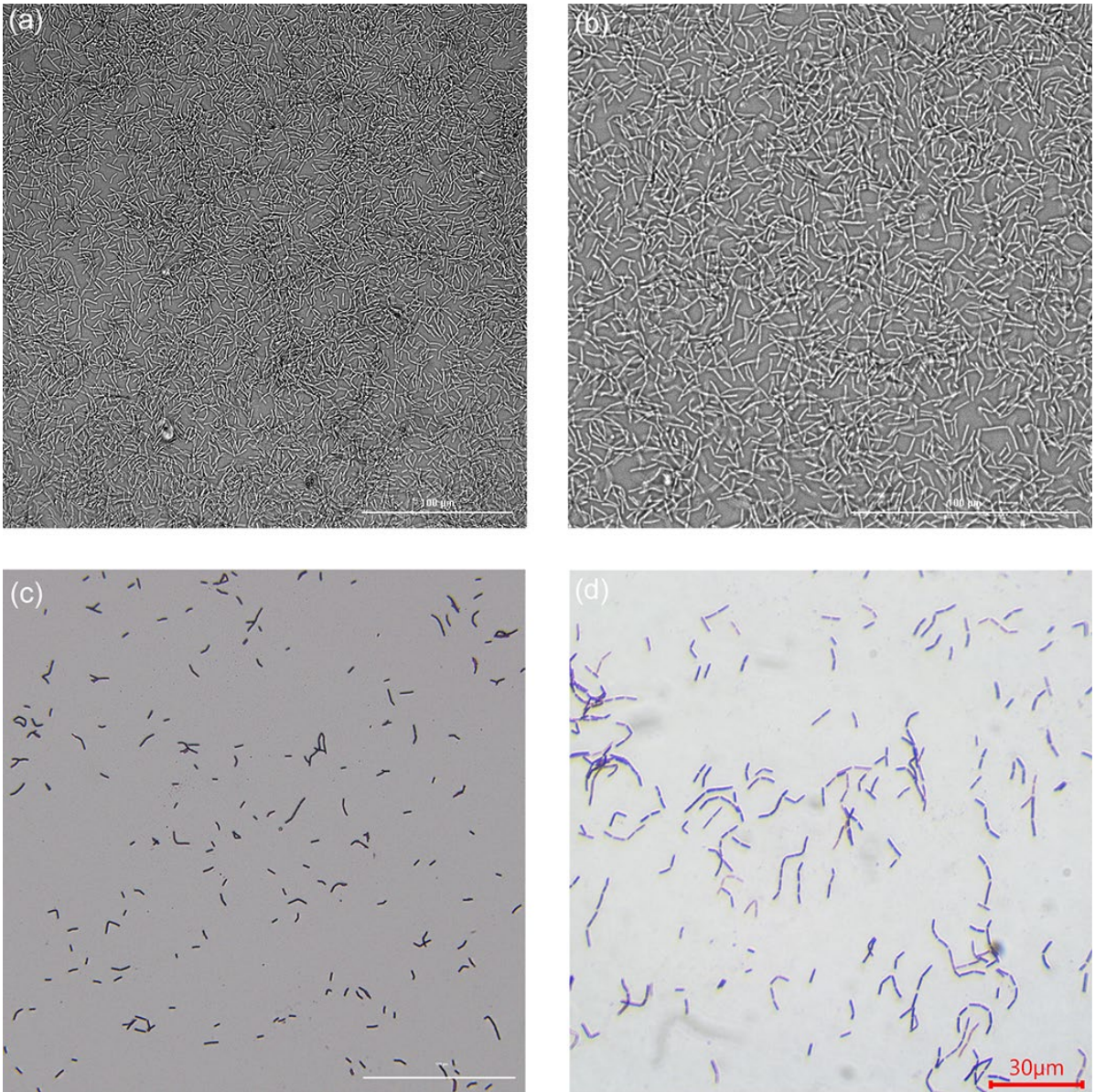


Figure B.36. Images of *B. cereus* after 24 h incubation at 35 °C in Müller-Hinton broth containing 4% DMSO (starting point 5×10^5 CFU/mL). (a) Image obtained after 1:10 dilution in in Müller-Hinton broth using a BioTek Cytation 5 Cell Imaging Multi-Mode Reader (40x objective, Brightfield). Scale bar represents 100 μ m. (b) Image obtained after 1:10 dilution in in Müller-Hinton broth using a BioTek Cytation 5 Cell Imaging Multi-Mode Reader (60x objective, Brightfield). Scale bar represents 100 μ m. (c) Image obtained after Gram staining using a BioTek Cytation 5 Cell Imaging Multi-Mode Reader (40x objective, Brightfield). Scale bar represents 100 μ m. (d) Image obtained after Gram staining using an Amscope Quintuple Plan Infinity Kohler Laboratory Trinocular Compound Microscope (100x oil objective, Brightfield). Scale bar represents 30 μ m.

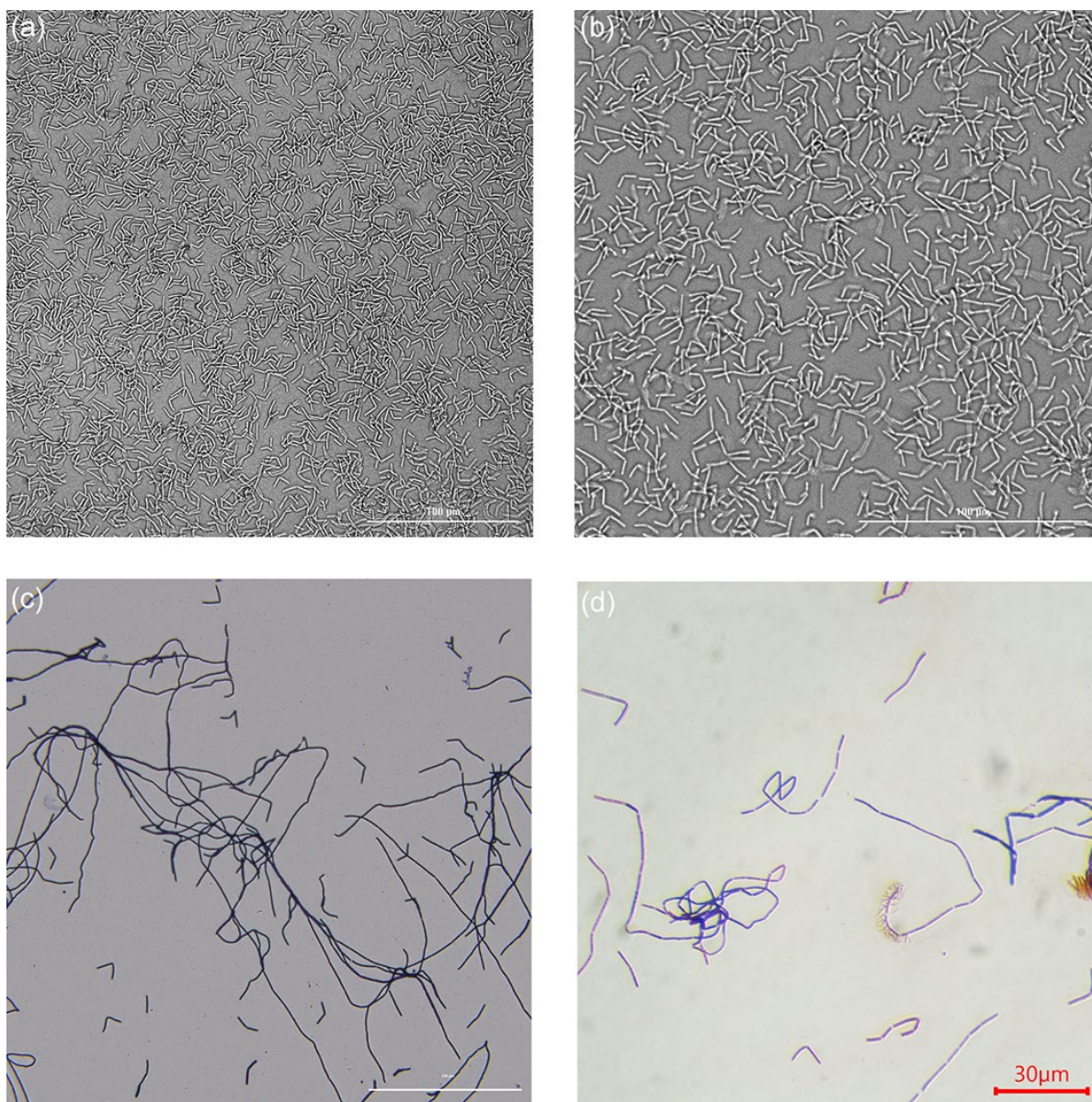


Figure B.37. Images of *B. cereus* after 24 h incubation at 35 °C in Müller-Hinton broth containing 4% DMSO and 20 μM 3.1 (<MIC) (starting point 5×10^5 CFU/mL). (a) Image obtained after 1:10 dilution in in Müller-Hinton broth using a BioTek Cytation 5 Cell Imaging Multi-Mode Reader (40x objective, Brightfield). Scale bar represents 100 μm. (b) Image obtained after 1:10 dilution in in Müller-Hinton broth using a BioTek Cytation 5 Cell Imaging Multi-Mode Reader (60x objective, Brightfield). Scale bar represents 100 μm. (c) Image obtained after Gram staining using a BioTek Cytation 5 Cell Imaging Multi-Mode Reader (40x objective, Brightfield). Scale bar represents 100 μm. (d) Image obtained after Gram staining using an Amscope Quintuple Plan Infinity Kohler Laboratory Trinocular Compound Microscope (100x oil objective, Brightfield). Scale bar represents 30 μm.

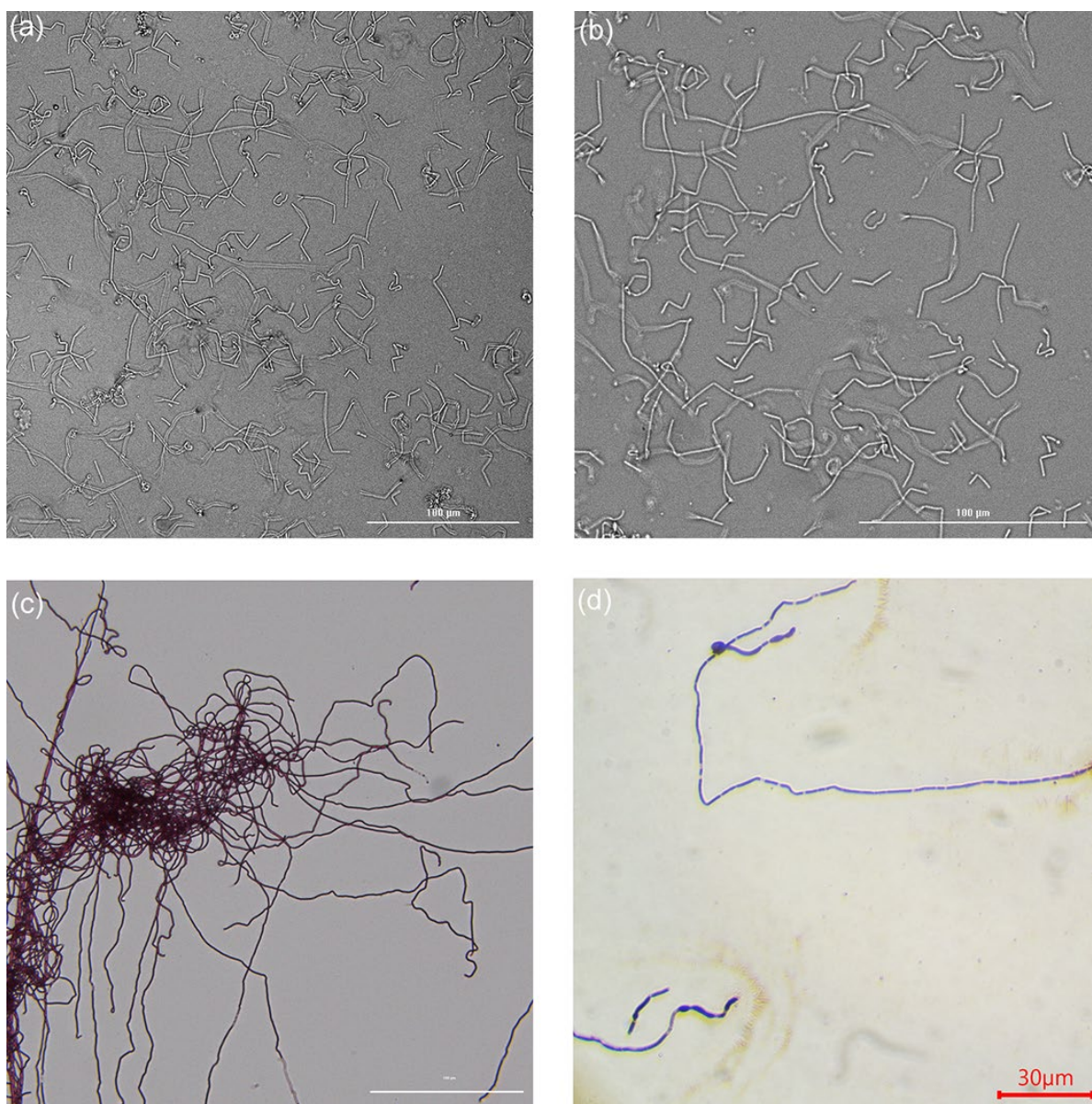


Figure B.38. Images of *B. cereus* after 24 h incubation at 35 °C in Müller-Hinton broth containing 4% DMSO and **25 μM 3.1** (=MIC) (starting point 5×10^5 CFU/mL). (a) Image obtained after 1:10 dilution in Müller-Hinton broth using a BioTek Cytation 5 Cell Imaging Multi-Mode Reader (40x objective, Brightfield). Scale bar represents 100 μm. (b) Image obtained after 1:10 dilution in Müller-Hinton broth using a BioTek Cytation 5 Cell Imaging Multi-Mode Reader (60x objective, Brightfield). Scale bar represents 100 μm. (c) Image obtained after Gram staining using a BioTek Cytation 5 Cell Imaging Multi-Mode Reader (40x objective, Brightfield). Scale bar represents 100 μm. (d) Image obtained after Gram staining using an Amscope Quintuple Plan Infinity Kohler Laboratory Trinocular Compound Microscope (100x oil objective, Brightfield). Scale bar represents 30 μm.

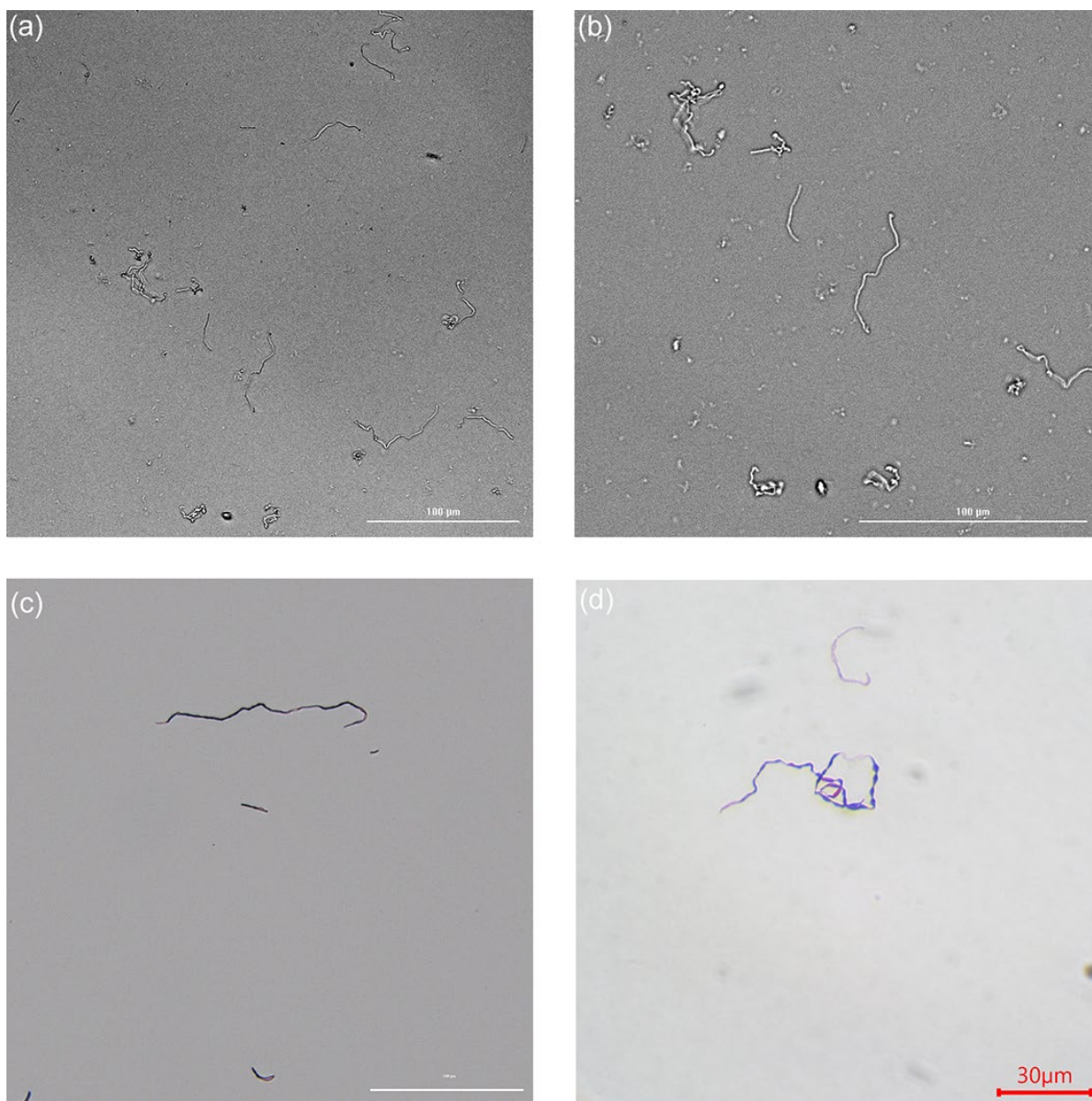


Figure B.39. Images of *B. cereus* after 24 h incubation at 35 °C in Müller-Hinton broth containing 4% DMSO and 30 μM 3.1 (>MIC) (starting point 5×10^5 CFU/mL). (a) Image obtained after 1:10 dilution in in Müller-Hinton broth using a BioTek Cytation 5 Cell Imaging Multi-Mode Reader (40x objective, Brightfield). Scale bar represents 100 μm. (b) Image obtained after 1:10 dilution in in Müller-Hinton broth using a BioTek Cytation 5 Cell Imaging Multi-Mode Reader (60x objective, Brightfield). Scale bar represents 100 μm. (c) Image obtained after Gram staining using a BioTek Cytation 5 Cell Imaging Multi-Mode Reader (40x objective, Brightfield). Scale bar represents 100 μm. (d) Image obtained after Gram staining using an Amscope Quintuple Plan Infinity Kohler Laboratory Trinocular Compound Microscope (100x oil objective, Brightfield). Scale bar represents 30 μm.

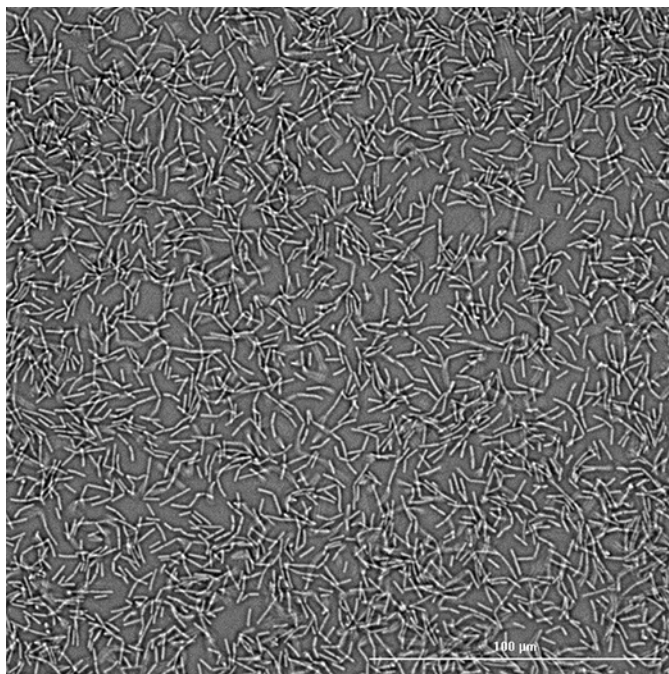


Figure B.40. Images of *B. cereus* after 24 h incubation at 35 °C in Müller-Hinton broth containing 4% DMSO and **100 μM 3.2** (starting point 5×10^5 CFU/mL). Image obtained after 1:10 dilution in in Müller-Hinton broth using a BioTek Cytation 5 Cell Imaging Multi-Mode Reader (60x objective, Brightfield). Scale bar represents 100 μm.

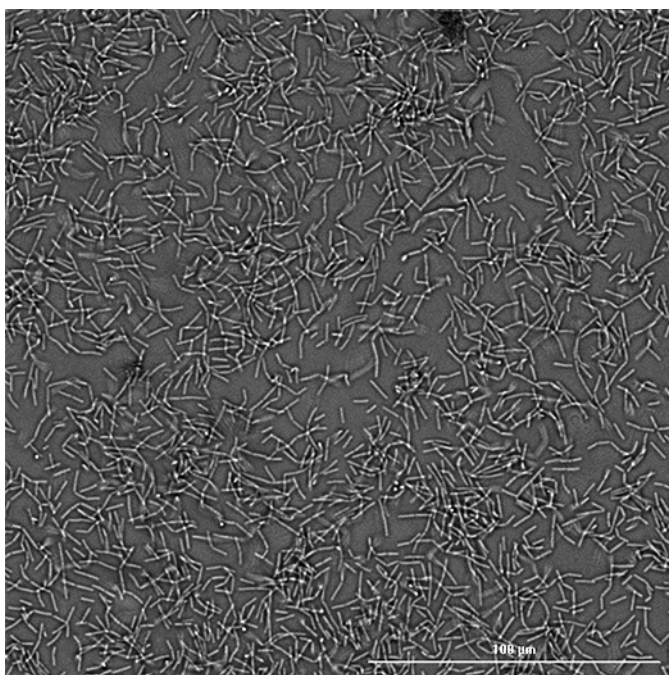


Figure B.41. Images of *B. cereus* after 24 h incubation at 35 °C in Müller-Hinton broth containing 4% DMSO and **100 μM 3.3** (starting point 5×10^5 CFU/mL). Image obtained after 1:10 dilution in in Müller-Hinton broth using a BioTek Cytation 5 Cell Imaging Multi-Mode Reader (60x objective, Brightfield). Scale bar represents 100 μm.

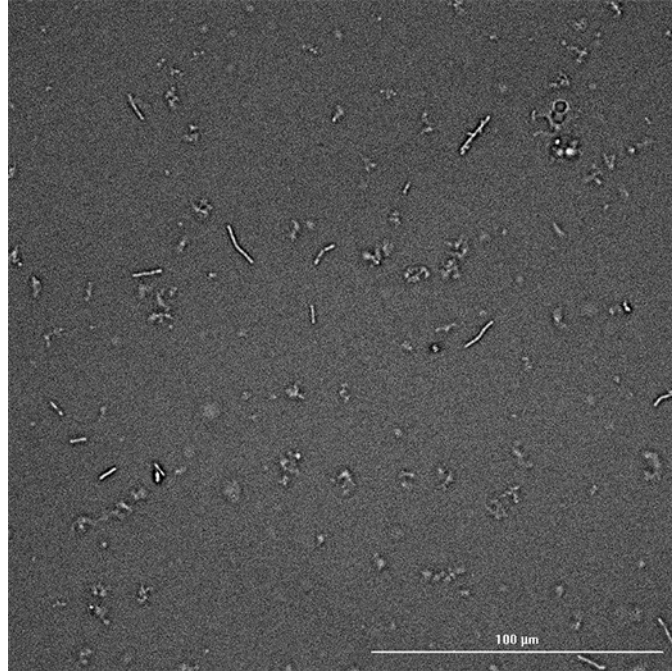


Figure B.42. Images of *B. cereus* after 24 h incubation at 35 °C in Müller-Hinton broth containing 4% DMSO and 6.25 μM **3.4** (starting point 5×10^5 CFU/mL). Image obtained after 1:10 dilution in in Müller-Hinton broth using a BioTek Cytation 5 Cell Imaging Multi-Mode Reader (60x objective, Brightfield). Scale bar represents 100 μm.

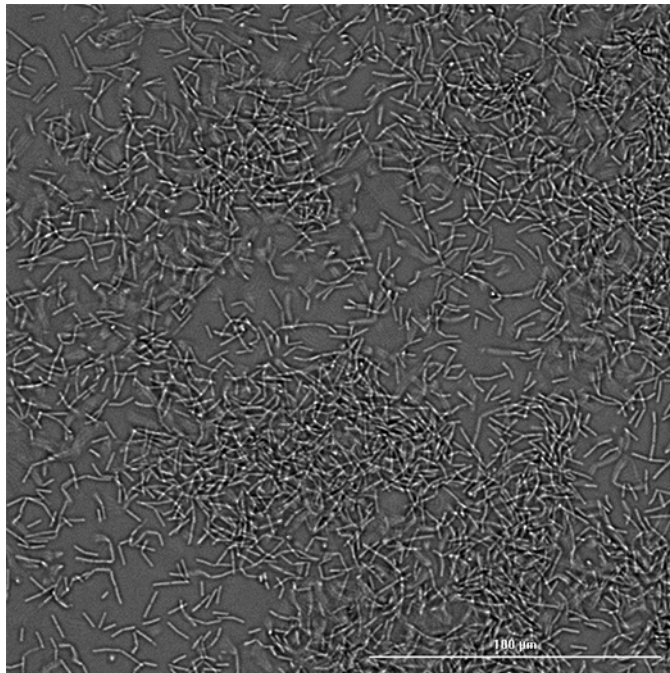


Figure B.43. Images of *B. cereus* after 24 h incubation at 35 °C in Müller-Hinton broth containing 4% DMSO and 100 μM **18-crown-6** (starting point 5×10^5 CFU/mL). Image obtained after 1:10 dilution in in Müller-Hinton broth using a BioTek Cytation 5 Cell Imaging Multi-Mode Reader (60x objective, Brightfield). Scale bar represents 100 μm.

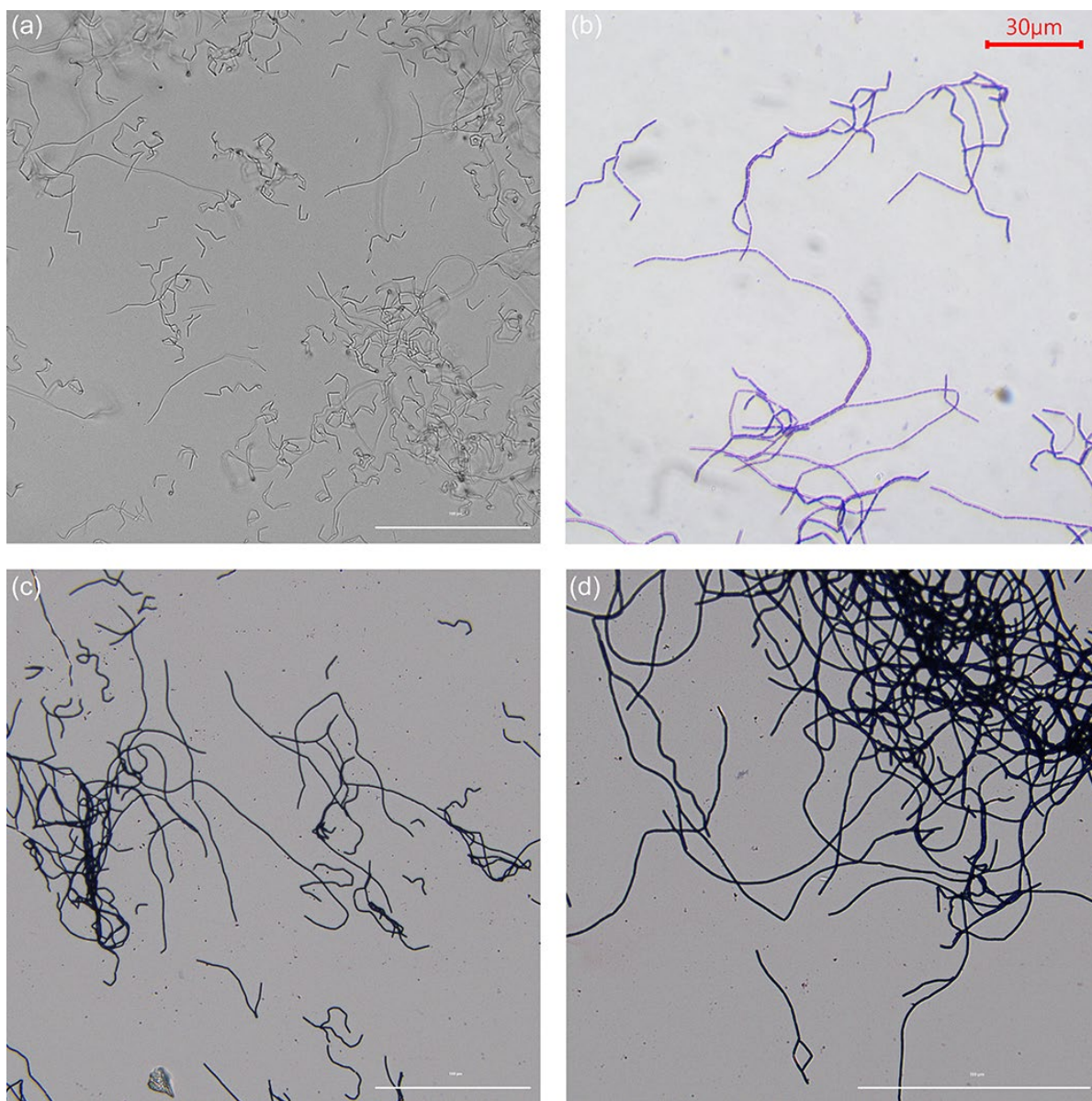


Figure B.44. Images of *B. cereus* after 24 h incubation at 35 °C in Müller-Hinton broth containing 4% DMSO and **64 μM duramycin** (=MIC) (starting point 5×10^5 CFU/mL). (a) Image obtained after 1:10 dilution in Müller-Hinton broth using a BioTek Cytation 5 Cell Imaging Multi-Mode Reader (40x objective, Brightfield). Scale bar represents 100 μm. (b) Image obtained after Gram staining using an Amscope Quintuple Plan Infinity Kohler Laboratory Trinocular Compound Microscope (100x oil objective, Brightfield). Scale bar represents 30 μm. (c) Image obtained after Gram staining using a BioTek Cytation 5 Cell Imaging Multi-Mode Reader (40x objective, Brightfield). Scale bar represents 100 μm. (d) Image obtained after Gram staining using a BioTek Cytation 5 Cell Imaging Multi-Mode Reader (60x objective, Brightfield). Scale bar represents 100 μm.

B.9 Membrane depolarization assay

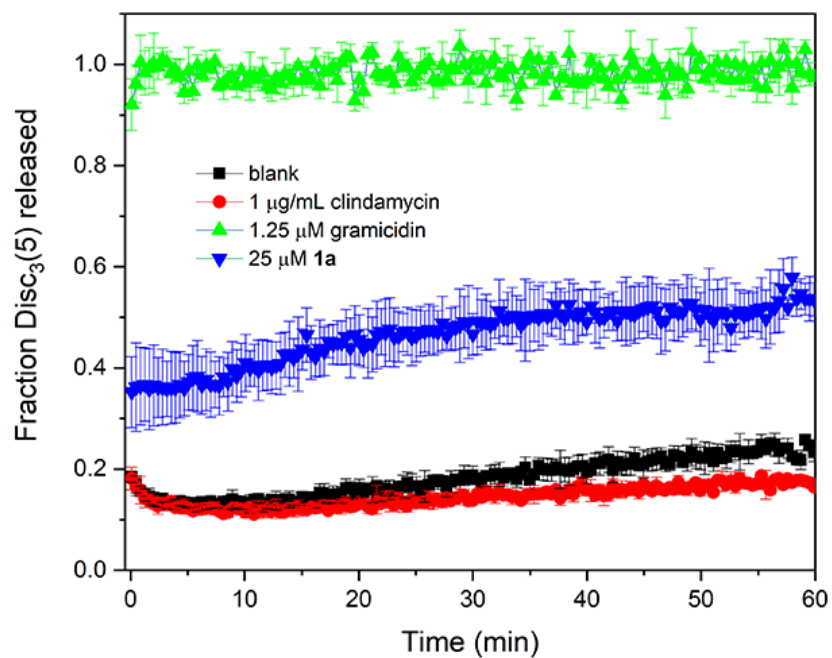


Figure B.45. Kinetic trace of the membrane depolarization of *B. cereus* by 1xMIC of clindamycin (negative control), gramicidin (positive control) and **3.1**, using Disc₃(5) as the voltage-dependent fluorophore.

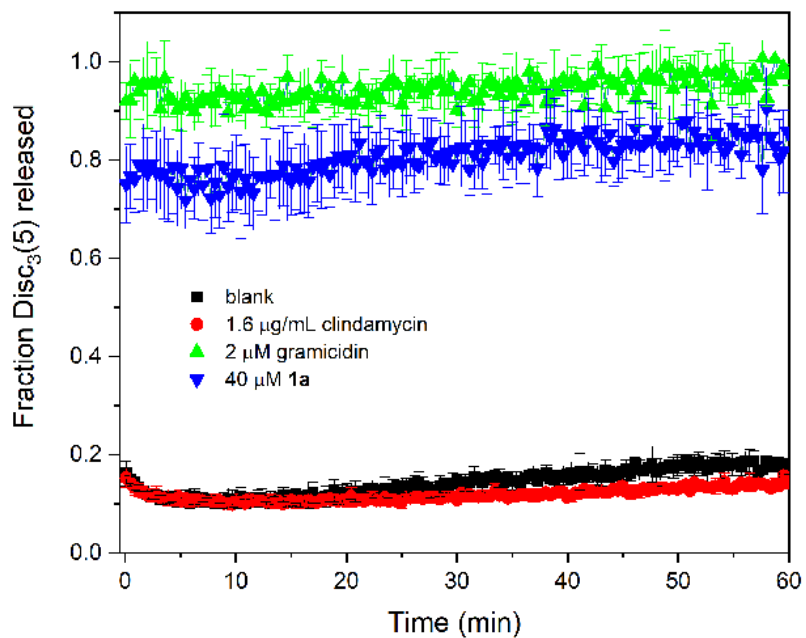


Figure B.46. Kinetic trace of the membrane depolarization of *B. cereus* by 1.6xMIC of clindamycin (negative control), gramicidin (positive control) and **3.1**, using Disc₃(5) as the voltage-dependent fluorophore.

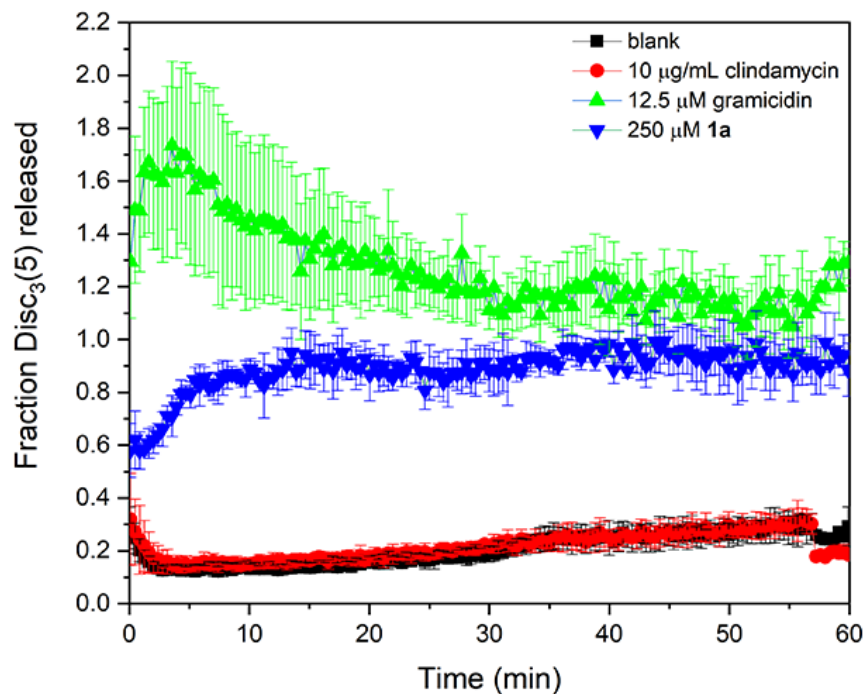


Figure B.47. Kinetic trace of the membrane depolarization of *B. cereus* by 10xMIC of clindamycin (negative control), gramicidin (positive control) and **3.1**, using Disc₃(5) as the voltage-dependent fluorophore.

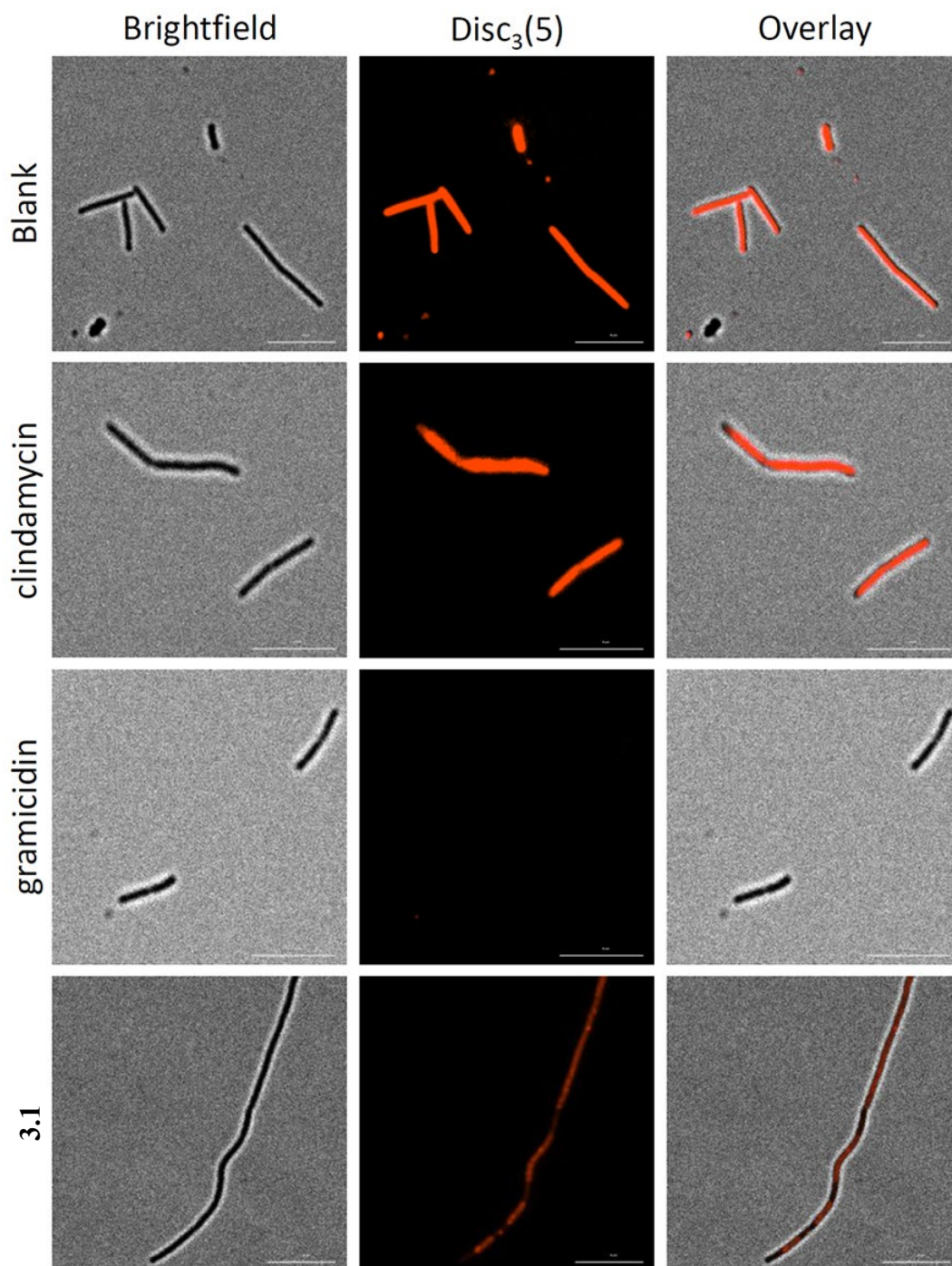


Figure B.48. Images of membrane depolarization of *B. cereus* by 1xMIC of clindamycin (negative control), gramicidin (positive control) and **3.1**, using Disc₃(5) as the voltage-dependent fluorophore. The *B. cereus* cells were incubated for 15 minutes with 4% DMSO (blank), 1 μg/mL clindamycin, 1.25 μM gramicidin, or 25 μM **3.1**. Absence of fluorescence indicates that the cells are depolarized. Scale bars represent 10 μm.

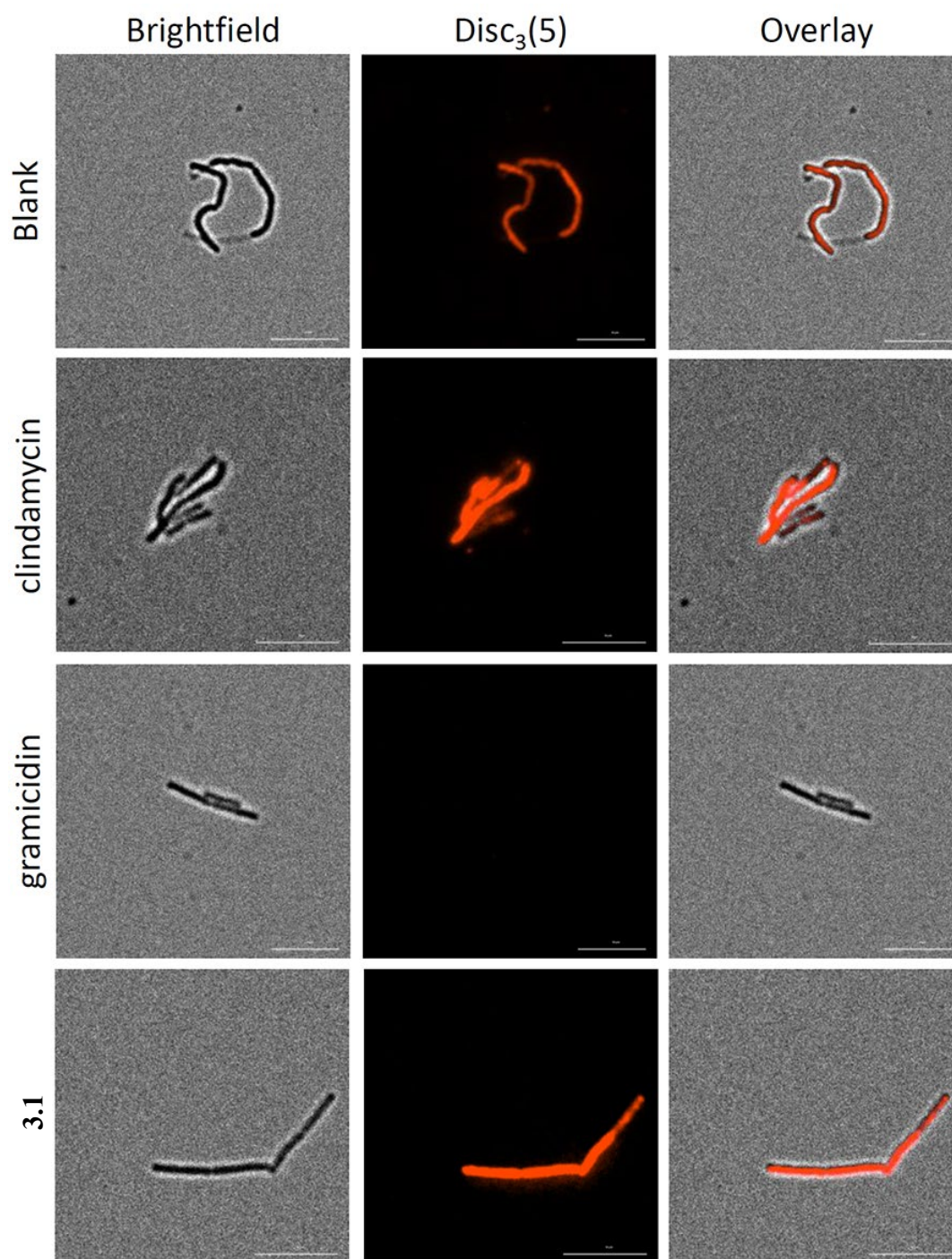


Figure B.49. Images of membrane depolarization of *B. cereus* by 1xMIC of clindamycin (negative control), gramicidin (positive control) and **3.1**, using Disc₃(5) as the voltage-dependent fluorophore. The *B. cereus* cells were incubated for 1 hour with 4% DMSO (blank), 1 µg/mL clindamycin, 1.25 µM gramicidin, or 25 µM **3.1**. Absence of fluorescence indicates that the cells are depolarized. Scale bars represent 10 µm.

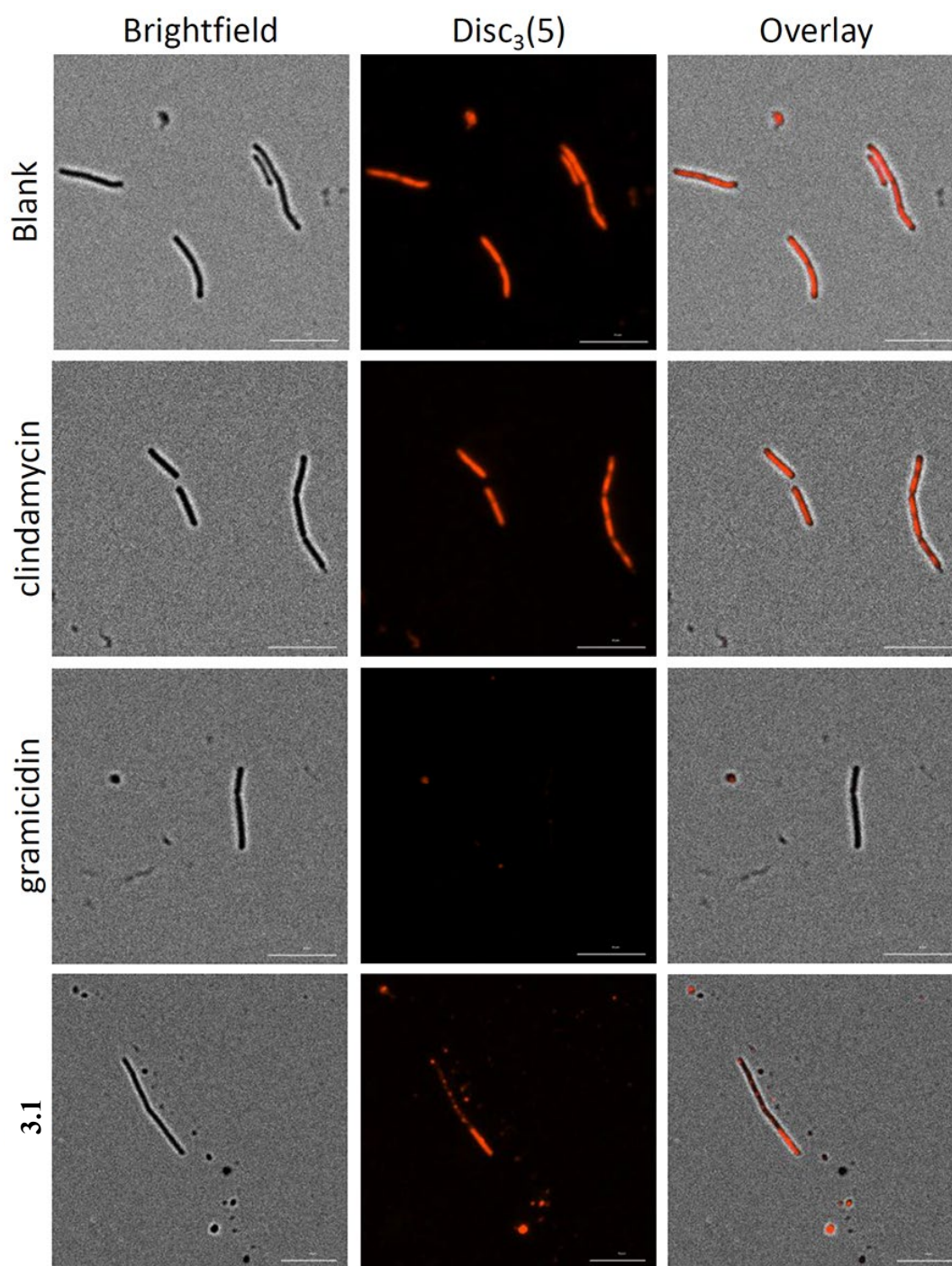


Figure B.50. Images of membrane depolarization of *B. cereus* by 1.6xMIC of clindamycin (negative control), gramicidin (positive control) and **3.1**, using Disc₃(5) as the voltage-dependent fluorophore. The *B. cereus* cells were incubated for 15 minutes with 4% DMSO (blank), 1.6 $\mu\text{g}/\text{mL}$ clindamycin, 2 μM gramicidin, or 40 μM **3.1**. Absence of fluorescence indicates that the cells are depolarized. Scale bars represent 10 μm .

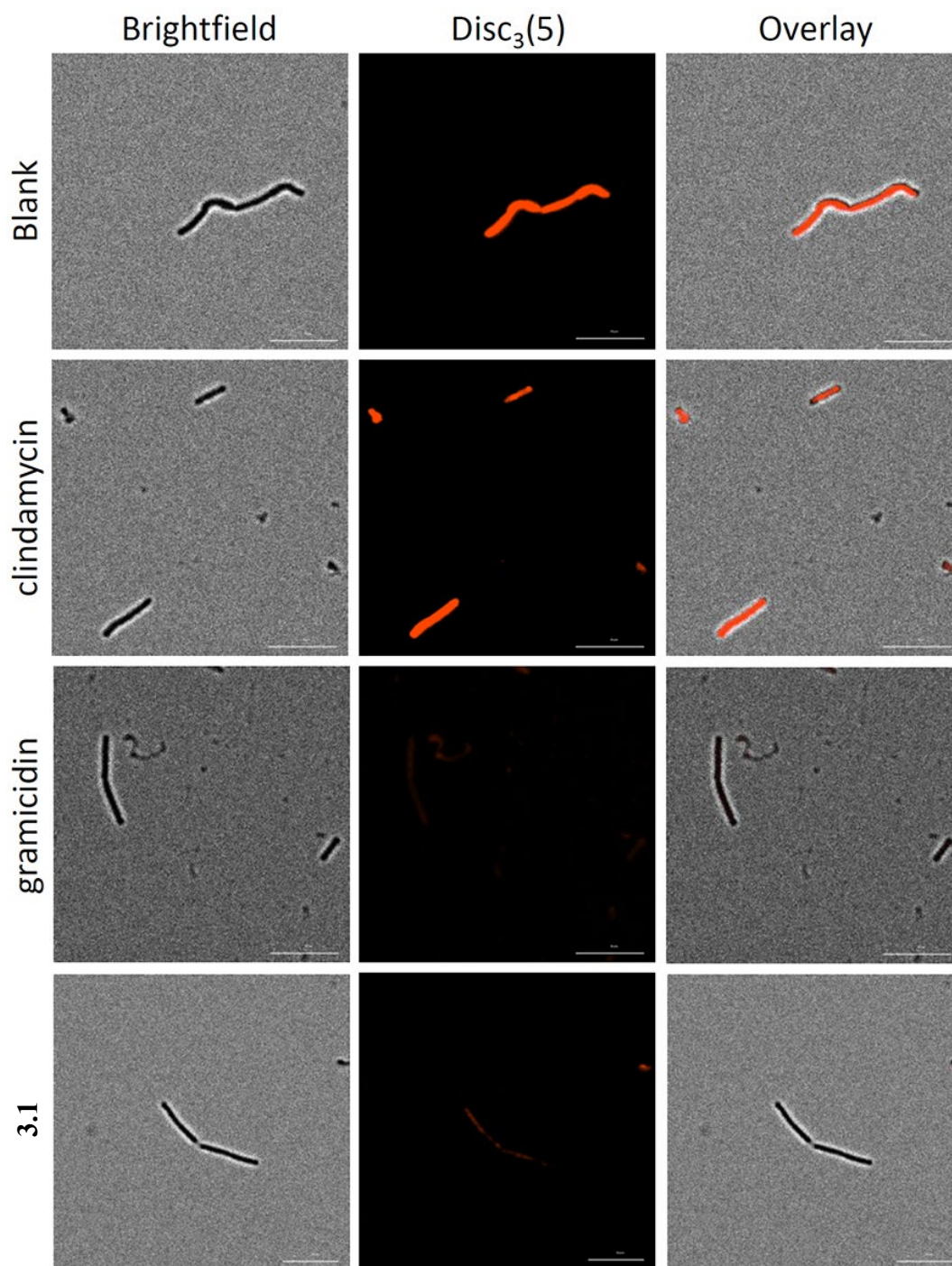


Figure B.51. Images of membrane depolarization of *B. cereus* by 1.6xMIC of clindamycin (negative control), gramicidin (positive control) and **3.1**, using Disc₃(5) as the voltage-dependent fluorophore. The *B. cereus* cells were incubated for 1 hour with 4% DMSO (blank), 1.6 $\mu\text{g}/\text{mL}$ clindamycin, 2 μM gramicidin, or 40 μM **3.1**. Absence of fluorescence indicates that the cells are depolarized. Scale bars represent 10 μm .

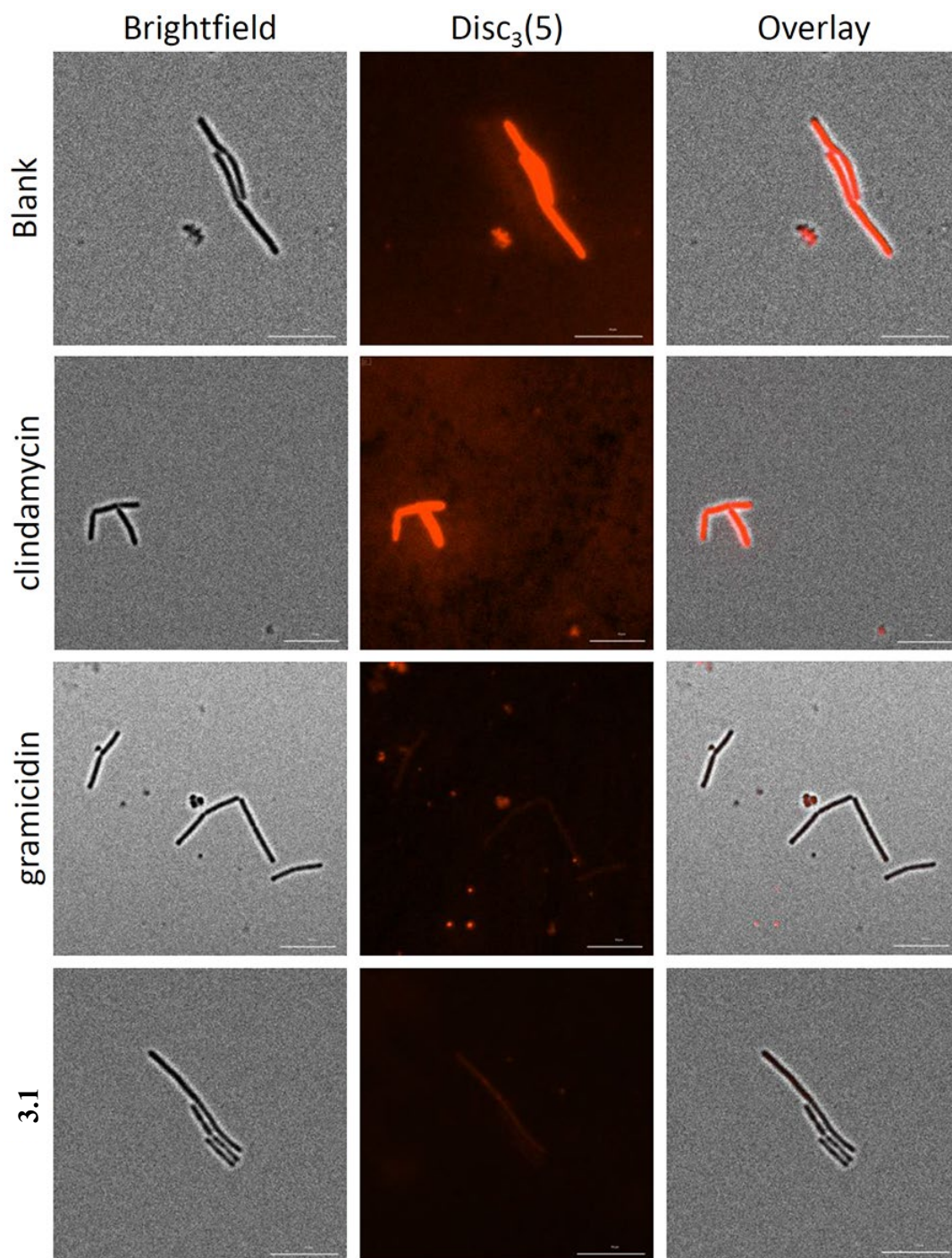


Figure B.52. Images of membrane depolarization of *B. cereus* by 10xMIC of clindamycin (negative control), gramicidin (positive control) and **3.1**, using Disc₃(5) as the voltage-dependent fluorophore. The *B. cereus* cells were incubated for 15 minutes with 4% DMSO (blank), 10 µg/mL clindamycin, 12.5 µM gramicidin, or 250 µM **3.1**. Absence of fluorescence indicates that the cells are depolarized. Scale bars represent 10 µm.

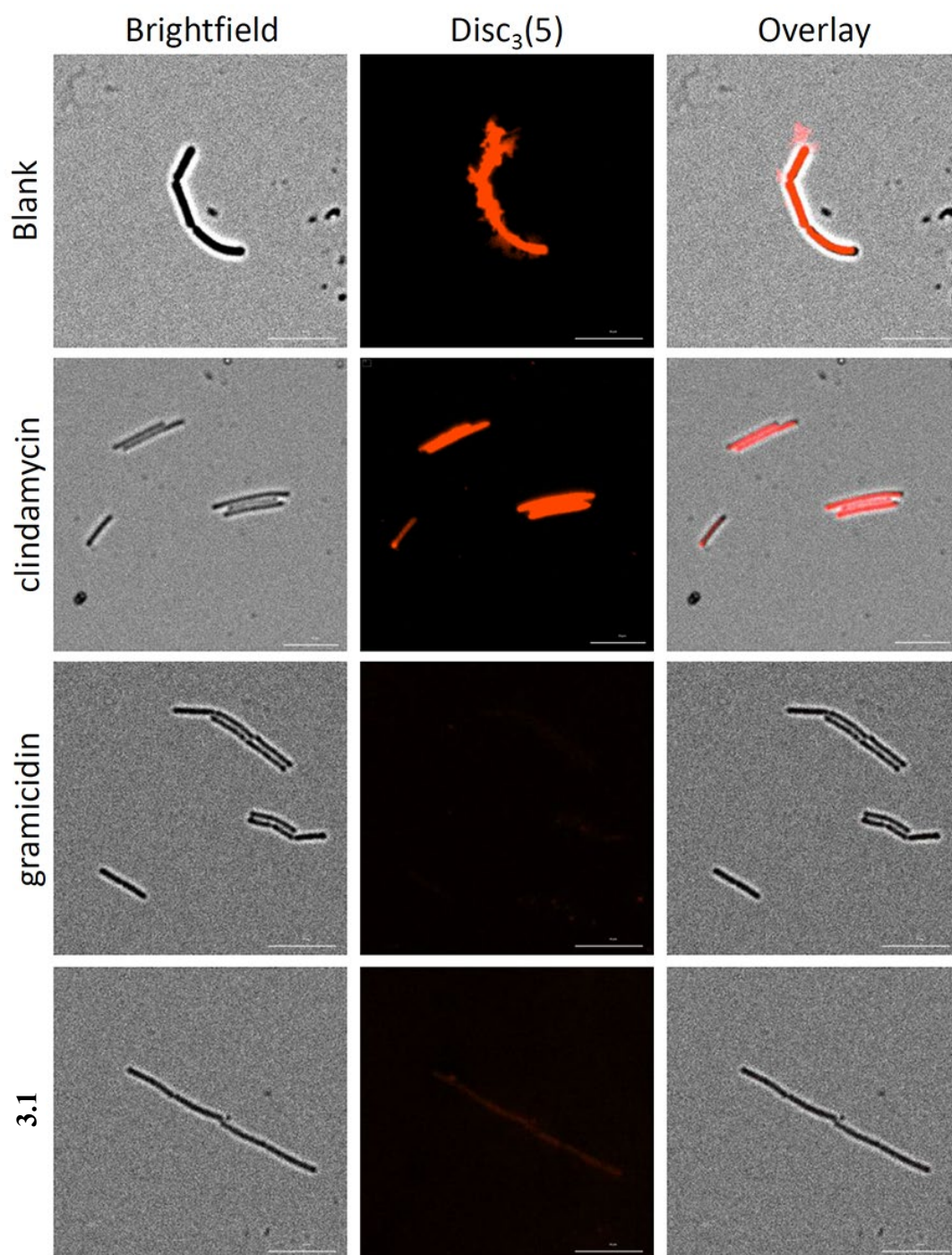


Figure B.53. Images of membrane depolarization of *B. cereus* by 10xMIC of clindamycin (negative control), gramicidin (positive control) and **3.1**, using Disc₃(5) as the voltage-dependent fluorophore. The *B. cereus* cells were incubated for 1 hour with 4% DMSO (blank), 10 $\mu\text{g}/\text{mL}$ clindamycin, 12.5 μM gramicidin, or 250 μM **3.1**. Absence of fluorescence indicates that the cells are depolarized. Scale bars represent 10 μm .

APPENDIX C

SUPPLEMENTARY INFORMATION FOR CHAPTER 4

C.1 Hemolysis data

Table C.1: Hemolytic activity for **compound 3.4** represented by the concentration of host needed to cause 50% hemolysis in red blood cells (HC_{50})

Concentration (μM)	Biological repeat 1			Biological repeat 2			average	STDEV
	repeat 1	repeat 2	repeat 3	repeat 1	repeat 2	repeat 3		
400		22.6257	20.7103	32.56652	29.24058	31.18071	27.26476	5.287463
350	24.06225	17.59777	20.47087	28.13193	24.25166	17.32262	21.97285	4.254758
300	19.03432	15.92179	14.00638	26.46896	18.98559	13.16519	17.93037	4.845177
250	13.52753	12.09098	13.04868	19.26275	10.39357	11.77938	13.35048	3.094362
200	13.28811	10.89385	13.76696	19.81707	12.88803	12.3337	13.83129	3.094829
150	10.89385	10.89385	10.415	16.21397	11.50222	12.3337	12.0421	2.147807
100	12.56983	11.13328	11.37271	19.26275	13.44235	17.32262	14.18392	3.346953
HC_{50} (μM)	468.654	568.0973	656.0027	560.9973	502.4643	437.2946	532.2517	79.21407

C.2 Software metadata from cell imaging

Camera Name: Nikon A1plus

Numerical Aperture: 1.4

Refractive Index: 1.515

Number of Picture Planes: 3

Plane #1:

Name: DAPI

Component Count: 1

Modality: Widefield Fluorescence, Laser Scan Confocal

Camera Settings:

{Scanner Selection}: Galvano

{Detector Selection}: DU4

{GaAsP}: CH2/3;

{Optical Path Mode}: Manual

{First Dichroic Mirror}: 405/488/561/640

{First Filter Cube}: 450/50

{Second Filter Cube}: 525/50

{Third Filter Cube}: 595/50

CH1 {Laser Wavelength}: 405.0 {Laser Power}: 20.3

{PMT HV}: 85 {PMT Offset}: 0

CH2 {Laser Wavelength}: 488.0 {Laser Power}: 1.7

{PMT HV}: 22 {PMT Offset}: 0

CH4 {Laser Wavelength}: 638.0 {Laser Power}: 10.9

{PMT HV}: 69 {PMT Offset}: 0

{Pinhole Size(um)}: 38.31

{HV LinearCorrection}: Off

{Scan Direction}: One way

{Scanner Zoom}: 1.715

```
{Scan Speed}: 1
{Channel Series Mode}: Custom
{Channel Series Pass}: [CH1][CH2][CH3][CH4]
{Line Skip}: None
{Frame Skip}: 0
{Line Average Mode}: None
{Line Average/Integrate Count}: 0
Stim1    {Type}: Nothing
         {Scan Speed}: 1
Stim2    {Type}: Nothing
         {Scan Speed}: 1
Stim3    {Type}: Nothing
         {Scan Speed}: 1
{Head type}: Legacy (FOV18)
```

Figure C.1: Metadata from the Nikon A1 microscope. General information is given in Materials and Methods.

C.3 Object selection in CellProfiler™

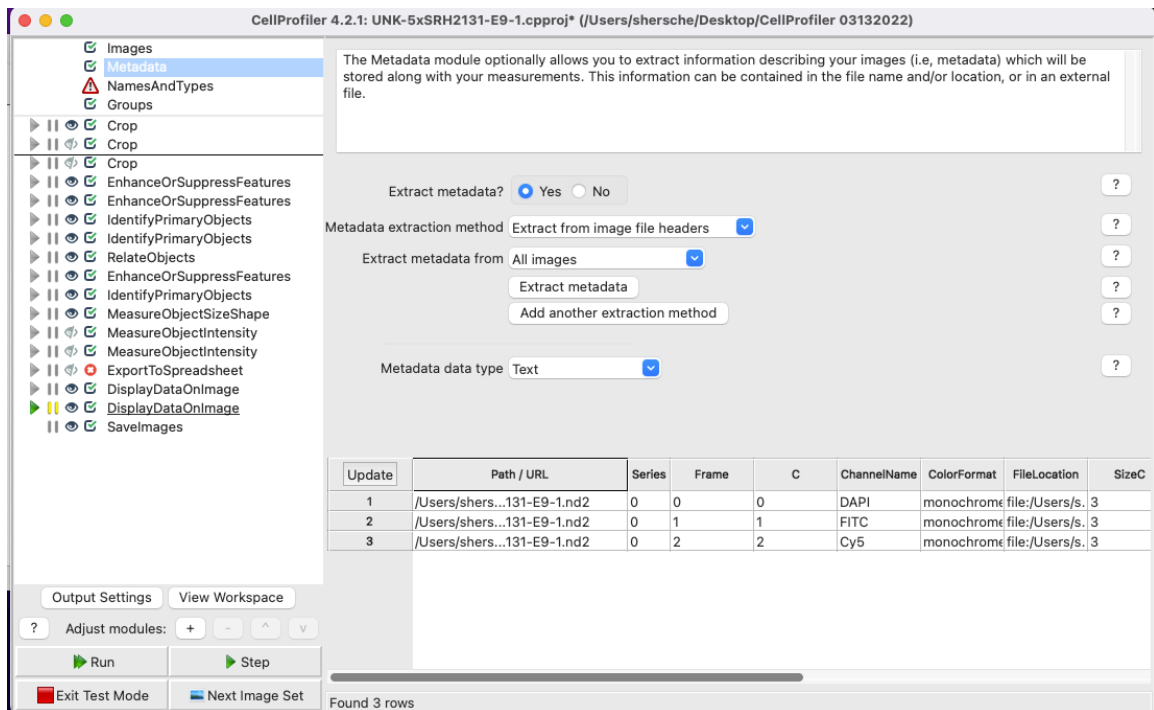


Figure C.2: CellProfiler interface and workflow list shown on the right. Each “primary object” refers to the images taken within the stain/channel selected. Object intensity was measured for each channel individually within the object’s bounds.

C.4 Example images of object selection in CellProfiler™

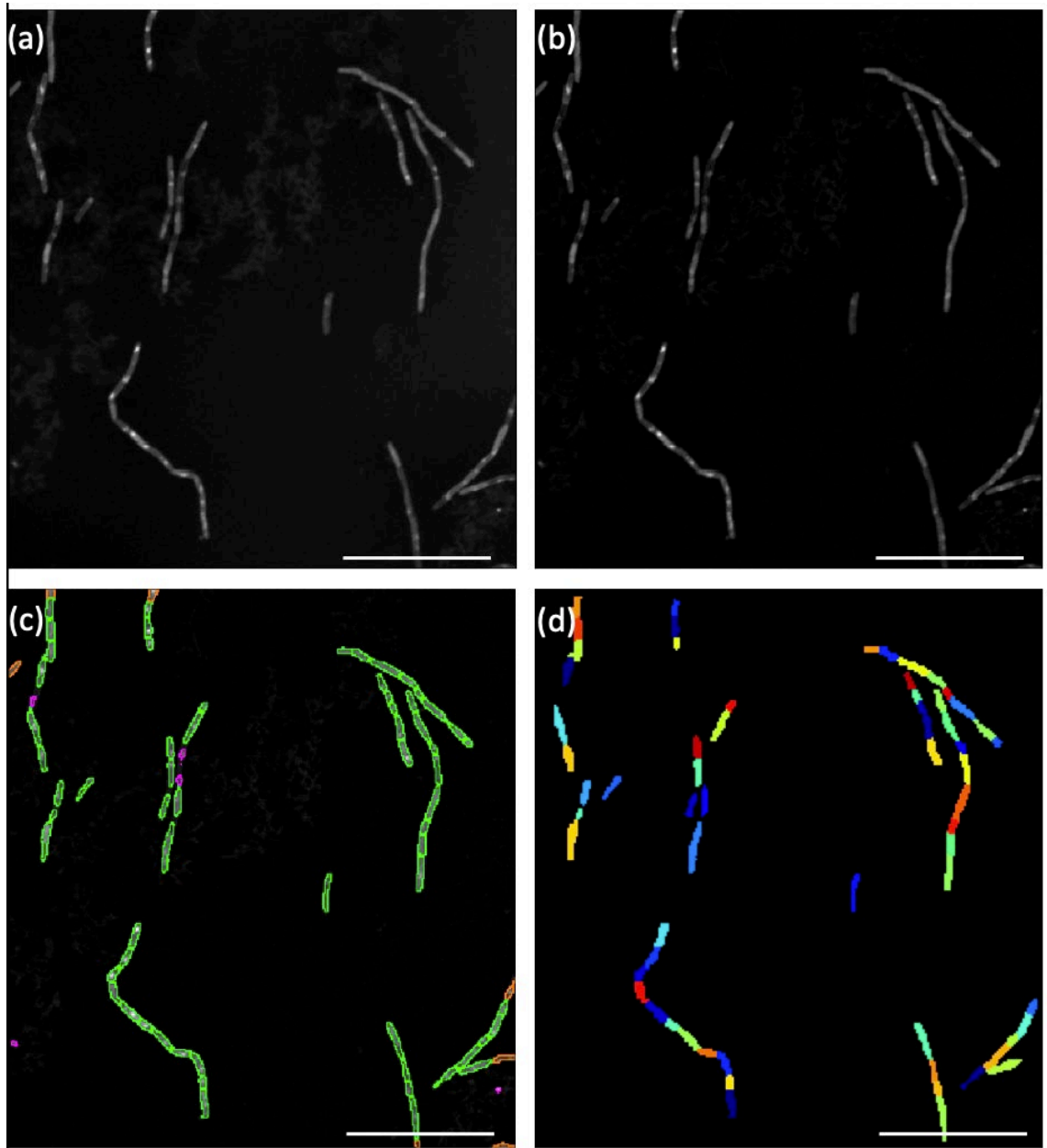


Figure C.3: Images stained with FM4-64 dye in the Cy5 channel. Images were cropped for visibility, a) cropped image, b) enhanced image, c) object outlines, d) object selection. Scale bar = 24 μm .

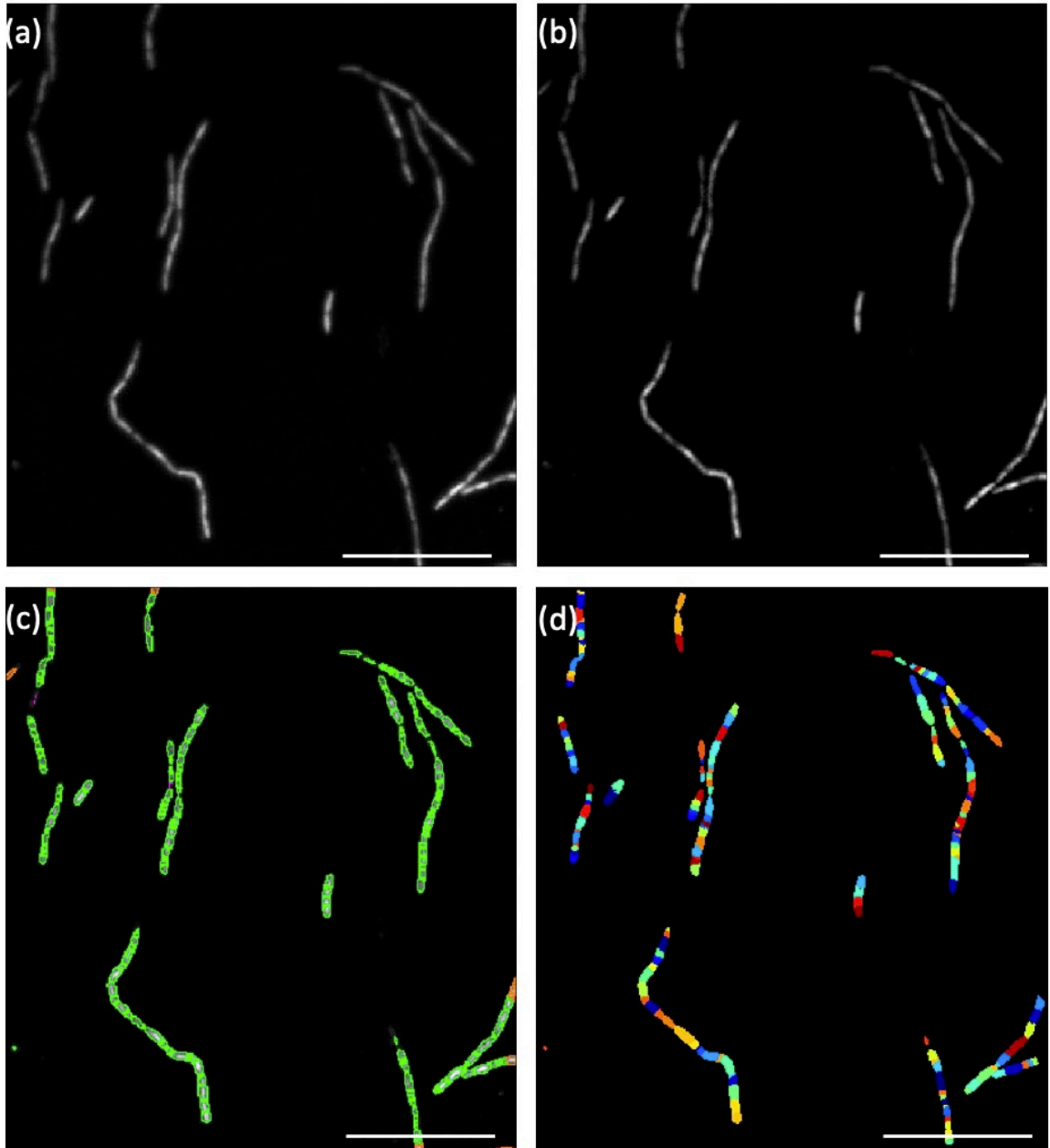


Figure C.4: Images stained with DAPI in the DAPI channel. Images were cropped for visibility, a) cropped image, b) enhanced image, c) object outlines, d) object selection. Scale bar = 24 μm .

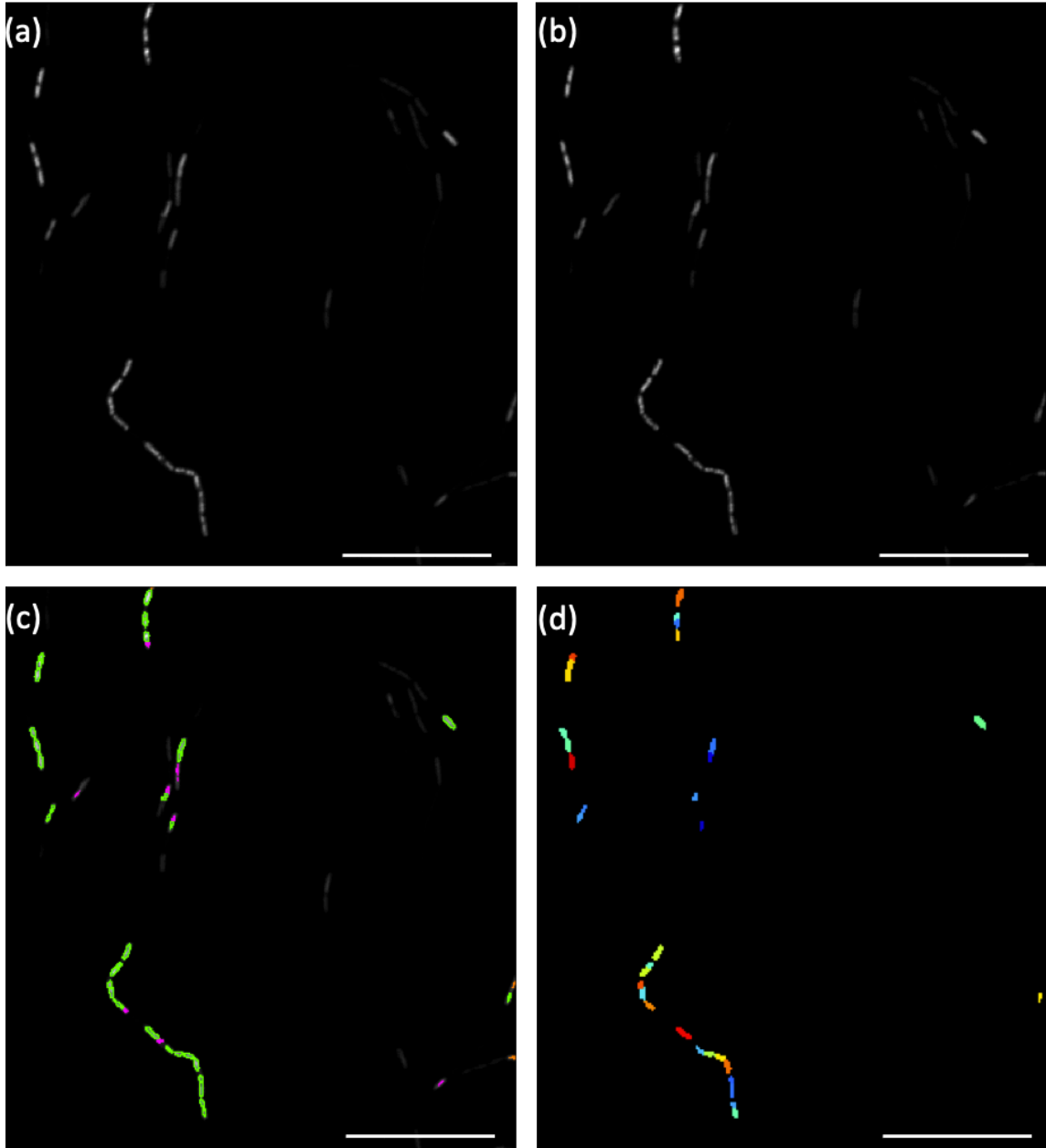


Figure C.5: Images from the FITC channel stained with Sytox Green dye to show nuclei with destabilized membranes. Images were cropped for visibility, a) cropped image, b) enhanced image, c) object outlines, d) object selection. Scale bar = 24 μm .

C.5 Variable plots and Euclidean distance tables from XLSTAT

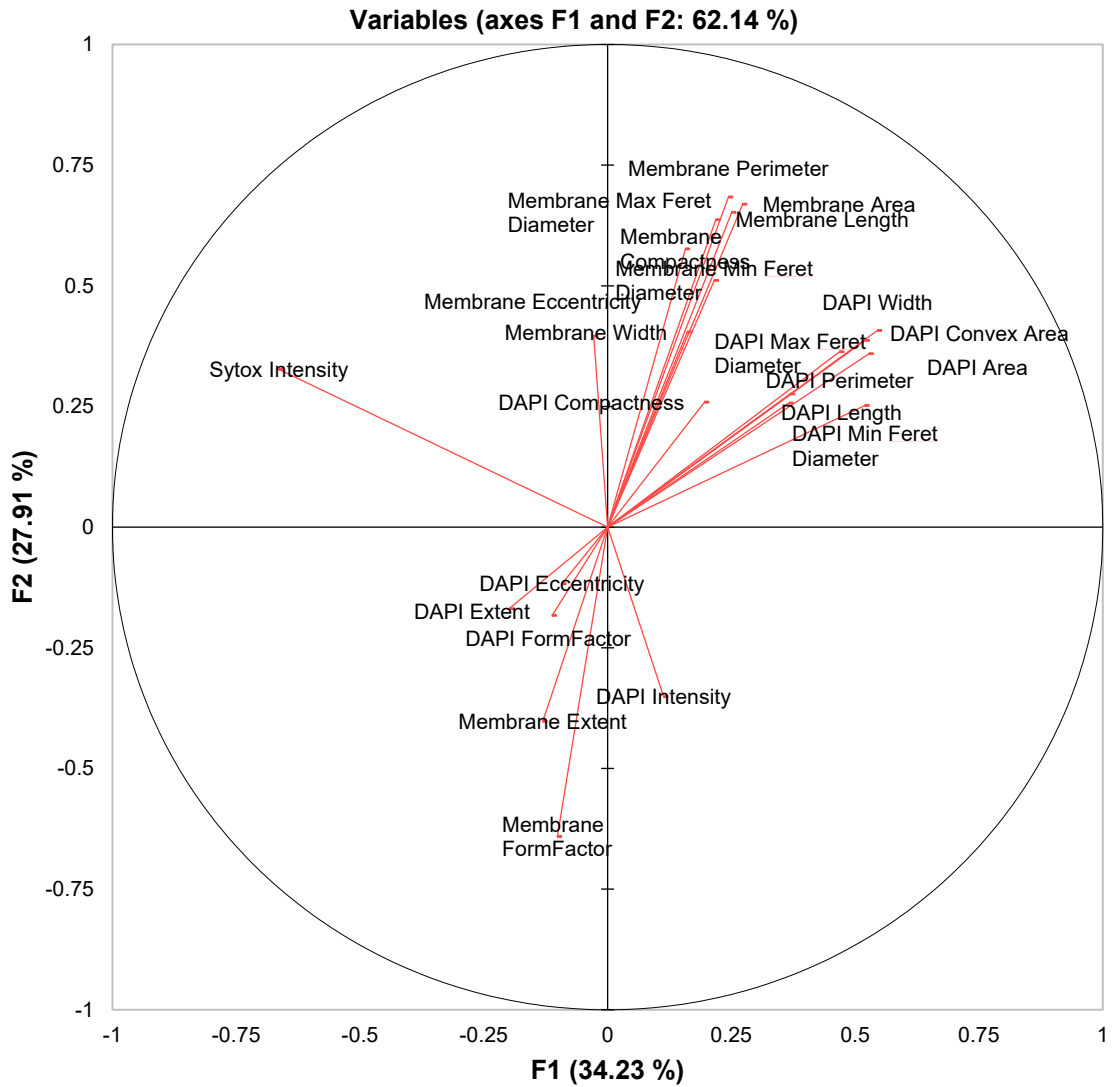


Figure C.6: Factor score plot generated by XLSTAT showing F1 and F2.

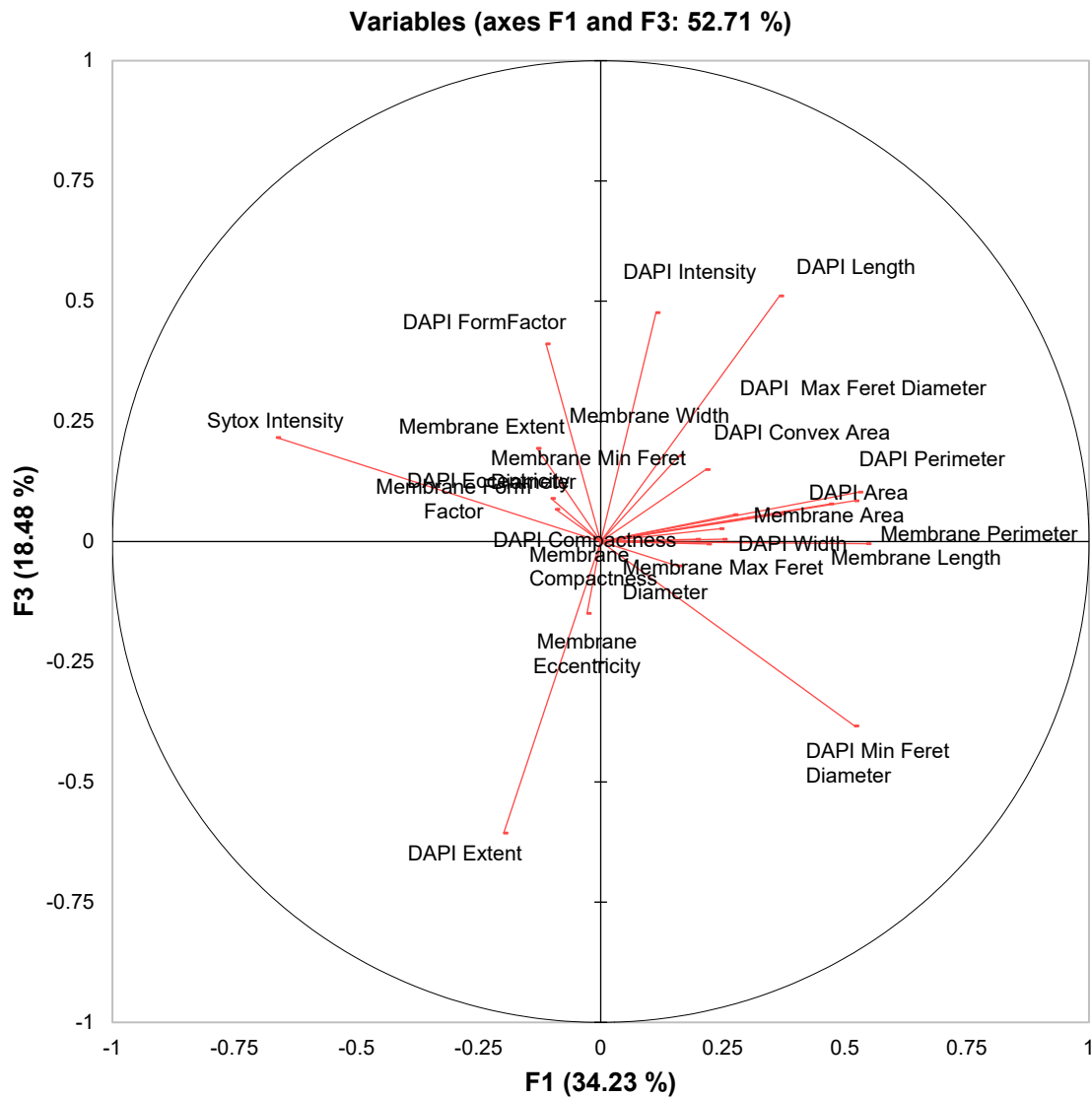


Figure C.7: Factor scores generated by XLSTAT showing F1 and F3.

Table C.2: Proximity matrix for Euclidean distances based on Ward's method. Lower values represent closer correlations in the dendrogram.

	CW	Ctrl	FS	MEM	PS	RNA	UNK
CW	0	3.106	1.738	3.174	3.403	1.555	2.680
Ctrl	3.106	0	2.273	3.159	3.708	1.754	3.426
FS	1.738	2.273	0	1.881	2.486	0.789	1.578
MEM	3.174	3.159	1.881	0	3.827	2.207	0.847
PS	3.403	3.708	2.486	3.827	0	3.026	3.437
RNA	1.555	1.754	0.789	2.207	3.026	0	2.081
UNK	2.680	3.426	1.578	0.847	3.437	2.081	0

C.6 Boxplots for cell object measurements

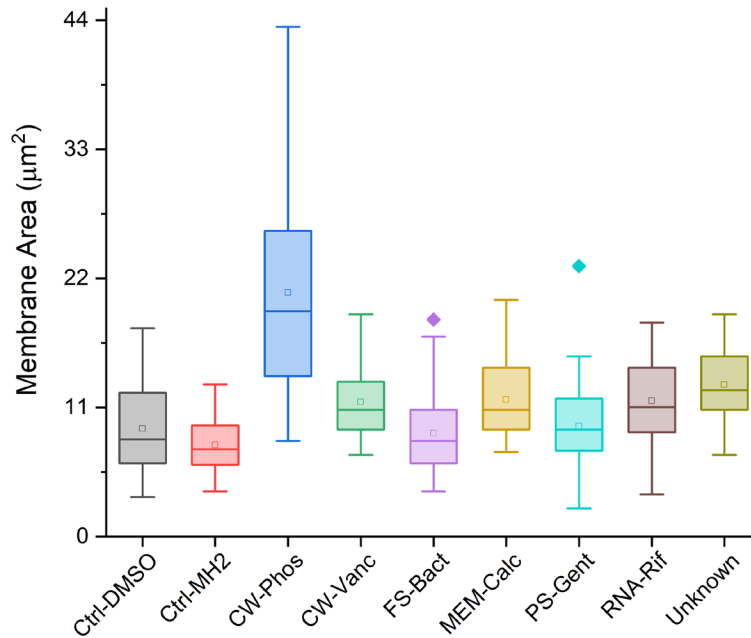


Figure C.8: Box plots for membrane area measurements ($n \geq 150$). Unfilled squares refer to the mean value for each treatment, boxes mark the 25th to 75th percentiles range, the whisker length includes the spread of the data and diamonds represent outliers.

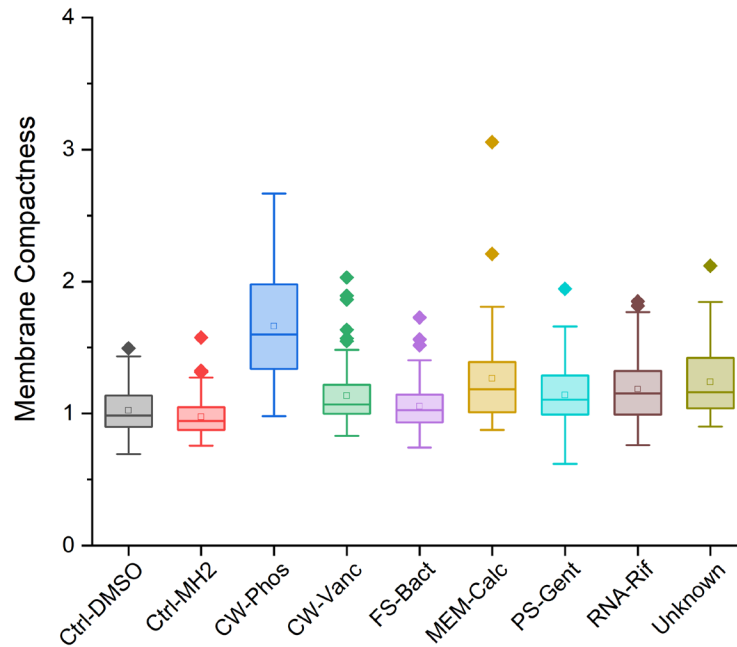


Figure C.9: Box plots for membrane compactness measurements ($n \geq 150$). Unfilled squares refer to the mean value for each treatment, boxes mark the 25th to 75th percentiles range, the whisker length includes the spread of the data and diamonds represent outliers.

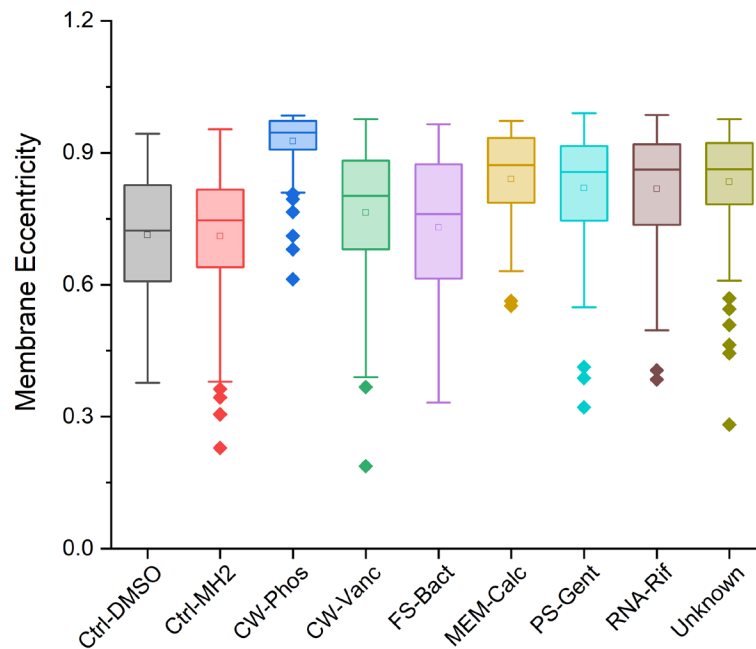


Figure C.10: Box plots for membrane eccentricity measurements ($n \geq 150$). Unfilled squares refer to the mean value for each treatment, boxes mark the 25th to 75th percentiles range, the whisker length includes the spread of the data and diamonds represent outliers.

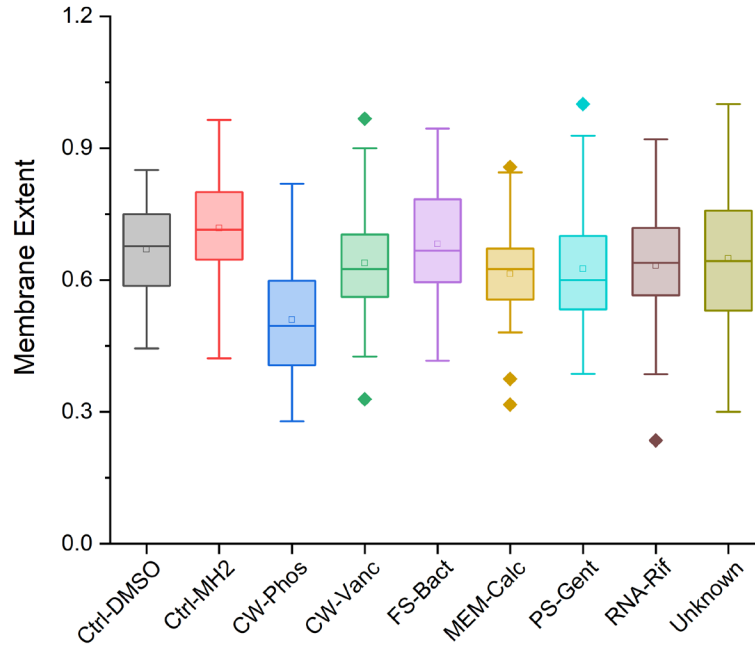


Figure C.11: Box plots for membrane extent measurements ($n \geq 150$). Unfilled squares refer to the mean value for each treatment, boxes mark the 25th to 75th percentiles range, the whisker length includes the spread of the data and diamonds represent outliers.

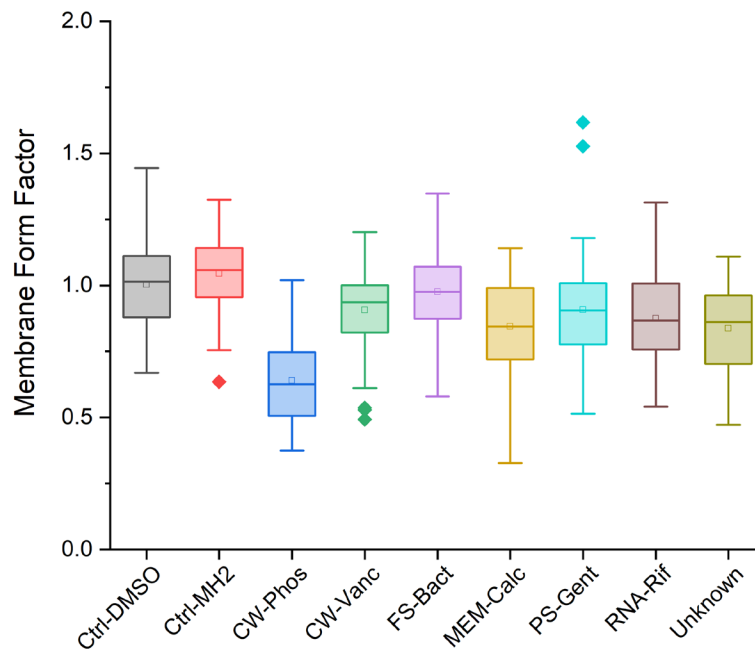


Figure C.12: Box plots for membrane form factor measurements ($n \geq 150$). Unfilled squares refer to the mean value for each treatment, boxes mark the 25th to 75th percentiles range, the whisker length includes the spread of the data and diamonds represent outliers.

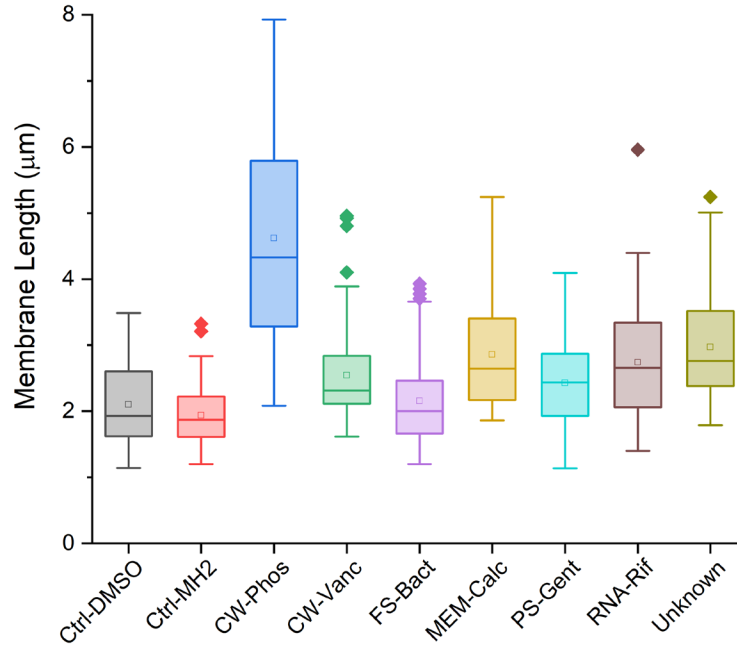


Figure C.13: Box plots for membrane length measurements ($n \geq 150$). Unfilled squares refer to the mean value for each treatment, boxes mark the 25th to 75th percentiles range, the whisker length includes the spread of the data and diamonds represent outliers.

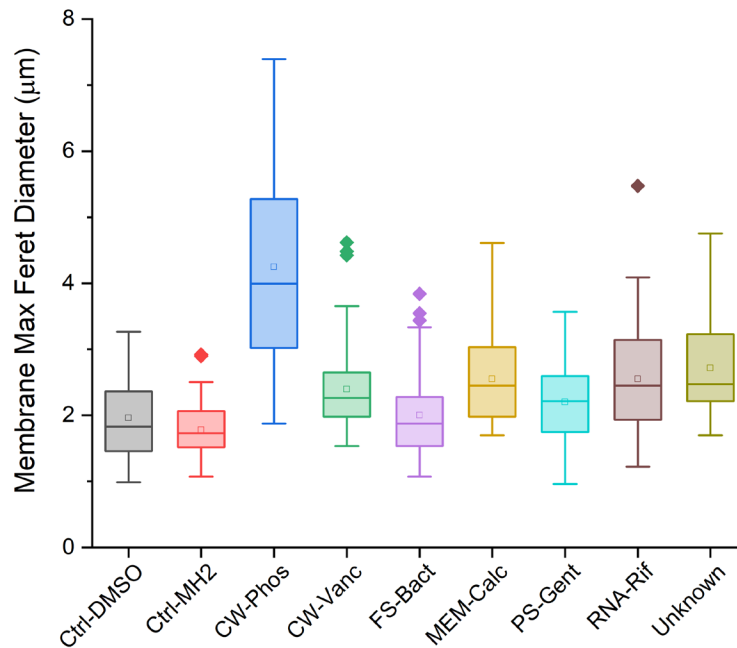


Figure C.14: Box plots for max fret diameter measurements ($n \geq 150$). Unfilled squares refer to the mean value for each treatment, boxes mark the 25th to 75th percentiles range, the whisker length includes the spread of the data and diamonds represent outliers.

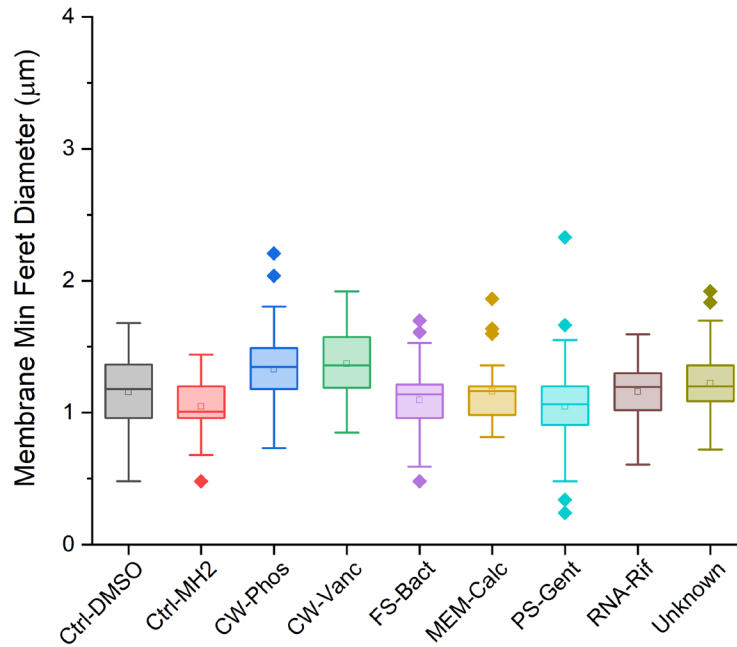


Figure C.15: Box plots for min fret diameter measurements ($n \geq 150$). Unfilled squares refer to the mean value for each treatment, boxes mark the 25th to 75th percentiles range, the whisker length includes the spread of the data and diamonds represent outliers.

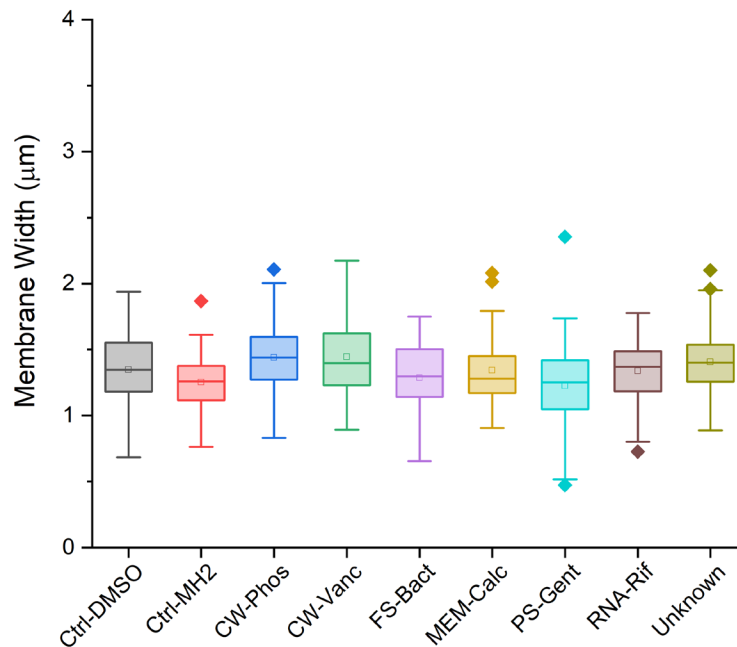


Figure C.16: Box plots for membrane width measurements ($n \geq 150$). Unfilled squares refer to the mean value for each treatment, boxes mark the 25th to 75th percentiles range, the whisker length includes the spread of the data and diamonds represent outliers.

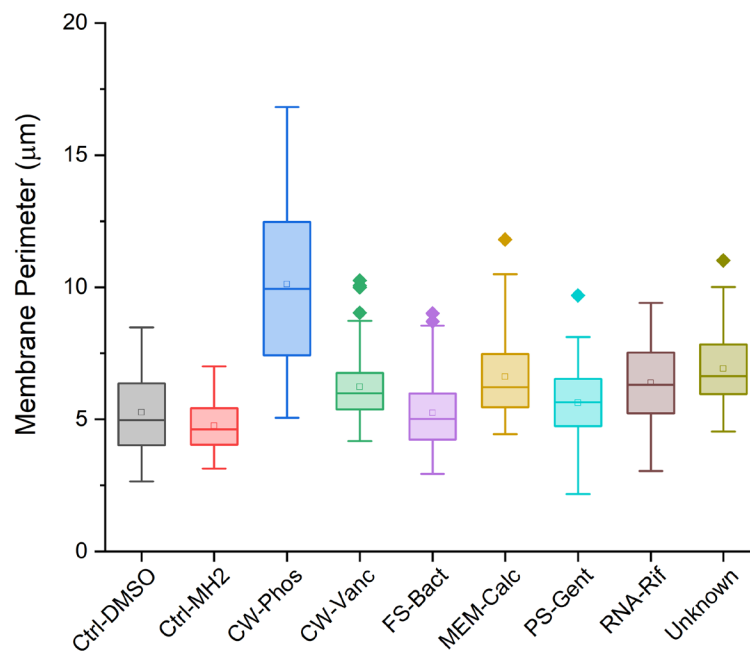


Figure C.17: Box plots for membrane perimeter measurements ($n \geq 150$). Unfilled squares refer to the mean value for each treatment, boxes mark the 25th to 75th percentiles range, the whisker length includes the spread of the data and diamonds represent outliers.

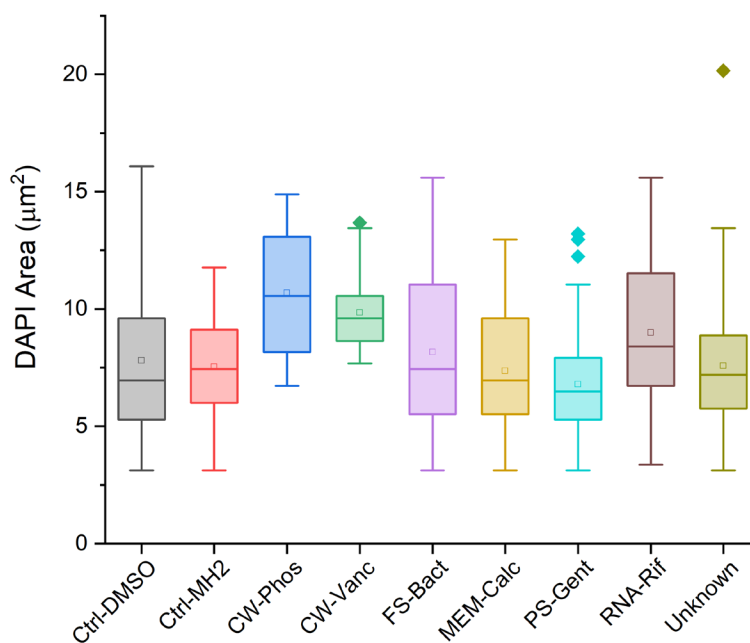


Figure C.18: Box plots for DAPI area measurements ($n \geq 150$). Unfilled squares refer to the mean value for each treatment, boxes mark the 25th to 75th percentiles range, the whisker length includes the spread of the data and diamonds represent outliers.

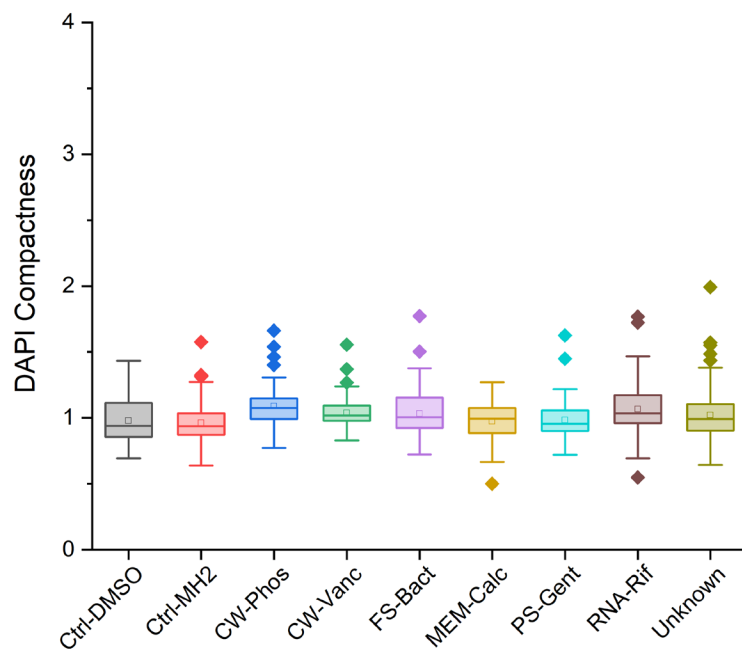


Figure C.19: Box plots for DAPI compactness measurements ($n \geq 150$). Unfilled squares refer to the mean value for each treatment, boxes mark the 25th to 75th percentiles range, the whisker length includes the spread of the data and diamonds represent outliers.

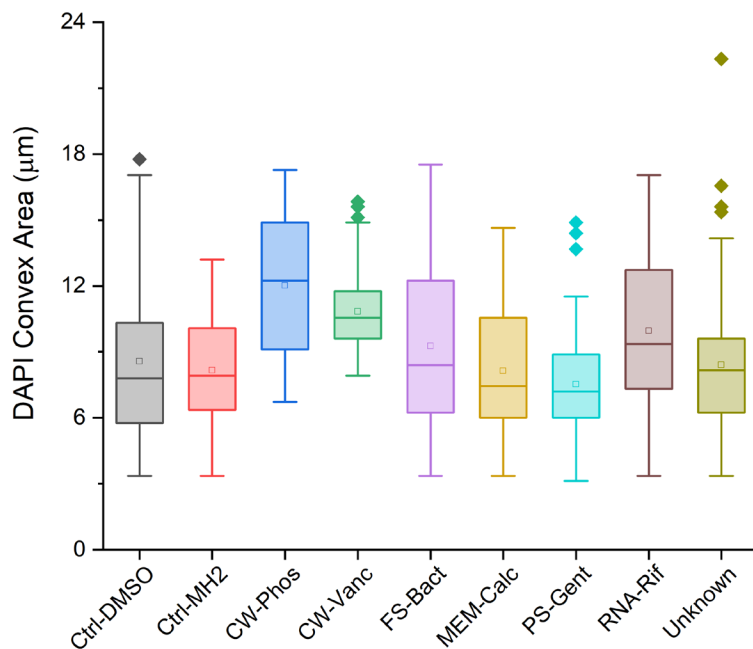


Figure C.20: Box plots for DAPI convex area measurements ($n \geq 150$). Unfilled squares refer to the mean value for each treatment, boxes mark the 25th to 75th percentiles range, the whisker length includes the spread of the data and diamonds represent outliers.

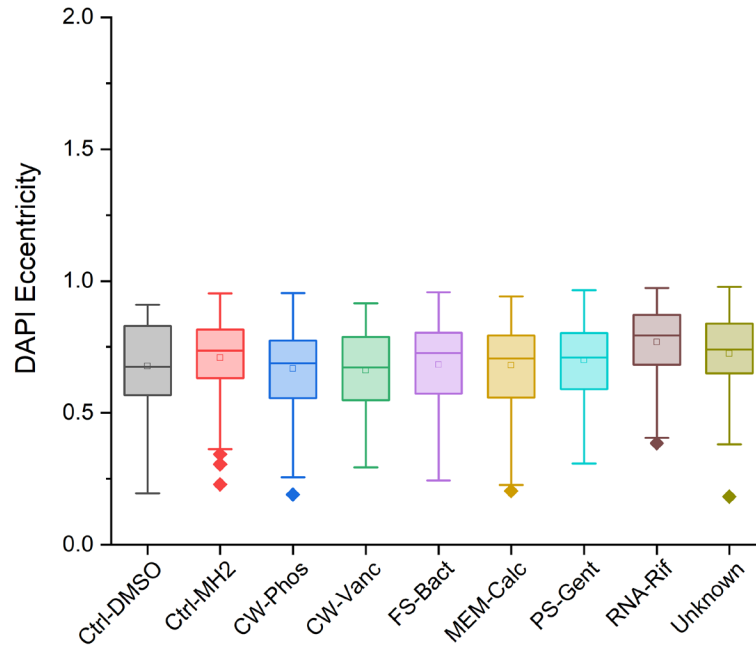


Figure C.21: Box plots for DAPI eccentricity measurements ($n \geq 150$). Unfilled squares refer to the mean value for each treatment, boxes mark the 25th to 75th percentiles range, the whisker length includes the spread of the data and diamonds represent outliers.

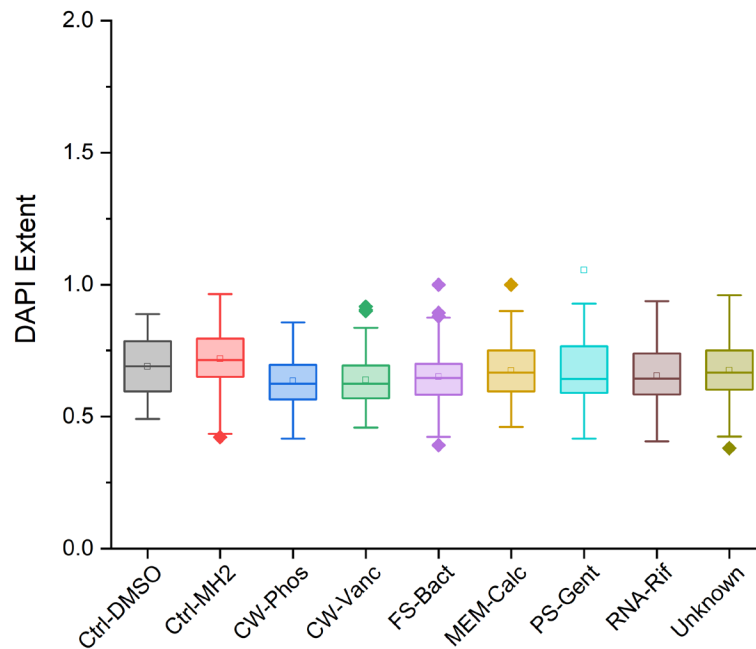


Figure C.22: Box plots for DAPI extent measurements ($n \geq 150$). Unfilled squares refer to the mean value for each treatment, boxes mark the 25th to 75th percentiles range, the whisker length includes the spread of the data and diamonds represent outliers.

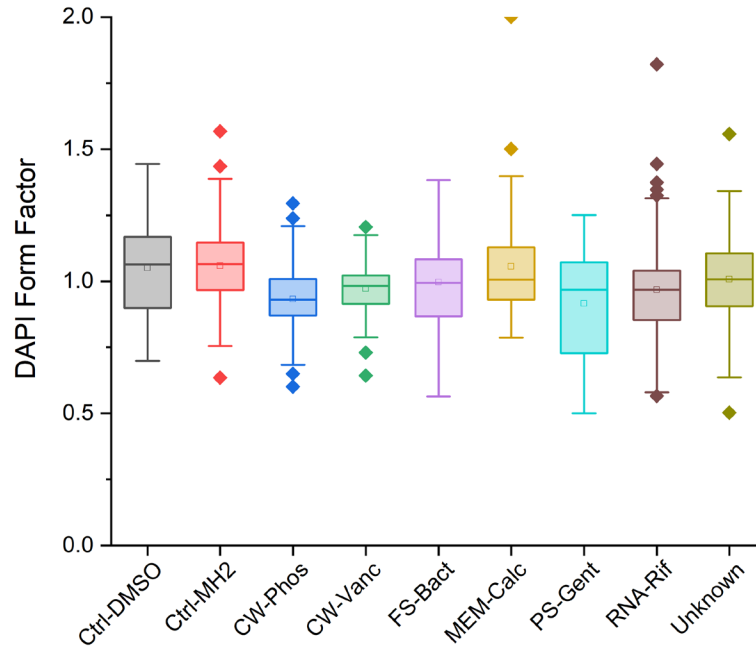


Figure C.23: Box plots for DAPI form factor measurements ($n \geq 150$). Unfilled squares refer to the mean value for each treatment, boxes mark the 25th to 75th percentiles range, the whisker length includes the spread of the data and diamonds represent outliers.

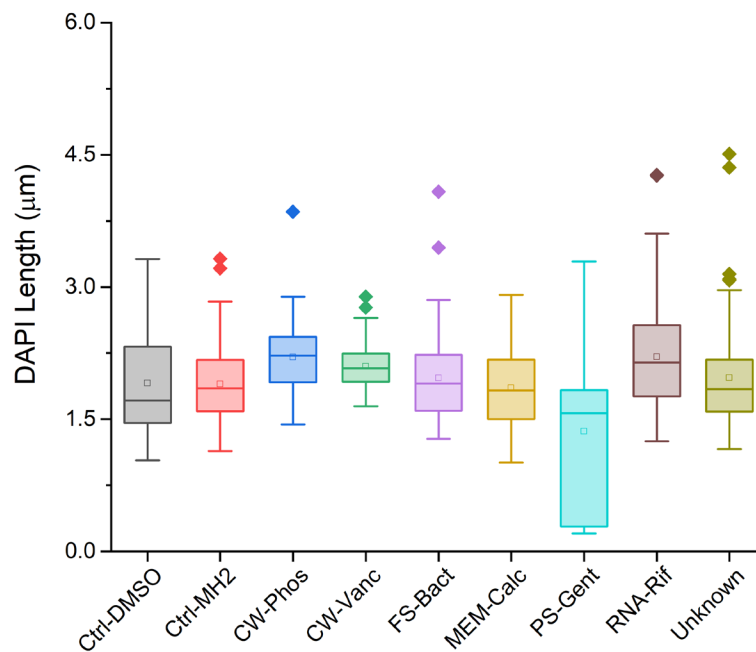


Figure C.24: Box plots for DAPI length measurements ($n \geq 150$). Unfilled squares refer to the mean value for each treatment, boxes mark the 25th to 75th percentiles range, the whisker length includes the spread of the data and diamonds represent outliers.

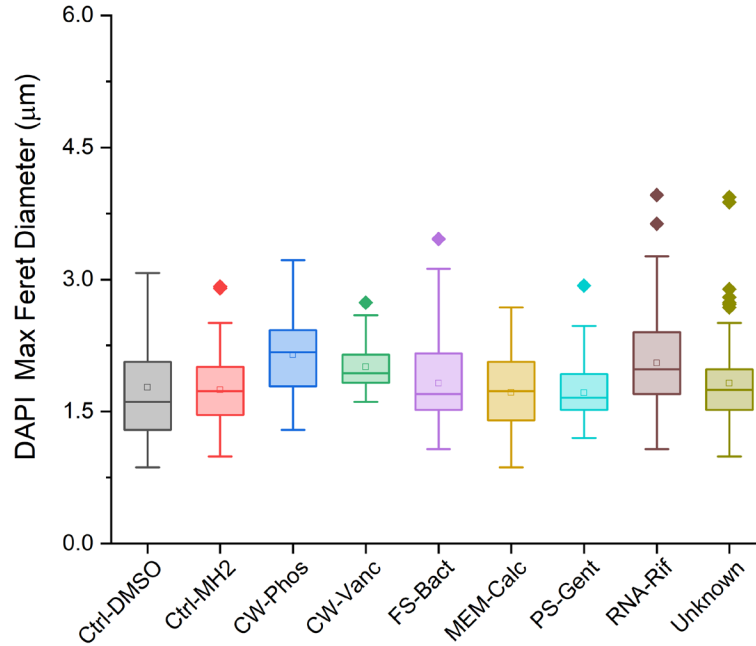


Figure C.25: Box plots for DAPI max fret diameter measurements ($n \geq 150$). Unfilled squares refer to the mean value for each treatment, boxes mark the 25th to 75th percentiles range, the whisker length includes the spread of the data and diamonds represent outliers.

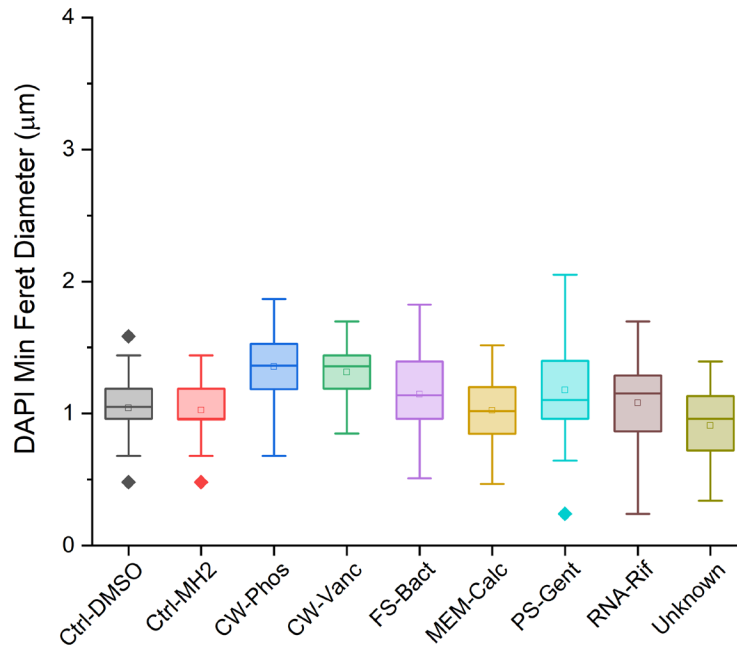


Figure C.26: Box plots for DAPI min fret diameter measurements ($n \geq 150$). Unfilled squares refer to the mean value for each treatment, boxes mark the 25th to 75th percentiles range, the whisker length includes the spread of the data and diamonds represent outliers.

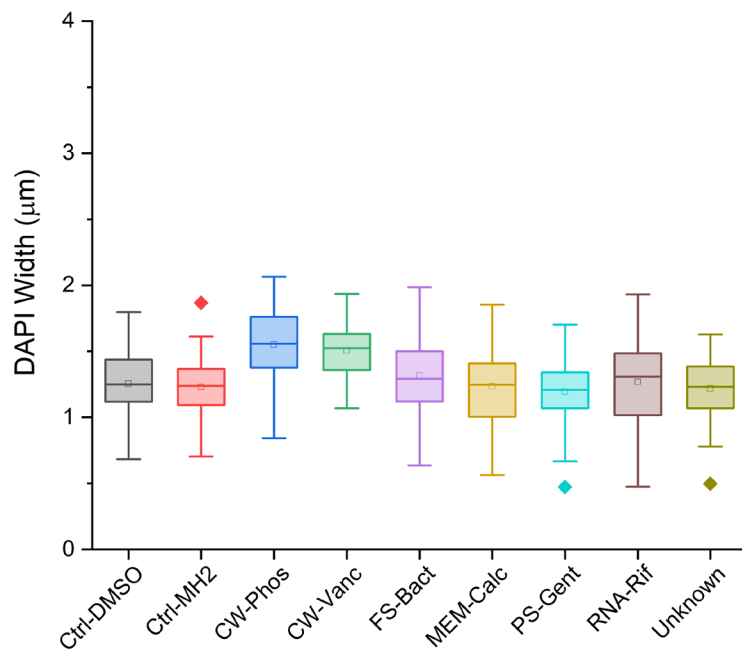


Figure C.27: Box plots for DAPI width measurements ($n \geq 150$). Unfilled squares refer to the mean value for each treatment, boxes mark the 25th to 75th percentiles range, the whisker length includes the spread of the data and diamonds represent outliers.

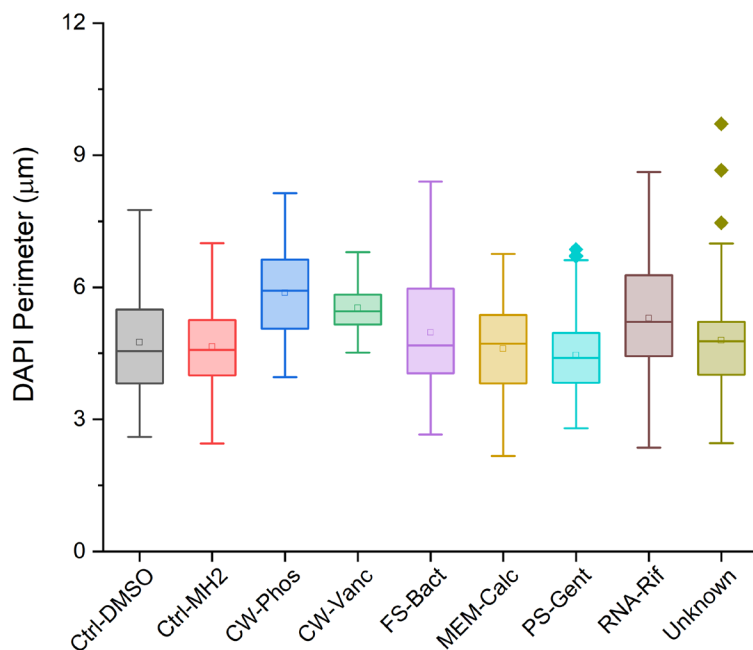


Figure C.28: Box plots for DAPI perimeter measurements ($n \geq 150$). Unfilled squares refer to the mean value for each treatment, boxes mark the 25th to 75th percentiles range, the whisker length includes the spread of the data and diamonds represent outliers.

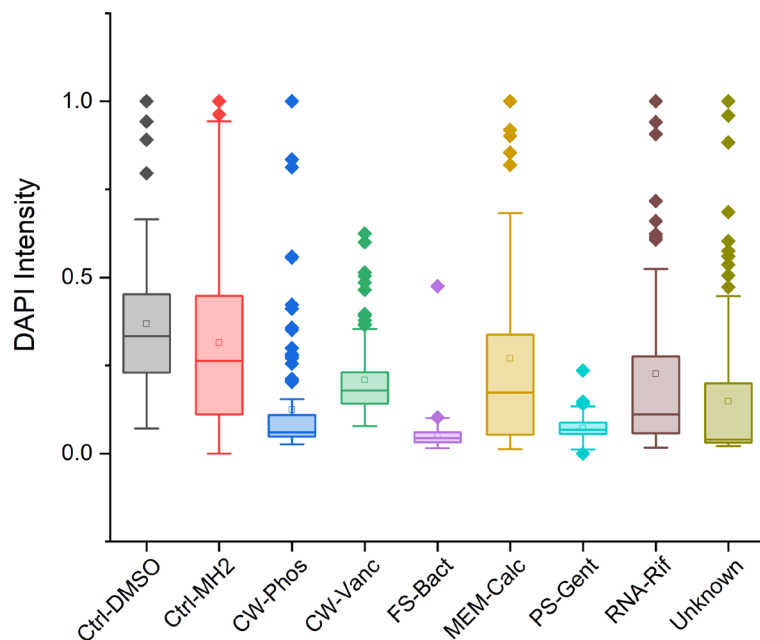


Figure C.29: Box plots for DAPI intensity measurements ($n \geq 150$). Unfilled squares refer to the mean value for each treatment, boxes mark the 25th to 75th percentiles range, the whisker length includes the spread of the data and diamonds represent outliers.

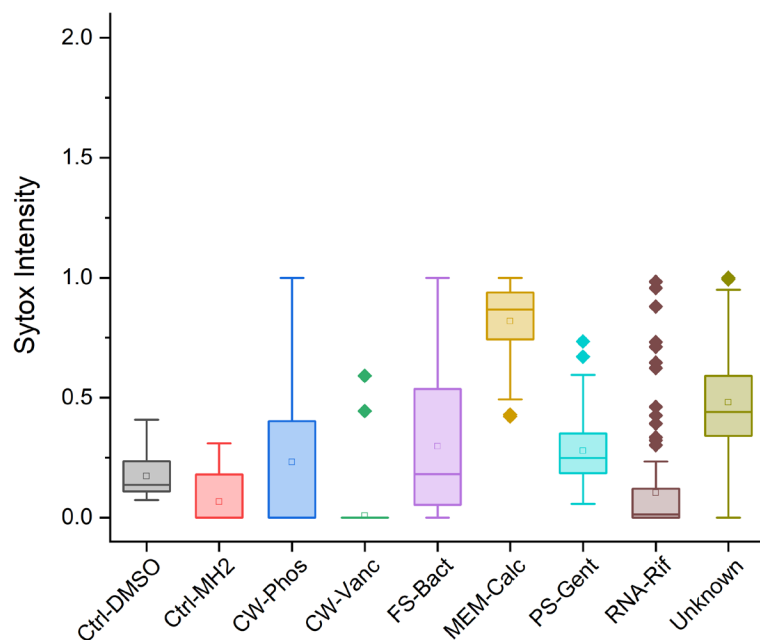


Figure C.30: Box plots for Sytox Green intensity measurements ($n \geq 150$). Unfilled squares refer to the mean value for each treatment, boxes mark the 25th to 75th percentiles range, the whisker length includes the spread of the data and diamonds represent outliers.

GLOSSARY

λ	wavelength (nm)
18:1-6:0 NBD-PE	1-oleoyl-2-(6-((7-nitro-2-1,3-benzoxadiazol-4-yl)amino)hexanoyl)- <i>sn</i> -glycero-3-phosphoethanolamine
^{13}C NMR	carbon-13 nuclear magnetic resonance
14:0 CDL	(1',3'-bis[1,2-dimyristoyl- <i>sn</i> -glycero-3-phospho]-glycerol)
18:1-6:0 NBD-PC	1-oleoyl-2-(6-((7-nitro-2-1,3-benzoxadiazol-4-yl)amino)hexanoyl)- <i>sn</i> -glycero-3-phosphocholine
^1H NMR	proton nuclear magnetic resonance
Abs	absorbance
ADP	adenosine diphosphate
AHC	agglomerative hierarchical clustering
AMP	antimicrobial peptide
AMP	adenosine monophosphate
ATP	adenosine triphosphate
BODIPY- CDL	1,1',2,2'-tetraoleoyl cardiolipin[4-(dipyrometheneboron difluoride)butanoyl] cardiolipin
cal	calories
CDL	cardiolipin
CFU	colony forming units
CH₃CN	acetonitrile

CM	Cytoplasmic membrane
Ctrl-DMSO	DMSO control
Ctrl-MH2	Müller Hinter broth, or untreated control
CW	cell wall
CW-Phos	phosphomycin treated bacteria
CW-Vanc	vancomycin treated bacteria
Cy5	cyanine-5
DAPI	4',6-diamidino-2-phenylindole
DCM	dichloromethane
Disc₃(5)	3,3'-dipropylthiadicarbocyanine iodide
DMF	dimethylformamide
DMPC	dimyristoylphosphatidylcholine
DMPE	dimyristoylphosphatidylethanolamine
DNA	deoxyribonucleic acid
DOPC	1,2-dioleoyl- <i>sn</i> -glycero-3-phosphocholine
DOPE	1,2-dioleoyl- <i>sn</i> -glycero-3-phosphoethanolamine
em	emission
eq	equivalents
ex	excitation
exo	present in the external leaflet
<i>F</i>	fluorescence intensity at time = <i>t</i>
F₀	initial fluorescence intensity (t = 0)
F1	discriminant factor score accounting for the highest variation in the data set (other factors include F2-F4)

F_{final}	fluorescence intensity after adding Triton X-100
FITC	fluorescein isothiocyanate
FS	folate synthesis
FS- Bact	Bactrim treated bacteria
G	Gibbs's free energy
h	hours
H	Enthalpy
HBA	hydrogen bond acceptor
HBD	hydrogen bond donor
HC₅₀	concentration of a drug causing 50% hemolysis
HDP	human defense proteins
ITC	isothermal calorimetry
J	joules
K	kelvins
K_a	association constant
kDa	kilodalton
K_{sv}	Stern-Volmer constant
L	liter
ln	the natural log
LDA	linear discriminant analysis
LPS	Lipopolysaccharide
Lys-PG	lysyl-phosphatidylglycerol
Lyso-PC	lysophosphatidylcholine
Lyso-PE	lysophosphatidylethanolamine

M	molarity (mol/L)
MDR	multi-drug resistant
MEM	membrane
MEM-Calc	calcimycin treated bacteria
MeOH	methanol
MHz	megahertz
MIC	minimum inhibitory concentration
mL	milliliter
mM	millimolar
MOA	mechanism of action
MOE	molecular operating environment
mol	mole
MRSA	methicillin resistant <i>Staphylococcus aureus</i>
n	population size or number of experiments
NAO	nonyl acridine orange
NBD	7-nitrobenz-2-oxa-1,3-diazol-4-yl
n.d.	not determined
nm	nanometers
OD₆₀₀	optical density at 600 nm
PC	phosphatidylcholine
PCA	principal component analysis
PE	phosphatidylethanolamine
Ph	phenyl
PI	phosphatidylinositol

PI(4,5)P₂	phosphatidylinositol (4,5)-bisphosphate
PM	plasma membrane
POPC	1-palmitoyl-2-oleoyl-glycero-3-phosphocholine
POPE	1-palmitoyl-2-oleoyl- <i>sn</i> -glycero-3-phosphoethanolamine
ppm	parts per million
PS	phosphatidylserine
PS-Gent	gentamicin treated bacteria
R	The ideal gas constant, $R = 8.314 \text{ J/K} \cdot \text{mol}$
RNA	ribonucleic acid
RNA-Rif	rifampicin treated bacteria
S	Entropy
s	seconds
δ	chemical shift
SG	Sytox Green
SM	Sphingomyelin
T	Temperature
<i>t</i>	time
TBA	tetra-butyl ammonium
TREN	tris(2-aminoethyl)amine
UNK	unknown
μL	microliter
μm	micrometer
μM	micromolar

REFERENCES

1. Murray, C. J.; Ikuta, K. S.; Sharara, F.; Swetschinski, L.; Aguilar, G. R.; Gray, A.; Han, C.; Bisignano, C.; Rao, P.; Wool, E., Global burden of bacterial antimicrobial resistance in 2019: a systematic analysis. *The Lancet* **2022**, *399* (10325), 629-655.
2. Bartholomew, J. W.; Mittwer, T., The gram stain. *Bacteriological reviews* **1952**, *16* (1), 1-29.
3. Fleming, A., Penicillin. *British medical journal* **1941**, *2* (4210), 386.
4. Rodgers, F.; Tzianabos, A.; Elliott, T., The effect of antibiotics that inhibit cell-wall, protein, and DNA synthesis on the growth and morphology of *Legionella pneumophila*. *J. Med. Microbiol.* **1990**, *31* (1), 37-44.
5. Baquero, F.; Levin, B. R., Proximate and ultimate causes of the bactericidal action of antibiotics. *Nat Rev Microbiol* **2020**, *19*, 123-132.
6. Kohanski, M. A.; Dwyer, D. J.; Collins, J. J., How antibiotics kill bacteria: from targets to networks. *Nat Rev Microbiol* **2010**, *8* (6), 423-35.
7. Blair, J. M.; Webber, M. A.; Baylay, A. J.; Ogbolu, D. O.; Piddock, L. J., Molecular mechanisms of antibiotic resistance. *Nat. Rev. Microbiol.* **2015**, *13* (1), 42-51.
8. Perkel, J. M., The software that powers scientific illustration. *Nature* **2020**, *582* (7810), 137-139.
9. Yeaman, M. R.; Yount, N. Y., Mechanisms of antimicrobial peptide action and resistance. *Pharmacol Rev* **2003**, *55* (1), 27-55.
10. Cong, Y.; Yang, S.; Rao, X., Vancomycin resistant *Staphylococcus aureus* infections: A review of case updating and clinical features. *Journal of Advanced Research* **2020**, *21*, 169-176.
11. Nonejuie, P.; Burkart, M.; Pogliano, K.; Pogliano, J., Bacterial cytological profiling rapidly identifies the cellular pathways targeted by antibacterial molecules. *Proc. Natl. Acad. Sci. U. S. A.* **2013**, *110* (40), 16169.
12. Zaman, S. B.; Hussain, M. A.; Nye, R.; Mehta, V.; Mamun, K. T.; Hossain, N., A Review on Antibiotic Resistance: Alarm Bells are Ringing. *Cureus* **2017**, *9* (6), e1403.
13. Peschel, A.; Sahl, H. G., The co-evolution of host cationic antimicrobial peptides and microbial resistance. *Nat Rev Microbiol* **2006**, *4* (7), 529-36.
14. Hurdle, J. G.; O'Neill, A. J.; Chopra, I.; Lee, R. E., Targeting bacterial membrane function: an underexploited mechanism for treating persistent infections. *Nat. Rev. Microbiol.* **2011**, *9* (1), 62-75.
15. Delcour, A. H., Outer membrane permeability and antibiotic resistance. *Biochim Biophys Acta* **2009**, *1794* (5), 808-16.
16. Dean, R. E.; O'Brien, L. M.; Thwaite, J. E.; Fox, M. A.; Atkins, H.; Ulaeto, D. O., A carpet-based mechanism for direct antimicrobial peptide activity against vaccinia virus membranes. *Peptides* **2010**, *31* (11), 1966-72.

17. Dias, C.; Rauter, A. P., Membrane-targeting antibiotics: Recent developments outside the peptide space. *Future Medicinal Chemistry* **2019**, *11* (3), 211-228.
18. Pedersen, C. J., The discovery of crown ethers. *Science* **1988**, *241* (4865), 536-540.
19. Pedersen, C. J.; Izatt, R.; Christensen, J., Synthetic multidentate macrocyclic compounds. *Synthetic multidentate macrocyclic compounds* **1978**, 1-51.
20. Mellencamp, F. J., Application of Gibbs-Helmholtz Equation to Concentration Cells. *Physical Review (Series I)* **1909**, *29* (4), 329.
21. Webb, J. E.; Crossley, M. J.; Turner, P.; Thordarson, P., Pyromellitimide aggregates and their response to anion stimuli. *J. Am. Chem. Soc.* **2007**, *129* (22), 7155-7162.
22. KA, K. C., Binding Constants. Wiley, New York: 1987.
23. Sauvage, J.-P.; Atwood, J. L., *Comprehensive supramolecular chemistry. 9. Templating, self-assembly, and self-organization*. Pergamon Press: 1996.
24. Artz, S. P.; Cram, D. J., Host-guest complexation. 28. Hemispherands with four self-organizing units. *J. Am. Chem. Soc.* **1984**, *106* (7), 2160-2171.
25. Gibb, C. L.; Gibb, B. C., The thermodynamics of molecular recognition. *Supramolecular Chemistry: from Molecules to Nanomaterials* **2012**.
26. Schneider, H. J., Binding mechanisms in supramolecular complexes. *Angew Chem Int Ed Engl* **2009**, *48* (22), 3924-77.
27. Hunter, C. A., Quantifying intermolecular interactions: guidelines for the molecular recognition toolbox. *Angew. Chem., Int. Ed.* **2004**, *43* (40), 5310-5324.
28. Pike, S. J.; Hutchinson, J. J.; Hunter, C. A., H-Bond acceptor parameters for anions. *J. Am. Chem. Soc.* **2017**, *139* (19), 6700-6706.
29. Biedermann, F.; Nau, W. M.; Schneider, H. J., The hydrophobic effect revisited--studies with supramolecular complexes imply high-energy water as a noncovalent driving force. *Angew Chem Int Ed Engl* **2014**, *53* (42), 11158-71.
30. Ernst, N. E.; Gibb, B. C., Water runs deep. *Supramolecular Chemistry in Water* **2019**, 1-33.
31. Atwood, J. L.; Steed, J. W., *Supramol. Chem.*. John Wiley & Sons: 2009.
32. Simmons, H.; Park, C., Macrobicyclic amines. I. Out-in isomerism of 1,(k+ 2)-diazabicyclo [klm] alkanes. *J. Am. Chem. Soc.* **1968**, *90* (9), 2428-2429.
33. Bell, R. A.; Christoph, G. G.; Fronczek, F. R.; Marsh, R. E., The cation H13O6+: a short, symmetric hydrogen bond. *Science* **1975**, *190* (4210), 151-152.
34. Ohishi, H.; Tozuka, Y.; Da-Yang, Z.; Ishida, T.; Nakatani, K., The rare crystallographic structure of d (CGCGCG) 2: the natural spermidine molecule bound to the minor groove of left-handed Z-DNA d (CGCGCG) 2 at 10 C. *Biochem. Biophys. Res. Commun.* **2007**, *358* (1), 24-28.
35. Katayev, E. A.; Ustynyuk, Y. A.; Sessler, J. L., Receptors for tetrahedral oxyanions. *Coord. Chem. Rev.* **2006**, *250* (23-24), 3004-3037.
36. Michael, A. J., Polyamines in eukaryotes, bacteria, and archaea. *J. Biol. Chem.* **2016**, *291* (29), 14896-14903.
37. Wichmann, K.; Antonioli, B.; Söhnel, T.; Wenzel, M.; Gloe, K.; Gloe, K.; Price, J. R.; Lindoy, L. F.; Blake, A. J.; Schröder, M., Polyamine-based anion receptors: Extraction and structural studies. *Coord. Chem. Rev.* **2006**, *250* (23-24), 2987-3003.
38. Hosseini, M. W.; Lehn, J. M.; Maggiora, L.; Mertes, K. B.; Mertes, M. P., Supramolecular catalysis in the hydrolysis of ATP facilitated by macrocyclic polyamines: mechanistic studies. *J. Am. Chem. Soc.* **1987**, *109* (2), 537-544.
39. Kimura, E.; Sakonaka, A.; Yatsunami, T.; Kodama, M., Macromonocyclic polyamines as specific receptors for tricarboxylate-cycle anions. *J. Am. Chem. Soc.* **1981**, *103* (11), 3041-3045.

40. Martell, A. E.; Motekaitis, R. J.; Lu, Q.; Nation, D. A., Phosphate anion binding by macrocyclic dinucleating ligands and their metal complexes. *Polyhedron* **1999**, *18* (25), 3203-3218.
41. Kimura, E.; Kuramoto, Y.; Koike, T.; Fujioka, H.; Kodama, M., A study of new bis (macrocyclic polyamine) ligands as inorganic and organic anion receptors. *J. Org. Chem.* **1990**, *55* (1), 42-46.
42. Kysela, D. T.; Randich, A. M.; Caccamo, P. D.; Brun, Y. V., Diversity Takes Shape: Understanding the Mechanistic and Adaptive Basis of Bacterial Morphology. *PLoS Biol* **2016**, *14* (10), e1002565.
43. Tabushi, I.; Imuta, J.; Seko, N.; Kobuke, Y., Highly discriminative binding of nucleoside phosphates by a lipophilic diammonium salt embedded in a bicyclic skeleton. *J. Am. Chem. Soc.* **1978**, *100* (19), 6287-6288.
44. Tabushi, I.; Kobuke, Y.; Imuta, J., Lipophilic diammonium cation having a rigid structure complementary to pyrophosphate dianions of nucleotides. Selective extraction and transport of nucleotides. *J. Am. Chem. Soc.* **1981**, *103* (20), 6152-6157.
45. Pascal Jr, R. A.; Spergel, J.; Van Engen, D., Synthesis and X-ray crystallographic characterization of a (1, 3, 5) cyclophane with three amide NH groups surrounding a central cavity. A neutral host for anion complexation. *Tetrahedron Lett.* **1986**, *27* (35), 4099-4102.
46. Morzherin, Y.; Rudkevich, D. M.; Verboom, W.; Reinhoudt, D. N., Chlorosulfonylated calix [4] arenes: precursors for neutral anion receptors with a selectivity for hydrogen sulfate. *J. Org. Chem.* **1993**, *58* (26), 7602-7605.
47. Evans, N. H.; Beer, P. D., Advances in anion supramolecular chemistry: from recognition to chemical applications. *Angew. Chem., Int. Ed.* **2014**, *53* (44), 11716-11754.
48. Lakshminarayanan, P.; Suresh, E.; Ghosh, P., Synthesis and characterization of a tripodal amide ligand and its binding with anions of different dimensionality. *Inorg. Chem.* **2006**, *45* (11), 4372-4380.
49. Hargrove, A. E.; Nieto, S.; Zhang, T.; Sessler, J. L.; Anslyn, E. V., Artificial receptors for the recognition of phosphorylated molecules. *Chem Rev* **2011**, *111* (11), 6603-782.
50. Kelly, T. R.; Kim, M. H., Relative binding affinity of carboxylate and its isosteres: Nitro, phosphate, phosphonate, sulfonate, and delta.-lactone. *J. Am. Chem. Soc.* **1994**, *116* (16), 7072-7080.
51. Smith, P. J.; Reddington, M. V.; Wilcox, C. S., Ion pair binding by a urea in chloroform solution. *Tetrahedron Lett.* **1992**, *33* (41), 6085-6088.
52. Chu, F.; Flatt, L. S.; Anslyn, E. V., Complexation of Phosphoric Acid Diesters with Polyaza-Clefts in Chloroform: Effects of Phosphodiester Dimerization, Changing Cavity Size, and Preorganizing Amine Recognition Units. *J. Am. Chem. Soc.* **1994**, *116* (10), 4194-4204.
53. Sasaki, S.-i.; Mizuno, M.; Naemura, K.; Tobe, Y., Synthesis and anion-selective complexation of cyclophane-based cyclic thioureas. *J. Org. Chem.* **2000**, *65* (2), 275-283.
54. Searle, M. S.; Sharman, G. J.; Groves, P.; Benhamu, B.; Beauregard, D. A.; Westwell, M. S.; Dancer, R. J.; Maguire, A. J.; Try, A. C.; Williams, D. H., Enthalpic (electrostatic) contribution to the chelate effect: a correlation between ligand binding constant and a specific hydrogen bond strength in complexes of glycopeptide antibiotics with cell wall analogues. *Journal of the Chemical Society, Perkin Transactions 1* **1996**, (23), 2781-2786.
55. Loll, P. J.; Axelsen, P. H., The structural biology of molecular recognition by vancomycin. *Annu. Rev. Biophys. Biomol. Struct.* **2000**, *29*, 265.
56. Jordan, J. H.; Wishard, A.; Mague, J. T.; Gibb, B. C., Binding properties and supramolecular polymerization of a water-soluble resorcin [4] arene. *Organic Chemistry Frontiers* **2019**, *6* (8), 1236-1243.

57. Lee, S.; Chen, C.-H.; Flood, A. H., A pentagonal cyanostar macrocycle with cyanostilbene CH donors binds anions and forms dialkylphosphate [3] rotaxanes. *Nature chemistry* **2013**, *5* (8), 704-710.
58. Yan, L.; Saha, A.; Zhao, W.; Neal, J. F.; Chen, Y.; Flood, A. H.; Allen, H. C., Recognition competes with hydration in anion-triggered monolayer formation of cyanostar supra-amphiphiles at aqueous interfaces. *Chemical science* **2022**, *13* (15), 4283-4294.
59. Hirsch, A. K.; Fischer, F. R.; Diederich, F., Phosphate recognition in structural biology. *Angew. Chem., Int. Ed.* **2007**, *46* (3), 338-352.
60. Busschaert, N.; Caltagirone, C.; Van Rossom, W.; Gale, P. A., Applications of Supramolecular Anion Recognition. *Chem Rev* **2015**, *115* (15), 8038-155.
61. Calzada, E.; Onguka, O.; Claypool, S. M., Phosphatidylethanolamine metabolism in health and disease. *International review of cell and molecular biology* **2016**, *321*, 29-88.
62. Clear, K. J.; Smith, B. D., Synthetic Receptors for Polar Lipids. In *Synthetic Receptors for Biomolecules*, 2015; pp 404-436.
63. Van Meer, G.; Voelker, D. R.; Feigenson, G. W., Membrane lipids: where they are and how they behave. *Nat. Rev. Mol. Cell Biol.* **2008**, *9* (2), 112-124.
64. Lee Kennedy, R.; Vangaveti, V.; Jarrod, G.; Shashidhar, V.; Shashidhar, V.; Baune, B. T., Free fatty acid receptors: emerging targets for treatment of diabetes and its complications. *Therapeutic advances in endocrinology and metabolism* **2010**, *1* (4), 165-175.
65. Gómez-Fernández, J. C.; Corbalán-García, S., Diacylglycerols, multivalent membrane modulators. *Chem. Phys. Lipids* **2007**, *148* (1), 1-25.
66. Blom, T.; Somerharju, P.; Ikonen, E., Synthesis and biosynthetic trafficking of membrane lipids. *Cold Spring Harbor perspectives in biology* **2011**, *3* (8), a004713.
67. Fukushima, N.; Ishii, I.; Contos, J. J.; Weiner, J. A.; Chun, J., Lysophospholipid receptors. *Annu. Rev. Pharmacol. Toxicol.* **2001**, *41* (1), 507-534.
68. Hla, T.; Dannenberg, A. J., Sphingolipid signaling in metabolic disorders. *Cell metabolism* **2012**, *16* (4), 420-434.
69. Mesmin, B.; Maxfield, F. R., Intracellular sterol dynamics. *Biochimica et Biophysica Acta (BBA)-Molecular and Cell Biology of Lipids* **2009**, *1791* (7), 636-645.
70. Stafford, R. E.; Fanni, T.; Dennis, E. A., Interfacial properties and critical micelle concentration of lysophospholipids. *Biochemistry* **1989**, *28* (12), 5113-5120.
71. Boon, J. M.; Lambert, T. N.; Sisson, A. L.; Davis, A. P.; Smith, B. D., Facilitated phosphatidylserine (PS) flip-flop and thrombin activation using a synthetic PS scramblase. *J. Am. Chem. Soc.* **2003**, *125* (27), 8195-8201.
72. Vance, J. E., Phospholipid synthesis and transport in mammalian cells. *Traffic* **2015**, *16* (1), 1-18.
73. Epand, R. M.; Epand, R. F., Lipid domains in bacterial membranes and the action of antimicrobial agents. *Biochim. Biophys. Acta* **2009**, *1788* (1), 289-94.
74. Teixeira, V.; Feio, M. J.; Bastos, M., Role of lipids in the interaction of antimicrobial peptides with membranes. *Prog Lipid Res* **2012**, *51* (2), 149-77.
75. Kay, J. G.; Grinstein, S., Phosphatidylserine-mediated cellular signaling. *Lipid-mediated Protein Signaling* **2013**, 177-193.
76. Swairjo, M.; Concha, N.; Kaetzel, M.; Dedman, J.; Seaton, B., Ca²⁺-bridging mechanism and phospholipid head group recognition in the membrane-binding protein annexin V. *Nat. Struct. Mol. Biol.* **1995**, *2* (11), 968-974.
77. Demchenko, A. P., Beyond annexin V: fluorescence response of cellular membranes to apoptosis. *Cytotechnology* **2013**, *65* (2), 157-172.

78. Rice, D. R.; Clear, K. J.; Smith, B. D., Imaging and therapeutic applications of zinc(ii)-dipicolylamine molecular probes for anionic biomembranes. *Chem Commun (Camb)* **2016**, 52 (57), 8787-801.
79. DiVittorio, K. M.; Leevy, W. M.; O'Neil, E. J.; Johnson, J. R.; Vakulenko, S.; Morris, J. D.; Rosek, K. D.; Serazin, N.; Hilkert, S.; Hurley, S.; Marquez, M.; Smith, B. D., Zinc(II) coordination complexes as membrane-active fluorescent probes and antibiotics. *Chembiochem* **2008**, 9 (2), 286-93.
80. Kotsogianni, I.; Wood, T. M.; Alexander, F. M.; Cochrane, S. A.; Martin, N. I., Binding studies reveal phospholipid specificity and its role in the calcium-dependent mechanism of action of daptomycin. *ACS infectious diseases* **2021**, 7 (9), 2612-2619.
81. Breukink, E.; de Kruijff, B., Lipid II as a target for antibiotics. *Nat. Rev. Drug Discovery* **2006**, 5 (4), 321-323.
82. Boon, J. M.; Smith, B. D., Facilitated Phospholipid Translocation across Vesicle Membranes Using Low-Molecular-Weight Synthetic Flippases. *J. Am. Chem. Soc.* **1999**, 121 (50), 11924-11925.
83. Boon, J. M.; Shukla, R.; Smith, B. D.; Licini, G.; Scrimin, P., Selective phosphatidylethanolamine translocation across vesicle membranes using synthetic translocases. *Chemical Communications* **2002**, (3), 260-261.
84. Alliband, A.; Meece, F. A.; Jayasinghe, C.; Burns, D. H., Synthesis and characterization of picket porphyrin receptors that bind phosphatidylglycerol, an anionic phospholipid found in bacterial membranes. *J. Org. Chem.* **2013**, 78 (2), 356-362.
85. Nishiyabu, R.; Kubo, Y.; James, T. D.; Fossey, J. S., Boronic acid building blocks: tools for self assembly. *Chemical Communications* **2011**, 47 (4), 1124-1150.
86. Lappert, M., Organic compounds of boron. *Chemical Reviews* **1956**, 56 (5), 959-1064.
87. Katan, M.; Cockcroft, S., Phosphatidylinositol (4, 5) bisphosphate: diverse functions at the plasma membrane. *Essays in biochemistry* **2020**, 64 (3), 513-531.
88. Mak, L. H.; Georgiades, S. N.; Rosivatz, E.; Whyte, G. F.; Mirabelli, M.; Vilar, R.; Woscholski, R., A small molecule mimicking a phosphatidylinositol (4,5)-bisphosphate binding pleckstrin homology domain. *ACS Chem Biol* **2011**, 6 (12), 1382-90.
89. Fossey, J. S.; James, T. D., Boronic acid based modular fluorescent saccharide sensors. In *Reviews in Fluorescence 2007*, Springer: 2009; pp 103-118.
90. Benfield, A. H.; Henriques, S. T., Mode-of-Action of Antimicrobial Peptides: Membrane Disruption vs. Intracellular Mechanisms. *Front Med Technol* **2020**, 2, 610997.
91. Chileveru, H. R.; Lim, S. A.; Chairatana, P.; Wommack, A. J.; Chiang, I. L.; Nolan, E. M., Visualizing attack of Escherichia coli by the antimicrobial peptide human defensin 5. *Biochemistry* **2015**, 54 (9), 1767-77.
92. Choung, S.-Y.; Kobayashi, T.; Inoue, J.-i.; Takemoto, K.; Ishitsuka, H.; Inoue, K., Hemolytic activity of a cyclic peptide Ro09-0198 isolated from Streptovorticillium. *Biochimica et Biophysica Acta (BBA)-Biomembranes* **1988**, 940 (2), 171-179.
93. Malanovic, N.; Lohner, K., Antimicrobial Peptides Targeting Gram-Positive Bacteria. *Pharmaceuticals (Basel)* **2016**, 9 (3).
94. López-Otín, C.; Bond, J. S., Proteases: multifunctional enzymes in life and disease. *J. Biol. Chem.* **2008**, 283 (45), 30433-30437.
95. Duplantier, A. J.; van Hoek, M. L., The Human Cathelicidin Antimicrobial Peptide LL-37 as a Potential Treatment for Polymicrobial Infected Wounds. *Front Immunol* **2013**, 4, 143.
96. Epand, R. M.; Epand, R. F., Bacterial membrane lipids in the action of antimicrobial agents. *Journal of Peptide Science* **2011**, 17 (5), 298-305.

97. Lakshminarayanan, P. S.; Ravikumar, I.; Suresh, E.; Ghosh, P., Trapped inorganic phosphate dimer. *Chem. Commun.* **2007**, (48), 5214-5216.
98. Matsuzaki, K., *Antimicrobial peptides: basics for clinical application*. Springer: 2019; Vol. 1117.
99. Hasim, S.; Allison, D. P.; Mendez, B.; Farmer, A. T.; Pelletier, D. A.; Retterer, S. T.; Campagna, S. R.; Reynolds, T. B.; Doktycz, M. J., Elucidating Duramycin's Bacterial Selectivity and Mode of Action on the Bacterial Cell Envelope. *Front. Microbiol.* **2018**, *9*, 219.
100. Iwamoto, K.; Hayakawa, T.; Murate, M.; Makino, A.; Ito, K.; Fujisawa, T.; Kobayashi, T., Curvature-dependent recognition of ethanolamine phospholipids by duramycin and cinnamycin. *Biophys J* **2007**, *93* (5), 1608-19.
101. Epand, R. M.; Walker, C.; Epand, R. F.; Magarvey, N. A., Molecular mechanisms of membrane targeting antibiotics. *Biochim. Biophys. Acta* **2016**, *1858* (5), 980-7.
102. Fredenhagen, A.; FENDRICH, G.; MÄRKI, F.; MÄRKI, W.; GRUNER, J.; RASCHDORF, F.; PETER, H. H., Duramycins B and C, Two New Lanthionine Containing Antibiotics as Inhibitors of Phospholipase A2 Structural Revision of Duramycin and Cinnamycin. *The Journal of antibiotics* **1990**, *43* (11), 1403-1412.
103. Lemmon, M. A., Membrane recognition by phospholipid-binding domains. *Nat Rev Mol Cell Biol* **2008**, *9* (2), 99-111.
104. Matsumoto, K.; Kusaka, J.; Nishibori, A.; Hara, H., Lipid domains in bacterial membranes. *Mol Microbiol* **2006**, *61* (5), 1110-7.
105. Arias-Cartin, R.; Grimaldi, S.; Arnoux, P.; Guigliarelli, B.; Magalon, A., Cardiolipin binding in bacterial respiratory complexes: structural and functional implications. *Biochim Biophys Acta* **2012**, *1817* (10), 1937-49.
106. Sathappa, M.; Alder, N. N., The ionization properties of cardiolipin and its variants in model bilayers. *Biochimica et Biophysica Acta (BBA)-Biomembranes* **2016**, *1858* (6), 1362-1372.
107. Marsh, D., *Handbook of lipid bilayers*. CRC press: 2013.
108. Tocanne, J.-F.; Teissié, J., Ionization of phospholipids and phospholipid-supported interfacial lateral diffusion of protons in membrane model systems. *Biochimica et Biophysica Acta (BBA)-Reviews on Biomembranes* **1990**, *1031* (1), 111-142.
109. Kates, M.; Syz, J.-Y.; Gosser, D.; Haines, T. H., pH-dissociation characteristics of cardiolipin and its 2'-deoxy analogue. *Lipids* **1993**, *28* (10), 877-882.
110. Olofsson, G.; Sparr, E., Ionization constants pKa of cardiolipin. *PLoS One* **2013**, *8* (9), e73040.
111. Xu, Z.; Chen, X.; Kim, H. N.; Yoon, J., Sensors for the optical detection of cyanide ion. *Chem. Soc. Rev.* **2010**, *39* (1), 127-137.
112. Septinus, M.; Berthold, T.; Naujok, A.; Zimmermann, H., Hydrophobic acridine dyes for fluorescent staining of mitochondria in living cells. 3. Specific accumulation of the fluorescent dye NAO on the mitochondrial membranes in HeLa cells by hydrophobic interaction. Depression of respiratory activity, changes in the ultrastructure of mitochondria due to NAO. Increase of fluorescence in vital stained mitochondria in situ by irradiation. *Histochemistry* **1985**, *82* (1), 51-66.
113. PETIT, J. M.; MAFTAH, A.; RATINAUD, M. H.; JULIEN, R., 10N-nonyl acridine orange interacts with cardiolipin and allows the quantification of this phospholipid in isolated mitochondria. *Eur. J. Biochem.* **1992**, *209* (1), 267-273.
114. Mileykovskaya, E.; Dowhan, W., Visualization of phospholipid domains in Escherichia coli by using the cardiolipin-specific fluorescent dye 10-N-nonyl acridine orange. *J. Bacteriol.* **2000**, *182* (4), 1172-1175.

115. Leung, C. W.; Hong, Y.; Hanske, J.; Zhao, E.; Chen, S.; Pletneva, E. V.; Tang, B. Z., Superior fluorescent probe for detection of cardiolipin. *Anal Chem* **2014**, *86* (2), 1263-8.
116. Verhaegh, R.; Becker, K. A.; Edwards, M. J.; Gulbins, E., Sphingosine kills bacteria by binding to cardiolipin. *J Biol Chem* **2020**, *295* (22), 7686-7696.
117. Fu, C.; Keller, L.; Bauer, A.; Bronstrup, M.; Froidbise, A.; Hammann, P.; Herrmann, J.; Mondesert, G.; Kurz, M.; Schiell, M.; Schummer, D.; Toti, L.; Wink, J.; Muller, R., Biosynthetic Studies of Telomycin Reveal New Lipopeptides with Enhanced Activity. *J Am Chem Soc* **2015**, *137* (24), 7692-705.
118. Roberts, T. C.; Langer, R.; Wood, M. J., Advances in oligonucleotide drug delivery. *Nat. Rev. Drug Discovery*. **2020**, *19* (10), 673-694.
119. Fariya, M.; Jain, A.; Dhawan, V.; Shah, S.; Nagarsenker, M. S., Bolaamphiphiles: a pharmaceutical review. *Advanced Pharmaceutical Bulletin* **2014**, *4* (Suppl 2), 483.
120. Marin-Menendez, A.; Montis, C.; Diaz-Calvo, T.; Carta, D.; Hatzixanthis, K.; Morris, C. J.; McArthur, M.; Berti, D., Antimicrobial Nanoplexes meet Model Bacterial Membranes: the key role of Cardiolipin. *Sci Rep* **2017**, *7*, 41242.
121. Thordarson, P., Determining association constants from titration experiments in supramolecular chemistry. *Chem Soc Rev* **2011**, *40* (3), 1305-23.
122. Dishong, D. M.; Gokel, G. W., Crown cation complex effects. 16. Solvent dependence of the 15-crown-5 and 18-crown-6 equilibria with sodium cation. *J. Org. Chem.* **1982**, *47* (1), 147-148.
123. Lin, Y.-P.; Carman, G., Kinetic analysis of yeast phosphatidate phosphatase toward Triton X-100/phosphatidate mixed micelles. *J. Biol. Chem.* **1990**, *265* (1), 166-170.
124. Lewis, R. N.; McElhaney, R. N., The physicochemical properties of cardiolipin bilayers and cardiolipin-containing lipid membranes. *Biochimica et Biophysica Acta (BBA)-Biomembranes* **2009**, *1788* (10), 2069-2079.
125. Garcia Fernandez, M. I.; Ceccarelli, D.; Muscatello, U., Use of the fluorescent dye 10-N-nonyl acridine orange in quantitative and location assays of cardiolipin: a study on different experimental models. *Anal Biochem* **2004**, *328* (2), 174-80.
126. Randle, C. L.; Albro, P. W.; Dittmer, J. C., The phosphoglyceride composition of Gram-negative bacteria and the changes in composition during growth. *Biochimica et Biophysica Acta (BBA)-Lipids and Lipid Metabolism* **1969**, *187* (2), 214-220.
127. Bos, M. P.; Tefsen, B.; Geurtsen, J.; Tommassen, J., Identification of an outer membrane protein required for the transport of lipopolysaccharide to the bacterial cell surface. *Proc. Natl. Acad. Sci.* **2004**, *101* (25), 9417-9422.
128. Stillwell, W., *An introduction to biological membranes: composition, structure and function*. Elsevier: 2016.
129. Daum, G., Lipids of mitochondria. *Biochimica et Biophysica Acta (BBA)-Reviews on Biomembranes* **1985**, *822* (1), 1-42.
130. Chan, E. Y.; McQuibban, G. A., Phosphatidylserine decarboxylase 1 (Psd1) promotes mitochondrial fusion by regulating the biophysical properties of the mitochondrial membrane and alternative topogenesis of mitochondrial genome maintenance protein 1 (Mgm1). *J. Biol. Chem.* **2012**, *287* (48), 40131-40139.
131. Tan, L. T.; Chan, K. G.; Pusparajah, P.; Lee, W. L.; Chuah, L. H.; Khan, T. M.; Lee, L. H.; Goh, B. H., Targeting Membrane Lipid a Potential Cancer Cure? *Front Pharmacol* **2017**, *8*, 12.
132. Bierbaum, G.; Sahl, H.-G., Lantibiotics: mode of action, biosynthesis and bioengineering. *Curr. Pharm. Biotechnol.* **2009**, *10* (1), 2-18.

133. Hasim, S.; Allison, D. P.; Mendez, B.; Farmer, A. T.; Pelletier, D. A.; Retterer, S. T.; Campagna, S. R.; Reynolds, T. B.; Doktycz, M. J., Elucidating duramycin's bacterial selectivity and mode of action on the bacterial cell envelope. *Frontiers in microbiology* **2018**, *9*, 219.
134. Vestergaard, M.; Berglund, N. A.; Hsu, P. C.; Song, C.; Koldso, H.; Schiott, B.; Sansom, M. S. P., Structure and Dynamics of Cinnamycin-Lipid Complexes: Mechanisms of Selectivity for Phosphatidylethanolamine Lipids. *ACS Omega* **2019**, *4* (20), 18889-18899.
135. Hosoda, K.; Ohya, M.; Kohno, T.; Maeda, T.; Endo, S.; Wakamatsu, K., Structure determination of an immunopotentiator peptide, cinnamycin, complexed with lysophosphatidylethanolamine by 1H-NMR. *J. Biochem.* **1996**, *119* (2), 226-230.
136. Kawai, H.; Chaudhry, F.; Shekhar, A.; Petrov, A.; Nakahara, T.; Tanimoto, T.; Kim, D.; Chen, J.; Lebeche, D.; Blankenberg, F. G., Molecular imaging of apoptosis in ischemia reperfusion injury with radiolabeled duramycin targeting phosphatidylethanolamine: effective target uptake and reduced nontarget organ radiation burden. *JACC: Cardiovascular Imaging* **2018**, *11* (12), 1823-1833.
137. Preta, G., New Insights Into Targeting Membrane Lipids for Cancer Therapy. *Front Cell Dev Biol* **2020**, *8*, 571237.
138. Xing, Y.; Li, G.; Gray, B.; Pak, K.; Zhao, J.; Conti, P.; Chen, K., Noninvasive monitoring of chemotherapy treatment with near-infrared fluorescence imaging using Cy5-Duramycin and CyAL5-cRGD. *Soc Nuclear Med*: 2014.
139. Allen, N.; White, L. J.; Boles, J. E.; Williams, G. T.; Chu, D. F.; Ellaby, R. J.; Shepherd, H. J.; Ng, K. K. L.; Blackholly, L. R.; Wilson, B.; Mulvihill, D. P.; Hiscock, J. R., Towards the Prediction of Antimicrobial Efficacy for Hydrogen Bonded, Self-Associating Amphiphiles. *ChemMedChem* **2020**, *15* (22), 2193-2205.
140. Boles, J. E.; Ellaby, R. J.; Shepherd, H. J.; Hiscock, J. R., Supramolecular self-associating amphiphiles (SSAs) as enhancers of antimicrobial agents towards Escherichia coli (E. coli). *RSC Adv* **2021**, *11* (16), 9550-9556.
141. White, L. J.; Tyuleva, S. N.; Wilson, B.; Shepherd, H. J.; Ng, K. K. L.; Holder, S. J.; Clark, E. R.; Hiscock, J. R., Towards the Prediction of Global Solution State Properties for Hydrogen Bonded, Self-Associating Amphiphiles. *Chemistry* **2018**, *24* (30), 7761-7773.
142. Dora, N. O.; Blackburn, E.; Boles, J. E.; Williams, G. T.; White, L. J.; Turner, S. E. G.; Hothersall, J. D.; Askwith, T.; Doolan, J. A.; Mulvihill, D. P.; Garrett, M. D.; Hiscock, J. R., Supramolecular self-associating amphiphiles (SSAs) as nanoscale enhancers of cisplatin anticancer activity. *RSC Adv* **2021**, *11* (23), 14213-14217.
143. White, L. J.; Boles, J. E.; Clifford, M.; Patenall, B. L.; Hilton, K.; Ng, K. K. L.; Ellaby, R. J.; Hind, C. K.; Mulvihill, D. P.; Hiscock, J. R., Di-anionic self-associating supramolecular amphiphiles (SSAs) as antimicrobial agents against MRSA and Escherichia coli. *Chem Commun (Camb)* **2021**, *57* (89), 11839-11842.
144. Kang, B.; Tang, H.; Zhao, Z.; Song, S., Hofmeister series: Insights of ion specificity from amphiphilic assembly and interface property. *ACS omega* **2020**, *5* (12), 6229-6239.
145. Bandyopadhyay, A.; McCarthy, K. A.; Kelly, M. A.; Gao, J., Targeting bacteria via iminoboronate chemistry of amine-presenting lipids. *Nat Commun* **2015**, *6*, 6561.
146. Bandyopadhyay, A.; Gao, J., Iminoboronate-Based Peptide Cyclization That Responds to pH, Oxidation, and Small Molecule Modulators. *J Am Chem Soc* **2016**, *138* (7), 2098-101.
147. Bandyopadhyay, A.; Gao, J., Targeting biomolecules with reversible covalent chemistry. *Curr Opin Chem Biol* **2016**, *34*, 110-116.
148. Amendola, V.; Fabbrizzi, L.; Mosca, L., Anion recognition by hydrogen bonding: urea-based receptors. *Chem Soc Rev* **2010**, *39* (10), 3889-915.

149. Späth, A.; König, B., Molecular recognition of organic ammonium ions in solution using synthetic receptors. *Beilstein journal of organic chemistry* **2010**, *6* (1), 32.
150. Busschaert, N.; Bradberry, S. J.; Wenzel, M.; Haynes, C. J. E.; Hiscock, J. R.; Kirby, I. L.; Karagiannidis, L. E.; Moore, S. J.; Wells, N. J.; Herniman, J.; Langley, G. J.; Horton, P. N.; Light, M. E.; Marques, I.; Costa, P. J.; Félix, V.; Frey, J. G.; Gale, P. A., Towards predictable transmembrane transport: QSAR analysis of anion binding and transport. *Chemical Science* **2013**, *4* (8), 3036-3045.
151. Kralj, M.; Tušek-Božić, L.; Frkanec, L., Biomedical Potentials of Crown Ethers: Prospective Antitumor Agents. *ChemMedChem* **2008**, *3* (10), 1478-1492.
152. Brynn Hibbert, D.; Thordarson, P., The death of the Job plot, transparency, open science and online tools, uncertainty estimation methods and other developments in supramolecular chemistry data analysis. *Chemical Communications* **2016**, *52* (87), 12792-12805.
153. Chattopadhyay, A., Chemistry and biology of N-(7-nitrobenz-2-oxa-1, 3-diazol-4-yl)-labeled lipids: fluorescent probes of biological and model membranes. *Chem. Phys. Lipids* **1990**, *53* (1), 1-15.
154. Seddon, J. M., Structure of the inverted hexagonal (HII) phase, and non-lamellar phase transitions of lipids. *Biochimica et Biophysica Acta (BBA) - Reviews on Biomembranes* **1990**, *1031* (1), 1-69.
155. Matsuzaki, K.; Murase, O.; Fujii, N.; Miyajima, K., An Antimicrobial Peptide, Magainin 2, Induced Rapid Flip-Flop of Phospholipids Coupled with Pore Formation and Peptide Translocation. *Biochemistry* **1996**, *35* (35), 11361-11368.
156. McConnell, H. M.; Kornberg, R. D., Inside-outside transitions of phospholipids in vesicle membranes. *Biochemistry* **1971**, *10* (7), 1111-1120.
157. McIntyre, J. C.; Sleight, R. G., Fluorescence assay for phospholipid membrane asymmetry. *Biochemistry* **1991**, *30* (51), 11819-11827.
158. Randle, C. L.; Albro, P. W.; Dittmer, J. C., The phosphoglyceride composition of gram-negative bacteria and the changes in composition during growth. *Biochimica et Biophysica Acta (BBA) - Lipids and Lipid Metabolism* **1969**, *187* (2), 214-220.
159. Bos, M. P.; Tommassen, J., Biogenesis of the Gram-negative bacterial outer membrane. *Current Opinion in Microbiology* **2004**, *7* (6), 610-616.
160. Melander, R. J.; Zurawski, D. V.; Melander, C., Narrow-spectrum antibacterial agents. *MedChemComm* **2018**, *9* (1), 12-21.
161. Nahaie, M.; Goodfellow, M.; Minnikin, D.; Hajek, V., Polar lipid and isoprenoid quinone composition in the classification of Staphylococcus. *Microbiology* **1984**, *130* (9), 2427-2437.
162. Bernat, P.; Paraszkiwicz, K.; Siewiera, P.; Moryl, M.; Płaza, G.; Chojniak, J., Lipid composition in a strain of Bacillus subtilis, a producer of iturin A lipopeptides that are active against uropathogenic bacteria. *World J Microbiol Biotechnol* **2016**, *32* (10), 157-157.
163. Haque, M. A.; Russell, N. J., Strains of Bacillus cereus vary in the phenotypic adaptation of their membrane lipid composition in response to low water activity, reduced temperature and growth in rice starch. *Microbiology* **2004**, *150* (5), 1397-1404.
164. Logan, N. A., Bacillus and relatives in foodborne illness. *Journal of Applied Microbiology* **2012**, *112* (3), 417-429.
165. Helgason, E.; Økstad, O. A.; Caugant, D. A.; Johansen, H. A.; Fouet, A.; Mock, M.; Hegna, I.; Kolstø, A.-B., & Bacillus anthracis & Bacillus cereus, and Bacillus thuringiensis—One Species on the Basis of Genetic Evidence. *Appl. Environ. Microbiol.* **2000**, *66* (6), 2627.
166. Balouiri, M.; Sadiki, M.; Ibsouda, S. K., Methods for in vitro evaluating antimicrobial activity: A review. *Journal of Pharmaceutical Analysis* **2016**, *6* (2), 71-79.

167. te Winkel, J. D.; Gray, D. A.; Seistrup, K. H.; Hamoen, L. W.; Strahl, H., Analysis of Antimicrobial-Triggered Membrane Depolarization Using Voltage Sensitive Dyes. *Frontiers in Cell and Developmental Biology* **2016**, *4* (29).
168. Kelkar, D. A.; Chattopadhyay, A., The gramicidin ion channel: A model membrane protein. *Biochimica et Biophysica Acta (BBA) - Biomembranes* **2007**, *1768* (9), 2011-2025.
169. Spížek, J.; Řezanka, T., Lincomycin, clindamycin and their applications. *Appl. Microbiol. Biotechnol. Biotechnology* **2004**, *64* (4), 455-464.
170. Mahlapuu, M.; Håkansson, J.; Ringstad, L.; Björn, C., Antimicrobial Peptides: An Emerging Category of Therapeutic Agents. *Frontiers in Cellular and Infection Microbiology* **2016**, *6* (194).
171. Ruiz, N.; Falcone, B.; Kahne, D.; Silhavy, T. J., Chemical conditionality: a genetic strategy to probe organelle assembly. *Cell* **2005**, *121* (2), 307-17.
172. Htoo, H. H.; Brumage, L.; Chaikeratisak, V.; Tsunemoto, H.; Sugie, J.; Tribuddharat, C.; Pogliano, J.; Nonejuie, P., Bacterial Cytological Profiling as a Tool To Study Mechanisms of Action of Antibiotics That Are Active against *Acinetobacter baumannii*. *Antimicrob Agents Chemother* **2019**, *63* (4).
173. Nguyen, T.; Ishida, K.; Jenke-Kodama, H.; Dittmann, E.; Gurgui, C.; Hochmuth, T.; Taudien, S.; Platzer, M.; Hertweck, C.; Piel, J., Exploiting the mosaic structure of trans-acyltransferase polyketide synthases for natural product discovery and pathway dissection. *Nature biotechnology* **2008**, *26* (2), 225-233.
174. Wu, Y.; Seyedsayamdost, M. R., The polyene natural product thailandamide A inhibits fatty acid biosynthesis in Gram-positive and Gram-negative bacteria. *Biochemistry* **2018**, *57* (29), 4247-4251.
175. Mohammad, H.; Younis, W.; Ezzat, H. G.; Peters, C. E.; AbdelKhalek, A.; Cooper, B.; Pogliano, K.; Pogliano, J.; Mayhoub, A. S.; Seleem, M. N., Bacteriological profiling of diphenylureas as a novel class of antibiotics against methicillin-resistant *Staphylococcus aureus*. *PLoS One* **2017**, *12* (8), e0182821.
176. Sridhar, S.; Forrest, S.; Warne, B.; Maes, M.; Baker, S.; Dougan, G.; Bartholdson Scott, J., High-content imaging to phenotype antimicrobial effects on individual bacteria at scale. *Msystems* **2021**, *6* (3), e00028-21.
177. Smith, T. C., 2nd; Pullen, K. M.; Olson, M. C.; McNellis, M. E.; Richardson, I.; Hu, S.; Larkins-Ford, J.; Wang, X.; Freundlich, J. S.; Ando, D. M.; Aldridge, B. B., Morphological profiling of tubercle bacilli identifies drug pathways of action. *Proc Natl Acad Sci U S A* **2020**, *117* (31), 18744-18753.
178. Quach, D. T.; Sakoulas, G.; Nizet, V.; Pogliano, J.; Pogliano, K., Bacterial Cytological Profiling (BCP) as a Rapid and Accurate Antimicrobial Susceptibility Testing Method for *Staphylococcus aureus*. *EBioMedicine* **2016**, *4*, 95-103.
179. Ziegler, S.; Sievers, S.; Waldmann, H., Morphological profiling of small molecules. *Cell Chem Biol* **2021**, *28* (3), 300-319.
180. Zoffmann, S.; Vercruyse, M.; Benmansour, F.; Maunz, A.; Wolf, L.; Blum Marti, R.; Heckel, T.; Ding, H.; Truong, H. H.; Prummer, M.; Schmucki, R.; Mason, C. S.; Bradley, K.; Jacob, A. I.; Lerner, C.; Araujo Del Rosario, A.; Burcin, M.; Amrein, K. E.; Prunotto, M., Machine learning-powered antibiotics phenotypic drug discovery. *Sci Rep* **2019**, *9* (1), 5013.
181. Chao, Y.; Zhang, T., Optimization of fixation methods for observation of bacterial cell morphology and surface ultrastructures by atomic force microscopy. *Appl Microbiol Biotechnol* **2011**, *92* (2), 381-92.
182. Barcellona, M.; Cardiel, G.; Gratton, E., Time-resolved fluorescence of DAPI in solution and bound to polydeoxynucleotides. *Biochem. Biophys. Res. Commun.* **1990**, *170* (1), 270-280.

183. Kubista, M.; Aakerman, B.; Norden, B., Characterization of interaction between DNA and 4', 6-diamidino-2-phenylindole by optical spectroscopy. *Biochemistry* **1987**, *26* (14), 4545-4553.
184. Lamsa, A.; Lopez-Garrido, J.; Quach, D.; Riley, E. P.; Pogliano, J.; Pogliano, K., Rapid inhibition profiling in *Bacillus subtilis* to identify the mechanism of action of new antimicrobials. *ACS chemical biology* **2016**, *11* (8), 2222-2231.
185. Thakur, S.; Cattoni, D. I.; Nöllmann, M., The fluorescence properties and binding mechanism of SYTOX green, a bright, low photo-damage DNA intercalating agent. *European Biophysics Journal* **2015**, *44* (5), 337-348.
186. Jelínková, A.; Malínská, K.; Petrášek, J., Using FM dyes to study endomembranes and their dynamics in plants and cell suspensions. In *Plant Cell Morphogenesis*, Springer: 2019; pp 173-187.
187. ThermoFisher.com ThermoFisher Fluorescence Spectra Viewer. <https://www.thermofisher.com/order/fluorescence-spectraviewer> (accessed July 21, 2022).
188. Sridhar, S.; Forrest, S.; Warne, B.; Maes, M.; Baker, S.; Dougan, G.; Bartholdson Scott, J., High-Content Imaging to Phenotype Antimicrobial Effects on Individual Bacteria at Scale. *mSystems* **2021**, *6* (3).
189. Muller, M., *Introduction to confocal fluorescence microscopy*. SPIE press: 2006; Vol. 69.
190. Lee, J.-Y.; Kitaoka, M., A beginner's guide to rigor and reproducibility in fluorescence imaging experiments. *Molecular Biology of the Cell* **2018**, *29* (13), 1519-1525.
191. Jeckel, H.; Drescher, K., Advances and opportunities in image analysis of bacterial cells and communities. *FEMS Microbiol Rev* **2021**, *45* (4).
192. Caicedo, J. C.; Cooper, S.; Heigwer, F.; Warchal, S.; Qiu, P.; Molnar, C.; Vasilevich, A. S.; Barry, J. D.; Bansal, H. S.; Kraus, O.; Wawer, M.; Paavolainen, L.; Herrmann, M. D.; Rohban, M.; Hung, J.; Hennig, H.; Concannon, J.; Smith, I.; Clemons, P. A.; Singh, S.; Rees, P.; Horvath, P.; Lington, R. G.; Carpenter, A. E., Data-analysis strategies for image-based cell profiling. *Nat Methods* **2017**, *14* (9), 849-863.
193. Bankhead, P., Analyzing fluorescence microscopy images with ImageJ. *ImageJ* **2014**, *1* (195), 10.1109.
194. Carpenter, A. E.; Jones, T. R.; Lamprecht, M. R.; Clarke, C.; Kang, I. H.; Friman, O.; Guertin, D. A.; Chang, J. H.; Lindquist, R. A.; Moffat, J., CellProfiler: image analysis software for identifying and quantifying cell phenotypes. *Genome biology* **2006**, *7* (10), 1-11.
195. Herschede, S. R.; Gneid, H.; Dent, T.; Jaeger, E. B.; Lawson, L. B.; Busschaert, N., Bactericidal urea crown ethers target phosphatidylethanolamine membrane lipids. *Organic & Biomolecular Chemistry* **2021**, *19* (17), 3838-3843.
196. Williams, E. S.; Gneid, H.; Marshall, S. R.; Gonzalez, M. J.; Mandelbaum, J. A.; Busschaert, N., A supramolecular host for phosphatidylglycerol (PG) lipids with antibacterial activity. *Org Biomol Chem* **2021**.
197. Shimizu, L. S.; Salpage, S. R.; Korous, A. A., Functional materials from self-assembled bis-urea macrocycles. *Acc Chem Res* **2014**, *47* (7), 2116-27.
198. Geer, M. F.; Walla, M. D.; Solntsev, K. M.; Strassert, C. A.; Shimizu, L. S., Self-assembled benzophenone bis-urea macrocycles facilitate selective oxidations by singlet oxygen. *J Org Chem* **2013**, *78* (11), 5568-78.
199. Oluwatoba, D. S.; Islam, M. F.; Som, B.; Sindt, A. J.; Smith, M. D.; Shimizu, L. S.; Do, T. D., Evaluating the Effects of Metal Adduction and Charge Isomerism on Ion-Mobility Measurements using m-Xylene Macrocycles as Models. *Journal of the American Society for Mass Spectrometry* **2022**.
200. Shimizu, L. S.; Smith, M. D.; Hughes, A. D.; Shimizu, K. D., Self-assembly of a bis-urea macrocycle into a columnar nanotube. *Chemical Communications* **2001**, (17), 1592-1593.

201. Roy, K.; Wang, C.; Smith, M. D.; Dewal, M. B.; Wibowo, A. C.; Brown, J. C.; Ma, S.; Shimizu, L. S., Guest induced transformations of assembled pyridyl bis-urea macrocycles. *Chem Commun (Camb)* **2011**, 47 (1), 277-9.
202. Gao, L.; Wang, H.; Zheng, B.; Huang, F., Combating antibiotic resistance: Current strategies for the discovery of novel antibacterial materials based on macrocycle supramolecular chemistry. *Giant* **2021**, 7, 100066.
203. Dabrowa, K.; Ulatowski, F.; Lichosyt, D.; Jurczak, J., Catching the chloride: searching for non-Hofmeister selectivity behavior in systematically varied polyamide macrocyclic receptors. *Org Biomol Chem* **2017**, 15 (28), 5927-5943.
204. Kauerhof, D.; Niemeyer, J., Functionalized Macrocycles in Supramolecular Organocatalysis. *Chempluschem* **2020**, 85 (5), 889-899.
205. Shimizu, L. S.; Hughes, A. D.; Smith, M. D.; Samuel, S. A.; Ciurtin-Smith, D., Assembled Columnar Structures from bis-urea Macrocycles. *Supramol. Chem.* **2006**, 17 (1-2), 27-30.
206. Cushnie, T.; O'Driscoll, N. H.; Lamb, A. J., Morphological and ultrastructural changes in bacterial cells as an indicator of antibacterial mechanism of action. *Cellular and molecular life sciences* **2016**, 73 (23), 4471-4492.
207. Ouyang, X.; Hoeksma, J.; Lubbers, R. J.; Siersma, T. K.; Hamoen, L. W.; den Hertog, J., Classification of antimicrobial mechanism of action using dynamic bacterial morphology imaging. *Scientific Reports* **2022**, 12 (1), 1-12.
208. Schindelin, J.; Arganda-Carreras, I.; Frise, E.; Kaynig, V.; Longair, M.; Pietzsch, T.; Preibisch, S.; Rueden, C.; Saalfeld, S.; Schmid, B., Fiji: an open-source platform for biological-image analysis. *Nature methods* **2012**, 9 (7), 676-682.
209. Wainwright, M.; Canham, L.; Al-Wajeeh, K.; Reeves, C., Morphological changes (including filamentation) in *Escherichia coli* grown under starvation conditions on silicon wafers and other surfaces. *Letters in applied microbiology* **1999**, 29 (4), 224-227.
210. Braga, P. C.; Sasso, M. D.; Sala, M. T., Sub-MIC concentrations of cefodizime interfere with various factors affecting bacterial virulence. *Journal of Antimicrobial Chemotherapy* **2000**, 45 (1), 15-25.
211. Sun, Y.; Heidary, D. K.; Zhang, Z.; Richards, C. I.; Glazer, E. C., Bacterial Cytological Profiling Reveals the Mechanism of Action of Anticancer Metal Complexes. *Mol Pharm* **2018**, 15 (8), 3404-3416.
212. Jana, S.; Deb, J., Molecular understanding of aminoglycoside action and resistance. *Appl. Microbiol. Biotechnol. biotechnology* **2006**, 70 (2), 140-150.
213. Kümmel, A.; Gubler, H.; Gehin, P.; Beibel, M.; Gabriel, D.; Parker, C. N., Integration of multiple readouts into the z'factor for assay quality assessment. *Journal of biomolecular screening* **2010**, 15 (1), 95-101.
214. Share, A. I.; Patel, K.; Nativi, C.; Cho, E. J.; Francesconi, O.; Busschaert, N.; Gale, P. A.; Roelens, S.; Sessler, J. L., Chloride anion transporters inhibit growth of methicillin-resistant *Staphylococcus aureus* (MRSA) in vitro. *Chem Commun (Camb)* **2016**, 52 (48), 7560-3.
215. Salam, R.; Chowdhury, S. M.; Marshall, S. R.; Gneid, H.; Busschaert, N., Increasing membrane permeability of carboxylic acid-containing drugs using synthetic transmembrane anion transporters. *Chem Commun (Camb)* **2021**, 57 (97), 13122-13125.
216. Olsen, G.; Ulstrup, J.; Chi, Q., Crown-ether derived graphene hybrid composite for membrane-free potentiometric sensing of alkali metal ions. *ACS Applied Materials & Interfaces* **2016**, 8 (1), 37-41.
217. Murzyn, K.; Róg, T.; Pasenkiewicz-Gierula, M., Phosphatidylethanolamine-phosphatidylglycerol bilayer as a model of the inner bacterial membrane. *Biophys. J.* **2005**, 88 (2), 1091-1103.

218. Humphries, R.; Bobenchik, A. M.; Hindler, J. A.; Schuetz, A. N., Overview of changes to the clinical and laboratory standards institute performance standards for antimicrobial susceptibility testing, M100. *Journal of clinical microbiology* **2021**, *59* (12), e00213-21.

219. Märki, F.; Hänni, E.; Fredenhagen, A.; van Oostrum, J., Mode of action of the lanthionine-containing peptide antibiotics duramycin, duramycin B and C, and cinnamycin as indirect inhibitors of phospholipase A2. *Biochem. Pharmacol.* **1991**, *42* (10), 2027-2035.

BIOGRAPHY

Sarah Renée Herschede was born in Pensacola, FL and raised in New Orleans, LA. She obtained her BSc. in Chemistry and Biology from the University of New Orleans, where she studied in different analytical chemistry and behavioral science research labs. Her honors thesis focused on enhancing oil degradation after the destructive Deepwater Horizon oil spill along the Gulf Coast using die sensitized TiO₂ nanotubes. After completing her undergraduate degree, she went to Thailand to study the declining coral ecosystem in the Gulf of Thailand. Sarah returned to New Orleans for graduate school to attend Tulane University under the study of Dr. Nathalie Busschaert, focusing on lipid binding in membranes and antibiotic development. On the weekends, she enjoys being around water or enjoying live music with her dog Benny.